

ELECTROMAGNETIC COMPOSITE NANOFIBERS

by

MASOUMEH BAYAT

B. Sc. Tehran University, Iran 2003

A THESIS SUBMITTED IN PARTIAL FULFILMENT OF THE

REQUIREMENTS FOR THE DEGREE OF

MASTER OF APPLIED SCIENCE

in

THE FACULTY OF GRADUATE STUDIES

(MATERIALS ENGINEERING)

THE UNIVERSITY OF BRITISH COLUMBIA

(Vancouver)

December 2011

© Masoumeh Bayat, 2011

ABSTRACT

Multifunctional composite nanofibers containing magnetite (Fe_3O_4) nanoparticles are developed in this work. The multifunctional composite nanofibers are proved to be electrically conductive and magnetically permeable. Polyacrylonitrile (PAN) is used as an appropriate polymer which is capable of being pyrolyzed to produce electrically conductive carbon nanofiber matrix. In order to develop magnetic nanofibers, various amounts of Fe_3O_4 nanoparticles ranging from 3 to 10wt.% are embedded in the PAN nanofiber matrix. In addition, the electromagnetic behaviour of nanocomposites made of two different sizes (GA:20-30nm and GB:10-20nm) of Fe_3O_4 nanoparticles is examined. Electrospun composite nanofibers are thermally treated at both 700°C and 900°C to produce electromagnetic carbon nanofiber composites. The composite nanofibers are characterized using scanning electron microscopy (SEM), transmission electron microscopy (TEM), X-ray diffractometry (XRD), Raman spectroscopy, four-point probe and Superconducting Quantum Interference Device (SQUID). Electromagnetic Interference Shielding Effectiveness (EMI SE) of the pristine carbon nanofibers as well as electromagnetic composite nanofibers is examined using Vector Network Analyzer with Thru-Reflect-Line (TRL) calibration. Uniform nanofibers are obtained for all samples with choosing 10wt.% PAN concentration in Dimethylformamide (DMF) with larger fiber diameters for composite nanofibers as compared with pristine carbon nanofiber. The magnetic properties of Fe_3O_4 nanoparticles are successfully transferred into the as-spun Fe_3O_4 /PAN composite nanofibrous structure. The electromagnetic properties of the composite materials are tuned by adjusting the amount and size of Fe_3O_4 nanoparticles in the matrix and carbonization process. By embedding 10wt.% of GA:20-30nm Fe_3O_4 nanoparticle, saturation magnetization (M_s) of 16emu/g is

obtained with electrical conductivity of 9.2S/cm for composite nanofiber carbonized at 900°C. However, the M_s and electrical conductivity values respectively decrease to 9.0emu/g and 1.96S/cm for composite made of 10wt.% GB:10-20nm Fe_3O_4 nanoparticle carbonized at 900°C. The high surface area provided by the ultrafine fibrous structures, the flexibility and tuneable electromagnetic properties are expected to enable the expansion of the design options for a wide range of electronic devices such as sensors and actuators as well as Electromagnetic Interference Shielding Effectiveness (EMI SE). The electromagnetic composite nanofibers are demonstrated to act as strong electromagnetic interference shield of up to 70-80dB.

TABLE OF CONTENTS

ABSTRACT.....	ii
TABLE OF CONTENTS.....	iv
LIST OF TABLES.....	x
LIST OF FIGURES.....	xii
LIST OF SYMBOLS AND ABBREVIATIONS.....	xx
ACKNOWLEDGMENTS.....	xxv
Chapter 1. Introduction and objectives.....	1
Chapter 2. Literature review and background.....	5
2.1 Introduction to electrospinning.....	5
2.2 Process fundamentals.....	6
2.3 Effect of processing parameters.....	8
2.3.1 Solution parameters.....	8
2.3.1.1 Solution viscosity.....	8
2.3.1.2 Surface tension.....	10
2.3.1.3 Ionic salt addition.....	10
2.3.1.4 Dielectricity of solvent.....	11
2.3.2 Processing conditions.....	12
2.3.2.1 Voltage.....	12
2.3.2.2 Feed rate.....	13
2.3.2.3 Diameter of pipette orifice/needle.....	13
2.3.2.4 Spinning distance.....	13

2.3.2.5	Temperature.....	14
2.3.2.6	Humidity.....	14
2.4	Potential applications for electrospun nanofibers.....	15
2.4.1	Biomedical applications.....	16
2.4.1.1	Medical prosthesis.....	16
2.4.1.2	Wound dressing.....	16
2.4.1.3	Tissue engineering.....	17
2.4.1.4	Drug delivery.....	18
2.4.2	Filtration.....	20
2.4.3	Nanofibers for electronic and optical device applications.....	22
2.4.3.1	Sensors.....	22
2.4.3.2	Energy generation.....	22
2.5	Multifunctional composite nanofibers.....	23
2.5.1	Electromagnetic Fe ₃ O ₄ /carbon composite nanofibers.....	24
2.5.2	PAN-based carbon nanofibers.....	25
2.5.2.1	Electrospinning of Polyacrylonitrile (PAN) solution.....	26
2.5.2.2	Stabilization of electrospun PAN nanofibers.....	27
2.5.2.3	Carbonization of electrospun PAN nanofibers.....	29
2.5.2.3.1	Chemical changes during carbonization.....	29
2.5.2.3.2	Microstructure evolution during carbonization.....	29
2.5.2.3.3	Electrical conductivity of PAN-based carbon fibers.....	30
2.5.3	Magnetite employed as magnetic nanofillers.....	30
2.5.3.1	Ferrimagnetism.....	30

2.5.3.2	Crystal structure of magnetite.....	31
2.5.3.3	Hysteresis curves of magnetic materials	32
2.5.3.4	Size-dependent magnetic properties	34
2.5.4	Electromagnetic Interference Shielding Efficiency (EMI SE)	36
2.5.4.1	Introduction	36
2.5.4.2	Shielding mechanism.....	38
2.5.4.3	Parameters affecting the shielding performance of a matter	40
2.5.4.3.1	Complex permeability and permittivity parameters.....	40
2.5.4.3.2	Electrical conductivity.....	41
2.5.4.3.3	Shield thickness.....	43
2.5.4.3.4	Filler aspect ratio.....	44
2.5.4.3.5	Nanosize effect of spherical fillers.....	44
2.5.4.4	Shielding materials	45
2.5.4.4.1	Metals	45
2.5.4.4.2	Intrinsically conducting polymers.....	45
2.5.4.4.3	CNT/CNF-polymer composites	46
2.5.4.4.4	Electromagnetic composites.....	48
2.5.4.4.5	Composite nanofibers.....	51
Chapter 3.	Experimental.....	53
3.1	Materials	53
3.2	Polymer solution preparation	53
3.3	Electrospun nanofiber fabrication.....	53
3.4	Carbonization process.....	54

3.5	Characterization methods.....	56
Chapter 4.	Results.....	59
4.1	Microstructural and compositional characterizations	59
4.1.1	SEM observations	59
4.1.2	TEM observations.....	62
4.1.3	XRD analysis	65
4.1.3.1	Fe ₃ O ₄ nanoparticles	65
4.1.3.2	GA:20-30nm Fe ₃ O ₄ /carbon nanofiber composites	67
4.1.3.3	GB:10-20nm Fe ₃ O ₄ /carbon nanofiber composites	70
4.1.3.4	GA:20-30nm/CNF and GB:10-20nm/CNF composites	73
4.1.4	Raman spectroscopy	75
4.1.4.1	GA:20-30nm Fe ₃ O ₄ / carbon nanofiber composites	75
4.1.4.2	GB:10-20nm Fe ₃ O ₄ / carbon nanofiber composites	78
4.1.4.3	GA:20-30nm Fe ₃ O ₄ and GB:10-20nm Fe ₃ O ₄ / carbon nanofiber composites..	80
4.2	Physical properties	81
4.2.1	Electrical conductivity	81
4.2.1.1	GA:20-30nm Fe ₃ O ₄ /carbon nanofiber composites	81
4.2.1.2	GB:10-20nm Fe ₃ O ₄ /carbon nanofiber composites	82
4.2.1.3	GA:20-30nm Fe ₃ O ₄ and GB:10-20nm Fe ₃ O ₄ /carbon nanofiber composites..	83
4.2.2	Magnetic properties	84
4.2.2.1	Magnetic properties of Fe ₃ O ₄ nanoparticles	84
4.2.2.2	Magnetic properties of as-spun nanofibers.....	86
4.2.2.3	Carbonized composite nanofibers	89

4.2.2.3.1	GA:20-30nm Fe ₃ O ₄ /carbon nanofiber composites.....	89
4.2.2.3.2	GB:10-20nm Fe ₃ O ₄ /carbon nanofiber composites.....	95
4.2.2.4	GA:20-30nm and GB:10-20nm Fe ₃ O ₄ /carbon nanofiber composites	99
4.3	Electromagnetic Interference Shielding Effectiveness	99
4.3.1	Effect of Fe ₃ O ₄ content	99
4.3.2	Pyrolysis effect.....	102
4.3.3	Thickness	103
4.3.4	Effect of the size of Fe ₃ O ₄ nanoparticles	105
Chapter 5.	Discussion.....	108
5.1	Microstructural and compositional characterizations	108
5.1.1	SEM observations	108
5.1.2	TEM observations.....	109
5.1.3	XRD analysis	109
5.1.3.1	Nanoparticles.....	109
5.1.3.2	GA:20-30nm Fe ₃ O ₄ /carbon nanofiber composites	110
5.1.3.3	GB:10-20nm Fe ₃ O ₄ /carbon nanofiber composites	113
5.1.4	Raman spectroscopy	114
5.1.4.1	GA:20-30nm Fe ₃ O ₄ /carbon nanofiber composites	114
5.1.4.2	GB:10-20nm Fe ₃ O ₄ /carbon nanofiber composites	117
5.2	Physical properties	118
5.2.1	Electrical conductivity	118
5.2.1.1	GA:20-30nm Fe ₃ O ₄ /carbon nanofiber composite.....	118
5.2.1.2	GB:10-20nm Fe ₃ O ₄ /carbon nanofiber composite.....	122

5.2.1.3	GA:20-30nm Fe ₃ O ₄ and GB:10-20nm Fe ₃ O ₄ / carbon nanofiber composites	124
5.2.2	Magnetic properties	125
5.2.2.1	Nanoparticles	125
5.2.2.2	Nanofibers	128
5.2.2.3	Carbonized nanofibers	130
5.2.2.4	Saturation magnetization (M _s).....	130
5.2.2.5	Coercivity (H _c) and remanent magnetization (M _r)	133
5.3	Electromagnetic Interference Shielding Effectiveness	136
5.3.1	Fe ₃ O ₄ effect on shielding	136
5.3.1.1	Total shielding effectiveness (SE _{total})	136
5.3.1.2	Shielding by reflection (SE _R) or absorption (SE _A)	139
5.3.2	Effect of pyrolysis process.....	141
5.3.3	Effect of thickness on shielding.....	142
5.3.3.1	Total shielding effectiveness (SE _{total})	142
5.3.3.2	Shielding by reflection (SE _R) or absorption (SE _A)	143
5.3.4	The effect of the size of Fe ₃ O ₄ nanoparticles.....	144
5.3.5	EMI SE of PDMS-coated pristine carbon nanofiber	145
5.3.6	Shielding performance at low frequencies.....	146
5.3.7	Comparison with published results.....	147
Chapter 6.	Conclusions.....	149
References	153

LIST OF TABLES

Table 2-1 Shielding effectiveness and the amount of leakage.....	37
Table 2-2 A summary of shielding performance study on CF/polymer composites	47
Table 2-3 A summary of EMI SE study on CNT/polymer composites	48
Table 2-4 A short summary of shielding performance of electromagnetic of selected polymer composites.....	51
Table 3-1 Summary of designated codes for different samples containing GA:20-30nm Fe ₃ O ₄ nanoparticles	56
Table 3-2 Summary of designated codes for different samples containing GB:10-20nm Fe ₃ O ₄ nanoparticles	56
Table 3-3 The experimental details (specimen dimension and mass) used for the electrical conductivity and SQUID measurements.....	57
Table 4-1 Fiber diameter (D _f) of as-spun and carbonized nanofibers	61
Table 4-2 Average particles size of GA:20-30nm Fe ₃ O ₄ nanoparticles and as-spun and carbonized composite nanofibers containing GA:20-30nm Fe ₃ O ₄ at two carbonization temperatures, 700°C and 900°C.....	65
Table 4-3 2θ ₍₀₀₂₎ and d ₍₀₀₂₎ (nm) of pristine and composite carbon nanofibers (900°C)	70
Table 4-4 2θ ₍₀₀₂₎ and d ₍₀₀₂₎ (nm) of pure and composite carbon nanofibers	73
Table 4-5 Degree of graphitization, R=I _G /I _D and the in-plane sizes of graphite crystals (L _a) of pristine and composite carbon nanofibers containing GA:20-30nm Fe ₃ O ₄	78
Table 4-6 Degree of graphitization, R=I _G /I _D and in-plane sizes of graphite crystals (L _a) of pristine and composite carbon nanofibers containing GB:10-20nm Fe ₃ O ₄	80

Table 4-7 M_s , M_r and H_c of GA:20-30nm Fe_3O_4 and GB:10-20nm Fe_3O_4 nanoparticles at 300K	86
Table 4-8 M_s , M_r and H_c of as-spun composite nanofibers containing GA:20-30nm Fe_3O_4 nanoparticles at 300K	89
Table 4-9 M_s , M_r and H_c of as-spun composite nanofibers containing GB:10-20nm Fe_3O_4 nanoparticles at 300K	89
Table 4-10 M_s , M_r and H_c of GA:20-30nm Fe_3O_4 /carbon nanofiber composites at 300K.....	92
Table 4-11 M_s , M_r and H_c of GB:10-20nm Fe_3O_4 /carbon nanofiber composites at 300K.....	98
Table 4-12 SE_{total} , SE_R and SE_A as a function of Fe_3O_4 content (wt.%) at $f=10.4GHz$	102
Table 4-13 SE_{total} , SE_R and SE_A of 5wt.% GA:20-30nm Fe_3O_4 / carbon nanofiber composite with various thicknesses at working frequency of 10.4GHz	105
Table 5-1 Electrical conductivity (σ) of GA: 20-30nm Fe_3O_4 /carbon nanofiber composites	122
Table 5-2 Electrical conductivity (σ) of GB:10-20nm Fe_3O_4 /carbon nanofiber composites.....	123
Table 5-3 SE_{total} of pristine carbon nanofiber and composite carbon nanofibers at 10.4GHz....	142
Table 5-4 SE_{total} , SE_A and SE_R of composite carbon nanofibers containing various Fe_3O_4 content (wt.%) as a function of fiber diameter, electrical conductivity, particles' size and thickness (at 10.4GHz).....	145

LIST OF FIGURES

Figure 2-1 The basic electrospinning setup.	7
Figure 2-2 Different regions of an electrospinning jet: Taylor cone, instability and instability regions.....	7
Figure 2-3 SEM images of electrospun 5wt.% Fe ₃ O ₄ /PAN nanofibers (a) 6wt%, (b) 7wt%, (c) 9wt.% and (d) 11wt% PAN/DMF solutions.	9
Figure 2-4 SEM image of a porous fiber.	15
Figure 2-5 Potential applications of electrospun polymer based nanofibers.	16
Figure 2-6 Cumulative release profiles of model drugs from (●) NAP-, (■) IND-, (▲) IBU-, and (▼) SUL-loaded electrospun CA fiber mats and (○) NAP-, (□) IND-, (Δ) IBU-, and (▽) SUL-loaded solvent-cast CA films by total immersion technique during (a) 0-1440 min and (b) 0-120 min.	20
Figure 2-7 The efficiency of a filter increases with decrease in fiber diameter.	21
Figure 2-8 Photocurrent density vs. voltage characteristics of TiO ₂ nanorod electrode with PVDF-HFP gel electrolyte at AM1.5 global (100mW/cm ²) illumination. The inset is IPCE spectrum for the same electrode. The TiO ₂ nanorod electrode area was 0.16cm ²	23
Figure 2-9 Chemical structure of Polyacrylonitrile (PAN).....	26
Figure 2-10 The process of stabilization and subsequent carbonization of PAN-based nanofibers.	28
Figure 2-11 A simple representation of the magnetic spins in a ferrimagnetic oxide.	31
Figure 2-12 Spinel crystal structure of Fe ₃ O ₄	32
Figure 2-13 Magnetization vs. magnetic field (Hysteresis) curve of ferromagnetic materials. ...	33

Figure 2-14 Effect of particle size on the coercivity of magnetic particles.	36
Figure 2-15 EMI SE mechanisms through reflection, absorption and multiple reflections.	39
Figure 2-16 a. EMI SE as a function of frequency measured in the 8.2-12.4 GHz range of CNT-PS foam composites with various CNT concentrations, b. EMI SE at 10 GHz as a function of electrical conductivity of CNT-PS foam composites which increases with CNT concentration (wt.%)	42
Figure 2-17 EMI SE as a function of sample thickness of 15wt.% SWCNT/EVA composites...	43
Figure 3-1 The tube furnace used to carbonize the as-spun nanofibers. (The as-spun Fe ₃ O ₄ /PAN nanofiber is shown that is placed in the sample holder.)	54
Figure 3-2 The procedure used to carbonize the as-spun PAN-based nanofibers.	55
Figure 3-3 Experimental plan for this study.	55
Figure 3-4 Four-point probe method to measure the electrical conductivity using 4 copper electrodes.	57
Figure 3-5 Scattering parameters measurement set-up.....	58
Figure 4-1(a-c) SEM micrographs of (a) as-spun pure PAN nanofibers (10PAN) and pure PAN nanofibers carbonized at (b) 700°C (10PAN700) and (c) 900°C (10PAN900) samples.....	59
Figure 4-2 SEM micrographs of (a) as-spun 5wt.% (20-30nm) Fe ₃ O ₄ /PAN composite nanofibers (A5F10PAN) and composite nanofibers carbonized at (b) 700°C (A5F700) and (c) 900°C (A5F900) samples.....	60
Figure 4-3 SEM micrographs of (a) as-spun 5wt.% (10-20nm) Fe ₃ O ₄ /PAN composite nanofibers (B5F10PAN) and composite nanofibers carbonized at (b) 700°C (B5F700) and (c) 900°C (A5F900) samples.....	61

Figure 4-4 TEM micrographs of two different sizes of (a) GA:20-30nm Fe ₃ O ₄ nanoparticles and (b) GB:10-20nm Fe ₃ O ₄ nanoparticles.....	62
Figure 4-5 TEM micrographs of as-spun composite nanofibers containing 10wt.%Fe ₃ O ₄ fabricated with	63
Figure 4-6 TEM micrographs of composite nanofibers (a) 10wt.% GA:20-30nm Fe ₃ O ₄ carbonized at 700°C and (b) 900°C, (c) 10wt.% GB:10-20nm Fe ₃ O ₄ carbonized at 700°C and (d) 900°C.....	64
Figure 4-7 TEM micrographs of composite nanofibers carbonized at 900°C made of GA:20-30nm containing (a) 10 and (b) 5wt.%Fe ₃ O ₄ nanoparticles.	65
Figure 4-8 XRD patterns of GA:20-30nm and GB:10-20nm Fe ₃ O ₄ nanoparticles with corresponding Fe ₃ O ₄ and NaCl peaks.....	66
Figure 4-9 XRD patterns of pure and composite carbon nanofibers containing GA:20-30nm Fe ₃ O ₄ nanoparticles.....	69
Figure 4-10 2θ ₍₀₀₂₎ shifts towards higher degrees with adding (GA:20-30nm) Fe ₃ O ₄ wt.% for samples carbonized at (a) 700°C and (b) 900°C.....	70
Figure 4-11 XRD patterns of pure and composite carbon nanofibers containing	72
Figure 4-12 2θ ₍₀₀₂₎ shifts towards higher degrees with adding (GB:10-20nm) Fe ₃ O ₄ wt.% for samples carbonized at (a) 700°C and (b) 900°C.....	73
Figure 4-13 XRD patterns of A10F700, B10F700, A10F900 and B10F900 samples.....	75
Figure 4-14 Raman spectroscopy of pristine carbon nanofibers carbonized at (a) 700°C and (b) 900°C and composite carbon nanofibers with 5wt.% GA:20-30nm Fe ₃ O ₄ nanoparticles carbonized at (c) 700°C and (d) 900°C.....	77

Figure 4-15 Raman spectroscopy of pristine carbon nanofibers carbonized at (a) 700°C and (b) 900°C and composite carbon nanofibers with 5wt.% GB:10-20nm Fe₃O₄ nanoparticles carbonized at (c) 700°C and (d) 900°C..... 79

Figure 4-16 Electrical conductivity of pristine carbon nanofiber and composite carbon nanofibers containing GA: 20-30nm Fe₃O₄ nanoparticles as a function of Fe₃O₄ wt.% and carbonization temperature (700°C and 900°C). 82

Figure 4-17 Electrical conductivity of pristine carbon nanofiber and composite carbon nanofibers containing GB:10-20nm Fe₃O₄ nanoparticles as a function of Fe₃O₄ wt.% and carbonization temperature (700°C and 900°C). 83

Figure 4-18 M-H curves of GA:20-30nm and GB:10-20nm Fe₃O₄ nanoparticles. 86

Figure 4-19 M-H curves of as-spun composite nanofibers containing 3, 5 and 10wt.% GA:20-30nm Fe₃O₄ nanoparticles (A3F, A5F and A10F respectively) and GA:20-30nm Fe₃O₄ nanoparticles (added in the inset). 88

Figure 4-20 M-H curves of as-spun composite nanofibers containing 3, 5 and 10wt.% GB:10-20nm Fe₃O₄ nanoparticles (B3F, B5F and B10F respectively). 88

Figure 4-21 M-H curves of as-spun and composite nanofibers containing 10wt.% GA:20-30nm Fe₃O₄ nanoparticles carbonized at 700°C and 900°C, (A10F, A10F700 and A10F900, respectively)..... 91

Figure 4-22 M-H curves of as-spun and composite nanofibers containing 5wt.% GA:20-30nm Fe₃O₄ nanoparticles carbonized at 700°C and 900°C, (A5F, A5F700 and A5F900, respectively). 91

Figure 4-23 M-H curves of as-spun and composite nanofibers containing 3wt.% GA:20-30nm Fe₃O₄ nanoparticles carbonized at 700°C and 900°C, (A3F, A3F700 and A3F900, respectively). 92

Figure 4-24 M-H curves of composite carbon nanofibers containing GA:20-30nm Fe₃O₄ nanoparticles carbonized at 700°C. 94

Figure 4-25 M-H curves of composite carbon nanofibers containing GA:20-30nm Fe₃O₄ nanoparticles carbonized at 900°C. 94

Figure 4-26 M-H curves of as-spun and composite nanofibers containing 10wt.% GB:10-20nm Fe₃O₄ carbonized at 900°C (B10F and B10F900, respectively) and GB:10-20nm Fe₃O₄ nanoparticles in the inset..... 96

Figure 4-27 M-H curves of as-spun and composite nanofibers containing 5wt.% GB:10-20nm Fe₃O₄ carbonized at 900°C (B5F and B5F900, respectively) and GB:10-20nm Fe₃O₄ nanoparticles in the inset..... 97

Figure 4-28 M-H curves of as-spun and composite nanofibers containing 3wt.% GB:10-20nm Fe₃O₄ carbonized at 900°C (B3F and B3F900, respectively) and GB:10-20nm Fe₃O₄ nanoparticles in the inset..... 97

Figure 4-29 M-H curves of composite nanofibers carbonized at 900°C containing 3, 5 and 10wt.%GB:10-20nm Fe₃O₄ nanoparticles respectively designated as B3F900, B5F900 and B10F900..... 98

Figure 4-30 The comparison of SE_{total} of 10PAN, 10PAN900, A3F900 and A5F900 samples as a function of frequency (8.2-12.4GHz). (The thickness of all samples is 0.7 mm). 101

Figure 4-31 SE_R (-dB) of pristine carbon nanofibers, 3wt.% and 5wt.% GA:20-30nm Fe_3O_4 /carbon nanofibers composites all carbonized at 900°C respectively designated as APAN900, A3F900 and A5F900.....	101
Figure 4-32 SE_A (-dB) of pristine carbon nanofibers, 3wt.% and 5wt.% GA:20-30nm Fe_3O_4 /carbon nanofibers composites all carbonized at 900°C respectively designated as 10PAN900, A3F900 and A5F900.....	102
Figure 4-33 Comparison of SE_{total} of 10PAN, 10PAN700 and 10PAN900 samples as a function of frequency. (The thickness of all samples is ~0.1 mm).	103
Figure 4-34 SE_{total} as a function of frequency for A5F900 samples with different thicknesses. 104	
Figure 4-35 SE_{total} as a function of frequency (8.2-12.4GHz) for 10PAN900, A5F900 and B5F900 samples. (The thickness of all samples is ~0.7mm).....	106
Figure 4-36 SE_{total} , SE_R and SE_A values of pristine carbon nanofiber, 5wt.% GA:20-30nm Fe_3O_4 and 5wt.% GB:10-20nm Fe_3O_4 nanoparticles /carbon nanofiber composites (respectively designated as A5F900 and B5F900) as a function of the size of nanoparticles. Data are reported at working frequency of 10.4GHz.	107
Figure 5-1 2θ and $d_{(002)}$ of pristine and composite carbon nanofibers composed of GA:20-30nm Fe_3O_4 at two carbonization temperatures, 700°C and 900°C.....	112
Figure 5-2 Schematic representation for the preparation of G-carbon.	113
Figure 5-3 $2\theta_{(002)}$ and $d_{(002)}$ of GA:20-30nm Fe_3O_4 and GB: 10-20nm Fe_3O_4 -based carbon nanofiber composites obtained at 900°C carbonization temperatures.....	114
Figure 5-4 R and L_a obtained for pristine carbon nanofiber and GA:20-30nm Fe_3O_4 -based carbon nanofiber composite.....	117

Figure 5-5 Graphitization of carbon nanofiber matrix using different sizes of Fe ₃ O ₄ nanoparticles (GA:20-30nm and GB:10-20nm) carbonized at 900°C.....	118
Figure 5-6 The R=I _G /I _D ratio, d ₍₀₀₂₎ and Electrical conductivity of GA:20-30nmFe ₃ O ₄ /carbon nanofiber composites carbonized at 700°C and 900°C.	121
Figure 5-7 R=I _G /I _D ratio, d ₍₀₀₂₎ and electrical conductivity of GA:20-30nmFe ₃ O ₄ /carbon nanofiber composites carbonized at 700°C and 900°C.	123
Figure 5-8 Electrical conductivity and d ₍₀₀₂₎ of pure carbon nanofiber and composite carbon nanofibers containing GA: 20-30nm and GB:10-20nm Fe ₃ O ₄ nanoparticles.	125
Figure 5-9 Magnetic properties of GA:20-30nm and GB:10-20nm Fe ₃ O ₄ nanoparticles	127
Figure 5-10 Comparison of M _s and H _c of as-spun nanofibers and nanoparticles containing GA:20-30nm and GB:10-20nm Fe ₃ O ₄ nanoparticles. (BFPAN: as-spun nanofibers containing GB nanoparticles, AFPAN: as-spun nanofibers containing GA nanoparticles).....	129
Figure 5-11 M _s as a function of Fe ₃ O ₄ content, size and carbonization temperature.	132
Figure 5-12 M _r and H _c as a function of both carbonization temperature and Fe ₃ O ₄ wt.%	135
Figure 5-13 Average SE _{total} values of pristine carbon nanofiber (10PAN900) and 3wt.% and 5wt.% GA:20-30nm Fe ₃ O ₄ nanoparticles in carbon nanofiber composites (respectively A3F900 and A5F900) with the thickness of 0.7mm and as a function of electrical conductivity of the composite nanofibers.	141
Figure 5-14 SE _{total} , SE _R and SE _A of A5F900 samples with various thicknesses (0.1mm-0.9mm).	143
Figure 5-15 (a) SE _{total} as a function of frequency (8.2-11.5GHz) for pristine carbon nanofiber (10PAN900) and PDMS-coated carbon nanofiber (10PAN900), (b) Flexibility of PDMS-coated carbon nanofiber. (The thickness of all samples is ~0.25mm).	146

Figure 5-16 SE_{total} of A3F900 sample with the thickness of 0.25mm. 147

Figure 5-17 A comparison of the EMI SE of 5wt.% GA:20-30nm Fe_3O_4 /carbon nanofiber composite with electrically conducting and electromagnetic composites reported in literature. 148

LIST OF SYMBOLS AND ABBREVIATIONS

σ_{ac}	Alternating electrical conductivity
$\mu_r = \mu' - j\mu''$	Complex permeability
$\varepsilon_r = \varepsilon' - j\varepsilon''$	Complex permittivity
σ_{dc}	DC electrical conductivity
ε_0	Dielectric constant of vacuum
$\tan \delta_\varepsilon$	Dielectric loss (loss tangent)
σ	Electrical conductivity
ρ	Electrical resistivity
f	Frequency
μ''	Imaginary part of complex permeability
ε''	Imaginary part of complex permittivity
$\tan \delta_\mu = \frac{\mu''}{\mu'}$	Magnetic loss
μ'	Real part of complex permeability
ε'	Real part of complex permittivity
T	Unit of applied magnetic field, tesla
Oe	Unit of magnetic field, oersted
S/cm	Unit of electrical conductivity, siemens per centimeter
Ω	Unit of electrical resistance, ohm
emu/g	Unit of magnetization

dB	Unit of shielding, decibel
A	Absorption
C ₃ H ₃ N	Acrylonitrile
–CH ₂ CH(CN)–	Acrylonitrile entities
K _{eff}	Anisotropy constant
H	Applied magnetic field
d ₍₀₀₂₎	Average interlayer d-spacing of (002) plane
BaF	Barium ferrite
BSU	Basic structural unit
CF	Carbon fiber
CNFs	Carbon nanofibers
CNTs	Carbon nanotubes
CA	Cellulose acetate
H _c	Coercivity
R=I _G /I _D	Degree of graphitization
A _{eff}	Effective absorbance
EMI SE	Electromagnetic Interference Shielding Effectiveness
EVA	Ethylene vinyl alcohol
GHz	Gigahertz
M-H	Hysteresis curve
IBU	Ibuprofen
IND	Indomethacin
ICPs	Intrinsically conducting polymers

Fe_3O_4 or Fe_2O_3	Iron oxide
Li	Lithium
M	Magnetic moment
MRI	Magnetic resonance imaging
Fe_3O_4	Magnetite
D_{SPM}	Multi domain size
MWCNT/SWCNT	Multi wall or single wall carbon nanotubes
MD	Multi-domain
SE_M	Multiple reflection
DMF	N, N-Dimethylformamide
NAP	Naproxen
$\text{C}\equiv\text{N}$	Nitrile group
1D	One dimensional
PEDOT	Poly (3,4-ethylenedioxy thiophene)
PVDF	Poly vinylidene fluoride
PDLA	Poly(D,L-lactic acid
PLGA	Poly(lactide-co-glycolide)
PLA	Poly(L-lactide)
PVP	Poly(N-vinyl pyrrolidone)
PVP	Poly(N-vinyl pyrrolidone)
PAN	Polyacrylonitrile
PANI	Polyaniline
CR	Polychloroprene

PDMS	Polydimethylsiloxane
PDS	Polydioxanone
PEG	Polyethylene glycol
PPy	Polypyrrole
PS	Polystyrene
C ₂ H ₅ CN	Propionitrile
PANI-TSA	P-toluene sulfonic acid doped polyaniline
RAMs	Radar absorbing materials
R	Reflection
M _r	Remanent magnetization
H _{sat}	Saturation field
M _s	Saturation magnetization
SEM	Scanning electron microscopy
SE _A	Shielding by absorption
SE _R	Shielding by reflection
Ag	Silver
SD	Single domain
D _{SD}	Single domain size
SMCs	Smooth Muscle Cells
M _r /M _s	Squarness ratio
SUL	Sulindac
SQUID	Superconducting Quantum Interference Device
SPM	Superparamagnetism

θ	The angle between the magnetization and the easy axis
$2\theta_{(002)}$	The angle of (002) graphitic plane
L_a	The in-plane crystallite size
$k_B T$	Thermally-activated random fluctuation of the net spins
TRL	Calibration Thru-Reflect-Line
TiO_2	Titanium dioxide
SE_{total}	Total shielding efficiency
S11 and S21	Transmission and reflection scattering parameters
TEM	Transmission electron microscopy
T	Transmittance
V	Volume of nanoparticle
8.2-12.4GHz	X-band frequency range
XRD	X-ray diffractometry

ACKNOWLEDGMENTS

I wish to thank God foremost since with no doubt this accomplishment would not be possible without his blessings.

It is my great pleasure to acknowledge my supervisor Professor Frank Ko for all his support, guidance and advices during my work at UBC which was great encouragement for me throughout my study. I would also like to thank to Professor Dave Michelson from the Electrical engineering department (radio science lab) helping me to set up and perform complete set of Electromagnetic shielding tests. I would like to thank to the AFML lab supervisor, Dr. Heejae Yang for his valuable suggestions and comments during this study. I am very grateful to Mary Fletcher for his assistance with SEM and TEM microscopes as well as XRD. I would also like to thank Professor Tom Troscynski and Professor Peyman Servati for their constructive and valuable comments.

I would like to express my gratitude to my family for their continuing support and encouragement. Last but not the least, I wish to express my deepest heart-felt appreciation to my husband because of all his encouragement and understanding during my work.

I would also like to acknowledge the supporters of this work by AOARD/AFOSR, MURI and NSERC through a Discovery Grant and CFI.

Chapter 1. Introduction and objectives

Recent advances in nanotechnology have greatly expedited the development of a new generation of multifunctional materials. Multifunctional materials possess more than one physical, chemical or biological property that can be changed significantly in a controlled fashion by external stimuli such as temperature, pressure/stress, electric field, magnetic field, optical wavelength, adsorbed gas molecules and the pH value. These functionalities can be provided using different nanofillers added into an appropriate matrix.

Nanotubes, nanowires and nanoparticles are promising nanofillers to produce various functionalities. As the material size is reduced to the nanoscale, outstanding and remarkable physical and chemical properties emerge. Examples of nanomaterials include carbon nanotubes, magnetic nanoparticles and so on. For example, carbon nanotubes are well-known as having an extremely high modulus which produce strong fibers and have remarkable electronic properties as well as unique characteristics because of their specific size and structure [1]. As the size of magnetic particle decreases to nanoscale, superparamagnets or very strong permanent magnets can be created which are of utmost attention for various applications such as drug delivery and hyperthermia or data storage applications [2]. Unfortunately, the discrete nature of the nanoparticles makes them difficult to create structural forms. In order to bridge the gap between nano and macro length scales and connect the nano effect to macro-performance, there is a need for suitable carriers that are capable of preserving the functionalities of the nanofillers. Recently, one dimensional (1D) nanocomposite fibers have attracted a great deal of interest due to their enhanced electronic, optical and chemical properties. Among different methods for producing 1D structures, electrospinning is one of the most attractive methods due to its simplicity which

enables the assembly of 1D structures into higher order linear, planar or 3D nanofibrous assemblies by means of electrostatic forces [3, 4]. Electrospinning has been demonstrated to be a simple technique to produce multifunctional composite nanofibers by incorporating various functionalities into the polymer solution using different nanofillers with specific physical, electrochemical and biological properties [5-8]. In this work, we propose the creation of composite fibers containing functional nanoparticles.

A major challenge hence the objective of the composite nanofiber concept is to demonstrate that whether or not the unique functional properties of nanoparticles can be translated to the composite nanofibrous structure.

Among various multifunctional nanocomposite materials, those with electrical and magnetic properties are suitable candidates for a wide range of functions such as electrochemical applications like batteries, microwave absorbers and electromagnetic device applications [9-15]. In order to generate the electromagnetic properties, both electrically conductive and magnetically permeable components are needed. Fe_3O_4 nanoparticles (two different sizes: GB:10-20nm superparamagnetic (SPM) Fe_3O_4 nanoparticles and GA:20-30nm ferromagnetic (FM) Fe_3O_4 nanoparticles) are employed as one of these constituents as a magnetic filler. In combination with a polymer matrix, Fe_3O_4 can be used as microwave absorption structures and dampers [16] and for medical applications [17] such as drug delivery and therapy [7]. Additionally, electrical conductivity can be provided either by using electrically conducting polymers such as Polyaniline (PANI) and Polypyrrole (PPy) or Polyacrylonitrile (PAN) as a carbon fiber precursor which can be electrospun and pyrolyzed to produce electrically conducting carbon fibers. Adding magnetic nanofillers into the electrically conducting polymer matrix such as PANI and PPy have been previously investigated [18, 19]. We have selected PAN which is a predominant carbon

fiber precursor that can be processed by thermal stabilization and subsequent high temperature carbonization. The carbonization induces electrical conductivity into the produced carbon fibers [3]. Electromagnetic multifunctional composite nanofibers can be produced by using Fe_3O_4 precursor (iron acetylacacate) dissolved in PAN followed by electrospinning and carbonization to fabricate magnetic composites which are electrically conductive [13, 20, 21]. These electromagnetic composite nanofibers have been reported to be used as anode materials for high performance lithium ion-batteries [13]. On the other hand, the morphology of electrospun magnetic Fe_3O_4 /PAN nanofibers prepared by direct dispersion of Fe_3O_4 nanoparticles into a polymer solution has been studied by others [5, 22]. However, these studies focused mainly on the morphology and magnetic properties of the as-spun magnetic nanofibers leaving the carbonization process unexplored and missing the opportunity to examine and cultivate the multifunctionality of these composite nanofibers.

Therefore, another objective of this study is to illustrate the creation of electromagnetic composite nanofibers using two different sizes of Fe_3O_4 nanoparticles in a carbon matrix thus combining the magnetic properties of Fe_3O_4 with the electrical conductivity derived from the carbon nanofiber matrix.

To demonstrate the multifunctional composite nanofiber concept, we begin by dispersing Fe_3O_4 nanoparticles into PAN/N,N-Dimethylformamide (DMF) to form the spinning dope solution for electrospinning. The resulting electrospun composite nanofibers were subsequently pyrolyzed at elevated temperatures (700°C and 900°C). The electromagnetic properties of these composite nanofibers were characterized by systematic examination of the effect of Fe_3O_4 content and size and also carbonization temperature on the fiber morphology, electrical conductivity, degree of graphitization and magnetic properties.

The final objective of this study is to demonstrate the application of these multifunctional nanofibers for electromagnetic interference shielding.

Further, the fabricated electromagnetic Fe₃O₄/carbon nanofibers were coated with very thin layer of Polydimethylsiloxane (PDMS) in order to create flexible and elastomeric film for wide range of applications. The high surface area provided by the ultrafine fibrous structures, the flexibility and tuneable electromagnetic properties are expected to enable the expansion of the design options for a wide range of electronic devices. The electromagnetic shielding effectiveness (EMI SE) of the Fe₃O₄/carbon nanofiber composite was investigated over X-band frequency range (8.2-12.4GHz). Also, Laird technology agreed to test the shielding efficiency of one of our composite membrane in the frequency range of 30kHz to 1GHz. X band is used in radar applications including continuous-wave, pulsed, single-polarization, dual-polarization, synthetic aperture radar, and phased arrays. X band radar frequency sub-bands are used in civil, military, and government institutions for weather monitoring, air traffic control, maritime vessel traffic control, defence tracking, and vehicle speed detection for law enforcement [23]. X band is often used in modern radars. The shorter wavelengths of the X band allow for higher resolution imagery from high-resolution imaging radars for target identification and discrimination.

Chapter 2. Literature review and background

2.1 Introduction to electrospinning

Refining fiber diameters from the microscale to the nanoscale provides valuable properties. A large surface area to volume ratio is one of the important characteristics of nanofibers. The surface to volume ratio of nanofibers can be 1000 times larger than that of a microfiber. Furthermore, polymer nanofibers have higher flexibility in surface functionalities with improved physical and mechanical properties. Some of the techniques recently developed to produce polymer nanofibers include drawing of polymer solution, template synthesis, self-assembly, phase separation and electrospinning. Amongst all these methods, electrospinning is the process by which mass production of continuous nanofibers from various polymers is viable [24]. In electrospinning, a uniaxial stretching of a viscoelastic polymer solution produces thin fibers. This method is similar to commercial methods for producing microfibers; however, instead of mechanical or shear force, an electrostatic repulsion between surface charges is used to make very thin fibers by continuously reducing the diameter of a viscoelastic jet [25]. In the 1930's, Formhals published a series of patents about the fundamental idea of "electrostatic spinning" [26-30] explaining the method of polymer filament production using an electrostatic force. In 1971, Baumgarten [31] produced electrospun acrylic fibers of approximately 0.05–1.1 μm diameter. A high voltage direct current (DC) was applied to a constant polymer drop produced in a stainless steel capillary tube and the fibers were then deposited on a grounded metal screen. Since then, the electrospinning process has remained similar to Baumgarten's approach [31] due to its ability to make ultrafine fibrous structures of various polymers with nano-size diameters. Polymers are prepared as a solution by the addition of a solvent or melted via heating before

electrospinning. Approximately one hundred different polymers have been electrospun to produce nanofibers [4].

2.2 Process fundamentals

A basic electrospinning setup is shown in Figure 2-1. The set-up has three major components including a high voltage supplier, a collector and a spinneret (a metallic needle). A syringe containing polymer solution is connected to the spinneret. The polymer solution comes out of the syringe using a syringe pump. Usually, a direct current power supply is used for electrospinning; however alternating current power supplies can also be used [32]. Polymer solutions can be fed through the spinneret connected to a syringe containing the solution by adjusting the suitable syringe pump at a constant and controllable rate. Applying an electrical field to the polymer drop at the tip of the spinneret causes a uniform distribution of charges on polymer surface. Due to the electric field, two types of electrostatic forces exist on the surface: the repulsive electrostatic force between the surface charges and the surface tension. As a result of the balance between applied voltage and polymer surface tension a conical polymer shape known as Taylor cone will be formed at the spinneret tip. With further increase of the applied voltage beyond a critical value, surface tension can be overcome by the electric field resulting in ejection of a charged liquid jet from the nozzle. The charged liquid jet travels in a straight line for a certain length (stability region) and then goes through a whipping instability which leads to bending and stretching (instability region). Meanwhile the solvent is evaporated from the elongated fiber producing a very thin and long thread. At the end, a non-woven, randomly distributed mat is deposited on the grounded collector surface [32, 33]. The three above

mentioned regions, Taylor cone, stability region and instability region are demonstrated in Figure 2-2.

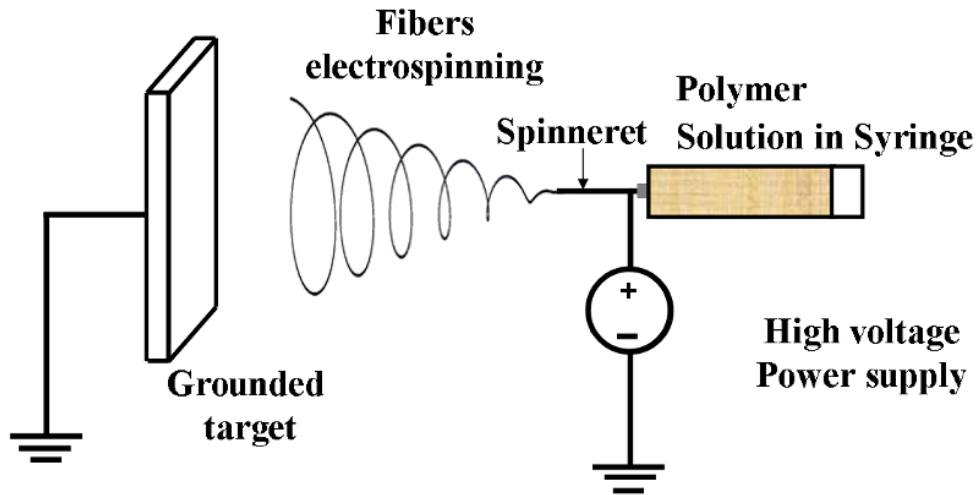


Figure 2-1 The basic electrospinning setup.

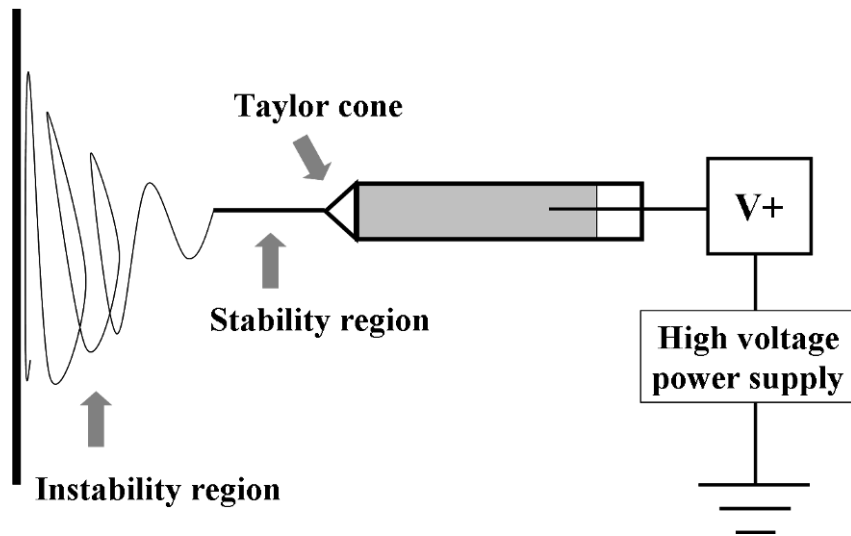


Figure 2-2 Different regions of an electrospinning jet: Taylor cone, instability and instability regions.

2.3 Effect of processing parameters

Parameters affecting the electrospinning process can be divided into two different categories: (i) solution (material) parameters including molecular weight, viscosity, conductivity, ionic conductivity and surface tension, (ii) process parameters including applied voltage, flow rate, travelling distance, ambient parameters such as temperature, humidity and air velocity in the chamber and motion of the target screen [4, 34-36]. The effect of some of these parameters on the morphology of final fiber mat is studied in the following section.

2.3.1 Solution parameters

2.3.1.1 Solution viscosity

The viscosity is one of the most significant solution parameters affecting the fiber morphology. The viscosity of final polymer solution is determined by polymer molecular weight and solution concentration and it increases with molecular weight and solution concentration [24]. Polymer solutions with lower molecular weight and/or solution concentration are prone to form beaded structure. The shape of the beads is also a function of the abovementioned parameters ranging from spherical to spindle-like structures [34, 35]. In comparison, uniform fibers with larger diameter results from viscose solutions [31, 36-38]. Thus, there is a critical viscosity below which a mixture of large beads forms. However, very viscous solutions cannot be even converted into fibers because of the cohesive nature of highly viscose solution and it is difficult to maintain and control the flow of polymer into the tip of the needle. Therefore, certain level of concentration is required in order to obtain enough entanglements of polymer molecules to get continuous electrospinning with uniform fibers [37]. Zong et al. [34] found that collection of continuous fibers during electrospinning of poly(D,L-lactic acid) (PDLA) solution of low

concentrations is challenging. However, at higher concentrations above 40wt.%, the droplet dries at the tip of the needle before the formation of a constant jet. Fiber morphology changes from a fully beaded structure for solutions of lower concentration to a uniform structure for solutions of higher concentration [34, 36, 37]. Figure 2-3 demonstrates the effect of polymer solution concentration on the morphology and uniformity of electrospun nanofibers. Lower polymer concentration (6, 8 and 9wt.% PAN/DMF in this case) results in fibers with beaded structure (Figure 2-3a, b and c) while increasing the polymer dope concentration (11wt.% PAN/DMF) leads to the formation of uniform fibers with larger diameter (Figure 2-3d). This is also confirmed in previous studies [39, 40].

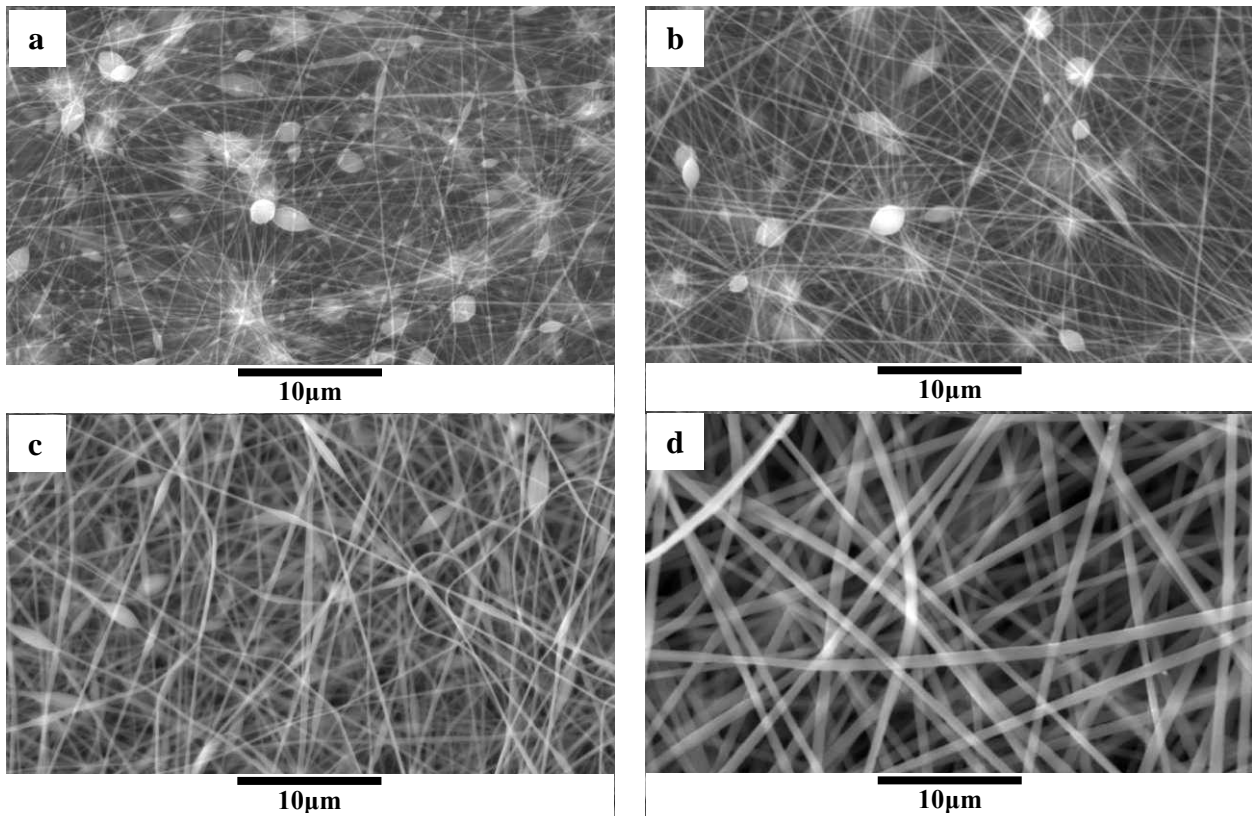


Figure 2-3 SEM images of electrospun 5wt.% Fe_3O_4 /PAN nanofibers (a) 6wt%, (b) 7wt%, (c) 9wt% and (d) 11wt% PAN/DMF solutions.

2.3.1.2 Surface tension

In the electrospinning process polymer droplet is being hold by its surface tension and charges are induced to the polymer drop due to the applied voltage. As the applied voltage is increased, the hemispherical surface of the droplet at the tip of the capillary is elongated to form a conical shape droplet known as Taylor cone. As the repulsive charge force of the charged solution overcomes its surface tension, a charged jet of solution is ejected from the capillary. The surface tension is a function of polymer concentration [41]. In the polymers with low concentrations, solvent molecules have higher tendency for congregation [35, 38] resulting in droplets and spherical bead formation [35, 37, 38]. With increasing the concentration of solution, as a result of low surface tension, the interaction between solvent and polymer molecules leads to stretching of the solution avoiding bead formation [35, 38]. Therefore, low surface tension as well as high polymer concentration or molecular weight favour the formation of more uniform fibers [42].

2.3.1.3 Ionic salt addition

In the electrospinning process, solution stretchability is caused by the charge repulsion. Adding ions will increase the charge density on the surface of the ejected polymer jet. Therefore, more electric charges are carried by the polymer jet. The increase in the charges carried by the electrospinning jet results in higher elongation forces imposed to the jet. It is known that the elongation force originates from the self-repulsion of charges in the spinning jet [34]. Increasing the charge density of polymer jet changes the shape of the beads from spherical to more spindle-like and finally uniform fibers [22, 34, 43]. Adding ionic salt raises the fluidity of the solution and surface charge of the spinning jet; as a result the spinning jet will be more fluent and larger

amount of polymer will come out of the needle and finally it increases the fiber diameter for PAN/DMF solution [44].

In addition to the effect of adding ionic salts into the polymer solution on varying its charge density, size of the ionic salts also affect on the resulting fiber diameter. Ions with smaller radius atoms have higher charge density and produce fibers with smaller average diameter [34]. The effect of adding LiCl [44-46], NaNO₃, NaCl, and CaCl₂ salts into the PAN/DMF solution and its spinnability have been studied [44]. Qin et al. [44] showed that PAN/DMF solutions containing LiCl offers the largest ionic conductivity while it decreases by adding NaNO₃, CaCl₂ and NaCl to the solution from low to the lowest. It is found that the dissolution of LiCl and also its spinning process is easier compared to other salts in PAN/DMF solution [44].

2.3.1.4 Dielectricity of solvent

The dielectric constant of a solvent is an important factor for achieving a higher productivity during the spinning process which determines its molecular polarity [42, 47]. Dielectric effect increases the electrical susceptibility of the solution and as a result increases the amount of the solution leaving the spinneret when the electrostatic field is applied. Solvents without polarity such as carbon tetrachloride are not considered as proper solvents for electrospinning process [47]. Watanog et al. [47] found that productivity of electrospinning increases with increasing the dielectric constant of solvent. Besides, beadless and well-aligned fibers were obtained for the solutions with higher dielectric constant solvents such as DMF [47].

2.3.2 Processing conditions

2.3.2.1 Voltage

One of the most important system parameters affecting on the shape of the initiating drop and also resultant fiber morphology is the magnitude of the applied voltage. The shape of the polymer drop at the tip of the capillary varies with the applied voltage. In the electrospinning process, as the applied voltage dominates the surface tension of the polymer droplet at the tip of capillary, polymer jet initiates from the droplet surface at the capillary. Increasing the applied voltage causes the reduction of the volume of Taylor cone droplet at the capillary. Therefore, the Taylor cone becomes asymmetrical and fibers with beaded structure form. The resulting fiber morphology varies from cylindrical shape fibers to a beaded structure. With further increase of the applied voltage, the polymer jet originates from inside the syringe tip which also causes the formation of beads in the fiber mat and the shape of the beads gradually varies from spindle-like to spherical-like structure [34, 37]. Demir et al. [48] showed that as the concentration or solution viscosity rises up the voltage required to initiate the polymer jet also increases. Voltage also affects on the crystallinity of the fibers. Higher voltage increases the crystallinity of the fibers. However, there is a critical voltage above which the crystallinity deteriorates as a result of short flight time [35]. Accordingly, bead formation can be prevented by increasing the polymer concentration and decreasing the applied voltage [34, 36]. There is a certain flow rate at which the electrostatic force can pull the charged jet towards the collector. If the experimental flow rate is lower than the optimal flow rate increasing the voltage decreases the collected fiber diameter [40].

2.3.2.2 Feed rate

Specific and minimum amount of solution should be supplied in order to form and maintain Taylor cone. At any given voltage, a specific feed rate is necessary to acquire a continuous jet. Higher feed rate usually increases the fiber average diameter as well as the size of the beads. At higher feeding rate, the droplet at the end of the spinneret is large. Therefore, solution is carried away with a larger velocity. Since the fibers do not have enough time to be dried before reaching the collector, larger junctions and beads can be formed [35]. In addition, the lower solution feeding rate results in the formation of smaller fibers with spindle-like beads [34].

2.3.2.3 Diameter of pipette orifice/needle

Decreasing the needle diameter results in polymer clogging and facilitates bead formation [35].

2.3.2.4 Spinning distance

Both the flight time and the strength of electric field are affected with the distance between the tip and the collector known as spinning distance. Shorter distance results in limited flight time and stronger electric field, i.e. more acceleration of the jet toward the collector, thus merging the fibers together [35]. Decreasing the travelling distance creates thick and curled PAN nanofibers with sponge like appearance which is related to the deposition of wet fibers on the collector and lack of drying time [39].

2.3.2.5 Temperature

Increasing the temperature leads to a decrease in solution viscosity and increase the polymer solubility. This leads to even more stretching the polymer and thus producing more uniform and fibers with smaller diameter [35]. Limitation to loose the functionalities of biological components in the electrospinning at higher temperature is a drawback of performing the process at high temperature [35].

2.3.2.6 Humidity

The morphology of electrospun nanofiber is also affected by the interactions caused between the surrounding electrospinning environment and the polymer solution. Highly humid spinning environment has been found to create pores on the surface of electrospun nanofibers. During the electrospinning, water vapours form on the surface of the fibers due to the cooling of the surface of the spinning jet. As both water vapour and solvent evaporate pores form on the surface of the fibers [35]. Medeiros et al. [49] demonstrated the fiber surface is no longer smooth and pores are created on the fiber surface above a certain critical humidity level (depending on the type of the polymer). Besides, the pore size is proved to enlarge with increasing the humidity. Figure 2-4 shows the pore formation on the electrospun fiber surface of polystyrene (PS).

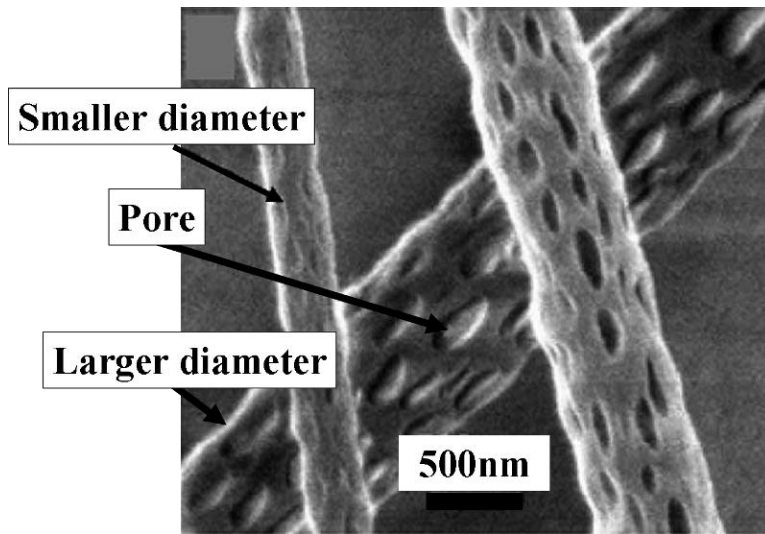


Figure 2-4 SEM image of a porous fiber.

2.4 Potential applications for electrospun nanofibers

Prospective applications of electrospun polymer nanofibers have been summarized in Figure 2-5. Potential applications of nanofiber based materials are divided into three major sections: biomedical, environmental and electronic areas. In the following sections, a few examples of biomedical, filtration and electronic applications of electrospun nanofibers are described.

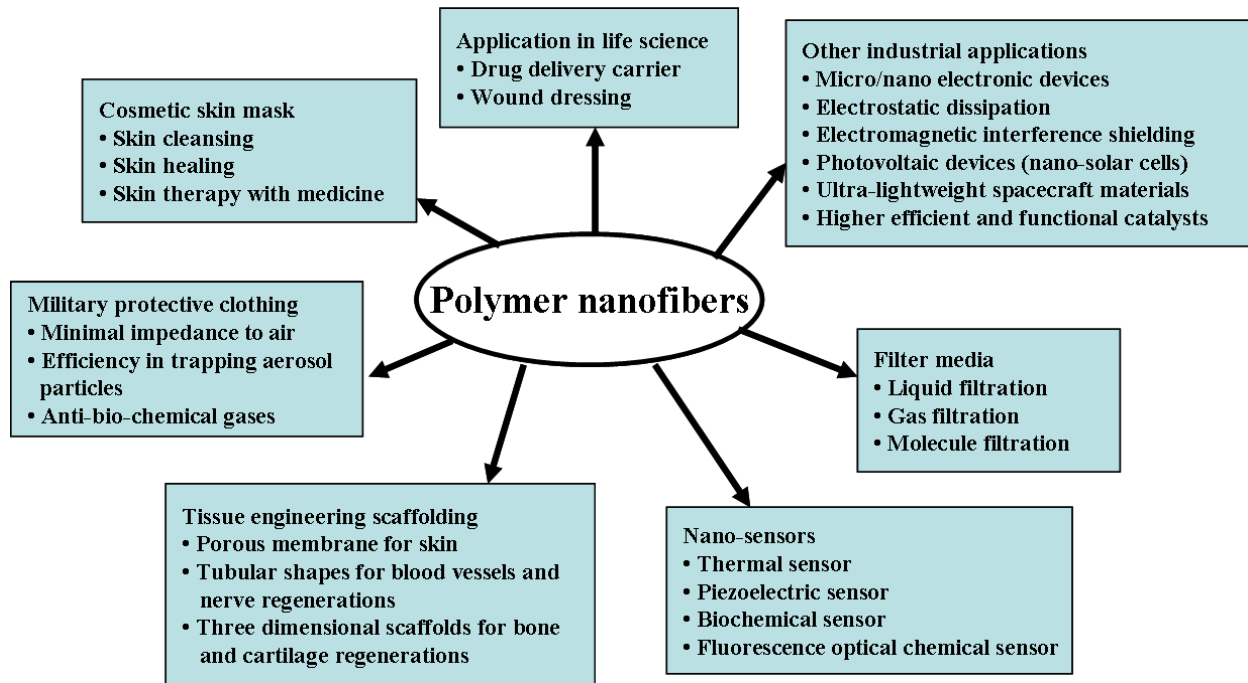


Figure 2-5 Potential applications of electrospun polymer based nanofibers.

2.4.1 Biomedical applications

2.4.1.1 Medical prosthesis

Electrospun nanofibers can be used as a thin porous film deposited on a hard tissue prosthetic device that is implanted in human body. Buchko et al. [50, 51] employed biocompatible electrospun nanofiber thin films in implants. The coating film resides in the interphase between the prosthetic device and the host tissue to reduce the stiffness mismatching at this interphase. This process helps to prevent implant failure [24].

2.4.1.2 Wound dressing

Because of the porous structure, nanofibers can be used to protect wounds from bacterial penetration providing a suitable path for vapour transports through the pores. Nanofibers exhibit

good adhesion to even moist wounds, higher liquid absorption and more efficient local release of drugs to skin at the contact surface thanks to their large surface area up to $100\text{m}^2/\text{g}$. Through direct spinning of biodegradable polymers onto wounds, a fibrous mat dressing forms that enhances the healing process. Unlike normal wound healing that is accompanied by the formation of scar tissues this process stimulated the formation of skin growth inhibiting the scar tissue formation [52, 53]. Polydioxanone (PDS) is a material of choice for wound closure sutures with colorless, crystalline and bioabsorbable characteristics [54]. Katti et al. [55] employed poly(lactide-co-glycolide) (PLGA) nanofiber for antibiotic delivery systems for wound treatment. They applied antibiotics such as cefazolin into nanofibers and showed that PLGA nanofiber has been a good candidate for developing an antibiotic delivery system for wound treatment.

2.4.1.3 Tissue engineering

Recently, nanofibers have been developed as scaffold for tissue engineering [56, 57]. Due to their large surface area to volume ratio and microporous structure, nanofibrous polymers acquire higher degree of cell adhesion, proliferation, migration and differentiation that are necessary for this application [58]. Therefore, the nanofibrous scaffolds are investigated as excellent candidates for musculoskeletal¹, skin, neural and vascular tissue engineering [37, 59]. Li et al. [57] reported the electrospinning of poly(D,L-lactide-co-glycolide) (PLGA) with a

¹ musculoskeletal tissue engineering is including in bone, cartilage, ligament, and skeletal muscle

unique architecture produced via electrospinning. The electrospun PLGA nanofiber is capable of cell attachment and cell proliferation and is suitable for soft tissues such as skin and cartilage.

The electrospun nanofibers can be also exploited in developing blood vessels. One of the challenges of developing small blood vessels is decreasing the graft patency rate via using the synthetic grafts to make small diameter arteries like coronary and infragenicular vessels. In order to mimic the natural small diameter vessels, three dimensional nano-structural matrix scaffolds can be made out of collagen or other cell-secreting natural substances to seed the Smooth Muscle Cells (SMCs). It has been proved that implanting the muscle cells in the scaffold will develop the same function, shape, morphology and cellular structure of the natural vessels of human body [60].

2.4.1.4 Drug delivery

Electrospun polymer nanofibers have potential applications for drug delivery thanks to their high surface area to volume ratio and easy processing [53]. The electrospun nanofibers are capable of maintaining molecular structure and the bioactivity of therapeutic compounds due to the mild process condition [61]. Depending on the morphology, porosity and the polymer as carrier a controlled drug release is expected [53, 61]. Two methods have been introduced in order to design a proper drug release system. One is preparation of drug-loaded ultrafine fibers carrying pharmaceuticals through blending both drug and polymer materials. The second one is the fabrication of drug-loaded electrospun core-shell nanofibers. Depending on the fabrication technique, rapid delay or modified drug release can be acquired. In summary, drug carriers can be created via controlling the mode of encapsulation and the architecture of electrospun nanofibers to accomplish suitable drug release profile [61]. The application of electrospun

nanofibers for drug delivery purpose has been extensively studied [7, 62-68]. For example, cellulose acetate (CA) electrospun nanofiber has been employed as four different types of drug including naproxen (NAP), indomethacin (IND), ibuprofen (IBU), and sulindac (SUL) for drug delivery purpose by Tungprapa et al. [63]. The greater drug release of the drug-loaded electrospun CA fiber mats compared to as-cast films with no drug aggregation was obtained [63]. Both the drug-loaded CA fiber mats and the drug-loaded as-cast CA films were immersed in the acetate buffer solution at 37°C in order to study the drug release characteristics. The drug release profile for both as-cast CA film and CA nanofibers are shown in Figure 2-6. At any immersion time point, the drug release from the drug-loaded electrospun CA fibers was greater than that from the corresponding as-cast CA film. Much slower and lower maximum amount of drug release from the films is attributed to the incapability of the cast films to swell due to its much lower surface area in comparison with nanofibers.

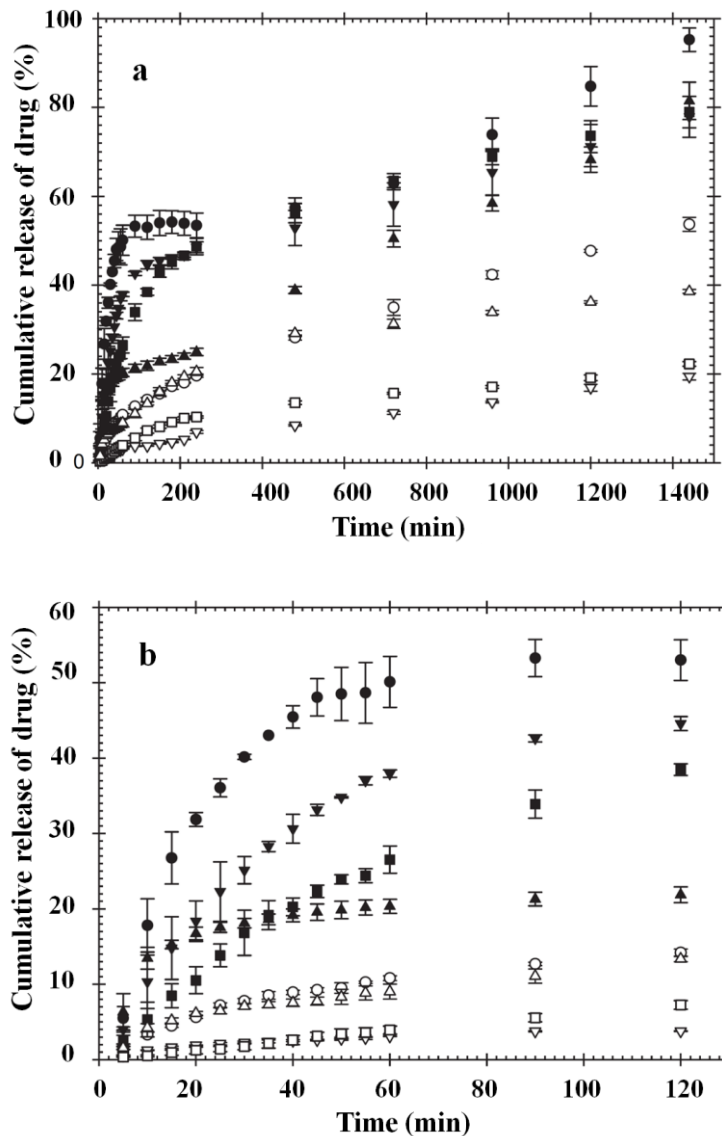


Figure 2-6 Cumulative release profiles of model drugs from (●) NAP-, (■) IND-, (▲) IBU-, and (▼) SUL-loaded electrospun CA fiber mats and (○) NAP-, (□) IND-, (△) IBU-, and (▽) SUL-loaded solvent-cast CA films by total immersion technique during (a) 0-1440 min and (b) 0-120 min.

2.4.2 Filtration

Electrospun nanofibrous membranes possess several attractive features making them productive in separation technology. These promising characteristics are high porosity with pore sizes ranging from tens of nanometer to a few micrometers, interconnected pore structure, higher

gas permeability and large surface area per unit volume [69]. Filtration efficiency is closely related to the fiber fineness. Figure 2-7 compares the porosity of fibrous structures with different fiber diameters. As demonstrated in Figure 2-7, fibers with smaller diameter have highly porous structure in comparison with those made of larger diameters. Therefore, higher filtration efficiency is acquired for fibers with the smaller diameter.

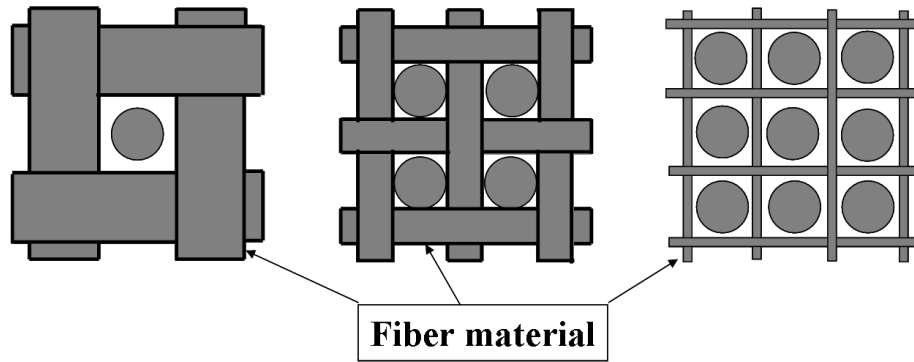


Figure 2-7 The efficiency of a filter increases with decrease in fiber diameter.

Tsai et al. [70] compared the filtration efficiency for three different types of filtration techniques and proved that amongst different techniques nanofiber filters exhibit the highest filtration efficiency of around 99.4% (normalized to 10g/m^2) via mechanical filtration mechanism. This is attributed to the fineness of the fibers. Gopal et al. [69] have explored the usage of fibrous materials prepared by electrospinning for liquid separation for particulate removal. They prepared electrospun Poly vinylidene fluoride (PVDF) nanofibers for this purpose. According to their findings, the electrospun membranes were capable of rejecting more than 90% of the micro-particles from solution. As a result, the nanofibers prepared by electrospinning have attracted great interest in the separation technology and found potential

applications for pre-treatment of water prior to reverse osmosis or as pre-filters to minimize fouling and contamination prior to ultra- or nano-filtration.

2.4.3 Nanofibers for electronic and optical device applications

Due to their highly porous structure, large surface area and their capability of being functionalized using various fillers, electrospun nanofibers produced via electrospinning have also been considered as excellent candidates for electronic and optical applications such as sensors [71-73], polymer batteries [8, 74] and photovoltaic solar cells [75, 76].

2.4.3.1 Sensors

Higher sensitivity and faster response of nanofibrous sensors to the target gases, in comparison with traditional flat surfaces which are being used as sensors, have been confirmed through experimental works. Luoh et al. [71] have reported electrospun composite nanofibers as optical gas sensors for CO₂ gas detection. They have used PAN nanofiber mats and nanocomposite fiber mats containing Fe₂O₃, Sb-SnO₂ and ZnO nanoparticles for enhanced sensing application. Because of their larger surface area and higher porosity electrospun nanofibers can quickly interact with the gas analyte. This results in a higher sensitivity and a quick response that has been demonstrated for Fe₂O₃/PAN nanofibers with reversible usage.

2.4.3.2 Energy generation

Functionalized nanofibers can also be employed as ion-batteries. Kim et al. [74] fabricated electrospun PVDF nanofibrous electrolytes for lithium ion polymer batteries. Song et al. [76] developed TiO₂ nanorods using electrospinning to make quasi-solid-state dye sensitized solar cells. Efficient photocurrent generation (60%) with a quasi-solid-state electrolyte was

obtained since the contact of the electrolyte with a TiO₂ web electrode was improved using nanofibers (Figure 2-8).

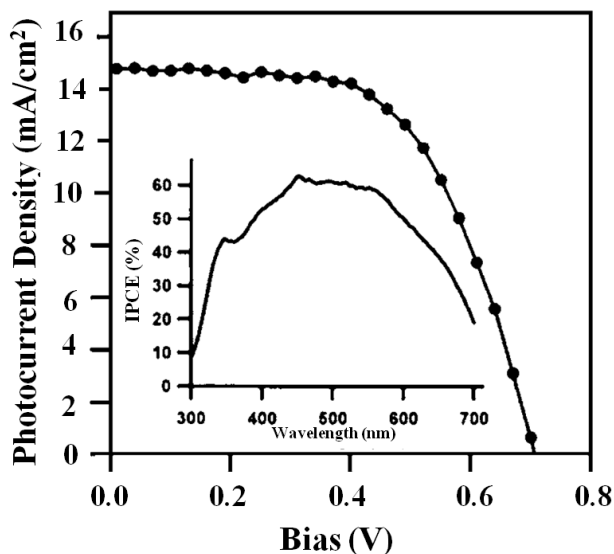


Figure 2-8 Photocurrent density vs. voltage characteristics of TiO₂ nanorod electrode with PVDF-HFP gel electrolyte at AM1.5 global (100mW/cm²) illumination. The inset is IPCE spectrum for the same electrode. The TiO₂ nanorod electrode area was 0.16cm².

2.5 Multifunctional composite nanofibers

Electrospinning can be employed to fabricate multifunctional composite nanofibers via incorporation of various fillers such as nanotubes, nanowires or nanoparticles in specific polymer nanofibers for various applications. Multifunctional materials are those made of more than one functional component which can be combined together to produce outstanding physical, chemical or biological functionalities. These multifunctional composite materials can be fabricated via encapsulation of functional nanofillers dispersed inside the polymer dope solutions. The incorporation of a variety of functional nanofillers such as multi-wall or single-wall carbon nanotubes (MWCNT/SWCNT) [77, 78], titanium dioxide (TiO₂) nanoparticles [6],

iron oxide (Fe_3O_4 or Fe_2O_3) nanoparticles [22, 71] and silver (Ag) nanoparticles [79] have been investigated.

Incorporation of functional fillers in nanofibrous structures has been investigated to develop multifunctional composites with improved mechanical strength, electrical conductivity, thermal conductivity or antimicrobial properties and so on. For example, the dispersion of carbon nanotubes into PAN nanofibers and post-carbonization treatment enhances the mechanical strength and electrical conductivity of PAN-based carbon nanofibers [77, 78, 80]. Ag nanoparticles are used to improve the electrical conductivity of PAN-based carbon nanofibers [79]. Fe_3O_4 nanoparticles are employed in PAN-based carbon nanofibers for Li-ion battery applications [13] and in poly(p-phenylene vinylene) (PPV) nanofiber for photoelectric performance [81]. Photo-catalytic activity can be enhanced via incorporation of TiO_2 nanoparticles and carbon nanotubes in PAN nanofibers [6] and antimicrobial properties can be improved via encapsulation of Ag nanoparticles in Polyvinyl alcohol (PVA) nanofibers [82].

2.5.1 Electromagnetic Fe_3O_4 /carbon composite nanofibers

Electromagnetic nanocomposites have been widely investigated for their electromagnetic device applications such as electromagnetic interference shielding and electrodes for Li-ion batteries [9-14, 83, 84]. More specifically, electromagnetic Fe_3O_4 /carbon nanofiber composite seems relevantly new since its electromagnetic characterization has recently been investigated by researchers. Besides, only one possible application is demonstrated for this composite nanofiber by Wang et al. [13]. Highly pure carbon nanofibers made of electrospun PAN nanofibers exhibit remarkable properties such as: large accessible surface area due to their nanometer size fiber diameter, relatively high electrical conductivity, high structural integrity, thin web macro-

morphology and large reversible capacity (~450mAh/g). The high internal surface area, large pore volume and long fiber length of conducting PAN-based carbon nanofiber membranes make them as suitable electrodes in Lithium (Li)-ion batteries [85]. The porous carbon nanofibers may be chosen as matrix to incorporate nano-size transition metal oxides. It has been proved that the incorporation of transition metal oxides into carbon nanofibers facilitate more complete access of Li ions to the inner sites of anodes, decreasing Li ion diffusion distance, and significantly increasing the rate of electron transport [86]. Fe₃O₄/carbon nanofiber composites also exhibit excellent electrochemical performance with high reversible capacity and excellent rate capability [13].

2.5.2 PAN-based carbon nanofibers

Polymeric materials which leave a carbon residue and do not melt during pyrolysis process are generally considered as candidates for carbon-fiber production [87]. PAN is the most popular carbon fiber precursor [3] and is composed of nitrogen, hydrogen and carbon atoms. The chemical structure of PAN is shown in Figure 2-9. PAN is made of a repeating chain of cyanoethylene molecules. It can be converted into electrically conductive carbon nanofiber mat via appropriate thermal process known as pyrolysis or carbonization process [3]. The details of this process will be explained later.

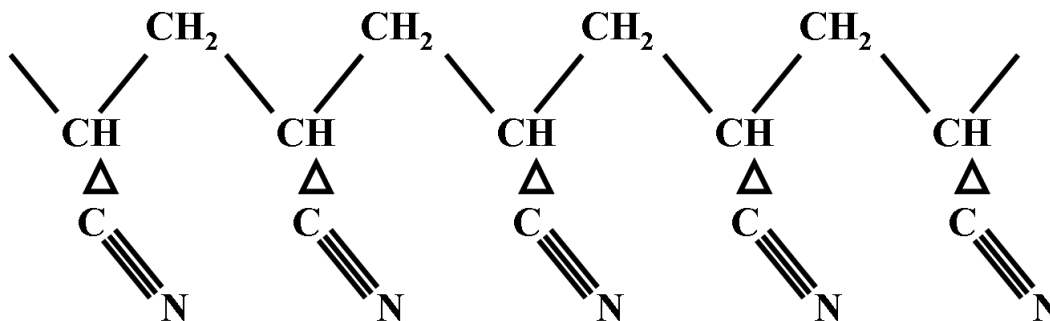


Figure 2-9 Chemical structure of Polyacrylonitrile (PAN).

In order to fabricate electrically conductive carbon nanofibers, first PAN/DMF polymer solution is electrospun in order to produce PAN-based nanofibers. Then, subsequent stabilization and carbonization processes turn PAN nanofibers into carbon nanofibers which are electrically conductive [88, 89]. Similar to other types of one-dimensional structures like nanowires, nanotubes and nanowires, carbon nanofibers have also attracted an extensive attention in nano-electronics, photonics, nano-sensors and electromagnetic shielding among other fields. PAN-based activated carbon nanofibers are demonstrated for applications such as electric double-layer supercapacitor and Li-ion batteries [90-92].

2.5.2.1 Electrospinning of Polyacrylonitrile (PAN) solution

In order to fabricate carbon nanofibers, PAN-based nanofibers are required to be fabricated via electrospinning of PAN/DMF solution. The effect of different material and system parameters on the final morphology of electrospun PAN nanofibers has been extensively studied [37, 39, 40, 93-95] (as explained in the electrospinning section).

2.5.2.2 Stabilization of electrospun PAN nanofibers

Oxidation stabilization is a time-consuming and reaction-controlling process which is required to be optimized in order to improve the final mechanical properties of carbon nanofibers. Stabilization step is carried out through heating PAN nanofibers to 200-260°C in air for 30min up to a few hours [3, 40]. It is an exothermic reaction which results in a weight loss at around 300°C [96] due to thermal polymerization of nitrile group ($C\equiv N$) [3, 40]. PAN mainly consists of cyclizable acrylonitrile entities ($-CH_2CH(CN)-$) (see Figure 2-9).

Stabilization of PAN nanofibers include dehydrogenation, cyclization and oxidation [97], see Figure 2-10. During the stabilization process, following chemical changes occur: first, reaction of nitriles causes the formation of conjugated $C=N$ containing structures. The reaction is either intramolecular resulting in cyclization or intermolecular ensuing crosslinking. Next, conjugated $C=C$ structures are generated which are produced due to the dehydrogenation or imine–enamine tautomerization and subsequent isomerization. And finally, oxidation occurs which forms carbonyl groups [98]. Stabilization is also accompanied by changing the colour of PAN nanofibers from white to reddish brown and dark brown at the end of the process [40].

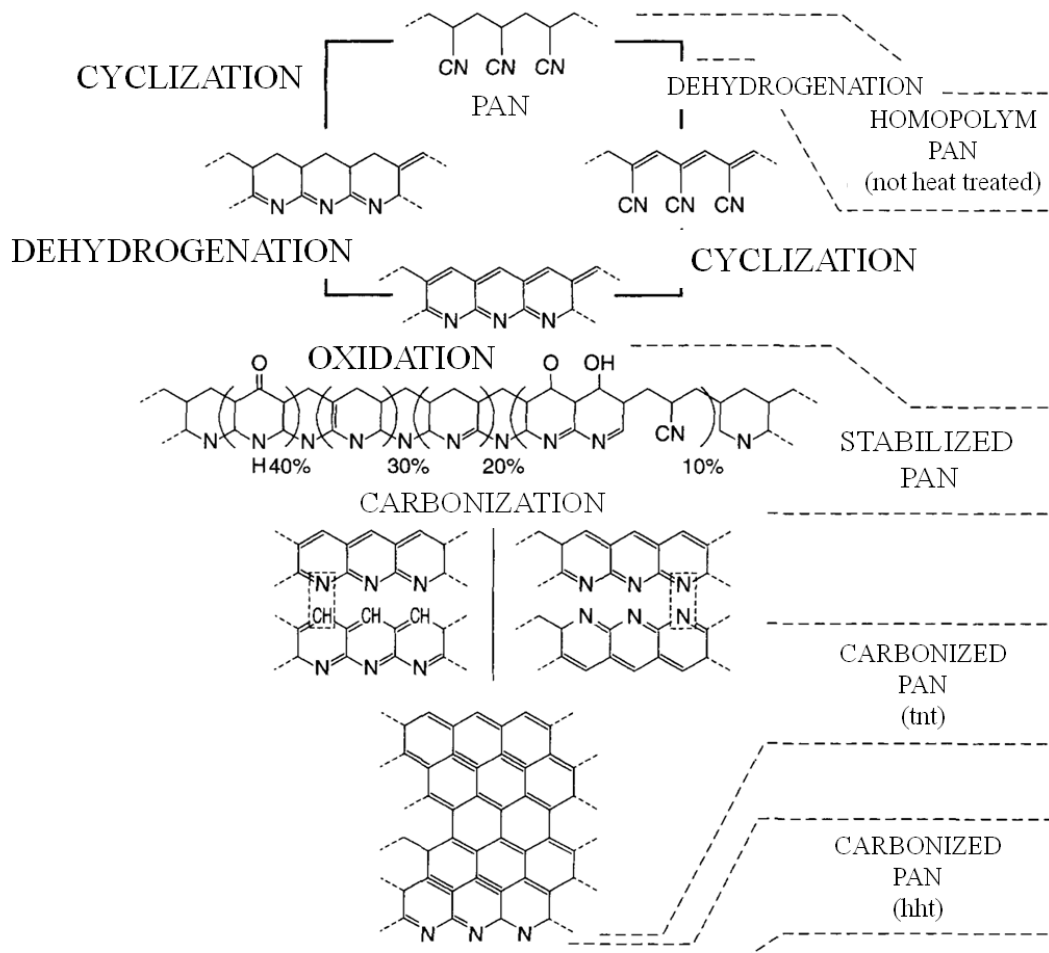


Figure 2-10 The process of stabilization and subsequent carbonization of PAN-based nanofibers.

Moreover, due to significant shrinkage of the polymer during the cyclization and stabilization process, fiber diameter is decreased [3]. Oxidative stabilization is considered to be the most decisive step, and it is also of the utmost importance in industrial fabrications, since it significantly governs the final structure and ultimate mechanical properties of the carbon fibers [99].

2.5.2.3 Carbonization of electrospun PAN nanofibers

2.5.2.3.1 Chemical changes during carbonization

Next step after stabilization is the carbonization of stabilized PAN fibers. Carbonization is carried out by controlled heating rate to a high temperature in the range between 400°C-1500°C under inert atmosphere which is usually nitrogen and sometimes argon [3, 40]. Upon heating, complex reactions occur resulting in by-products formed due to the cross linking of individual molecules. Large quantities of HCN and NH release during the early stage of heating. As the temperature reaches 450°C HCN, acrylonitrile (C₃H₃N), propionitrile (C₂H₅CN), NH₃ and H₂O release from PAN nanofibers. Further release of HCN and H₂O takes place upon heating up to respectively 500°C and 700°C. Above 700°C, nitrogen release starts and continues with increasing temperature until 5.8wt% nitrogen exists in the fiber structure at 1000°C. Overall, 50% weight loss occurs in PAN during the carbonization process. At even higher temperatures above 1500°C, most of the residual nitrogen is removed and subsequently the conversion of PAN fibers into the anisotropic carbon sheets will be completed. Graphitization of carbon sheets occurs upon heating above 2500°C [3].

2.5.2.3.2 Microstructure evolution during carbonization

Heating at the early stage of carbonization causes the formation of graphite-like ribbons through a dehydrogenation mechanism. As the temperature increases, denitrogenation occurs that results in growth and transformation of the ribbon-like structure into a thin sheet-like structure. These adjacent sheets can be bonded together as temperature goes up further. These sheets contain many vacancy imperfections and defects. Pencil-shaped voids are oriented in the general

direction of the fiber axis. Further heating aligns graphite layers parallel to fiber axis. However, due to the short length of each block, they are not well-oriented with respect to its neighbour. Increasing the pyrolysis temperature leads to the formation of longer and well-oriented graphite sheets which results in higher electrical and thermal conductivity of carbon fibers [3, 97].

2.5.2.3.3 Electrical conductivity of PAN-based carbon fibers

Basic structural unit (BSU) of carbon fibers are a group of conductive turbostratic layers. These layers can join together with random twisting and interlocking to form micro-domains and further join to each other to produce carbon fibers. After stabilization step, the oriented BSUs are not conductive due to their isolation by voids and heteroatoms. More oriented structure at higher temperature is a result of reduction in interlayer spacing, void population and growth of graphite crystallites. Consequently, elastic modulus, thermal and electrical conductivity increases [3, 97]. The graphitization of PAN nanofiber leads to a sharp increase in conductivity to approximately 490S/m [100]. The degree of graphitization is correlated with the carbonization temperature [88, 101-103]. Electrical conductivity mechanism in carbon fiber is explained via movement of π electrons within the graphite layer. Due to the growth of carbon graphite layers and decreasing the space between these layers, the mobility of π electrons increases resulting in higher electrical conductivity [104].

2.5.3 Magnetite employed as magnetic nanofillers

2.5.3.1 Ferrimagnetism

One complex type of magnetic ordering which occurs in ionic compounds such as oxides due to the specific crystal structure is known as ferrimagnetism. Figure 2-11 shows a simple

representation of the magnetic spins in a ferrimagnetic oxide. The magnetic structure of an oxide is composed of two magnetic sublattices (called A and B). These sublattices are separated by oxygen anions. The exchange interaction (that causes two nearby magnetic dipoles to align parallel in the same direction) will be mediated by oxygen anions. Therefore, the interactions are named as indirect or super exchange interactions. The strongest super exchange interaction leads to an antiparallel alignment of spins between the A and B sublattices. Not equal magnetic moments of the A and B sublattices results in a net magnetic moment. It is noteworthy to mention that ferro- and ferrimagnets are the same in all magnetic properties except for different magnetic ordering. Magnetite is a well known ferrimagnetic material [105].

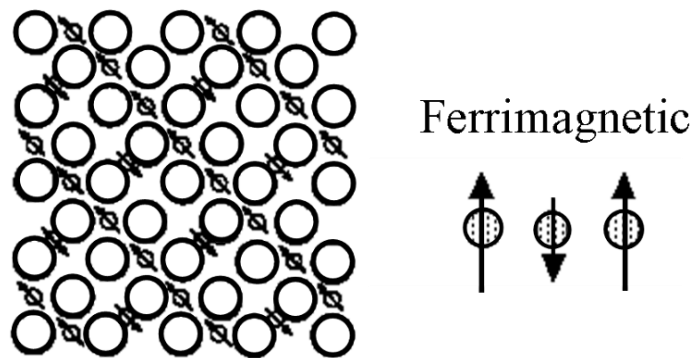


Figure 2-11 A simple representation of the magnetic spins in a ferrimagnetic oxide.

2.5.3.2 Crystal structure of magnetite

Magnetite belongs to a group of magnetic ceramics known as ferrites with $MO \cdot Fe_2O_3$ ($M=Fe, Ni, Co, Mn$ or Cu) formula (structural formula of magnetite is $(Fe^{3+})_A (Fe^{3+}, Fe^{2+})_B O_4$), A and B refer to interstitial, i.e. tetrahedral and octahedral sites, respectively [106, 107]. Figure 2-12(a) demonstrates the crystal structure of magnetite. Magnetite has a cubic inverse spinel

crystal structure with oxygen anions forming a face centered cubic (FCC) structure and iron cations reside at the interstitial tetrahedral and octahedral sites. Tetrahedral sites and half of the octahedral sites are occupied by Fe^{3+} and the rest of the octahedral sites are filled with Fe^{2+} (as shown in Figure 2-12) [106, 107]. The B sublattice is antiferromagnetically aligned to the ferromagnetic order on the A sublattice. The Fe^{2+} cation can be viewed as Fe^{3+} and an “extra” electron, hopping freely between the octahedral sites [107]. The magnetite molecule has a net magnetic moment of $4\mu_B$ (where μ_B is the Bohr magneton) which usually originates from Fe^{2+} ions, since magnetic moments of Fe^{3+} ions in two tetrahedral and octahedral sites have been cancelled with each other [106, 108].

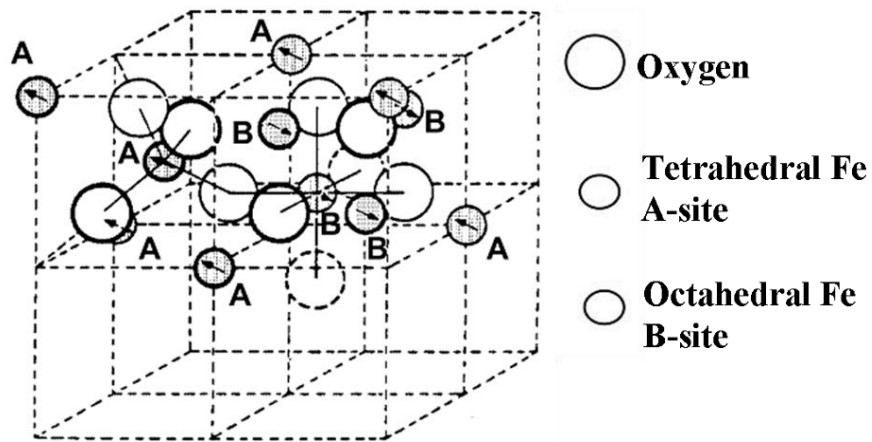


Figure 2-12 Spinel crystal structure of Fe_3O_4 .

2.5.3.3 Hysteresis curves of magnetic materials

The magnetic properties of magnetic materials are generally represented in the magnetic moment (M) vs. applied magnetic field (H) known as M-H curves or hysteresis curves. A typical

M-H curve of a magnetic material is shown in Figure 2-13. The saturation magnetization (M_s) is defined as the maximum induced magnetic moment obtained in a magnetic field (H_{sat}). By increasing the applied magnetic field higher than H_{sat} no further increase in magnetization can be observed. Remanent magnetization (M_r) is the remained magnetization of a material after removing an external magnetic field. Intensity of the magnetic field required to decrease the magnetization of material to zero after being saturated is known as the coercivity (H_c) (Figure 2-13). Superparamagnetic nanoparticles tend to have a very large magnetic susceptibility but little to no coercivity and remanent magnetization [109, 110]. In comparison, ferromagnetic materials in the single domain region exhibit hysteresis [109]. In electromagnetism, the magnetic susceptibility is the degree of magnetization of a material in response to the applied magnetic field [111].

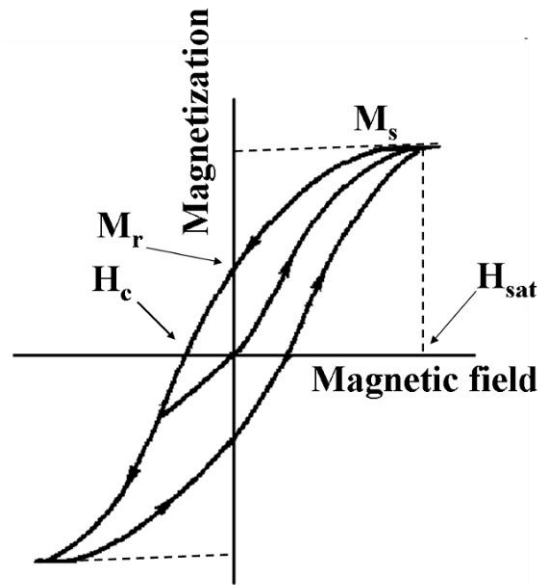


Figure 2-13 Magnetization vs. magnetic field (Hysteresis) curve of ferromagnetic materials.

2.5.3.4 Size-dependent magnetic properties

Ferromagnetic materials are composed of small units known as magnetic domains each with its specific magnetic orientation. Depending on the size of magnetic particles, they are either single domain (SD) or multi-domain (MD) structures [112]. Magnetic properties of ferromagnetic materials are size-dependent. Basically, ferromagnetic materials with the diameter below a critical size known as D_{SD} are composed of single domain particles. Particles with even smaller size below D_{SPM} exhibit superparamagnetism showing no hysteresis [109]. For Fe_3O_4 nanoparticles, D_{SD} value of 128nm [109] and D_{SPM} value of 25-30nm are reported [113].

The responsible energy for holding the magnetic moment of each magnetic particle (with single domain structure) along with a certain direction is known as magnetic anisotropy energy represented as follow: $E(\theta)=K_{eff}V\sin^2\theta$, where V is the volume of particle, K_{eff} is anisotropy constant and θ is the angle between the magnetization and the easy axis (energetically favourable direction for spontaneous magnetization). Two easy axis of magnetization with equal energy are separated via energy barrier $K_{eff}V$. As the size of magnetic particle decreases below a certain size ($D < D_{SPM}$) which the thermally-activated random fluctuation of the net spins ($k_B T$) surpasses the energy barrier, $K_{eff}V$, the magnetization can be easily flipped. Therefore, the net magnetic moment without any applied magnetic field is zero in randomly orientated spins representing zero magnetization. Applying an external magnetic field leads to the alignment of magnetic spins for the system that behaves like a paramagnet ($k_B T > K_{eff}V$) however contains a super magnetic moment [109]. Because of relatively large net magnetic moment of Fe_3O_4 particles, the magnetic behaviour is known as superparamagnetism [114]. The M_s of Fe_3O_4 nanoparticles is smaller than that of bulk Fe_3O_4 that is equal to 88emu/g [115]. The lower M_s value of Fe_3O_4 nanoparticles is attributed to disordered surface spins due to the large surface area of nanoparticles that lowers

the net magnetization level. Decreasing the size of magnetic particles essentially dominates the surface effects [116, 117]. Figure 2-14 represents the effect of change in particle size in the coercivity (H_c) of the magnetic particles. As shown in Figure 2-14, no coercivity ($H_c \sim 0$) is observed for superparamagnetic nanoparticles. When the size exceeds the D_{SPM} , the magnetic property does not revert to that of the bulk material. As the size increases further, thermal energy is not sufficient enough to be able to rotate the spins freely. Hence, H_c starts to increase and hysteresis is observed in M-H curve which increases with increasing diameter as $D^{2/3}$, until reaches to a maximum value in H_c . At the maximum H_c value, the particles are no longer single domain and they break into multi-domain structures. Therefore, the H_c decreases as D^{-1} by further increasing the size of particles. (This discussion only considers H_c resulting from the magnetocrystalline anisotropy for spherical particles). By considering shape anisotropy for non-spherical particles, the H_c is enhanced because of the shape anisotropy [118].

Fe_3O_4 nanoparticles have been identified as excellent candidates in magnetic separation and guiding as well as bio-imaging [119], magnetic resonance imaging (MRI) [120], localized hyperthermia for cancer treatment [121] and microwave absorption properties [122]. Mi et al. [119] reported the synthesis of new kind of magnetic/luminescent multifunctional nanoparticles. The resulted nanocomposite exhibits good superparamagnetic and excellent green up-conversion photo-luminescent properties that can be exploited in magnetic separation and guiding as well as bio-imaging [119]. The superparamagnetic Fe_3O_4 nanoparticles coated with poly(N-vinyl pyrrolidone) (PVP) via covalent bonds were prepared for magnetic resonance imaging (MRI) [120]. The Fe_3O_4 /polyethylene glycol (PEG) magnetic composite nanoparticles with a core-shell structure were synthesized that will be useful as good thermo-seeds for localized hyperthermia treatment of cancers [121].

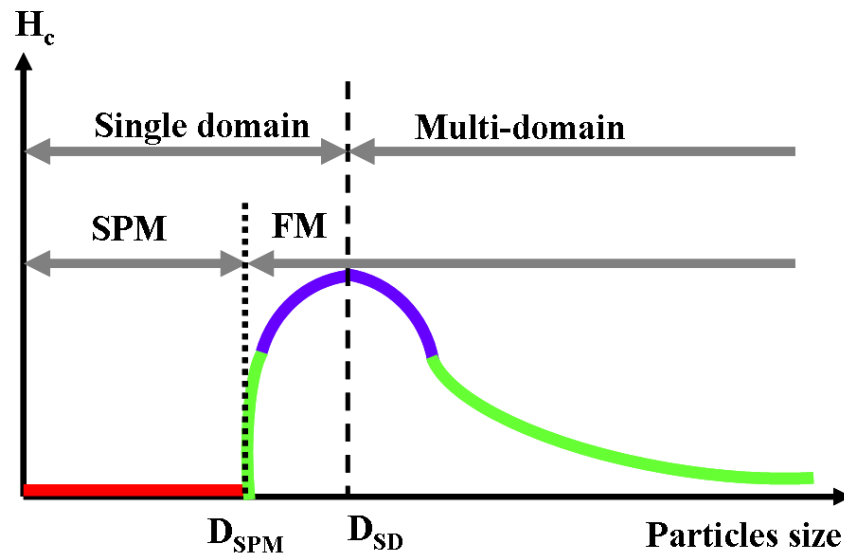


Figure 2-14 Effect of particle size on the coercivity of magnetic particles.

2.5.4 Electromagnetic Interference Shielding Efficiency (EMI SE)

2.5.4.1 Introduction

With the advanced development in the electronic industry, electronic devices and telecommunication equipments have been drastically used during the past few decades. The electromagnetic interference has been a major issue since it interferes with the safety operation of the electronic and telecommunication devices and reduces the working efficiency of these equipments [123]. Besides, the leakage of electromagnetic radiation causes interferences with the environment and human body. Most notably, the cell phone usage and high power lines disrupt the human body and can cause diseases like cancers [124]. To address these issues, all electronic devices must be shielded against electromagnetic radiation. Hence, an electromagnetic interference (EMI) property of any shielding materials is of great importance since it affects the

lifetime and efficiency of the instruments and also impacts the safety operation of many electronic devices and biological systems. Recently, extensive research has been devoted to the development of new lightweight shielding materials with high efficiency and durability [123]. The aim of EMI shielding is to block the electromagnetic radiation from passing through a medium. For example, electronic devices such as computers must be shielded against radio frequency radiate. Reflection and absorption are the main mechanisms of shielding. Electrical conductors such as metals and carbon mainly shield EMI by reflection mechanism. Whereas, magnetic materials mainly shield by absorption [125]. Materials used for shielding are metals in bulk, porous and coating forms; polymer composites; cement and carbon matrices and carbons [126]. Depending on the application, different levels of shielding is required. The target EMI for real-life applications is around 20dB. For example a shielding effectiveness of 20dB is usually appropriate for building or cell phone while higher level is required for the military applications [125, 127]. For example, for space applications an EMI level of 60dB and above is considered acceptable [128]. Table 2-1 shows the common measure of shielding in (-dB) and the amount of leakage [129].

Table 2-1 Shielding effectiveness and the amount of leakage

Shielding effectiveness (-dB)	% Leakage through shield
20	10.0
40	1.0
60	0.1
80	0.01
100	0.001
120	0.0001

2.5.4.2 Shielding mechanism

When an electromagnetic wave hits a shield, it can be reflected from the surface or absorbed by the shield as heat and finally it can be multiply reflected through the material. Therefore, three shielding mechanisms that attenuate the EMI are reflection (R), absorption (A) and multiple reflections (M) [130]. The capability of a shield to be considered as suitable shielding material depends on the overall response of material to EM wave as reflection, absorption and multiple reflections. There are intrinsic and extrinsic parameters of a shielding material which affect on the amount of attenuation that will be discussed later in this chapter. Shielding efficiency of a material expressed in dB is the ratio of transmitted to incident power and is expressed as following equation (1):

$$SE = -10\log(P_t / P_i) \quad (1)$$

where P_t is the power of transmitted and P_i is the power of incident electromagnetic wave [131].

Total shielding of a single layer shield is the sum of contribution of reflection (SE_R), absorption (SE_A) and multiple reflections (SE_M) given by following expression (2):

$$SE_{total} = SE_R + SE_A + SE_M \quad (2)$$

When $SE_A > 15\text{dB}$, it is usually assumed that SE_{total} is presented by the following equation (3):

$$SE_{total} = SE_R + SE_A \quad (3)$$

[132]. The shielding material attenuates the radiated electromagnetic energy through reflections (direct reflection R, and multiple reflections M) and absorption (A) as depicted in Figure 2-15.

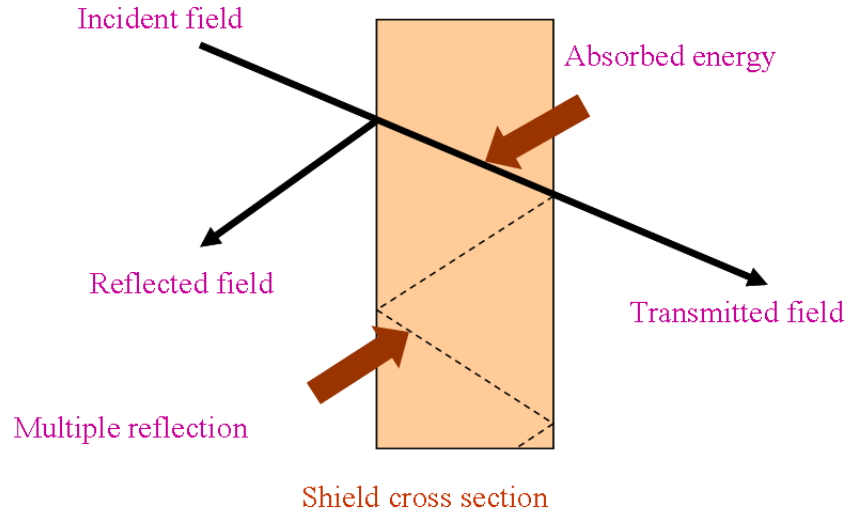


Figure 2-15 EMI SE mechanisms through reflection, absorption and multiple reflections.

From the measured transmission and reflection scattering parameters (S_{11} and S_{21}) the transmittance (T), reflection (R), and absorption (A) of a shielding material are calculated according to the following equations:

$$T = (S_{12})^2 = (S_{21})^2 \quad (4)$$

$$R = (S_{11})^2 = (S_{22})^2 \quad (5)$$

$$A = 1 - R - T \quad (6)$$

In equation (6), absorption (A) is calculated with respect to the power of the incident EM wave. The effective absorbance (A_{eff}) can be described as equation (7) with respect to the power of the effectively incident electromagnetic wave inside the shielding material.

$$A_{eff} = (1 - R - T) / (1 - R) \quad (7)$$

It is convenient to express reflectance and effective absorbance logarithmically as the following equations [133]:

$$SE_r(dB) = -10 \text{Log}(1 - R) \quad (8)$$

$$SE_A(dB) = -10\text{Log}(1 - A_{eff}) = -10\text{Log}\left(\frac{T}{1-R}\right) \quad (9)$$

The main mechanism in electrically conductive materials such as metals is reflection. Reflection is dependent on mobile charge carriers such as electrons in metals, thus the shielding is influenced by electrical conductivity. The second shielding mechanism is absorption. In terms of absorption, shielding effectiveness is relative to the interaction of electromagnetic radiation with the shield [134]. Absorption can also be enhanced with magnetic and electric dipoles which can be respectively provided via incorporation of magnetic and dielectric components such as Fe₃O₄ and TiO₂ particles in a matrix or combination of both [123, 125, 135-138].

2.5.4.3 Parameters affecting the shielding performance of a matter

The electromagnetic shielding performance of any material depends on its intrinsic electromagnetic properties such as electrical conductivity, complex permittivity and permeability as well as extrinsic properties for example thickness and working frequencies (at which the shield is operating or being tested) [139].

2.5.4.3.1 Complex permeability and permittivity parameters

Complex permittivity $\epsilon_r = \epsilon' - j\epsilon''$ and complex permeability $\mu_r = \mu' - j\mu''$ of any material in the form of magnetic and dielectric losses affect its electromagnetic absorption performance [123]. Dielectric loss is defined as $\tan\delta_\epsilon = \frac{\epsilon''}{\epsilon'}$ (loss tangent) where the real (ϵ') and imaginary (ϵ'') parts of complex permittivity respectively display the amount of polarization created in the material and the amount of energy dissipated in the material [135, 139, 140]. The dielectric loss or loss tangent provides an indication for how well material can be penetrated by

an electric field and how well material is able to dissipate the electromagnetic energy as heat [132]. The dielectric performance of a material depends on ionic, electronic, molecular (dipolar or orientational) and interfacial (space charge) polarization [141]. According to the theory of complex permittivity, when the electromagnetic radiation is incident on metallic surfaces, the electric field induces two types of electrical currents within the material, i.e. conduction current and displacement current. The former arises from free electrons and gives rise to electric loss (imaginary permittivity) and the latter coming from the bound charges, i.e. polarization effect (real permittivity) which mainly involves the unpaired point defects. Accordingly, the increase of the real part of the complex permittivity can be mainly ascribed to dielectric relaxation and space charge polarization effect and the increase of the imaginary part of the complex permittivity can be attributed to the enhanced electrical conductivity for the composites [142, 143].

Besides, magnetic loss is defined as $\tan \delta_{\mu} = \frac{\mu''}{\mu'}$. The enhancement of microwave absorbing properties by μ'' and μ' values is caused by transferring the electromagnetic energy into heat [139]. There are four main contributors to magnetic loss including magnetic hysteresis, domain-wall displacement, eddy current loss and natural ferromagnetic resonance which is the frequency corresponding to the maximum value of μ'' [130].

2.5.4.3.2 Electrical conductivity

Electrical conductivity is an important material property that can change its shielding performance. There is a direct correlation between the electrical conductivity of a shield and its shielding effectiveness [144, 145]. Electrical conductivity is essential for acquiring good shielding performance. It has been shown that in the absence of conductive filler, magnetic

materials are not effective shields [123, 125]. Figure 2-16 demonstrates the effect of CNT concentration and electrical conductivity in the shielding performance of CNT-PS foam composites. The SE is improved with CNT loading from 0wt.% to 0.5wt.%, 1wt.%, 3wt.% and 7wt.% (Figure 2-16a) which is attributed to the increase in the electrical conductivity of the composite (Figure 2-16b).

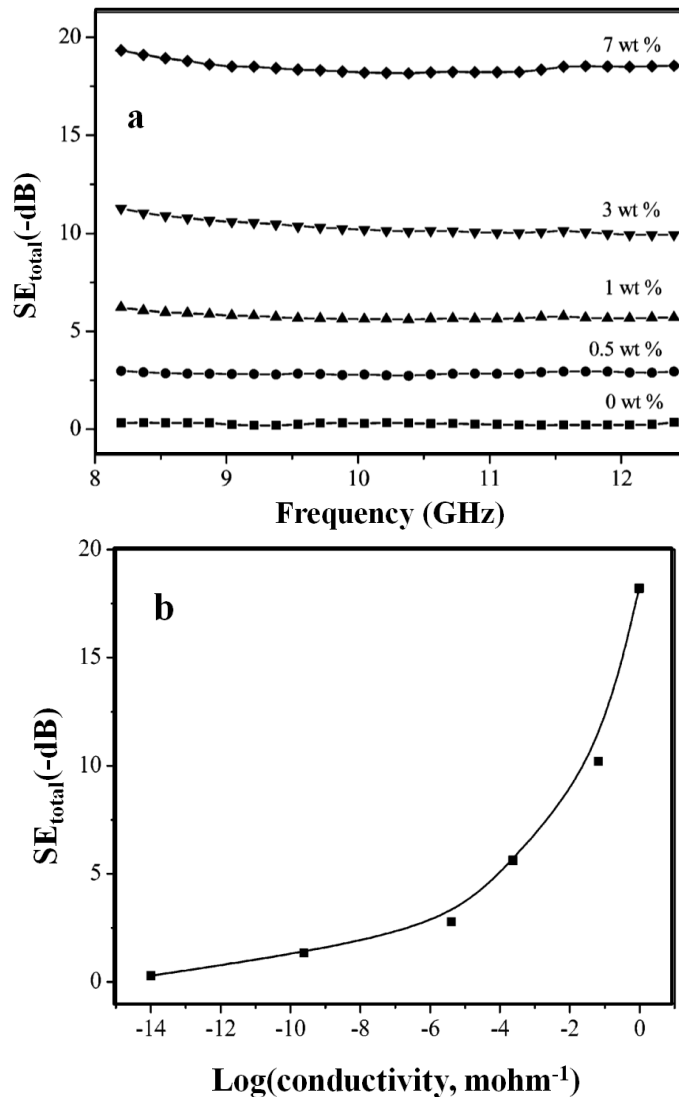


Figure 2-16 a. EMI SE as a function of frequency measured in the 8.2-12.4 GHz range of CNT-PS foam composites with various CNT concentrations, b. EMI SE at 10 GHz as a function of electrical conductivity of CNT-PS foam composites which increases with CNT concentration (wt.%) .

2.5.4.3.3 Shield thickness

An effective extrinsic parameter influencing the shielding performance of a shield is the shield thickness of the shield. Increasing the thickness shows improved shielding efficiency and enhances the absorption of radiation [144, 146, 147]. The increase in the shielding effectiveness with thickness is attributed to the increase of the conductive networks interacting with the electromagnetic waves. It in turn improves the absorption of electromagnetic waves [144, 146, 147]. Figure 2-17 shows the shielding efficiency of single wall carbon nanotube (SWCNT)/ethylene vinyl alcohol (EVA) composites containing 15 wt.% SWCNT as a function of sample thickness. SE increases from 15dB to 27dB at 1000MHz and from 23dB to 35dB at 12GHz as sample thickness increases from 1.5mm to 4.5mm.

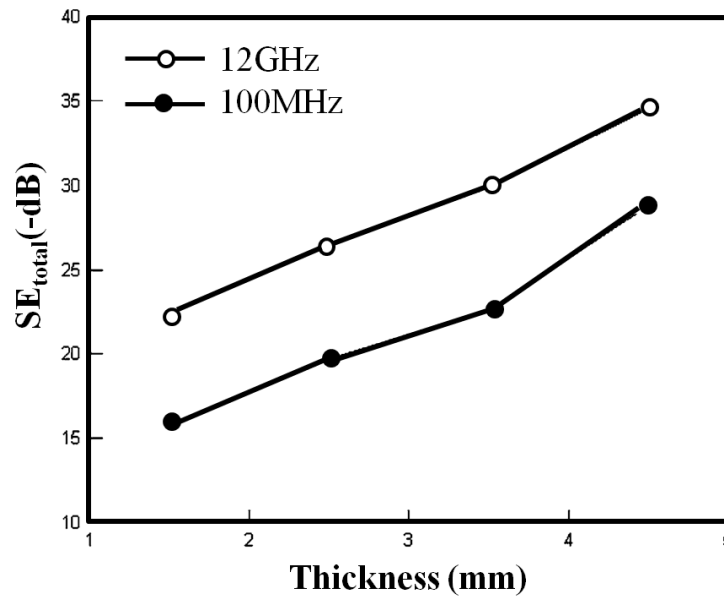


Figure 2-17 EMI SE as a function of sample thickness of 15wt.% SWCNT/EVA composites.

2.5.4.3.4 Filler aspect ratio

Among different nanofillers added into the polymer matrix, carbon nanofibers (CNFs) and carbon nanotubes (CNTs) are widely used due to their contribution to the electrical conductivity and dielectric loss of the polymer composite [138, 145-152]. Jana et al. investigated the shielding performance of carbon fiber (CF) filled polychloroprene composites in the x-band frequency range [146] and short carbon fibre-filled polychloroprene vulcanized by barium ferrite (BaF) in the working frequency range of 0.1-2GHz [147]. They found that for the same thickness, composites made of carbon fibers with larger aspect ratio show higher shielding effectiveness than the composites prepared with carbon fibers of lower fiber aspect ratio. Better shielding performance of composites made of higher fiber aspect ratio is ascribed to the enhanced electrical conductivity of the composite as well as increased fiber randomness in the matrix. Composites with larger carbon fiber concentration and higher fiber aspect ratio demonstrate higher absorption than reflection due to the formation of highly random structure [146, 147].

2.5.4.3.5 Nanosize effect of spherical fillers

Nanofillers with magnetic and dielectric properties such as titanium dioxide (TiO_2), BaF and $\gamma\text{-Fe}_2\text{O}_3$ are widely used as effective fillers in polymer matrices such as PANI and poly (3,4-ethylenedioxy thiophene) (PEDOT) [9, 10, 123, 135, 137, 141]. As the size of particles decreases to nanometer range, surface area, dangling bonds and unsaturated coordination on the surface are enhanced which increases the interface polarization and multiple scattering [9, 123]. Besides, as the size of magnetic nanoparticles is reduced down to the nanometer range, the higher magnetic anisotropy is enhanced due to the disordered surface spins and microstructural

defects [153]. The large anisotropy field of magnetic nanoparticles (single domain ferromagnetic particles) are demonstrated to increase the interfacial polarization and multiple scattering which are useful for higher absorption phenomena [153].

2.5.4.4 Shielding materials

In the following section, a brief description of the reported EMI SE performance of metals, intrinsically conducting polymers (ICPs), electrically conductive nanofiller/polymer composites and electromagnetic polymer composites is represented.

2.5.4.4.1 Metals

Metals are commonly used for the electromagnetic interference shielding effectiveness (EMI SE). They acquire high shielding efficiencies due to their high level of electrical conductivity. However, metals are heavy, cost effective and have less corrosion resistance than polymers [129]. Thus, employing lightweight, cost effective and corrosion resistant materials with the same or higher shielding efficiency is required.

2.5.4.4.2 Intrinsically conducting polymers

As compared with typical metals, intrinsically conducting polymers (ICPs) such as polyaniline (PANI) and polypyrrole (PPy) have been identified as new alternative candidates for Electromagnetic interference shielding applications. The ICPs are promising candidates for electromagnetic shielding purpose because of their lightweight, corrosion resistance, ease of processing and tunable conductivities as compared with typical metals [154]. Higher shielding efficiency of PANI is due to the occurrence of strong polarization because of polaron/bipolaron and other band charges that lead to high real and imaginary permittivity required to obtain higher

shielding [135, 141]. Electromagnetic interference shielding effectiveness of electrically conducting polymers such as PANI and PPy was reviewed by Wang and Jing [154]. Specifically, the electromagnetic interference shielding effectiveness of p-toluene sulfonic acid doped polyaniline (PANI-TSA)/polyacrylate composite with various PANI loading. The electromagnetic interference shielding effectiveness of the composite was investigated over the frequency range of 14kHz to 15GHz. These results indicated that electrical conductivity increases with PANI-TSA content. Incorporation of polyaniline (PANI) in insulating polyacrylate coating enhances the electrical conductivity of the composite. The highest EMI shielding value of 79dB was obtained for PANI/polyacrylate composite at 200MHz. However, it was reduced to 30dB at 15GHz [155].

2.5.4.4.3 CNT/CNF-polymer composites

Electrically conductive polymer-based composites can be prepared via embedding conductive nanofillers such as carbon nanotube (CNT) or short carbon nanofiber (CNF) in the polymer matrix. The CNT-polymer and CNF-polymer composites have been introduced as promising lightweight candidates for electromagnetic interference shielding applications. These fillers are widely employed as well-known conductive fillers due to their unique structure and properties such as small diameter, large aspect ratio, high conductivity, light weight and high mechanical strength [146-148, 150, 156]. These properties have made them excellent choices for fabricating high performance electromagnetic interference shields. Electromagnetic interference shielding behaviour of a polymer based composites fabricated with the abovementioned conductive fillers are widely investigated [144-148, 151, 152, 156-159].

According to the previous studies, polymer composites made of CNT as conductive filler display higher shielding efficiency than those made of CNF. Yang et al. [152, 156] have compared the shielding performance of CNT/PS foam composite [152] with CNF/PS foam composite [156]. The higher EMI SE of CNT-polymer composite is mainly due to its higher conductivity and larger aspect ratio in comparison with the polymer composite made with CNF as filler [149, 152, 156]. The EMI SE of 10dB was obtained for 15wt.% CNF/PS foam composite in working frequency range of 8.4-12GHz [156]; however, the same EMI SE was acquired for the composite containing 7wt.%CNT in PS foam composite [152, 156]. Electromagnetic interference shielding performance of some of CNF or CNT/polymer composites has been revealed respectively in Table 2-2 and Table 2-3.

Table 2-2 A summary of shielding performance study on CF/polymer composites

Polymer composite	Shielding performance				Frequency
CF/polychloroprene (CR) [146] (30wt.% CF/CR)	t= 3.5cm, f=10GHz		t=1.7cm, f=10GHz		X-band: 8.2-12.4GHz
	L/D ¹ =100	SE _{total} =72dB	L/D=100	SE _{total} =64dB	
	L/D=25	SE _{total} =45dB	L/D=25	SE _{total} =26dB	
CF/CR [147] (30wt.% CF/CR)	t=3.5mm, f=2000MHz		t=1.7mm, f=2000MHz		100-2000MHz
	L/D=100	SE _{total} =32dB	L/D=100	SE _{total} =30dB	
	L/D=25	SE _{total} =20dB	L/D=25	SE _{total} =17.5dB	
CNF/PS foam [156] (15wt.% CNF/PS)	L:30-100µm, D=100-200nm		SE _{total} =19dB		X-band: 8.2-12.4GHz
	(no thickness)				
VGCNF/LCP [150] 15wt.% VGCNF/LCP L/D=500, t=1.45mm	wt.% VGCNF	5wt.%	10wt.%	15wt.%	F (MHz)
	SE _{total} (dB)	19	39	41	15MHz
	SE _{total} (dB)	11	21	26	200MHz
	SE _{total} (dB)	13	16	21	1500MHz

¹ L/D=length/diameter of CF or CNT

² LCP: Liquid crystal polymer

³ VGCNF: vapour grown carbon nanofiber

Table 2-3 A summary of EMI SE study on CNT/polymer composites

Polymer composite	Shielding performance					Frequency	
SWCNT/epoxy [157]	L/D=139(0.04S/cm)					SE _{total} =16dB	X-band:
15wt.% SWCNT/epoxy, t=2mm	L/D=240(0.2S/cm)					SE _{total} =256dB	8.2-12.4GHz
SWCNT/epoxy [145]	L/D=240(0.2S/cm)					SE _{total} =49dB	f=10MHz
15wt.% SWCNT/epoxy	(no thickness)					SE _{total} =15-20dB	f=500MHz-1.5GHz
CNT/ethylenevinylacetate (EVA) [144]	t(mm)	1.5	2.5	3.5	4.5	-	
15wt.%SWCNT/EVA	SE _{total} (dB)	16	20	23	28	200-1000MHz	
L/D~200-400, t: 1.5mm-4.5mm	SE _{total} (dB)	23	27	30	34	8-12GHz	
SWCNT/polyurethane (PU) [132]	SE _{total} (dB)					17dB	X-band:
20wt.%SWCNT/PU, t=2mm							8.2-12.4GHz
CNT/polystyrene foam [156]	SE _{total} (dB)					18.5dB	X-band:
7wt.%CNT/PS foam (no thickness)							8.2-12.4GHz

2.5.4.4.4 Electromagnetic composites

In spite of the dominance of electrically conducting materials as promising electromagnetic interference shields, electromagnetic composites are also studied for this purpose. Electromagnetic microwave absorbing materials such as ferrite (as magnetic filler)-conducting polymer (as electrically conductive matrix) composites with different magnetic nanofillers such as Fe₃O₄, γ -Fe₂O₃ and BaF nanoparticles [9, 18, 123, 135, 137, 160] and electromagnetic composites with combined magnetic and conductive fillers [105, 116, 124, 130] are known as promising absorbers at high frequencies over gigahertz (GHz) range because of their high dielectric and magnetic losses.

Magnetic particles are found to enhance the microwave absorption capability of composite through absorption by increasing its magnetic loss. It has been reported that shielding efficiency (SE) is dependent on complex permittivity and permeability through following equations [161]:

$$SE_A(dB) = 20d\left(\frac{\mu_r\omega\sigma_r}{2}\right)^{1/2} \text{Log}(e) \quad (10)$$

$$SE_R(dB) = 10\text{Log}\left(\frac{\sigma_r}{16\mu_r\omega\epsilon_0}\right) \quad (11)$$

$$SE_{total}(dB) = 20d\left(\frac{\mu_r\omega\sigma_r}{2}\right)^{1/2} \text{Log}(e) + 10\text{Log}\left(\frac{\sigma_r}{16\mu_r\omega\epsilon_0}\right) \quad (12)$$

where d: sample thickness (cm), $e=2.718$, σ_r : electrical conductivity (S/cm), μ_r : relative magnetic permeability, $\omega = 2\pi f$: angular frequency, ϵ_0 : dielectric constant of vacuum.

There is also a direct correlation between ϵ'' and electrical conductivity (σ) of a shield known as the free electron theory in which $\epsilon'' = \frac{\sigma}{2\pi\epsilon_0 f}$ where $\sigma (= 1/\rho)$: electrical conductivity, ρ : electrical resistivity, f: frequency, ϵ_0 : dielectric constant of vacuum [162]. This equation suggests that ϵ'' increases with increasing the electrical conductivity [148, 163]. According to the equations 9, 10 and 11, better microwave absorption properties can be achieved for thicker shield with higher electrical conductivity and magnetic permeability. Hence, the total shielding efficiency can be improved. It is known that microwave absorption behaviour of ferrite-conducting polymer composites with higher SE_A attributed to higher dielectric and magnetic losses [9, 123, 135, 137].

The microwave absorption behaviour of core-shell BaF/poly (3,4-ethylenedioxy thiophene) (PEDOT) nanocomposites was studied by Ohlan and co-workers [141]. Enhanced microwave absorption is attributed to the increase in both dielectric and magnetic losses. The increment in both real and imaginary parts of complex permittivity, ϵ' and ϵ'' values is referred to the difference in relative dielectric constant of BaF and PEDOT in matrix. This difference

increases the accumulation of more space charge and strong orientational polarization and consequently enhanced microwave absorption property. The contribution to the space charge polarization appears due to the heterogeneity of the material. For example, the presence of insulating BaF in the conducting matrix results in the formation of more interfaces and a heterogeneous system due to some space charge accumulating at the interface that contributes toward the higher microwave absorption in the composites [141]. Microwave absorption behaviour of BaF/PEDOT composite is also attributed to the magnetic properties of BaF nanoparticles. The larger the magneto-crystalline anisotropy of magnetic nanoparticles, the stronger is the coupling of magnetic dipoles. As the frequency increases, the rotation of magnetic dipoles becomes more difficult due to the strong anisotropy of BaF nanoparticles which causes more magnetic loss. The effective anisotropy coefficient enhances more in magnetic nanoparticles with decreasing the size of nanoparticles due to the surface effect and microstructural defects. As a result, increase in BaF loading in the composite leads to higher magnetic loss which in turn enhances the microwave absorption behaviour of the composite [141].

Besides, microwave absorption behaviour of conducting PANI-based composites combined with inorganic magnetic (Fe_3O_4 or $\gamma\text{-Fe}_2\text{O}_3$) and dielectric (TiO_2) nanoparticles are known to become even stronger than that of conducting PANI with either one of these nanoparticles [104, 132]. Dhawan et al. [123] examined the microwave absorption of conducting PANI polymer embedded with $\gamma\text{-Fe}_2\text{O}_3$ and TiO_2 nanoparticles in 12.4-18GHz (Ku-band) frequency range. Shielding effectiveness was proved to be dominated by the absorption mechanism.

The γ -Fe₂O₃-TiO₂-PANI nanocomposite showed better absorption ($SE_A \sim 45$ dB) than the γ -Fe₂O₃-PANI ($SE_A \sim 8.8$ dB) and TiO₂-PANI ($SE_A \sim 22.4$ dB) nanocomposites. Both magnetic and dielectric losses are demonstrated to be enhanced because of the combined effect of both γ -Fe₂O₃ and TiO₂ nanoparticles [123]. Shielding performance of a few electromagnetic polymer based composites is summarized in Table 2-4.

Table 2-4 A short summary of shielding performance of electromagnetic of selected polymer composites

Electromagnetic composite	Shielding performance			Frequency
	TiO ₂ : γ -Fe ₂ O ₃ :PANI	SE _A (dB)	SE _R (dB)	
TiO ₂ / γ -Fe ₂ O ₃ /PANI [135] t=2mm	0:1:1	8.8	~2	Ku-band: 12.4-18GHz (SE _{total} values at f~14.7GHz)
	1:0:1	22.4	~2	
	1:1:1	33	~2	
	1:2:1	45	~2	
γ -Fe ₂ O ₃ /PANI [137] (no thickness reported)	Pure γ -Fe ₂ O ₃ NPs	SE _{total} =11.2dB		X-band: 8.2-12.4GHz (SE _{total} values at f=8.2GHz)
	γ -Fe ₂ O ₃ -PANI	SE _{total} =2.5dB		
γ -Fe ₂ O ₃ /PEDOT [10] (no thickness reported)	SE(dB)	SE _A (dB)	SE _R (dB)	Ku-band: 12.4-18GHz (SE values at f=15.2GHz)
	Pure PEDOT	8.41	1.63	
	γ -Fe ₂ O ₃ /PEDOT	20.7	3.82	

2.5.4.4.5 Composite nanofibers

Composite nanofibers are first created via combining two or more functional components to form a stable polymer dope. Electrically conductive nanofillers such as CNTs, CNF, magnetic and dielectric nanoparticles such as TiO₂, γ -Fe₂O₃, Fe₃O₄, Fe, Ni can be combined with appropriate polymer solution to produce a composite solution. Then, these fillers are encapsulated inside the nanofibers via electrospinning of the composite polymer dope. Through encapsulating by polymer nanofibers, the nanofillers can be protected from environmental attack such as oxidation. Besides, due to the discrete nature of nanoparticles they cannot form

structures. Hence, embedding nanoparticles inside the fibers provide higher order structures functioning based on the combined properties of nanofillers and carrier. Composite sheets of interconnected composite fibers can be created afterwards. In order to enhance the mechanical properties such as flexibility or strength, the interconnected fibrous structures are cast by an appropriate polymer. For example, PDMS can be used as an elastomeric polymer to add flexibility to the structures which is so fragile.

In this work, magnetic nanoparticles (Fe_3O_4 nanoparticles) and electrically conducting PAN-based carbon nanofiber matrix are developed via electrospinning technique. The PAN polymer is used first to make the PAN based nanofibers containing Fe_3O_4 nanoparticles. PAN becomes conductive as it goes through an appropriate carbonization process which turns it into conductive carbon nanofibers carrying magnetic nanoparticles. However, the resulting Fe_3O_4 /carbon nanofiber composite is fragile and brittle. Therefore, an elastomeric polymer such as PDMS is cast on the sample in order to make it flexible. As a result, flexible sample will be obtained and it can be easily cut into different forms and structures needed for various applications.

The electromagnetic shielding effectiveness of nanofiber based composites has yet to be studied. This is an area of novelty in the present work. Liu et al. [164] introduced the Fe_2O_3 /cellulose nanocomposite microfiber as promising functional composite fiber for the purpose of electromagnetic interference shielding. However, no shielding efficiency performance of this functional composite is reported. In this work, one of the promising applications of the Fe_3O_4 /carbon nanofiber composites is studied. The shielding effectiveness of pristine carbon nanofibers and multifunctional electromagnetic composite nanofibers are presented to demonstrate the effect of particle size and content and also membrane thickness.

Chapter 3. Experimental

3.1 Materials

Materials used in this study are PAN with 150,000 average molecular weight purchased from Scientific Polymer Products, Inc., N,N-Dimethylformamide (DMF, 99.9%) purchased from Fisher Scientific, (GA:20-30nm Fe₃O₄) nanoparticles purchased from Nanostructured, (GB:10-20nm) Fe₃O₄ nanoparticles purchased from Sky Spring and Amorphous Materials Inc., Triton X-100 (contains less than 3% Polyethylene glycol) purchased from Sigma-Aldrich.

3.2 Polymer solution preparation

Pure 10wt.% PAN/DMF and composite Fe₃O₄/PAN/DMF solutions were prepared in this study. To make composite solutions, 3, 5 and 10wt.% Fe₃O₄ (GA:20-30nm or GB:10-20nm) to the PAN were dispersed in 10wt.% PAN/DMF solution. The solutions were prepared using Triton X-100 as surfactant and DMF as solvent for PAN. The Fe₃O₄ nanoparticles were first bath sonicated in DMF for 9h. Then, Triton X-100 (with the same weight as Fe₃O₄) was added to the solution and solution was bath sonicated for another 9h to obtain uniform dispersion of Fe₃O₄ in the solvent. In the final step, an appropriate amount of PAN was added to the previously prepared Fe₃O₄/TritonX-100/DMF solution and the sample was then bath sonicated for 9h.

3.3 Electrospun nanofiber fabrication

Electrospinning unit (KATO TECH CO. LTD.) was used to prepare the nanofibrous samples from the solutions containing different amount of Fe₃O₄ nanoparticles. The polymer solutions (PAN/DMF and Fe₃O₄/PAN/DMF) were first loaded into a plastic syringe with G18 needle (inner and outer diameter of respectively 0.8mm and 1.2mm). A collector at 17cm distance from

the spinneret was placed as a grounded counter electrode. A constant volume of solution was delivered to the needle at a flow rate of 2ml/hour and a high potential of 11-12kV was applied to the polymer solution coming out of the needle. The non-woven fiber mat was collected on the aluminum foil placed on the grounded electrode.

3.4 Carbonization process

The pristine and composite electrospun nanofibers were carbonized using tube furnace (79400 Thermolyne) shown in Figure 3-1. The carbonization process of electrospun PAN-based nanofibers is also shown in Figure 3-2.

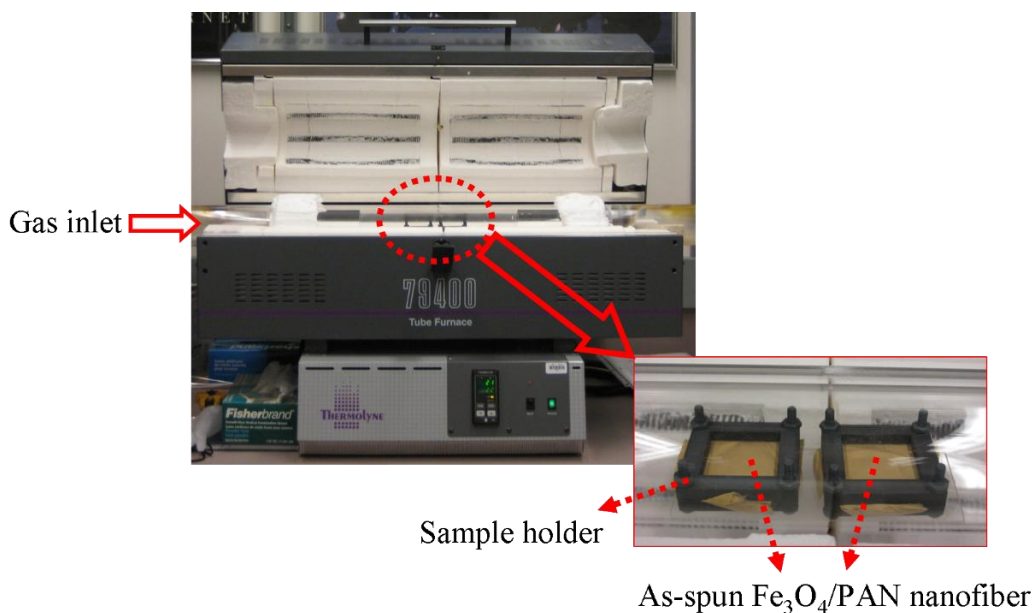


Figure 3-1 The tube furnace used to carbonize the as-spun nanofibers. (The as-spun $\text{Fe}_3\text{O}_4/\text{PAN}$ nanofiber is shown that is placed in the sample holder.)

The as-spun nanofibers were first weighed and placed in the furnace. The samples were heated to 250°C with a ramping rate of 5°C/min and then stabilized for 100min under ambient atmosphere. The stabilized samples were then exposed to nitrogen at 250°C for 20min and

heated to 700°C or 900°C with the ramping rate of 5°C/min. The samples were carbonized at each of these processing temperatures for 60min. The carbon fibers were then cooled down to the room temperature under nitrogen atmosphere and weighed to measure the carbon yielding during the carbonization process. Figure 3-3 shows a flowchart summarising the detail design of experimental works. A summary of sample designation code for different samples used in this study is shown in Table 3-1 and Table 3-2.

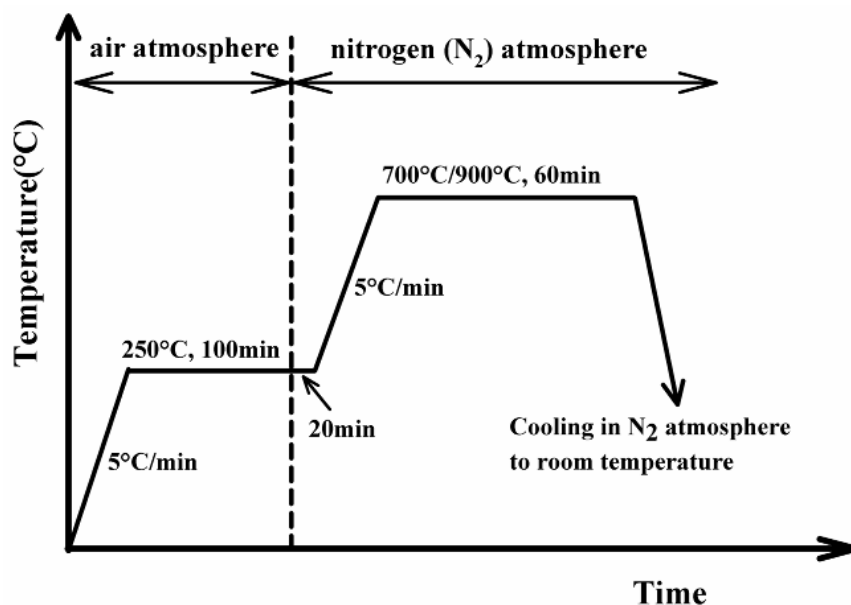


Figure 3-2 The procedure used to carbonize the as-spun PAN-based nanofibers.

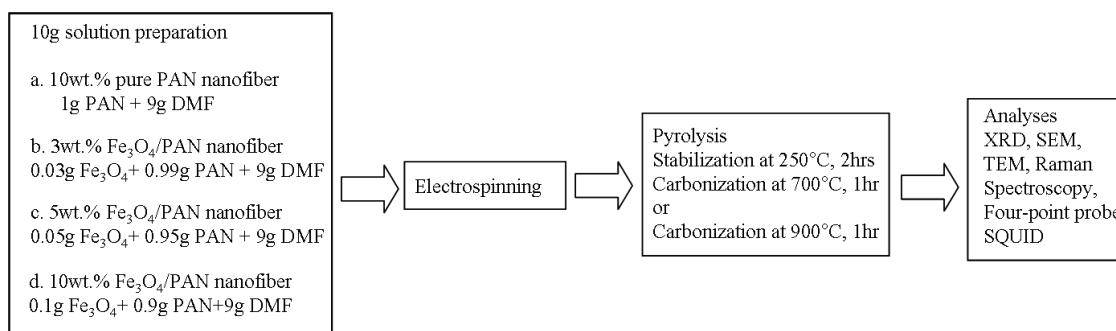


Figure 3-3 Experimental plan for this study.

Table 3-1 Summary of designated codes for different samples containing GA:20-30nm Fe₃O₄ nanoparticles

Fe ₃ O ₄ (wt.%) in PAN	As-spun fiber	Carbonized at 700°C	Carbonized at 900°C
0wt.% Fe ₃ O ₄ 10wt.% PAN/DMF	10PAN	10PAN700	10PAN900
3wt.% Fe ₃ O ₄	A3F	A3F700	A3F900
5wt.% Fe ₃ O ₄	A5F	A5F700	A5F900
10wt.% Fe ₃ O ₄	A10F	A10F700	A10F900

Table 3-2 Summary of designated codes for different samples containing GB:10-20nm Fe₃O₄ nanoparticles

Fe ₃ O ₄ (wt.%) in PAN	As-spun fiber	Carbonized at 700°C	Carbonized at 900°C
3wt.% Fe ₃ O ₄	B3F	B3F700	B3F900
5wt.% Fe ₃ O ₄	B5F	B5F700	B5F900
10wt.% Fe ₃ O ₄	B10F	B10F700	B10F900

3.5 Characterization methods

Fiber morphologies and nanoparticles distribution of pristine carbon nanofibers and Fe₃O₄/carbon composite nanofibers were studied using Scanning Electron Microscope (SEM) (Hitachi S-2300) and Transmission Electron Microscope (TEM) (Hitachi H-800). X-ray diffraction (XRD) with Rigaku Multiflex diffractometer using Cu-K_α radiation was used to verify the chemical composition of nanofibers after carbonization. The 2θ angle was varied from 10° to 90° with the scanning speed of 2°/min. The prepared pristine and composite carbon nanofibers were also subjected to Renishaw InVia Raman microscope using He-Ne laser at 633nm excitation. The electrical conductivity was measured using four-point probe method. Electrical conductivity, σ, was calculated by the expression, $\sigma(\text{S/cm})=L/(t \times R)$, where R is electrical resistance in Ω, t is thickness of the specimen in cm and L is distance the between electrodes in cm (0.6cm in this study). Figure 3-3 illustrates the experimental setup of measuring the electrical conductivity using the four-point probe technique.

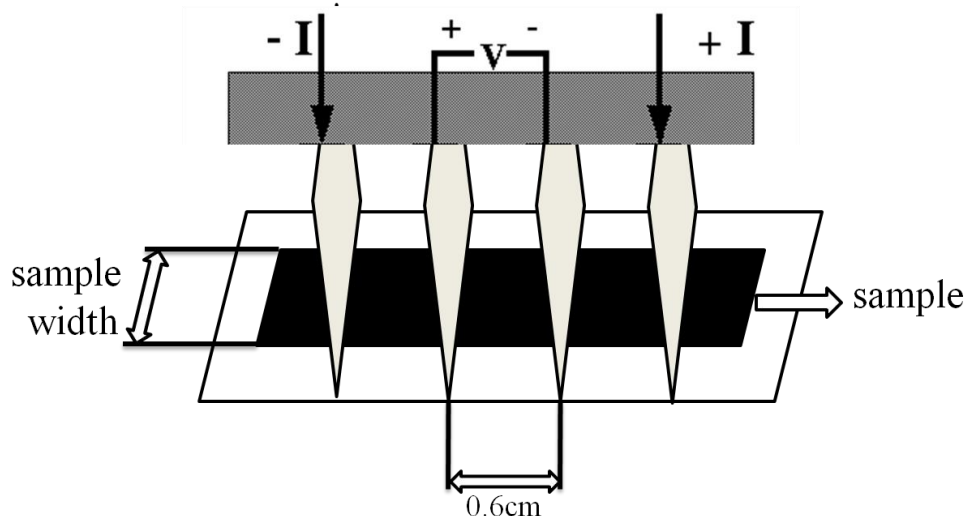


Figure 3-4 Four-point probe method to measure the electrical conductivity using 4 copper electrodes.

The plots of magnetization versus magnetic field were generated using Superconducting Quantum Interference Device (SQUID) (Quantum Design, CA, USA). The SQUID was used to measure the magnetic moment (emu) as a function of applied magnetic field (Oe) at room temperature (300K). The information related to sample dimension and mass used respectively for four-point probe and SQUID measurements is summarized in Table 3-3.

Table 3-3 The experimental details (specimen dimension and mass) used for the electrical conductivity and SQUID measurements

Sample	SQUID Mass (g)	Electrical conductivity (cm)	Sample	SQUID Mass (g)	Electrical conductivity (cm)
APAN700	-	$2.7 \times 0.6 \times 0.01$	APAN900	-	$2.4 \times 0.6 \times 0.01$
A3F700	0.0066	$2.7 \times 0.6 \times 0.02$	A3F900	0.0037	$2.7 \times 0.6 \times 0.01$
A5F700	0.0094	$3 \times 0.6 \times 0.01$	A5F900	0.0039	$2.25 \times 0.6 \times 0.01$
A10F700	0.0075	$1.4 \times 0.6 \times 0.16$	A10F900	0.0036	$1.8 \times 0.6 \times 0.01$
A3F	0.0049	-	A5F	0.0090	-
A10F	0.0096	-	(GA: 20-30nm)Fe ₃ O ₄	0.0304	-
B3F700	-	$2.7 \times 0.6 \times 0.014$	B3F900	0.0030	$2.6 \times 0.6 \times 0.01$
B5F700	-	$2.6 \times 0.6 \times 0.02$	B5F900	0.0065	$2.4 \times 0.6 \times 0.01$
B10F700	-	$1.9 \times 0.6 \times 0.01$	B10F900	0.0076	$2 \times 0.6 \times 0.02$
B3F	0.0079	-	B5F	0.0047	-
B10F	0.0080	-	(GB: 10-20nm) Fe ₃ O ₄	0.0460	-

The Agilent PNA E8362C is used to measure the electromagnetic interference shielding effectiveness of the pristine carbon nanofiber and Fe_3O_4 /carbon nanofiber composites with various Fe_3O_4 content, size and membrane thickness. The test setup is shown in Figure 3-5. The data is collected as S_{ij} parameters from the PNA network and analyzed using a matlab code to acquire SE_{total} , SE_R and SE_A values over 8.2-12.4GHz using equations (3-9) explained in section 2.5.4.2.

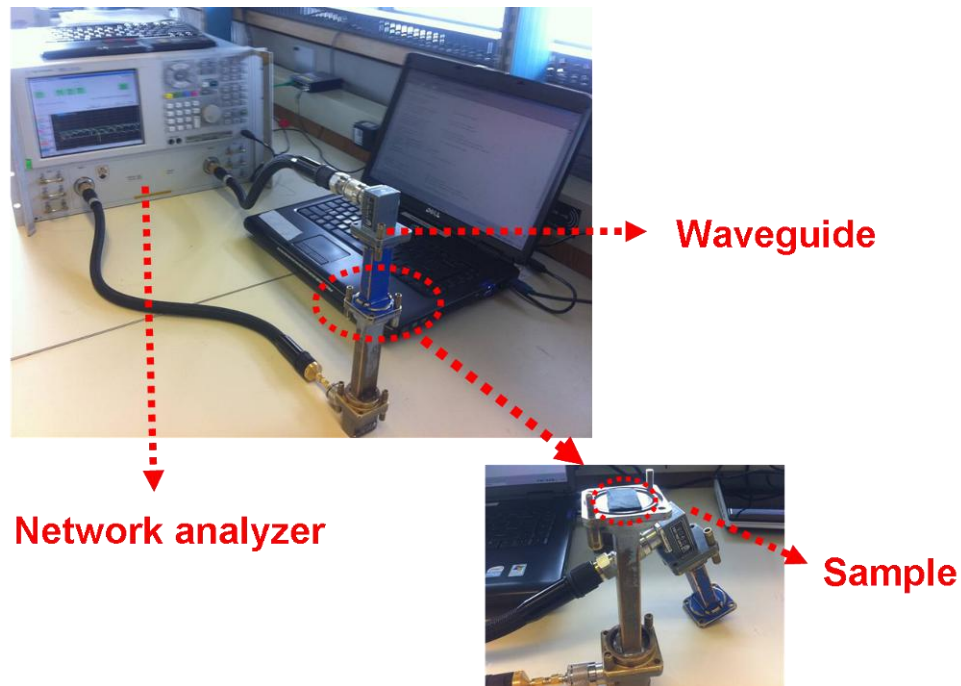


Figure 3-5 Scattering parameters measurement set-up.

Chapter 4. Results

4.1 Microstructural and compositional characterizations

4.1.1 SEM observations

Scanning Electron Microscope (SEM) was used to show the morphological features of electrospun nanofibers before and after carbonization. Figure 4-1(a-c) respectively represents the SEM images of (a) as-spun pure PAN nanofiber (10PAN) and pure PAN-based carbon nanofibers carbonized at (b) 700°C (10PAN700) and (c) 900°C (10PAN900).

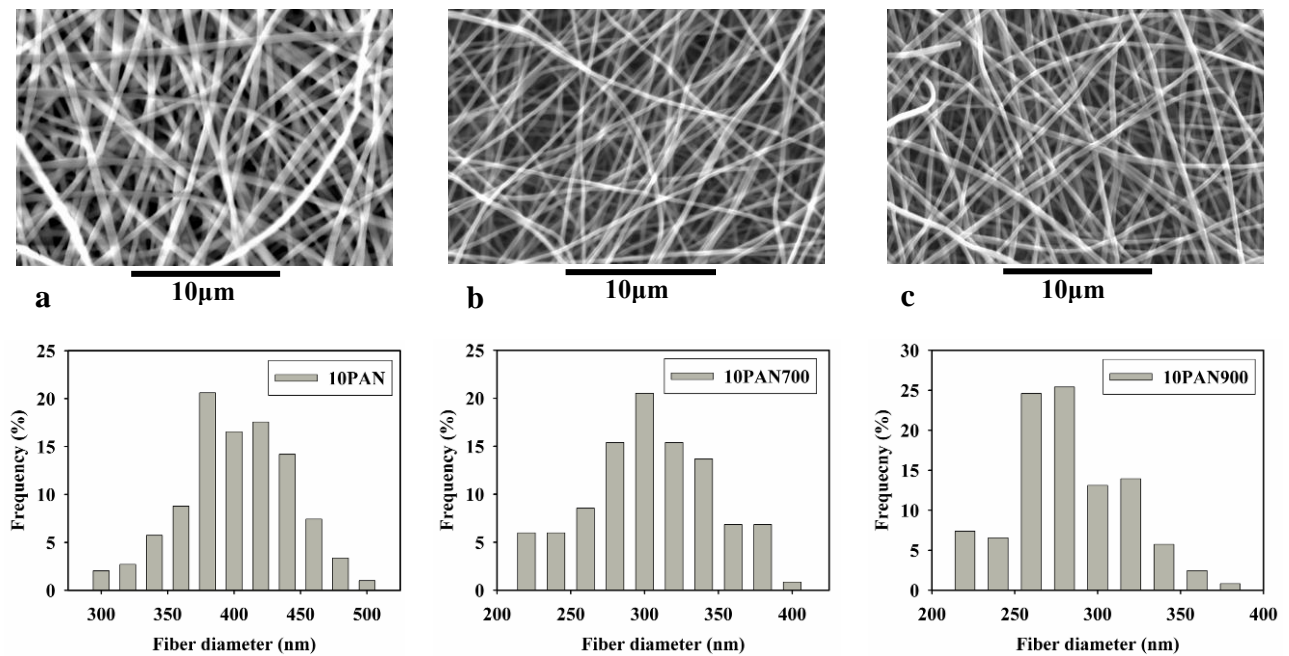


Figure 4-1(a-c) SEM micrographs of (a) as-spun pure PAN nanofibers (10PAN) and pure PAN nanofibers carbonized at (b) 700°C (10PAN700) and (c) 900°C (10PAN900) samples.

SEM images of composite nanofibers containing two different sizes of Fe_3O_4 nanoparticles, GA:20-30nm and GB:10-20nm are shown in Figure 4-2 and Figure 4-3. Figure 4-2(a-c) respectively depicts the SEM images of (a) as-spun 5% Fe_3O_4 (GA:20-30nm)/PAN

composite nanofiber (A5F10PAN) and its corresponding carbon nanofibers carbonized at (b) 700°C (A5F700) and (c) 900°C (A5F900).

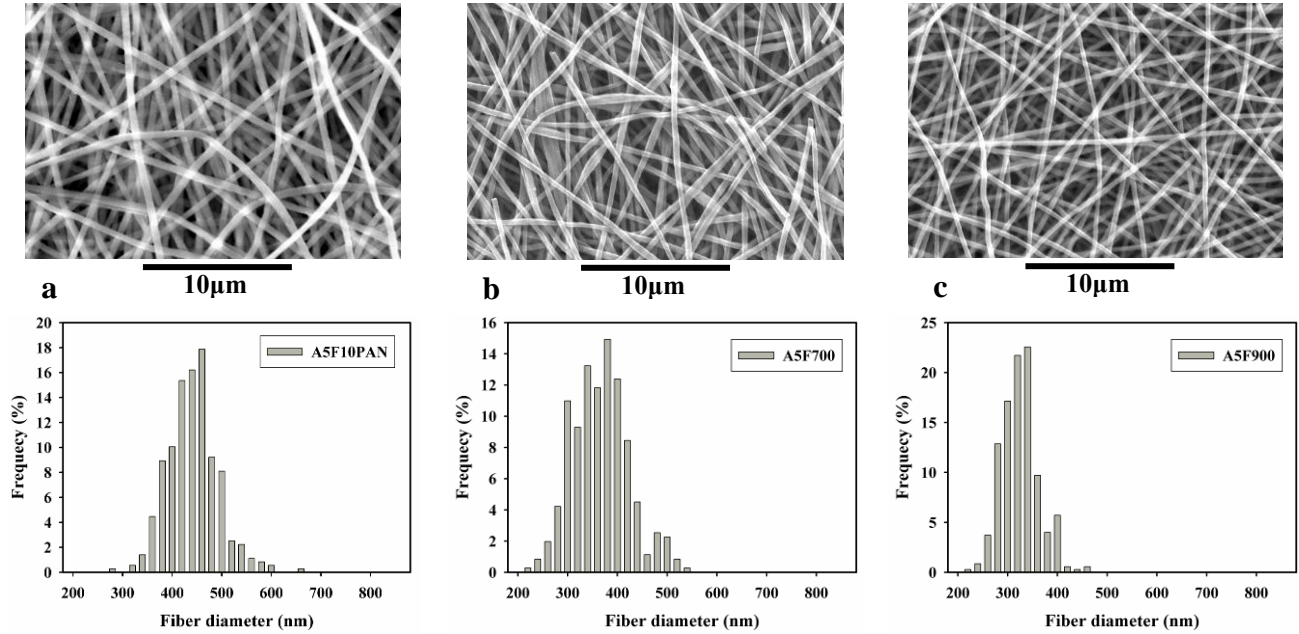


Figure 4-2 SEM micrographs of (a) as-spun 5wt.% (20-30nm) Fe₃O₄/PAN composite nanofibers (A5F10PAN) and composite nanofibers carbonized at (b) 700°C (A5F700) and (c) 900°C (A5F900) samples.

Figure 4-3(a-c) exhibits the SEM images of (a) as-spun 5%Fe₃O₄ (GB:10-20nm)/PAN composite nanofiber (B5F10PAN) and its corresponding nanofibers carbonized at (b) 700°C (B5F700) and (c) 900°C (B5F900). A summary of the measured average fiber diameter and standard deviations is presented in Table 4-1.

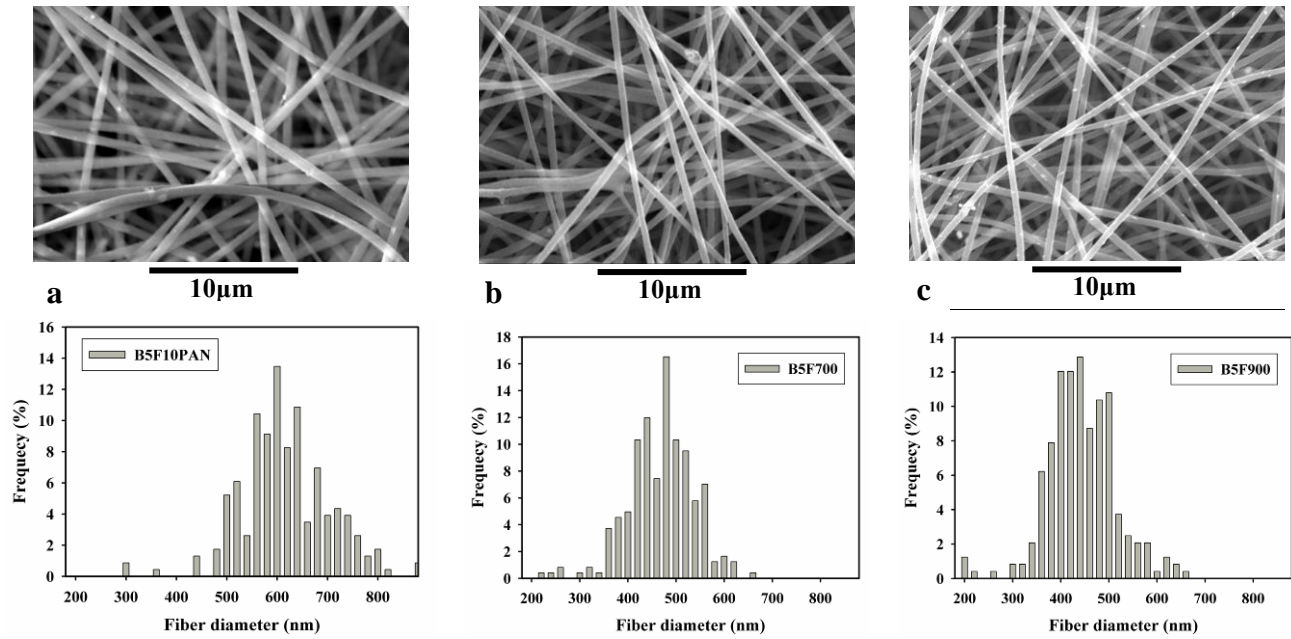


Figure 4-3 SEM micrographs of (a) as-spun 5wt.% (10-20nm) $\text{Fe}_3\text{O}_4/\text{PAN}$ composite nanofibers (B5F10PAN) and composite nanofibers carbonized at (b) 700°C (B5F700) and (c) 900°C (A5F900) samples.

Table 4-1 Fiber diameter (D_f) of as-spun and carbonized nanofibers

As-spun	D_f (nm)	700°C	D_f (nm)	900°C	D_f (nm)
10PAN	390±40	10PAN700	290±48	10PAN900	272±33
A3F10PAN	434±48	A3F700	304±34	A3F900	252±25
A5F10PAN	431±51	A5F700	356±56	A5F900	315±37
A10F10PAN	538±60	A10F700	429±67	A10F900	370±74
B3F10PAN	805±150	B3F700	570±88	B3F900	533±71
B5F10PAN	605±89	B5F700	458±68	B5F900	432±71
B10F10PAN	837±52	B10F700	646±167	B10F900	597±151

Random distribution of uniform fibers can be seen in all the nonwoven mat samples. As shown in Figure 4-1(a-c) and according to the data summarized in Table 4-1, the average diameter of pure PAN nanofiber decreases from 390±40nm for as-spun 10PAN sample to 290±48nm and 272±33nm after carbonization for 10PAN700 and 10PAN900 samples, respectively. As shown in Figure 4-2, Figure 4-3 and Table 4-1, fiber diameter also decreases for composite nanofibers after carbonization process in comparison with their corresponding as-spun nanofibers. The average fiber diameter decreases from 431±51nm for A5F10PAN sample to

356±56nm and 315±37nm for A5F700 and A5F900 samples, respectively. Similarly, the average fiber diameter of B5F10PAN samples reduces from 605±89nm to 458±68nm and 432±71nm after carbonization for B5F700 and B5F900 samples, respectively.

In addition, composite nanofibers show the same morphology of as-spun pure PAN except for larger fibers obtained for samples containing Fe₃O₄ nanoparticles. The average fiber diameter of electrospun pristine PAN nanofiber, 10PAN increases from 390±40nm to 431±51nm and 605±89nm for as-spun A5F10PAN and B5F10PAN nanofibers (each containing 5wt.% GA:20-30nm and GB:10-20nm Fe₃O₄ nanoparticle).

4.1.2 TEM observations

Transmission Electron Microscope (TEM) micrographs of Fe₃O₄ nanoparticles (GA:20-30nm and GB:10-20nm) is shown in Figure 4-4(a,b) that further confirms the larger size of GA:20-30nm Fe₃O₄ nanoparticles compared to GB:10-20nm Fe₃O₄ nanoparticles.

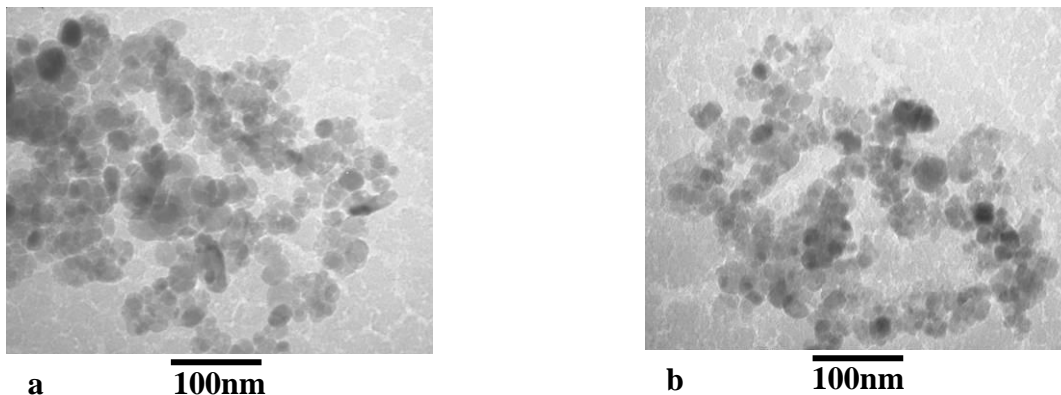


Figure 4-4 TEM micrographs of two different sizes of (a) GA:20-30nm Fe₃O₄ nanoparticles and (b) GB:10-20nm Fe₃O₄ nanoparticles.

To observe the dispersion of nanoparticles inside the nanofibers and also the size variation of nanoparticles before and after carbonization, TEM studies were conducted. Figure

4-5(a,b) shows the dispersion of (a) 10wt.% GA:20-30nm Fe₃O₄ nanoparticles and (b) 10wt.% GB:10-20nm Fe₃O₄ nanoparticles in the as-spun PAN-based nanofiber.

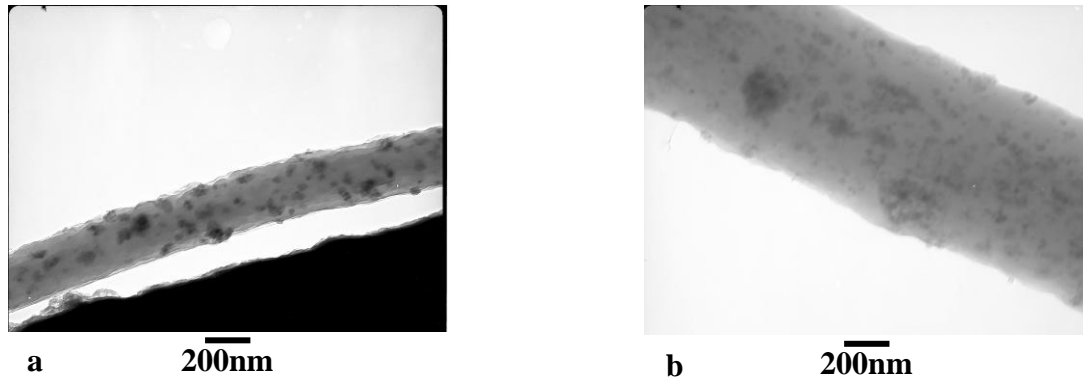


Figure 4-5 TEM micrographs of as-spun composite nanofibers containing 10wt.%Fe₃O₄ fabricated with (a) GA:20-30nm (A10F10PAN) and (b) GB:10-20nm (B10F10PAN).

The dispersion of Fe₃O₄ nanoparticles is also demonstrated in Figure 4-6(a-d) for carbonized samples. Figure 4-6(a,b) displays the TEM images of carbonized fibers containing 10wt.%Fe₃O₄ GA:20-30nm Fe₃O₄ carbonized at (a) 700°C (A10F700) and (b) 900°C (A10F900). Figure 4-6(c,d) also shows the TEM images of carbonized fibers containing 10wt.% GB:10-20nm Fe₃O₄ carbonized at (c) 700°C (B10F700) and (d) 900°C (B10F900). Average particles size of carbonized samples containing 5wt.% and 10wt.% GA:20-30nm Fe₃O₄ carbonized at 700°C and 900°C are also measured and reported in Table 4-2.

An important observation from the TEM images of as-spun and carbonized composite nanofibers shown in Figure 4-5(a,b) and Figure 4-6(a-d) is that the size of Fe₃O₄ particles increases after the pyrolysis process and it becomes somewhat larger for samples carbonized at higher temperature, i.e. 900°C (Figure 4-6(b,d)). According to Table 4-2 the size of Fe₃O₄ nanoparticle increases from 22±7nm for as-spun sample to 60±22nm and 66±30nm respectively

for carbonized samples containing 10wt.% GA:20-30nm Fe_3O_4 carbonized at 700°C (A10F700) and 900°C (A10F900). Besides, composite fibers containing larger nanoparticles, (GA:20-30nm) show the formation of larger particles (Figure 4-6(a,b)) as compared with the composites containing smaller particles (GB:10-20nm) (Figure 4-6(c,d)).

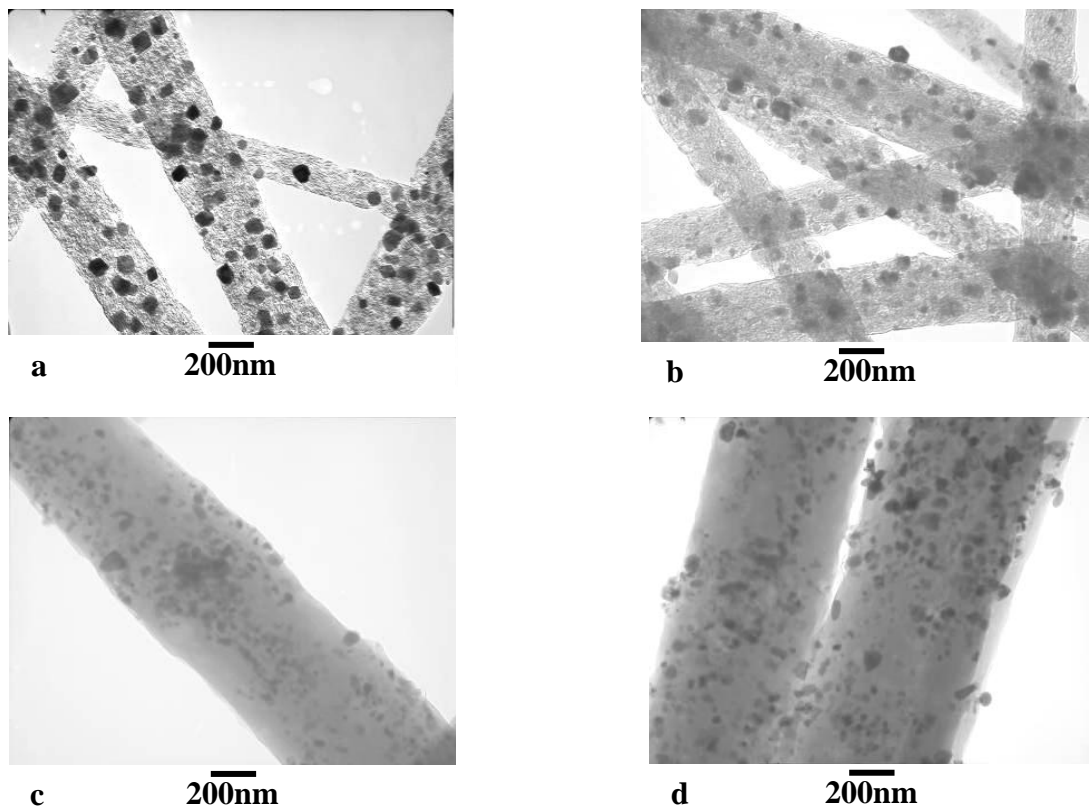


Figure 4-6 TEM micrographs of composite nanofibers (a) 10wt.% GA:20-30nm Fe_3O_4 carbonized at 700°C and (b) 900°C, (c) 10wt.% GB:10-20nm Fe_3O_4 carbonized at 700°C and (d) 900°C.

The effect of the amount of GA:20-30nm Fe_3O_4 loading in the size of particles after carbonization process has also been demonstrated in Figure 4-7 (a,b). Comparing the TEM micrographs of (a) 5wt.% and (b) 10wt% Fe_3O_4 nanoparticles after carbonization at 900°C shows that higher Fe_3O_4 loading (10wt.%) results in obtaining larger particles distributed in the carbon fiber matrix.

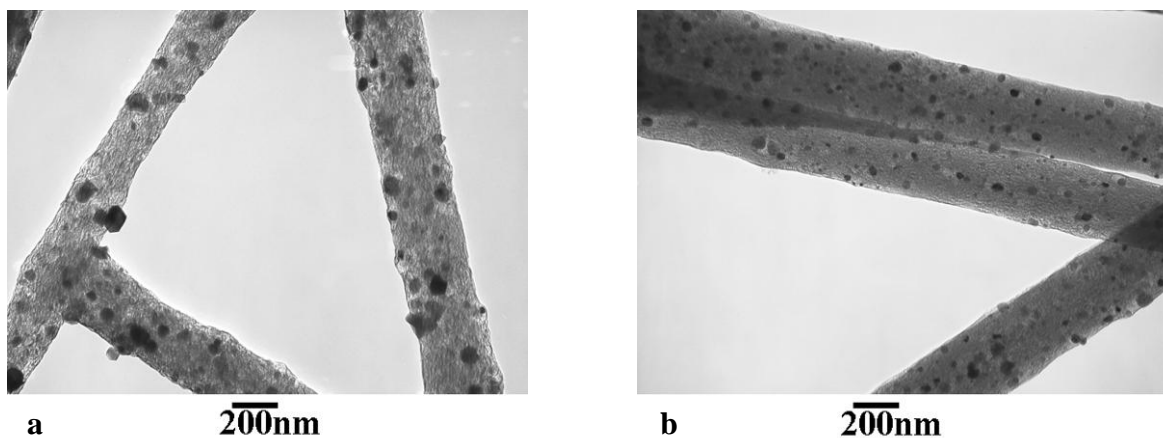


Figure 4-7 TEM micrographs of composite nanofibers carbonized at 900°C made of GA:20-30nm containing (a) 10 and (b) 5wt.%Fe₃O₄ nanoparticles.

Table 4-2 Average particles size of GA:20-30nm Fe₃O₄ nanoparticles and as-spun and carbonized composite nanofibers containing GA:20-30nm Fe₃O₄ at two carbonization temperatures, 700°C and 900°C

Sample code	Average size of particles
A5F	22±7
A5F700	36±13
A5F900	44±17
A10F	22±7
A10F700	60±22
A10F900	66±30
GA:20-30nm Fe ₃ O ₄ nanoparticles	22±7

4.1.3 XRD analysis

Phase identification of nanoparticles, pristine and composite carbon nanofibers are performed using X-ray diffractometer (XRD). MDI Jade software was used to identify the phases exist in different samples.

4.1.3.1 Fe₃O₄ nanoparticles

Figure 4-8 illustrates the XRD patterns of two different sizes of GA:20-30nm and GB:10-20nm Fe₃O₄ nanoparticles. The Fe₃O₄ (magnetite) peaks (reference number: #01-071-6337) was obtained using MDI Jade software (shown in Figure 4-8). The 2θ angles of 18.371°,

30.221°, 35.598°, 37.237°, 43.266°, 53.682°, 57.227°, 62.848°, 66.084°, 71.310°, 74.367°, 75.374°, 79.366°, 87.212°, 90.134°, 95.008°, 102.896°, 105.911°, 106.962°, 111.045°, 119.670°, 123.091 and 129.118° respectively correspond to the magnetite crystal planes of (111), (220), (311), (222), (400), (422), (511), (440), (531), (620), (533), (622), (444), (642), (731), (800), (822), (751), (662), (840), (664), (931) and (844). However, there are a few extra peaks observed for GB:10-20nm Fe₃O₄ nanoparticles which might belong to NaCl (ref.: #01-070-2509). The peaks related to NaCl are also marked shown in Figure 4-8.

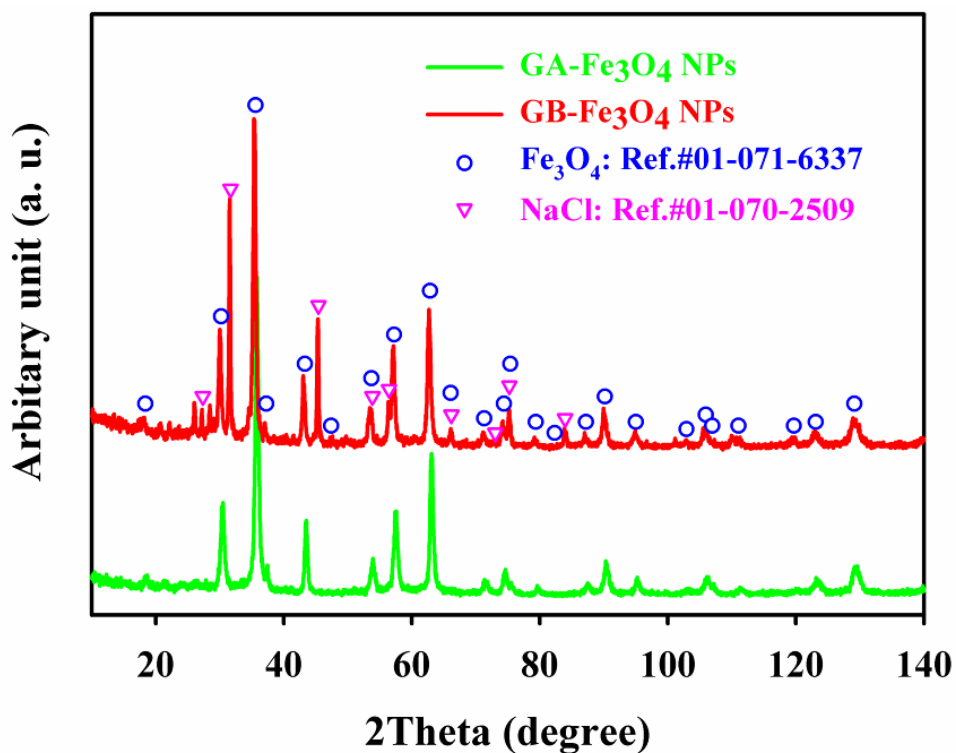


Figure 4-8 XRD patterns of GA:20-30nm and GB:10-20nm Fe₃O₄ nanoparticles with corresponding Fe₃O₄ and NaCl peaks.

4.1.3.2 GA:20-30nm Fe₃O₄/carbon nanofiber composites

Figure 4-9(a,b) illustrates the effect of Fe₃O₄ content (0, 3, 5 and 10wt.% Fe₃O₄) and pyrolysis temperature, (a) 700°C and (b) 900°C on the XRD patterns of carbonized samples containing GA:20-30nm Fe₃O₄ nanoparticles. Figure 4-10(a,b) also magnifies the $2\theta_{(002)}$ of the (002) graphite plane of the abovementioned samples at two different carbonization temperatures, i.e. (a) 700°C and (b) 900°C. According to the XRD results, the 2θ and the average interlayer planar d-spacing of the (002) graphite plane ($2\theta_{(002)}$ and $d_{(002)}$) pristine carbon nanofibers and composite carbon nanofibers containing GA:20-30nm Fe₃O₄ nanoparticles carbonized at 700°C and 900°C are summarized in Table 4-3.

All carbonized samples exhibit the formation of graphitic structure near 2θ angles of 24° and 44° respectively corresponding to (002) and (010) layers with small difference in the sharpness and position of the peaks as demonstrated in Figure 4-9. Fe₃O₄ peaks are also identified in Figure 4-9(a,b). Other than graphite and Fe₃O₄, XRD results reveal the presence of two metallic α -Fe (Ref.#98-000-0064) and Fe₃C (Ref.#99-000-0796) phases formed during the carbonization process. The peaks related to α -Fe and Fe₃C phases are also shown in Figure 4-9. Figure 4-9a shows the XRD patterns of pristine carbon nanofibers (10PAN700), 3wt.%Fe₃O₄ (A3F700) 5wt.%Fe₃O₄ (A5F700) and 10wt.%Fe₃O₄ (A10F700) composite carbon nanofibers carbonized at 700°C. The intensity and sharpness of the Fe₃O₄ peaks increase with Fe₃O₄ concentration from 0 to 3, 5 and 10wt.%. The same trend is observed for samples carbonized at 900°C (see Figure 4-9b). The carbonization temperature also causes some variation in the intensity of peaks. The intensity of the peaks becomes higher and sharper as the carbonization temperature increases. More intensive Fe₃O₄ peaks are observed for samples carbonized at higher temperatures as we compare the XRD patterns of samples carbonized at 700°C in Figure 4-9a

with those carbonized at 900°C shown in Figure 4-9b. It should also be considered that the metallic α -Fe and Fe₃C phases are appeared for samples with higher Fe₃O₄ loading (5wt.% and 10wt.%).

As mentioned previously in this section, graphite peak of (002) plane with 2θ angle of 24° shifts slightly towards higher degrees with Fe₃O₄ loading and carbonization temperature. Figure 4-10(a,b) demonstrates the shift of $2\theta_{(002)}$ corresponding to the graphite peak position with Fe₃O₄ content at different carbonization temperatures, (a) 700°C and (b) 900°C.

The XRD patterns of the abovementioned carbonized samples are magnified in the 2θ range of 18°-30° for samples carbonized at (a) 700°C and (b) 900°C. Increasing the Fe₃O₄ wt.% leads to the shift of $2\theta_{(002)}$ peak for both carbonization temperatures. Besides, as summarized in Table 4-3, the corresponding $2\theta_{(002)}$ increases from 24.20° to 25.27°, 25.67° and 25.99°. Simultaneously, the interlayer d-spacing of (002) graphite plane ($d_{(002)}$) decreases from 3.67nm to 3.52nm, 3.47nm and 3.43nm, respectively for pristine carbon nanofiber (10PAN900), 3wt.%Fe₃O₄ (A3F900), 5wt.%Fe₃O₄ (A5F900) and finally 10wt.%Fe₃O₄ (A10F900) composite carbon nanofibers (carbonized at 900°C). The same trend is observed for samples carbonized at 700°C as shown in Figure 4-10a. However, less sharp and broader graphite peaks are acquired for samples carbonized at 700°C in comparison with those pyrolyzed at 900°C.

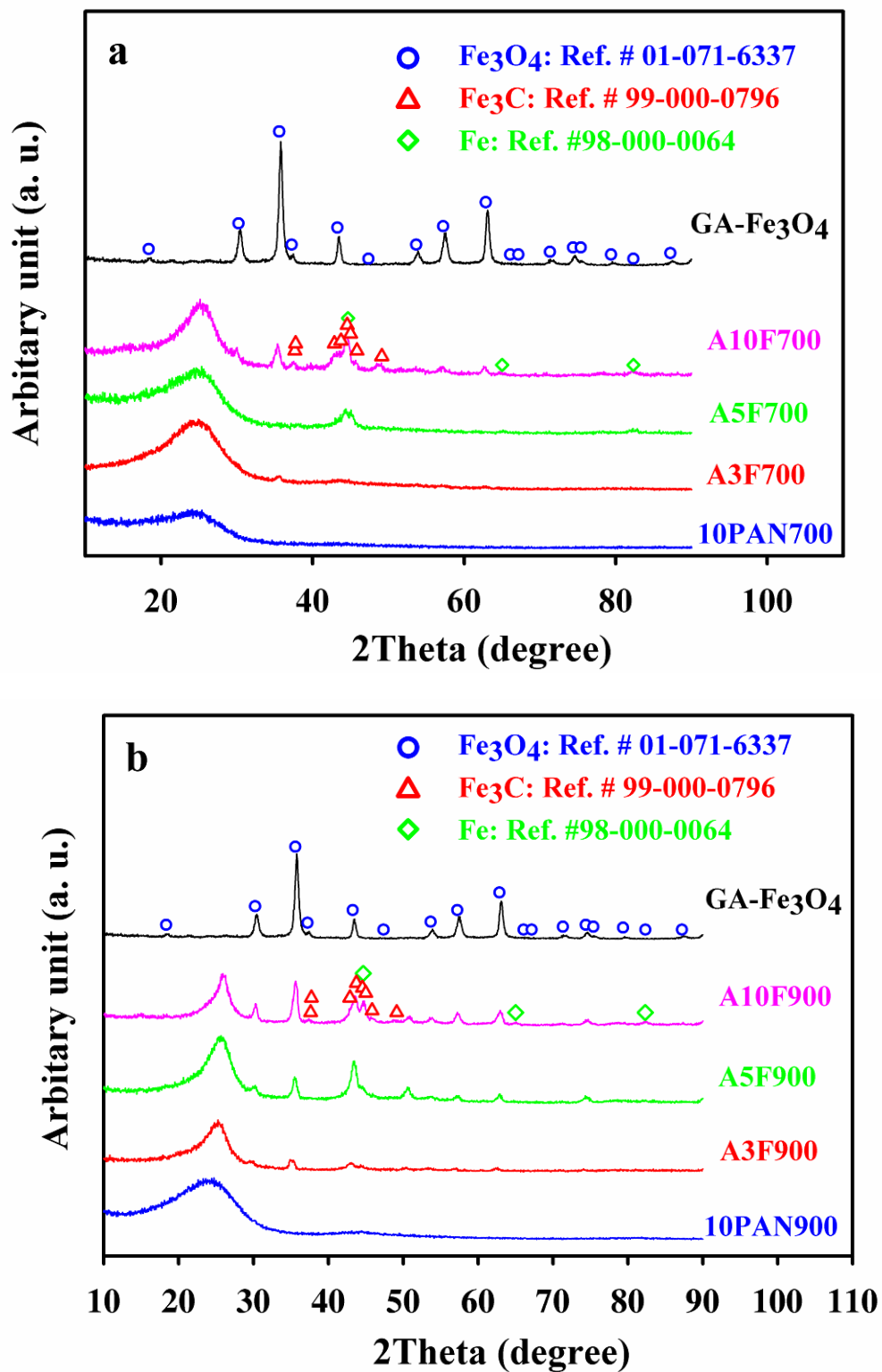
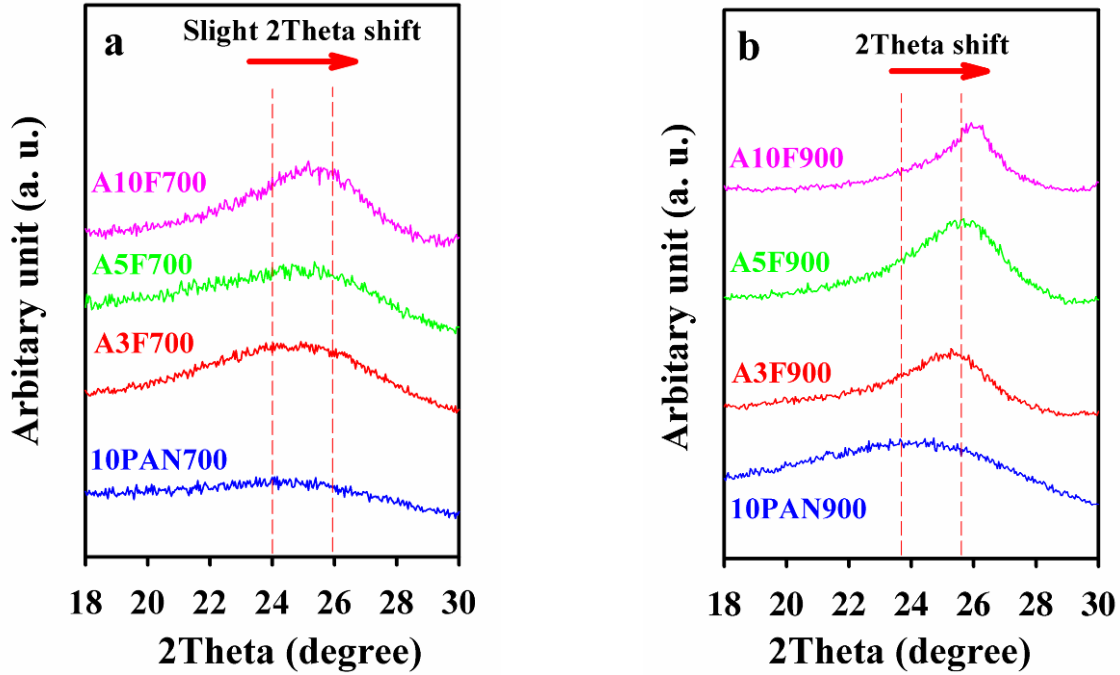


Figure 4-9 XRD patterns of pure and composite carbon nanofibers containing GA:20-30nm Fe_3O_4 nanoparticles.

Table 4-3 $2\theta_{(002)}$ and $d_{(002)}$ (nm) of pristine and composite carbon nanofibers (900°C)

Sample	$2\theta_{(002)}$	$d_{(002)}$ (nm)
10PAN900	24.20	3.67
A3F900	25.27	3.52
A5F900	25.67	3.47
A10F900	25.99	3.43

**Figure 4-10** $2\theta_{(002)}$ shifts towards higher degrees with adding (GA:20-30nm) Fe_3O_4 wt.% for samples carbonized at (a) 700°C and (b) 900°C.

4.1.3.3 GB:10-20nm Fe_3O_4 /carbon nanofiber composites

Figure 4-11(a,b) shows the XRD patterns of pristine carbon nanofibers and composite carbon nanofibers containing GB:10-20nm Fe_3O_4 nanoparticles carbonized at both (a) 700°C and (b) 900°C. The magnified XRD patterns of various carbonized samples at both carbonization temperature, (a) 700°C and (b) 900°C are represented in Figure 4-12 in 2θ range of 18°-30° to depict the peak shift in this range. The $2\theta_{(002)}$ and $d_{(002)}$ (nm) of pure and composite carbon nanofibers containing GB:10-20nm Fe_3O_4 nanoparticles and carbonized at 900°C are also

summarized in Table 4-4. Similar to the results obtained for samples made of GA:20-30nm Fe_3O_4 nanoparticles, the XRD results demonstrate the graphitic peaks near the 2θ angles of 24° and 44° and the presence of Fe_3O_4 phase; however, negligible amount of shift in the position and intensity of the graphite peak can be observed which will be discussed later. Other than those two phases, it is found that Fe_3C is also formed only for sample with 5 and 10wt.% Fe_3O_4 and carbonized at 900°C (designated as B5F900 and B10F900 samples). Moreover, the NaCl peaks identified for GB:10-20nm Fe_3O_4 nanoparticles (Figure 4-8) are disappeared during the carbonization process. The intensity and sharpness of the Fe_3O_4 peaks are shown to increase with Fe_3O_4 loading and with increasing the carbonization temperature from 700°C to 900°C (Figure 4-11(a,b)).

Increasing the Fe_3O_4 loading leads to a negligible amount of shift of the 2θ angle of (002) graphitic plane ($2\theta_{(002)}$) for samples carbonized at higher carbonization temperature, 900°C rather than 700°C . In addition, the average interlayer d-spacing of (002) plane ($d_{(002)}$) barely changes with Fe_3O_4 loading. With increasing the Fe_3O_4 concentration from 0wt.% for pristine carbon nanofibers (10PAN900) sample to 3wt.% (B3F900), 5wt.% (B5F900) and 10wt.% (B10F900) samples, the $2\theta_{(002)}$ barely varies from 24.20° to 24.43° , 24.62° and 24.74° and the $d_{(002)}$ very slightly from 3.67nm to 3.64nm, 3.61nm and 3.50nm.

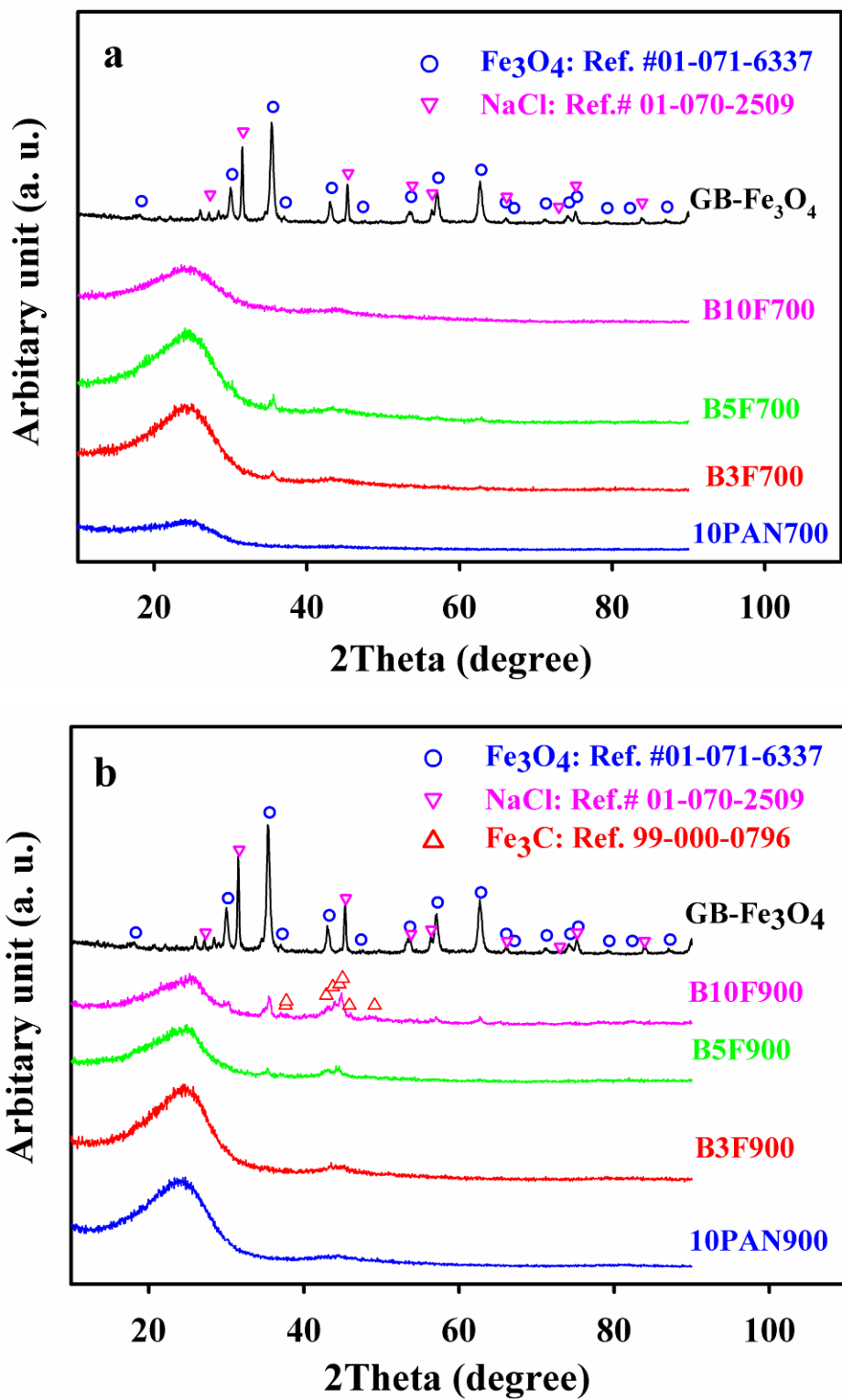
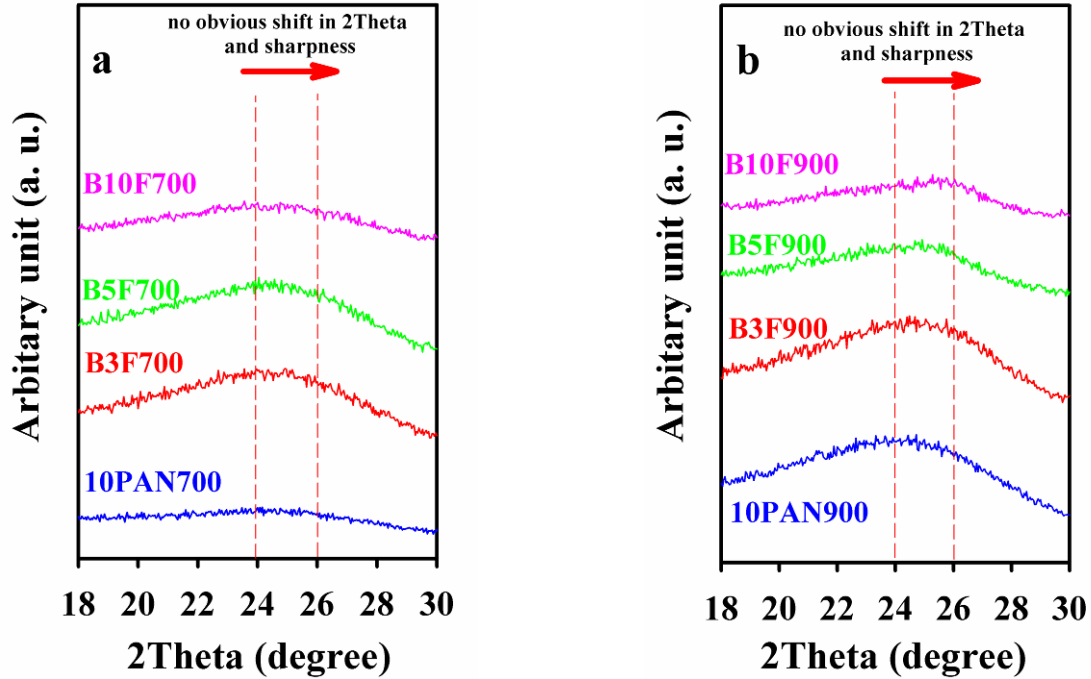


Figure 4-11 XRD patterns of pure and composite carbon nanofibers containing GB:10-20nm Fe_3O_4 nanoparticles.

Table 4-4 $2\theta_{(002)}$ and $d_{(002)}$ (nm) of pure and composite carbon nanofibers

Sample	$2\theta_{(002)}$	$d_{(002)}$ (nm)
10PAN900	24.20	3.67
B3F900	24.43	3.64
B5F900	24.62	3.61
B10F900	24.74	3.50

**Figure 4-12** $2\theta_{(002)}$ shifts towards higher degrees with adding (GB:10-20nm) Fe_3O_4 wt.% for samples carbonized at (a) 700°C and (b) 900°C.

4.1.3.4 GA:20-30nm/CNF and GB:10-20nm/CNF composites

Graphite and Fe_3O_4 peaks are identified in both groups of samples containing different sizes of Fe_3O_4 nanoparticles. The metallic α -Fe and Fe_3C phases are formed for samples containing larger (GA:20-30nm) Fe_3O_4 nanoparticles whereas only small intensity of Fe_3C peaks is confirmed to be formed in two samples with 5wt.% and 10wt.% GB:10-20nm Fe_3O_4 carbonized at higher temperature, i.e. 900°C.

It is observed that samples containing larger GA:20-30nm Fe₃O₄ nanoparticles illustrate highly intensive Fe₃O₄ peaks even at the same Fe₃O₄ loading with those containing smaller GB:10-20nm Fe₃O₄ nanoparticles (see Figure 4-9 and Figure 4-11). Higher carbonization temperature also induces the formation of larger Fe₃O₄ crystallites and as a result more intensive Fe₃O₄ peaks are obtained.

Besides, comparing the results shown in Table 4-3 and Table 4-4, larger $2\theta_{(002)}$ and smaller $d_{(002)}$ are obtained for samples containing larger nanoparticles (GA:20-30nm) in comparison with those containing smaller nanoparticles (GB:10-20nm). For example, the corresponding $2\theta_{(002)}$ and $d_{(002)}$ for 10wt.% GB:10-20nm Fe₃O₄ sample carbonized at 900°C (B10F900) are 24.74° and 3.50nm; however, these numbers change to larger $2\theta_{(002)}$ equal to 25.99° and shorter $d_{(002)}$ of 3.43nm for 10wt.% GA:20-30nm Fe₃O₄ sample carbonized at 900°C (A10F900).

Figure 4-13 demonstrates a comparison between the XRD patterns of composite nanofibers containing 10wt.%Fe₃O₄ carbonized at two different temperatures and Fe₃O₄ sizes. As shown in Figure 4-13, samples carbonized at 900°C show sharper and more intensive Fe₃O₄ peaks than samples carbonized at lower temperatures, 700°C. Moreover, composites containing larger Fe₃O₄ nanoparticles (GA:20-30nm) show sharper and more intensive peaks than those prepared by smaller nanoparticles (GB:10-20nm).

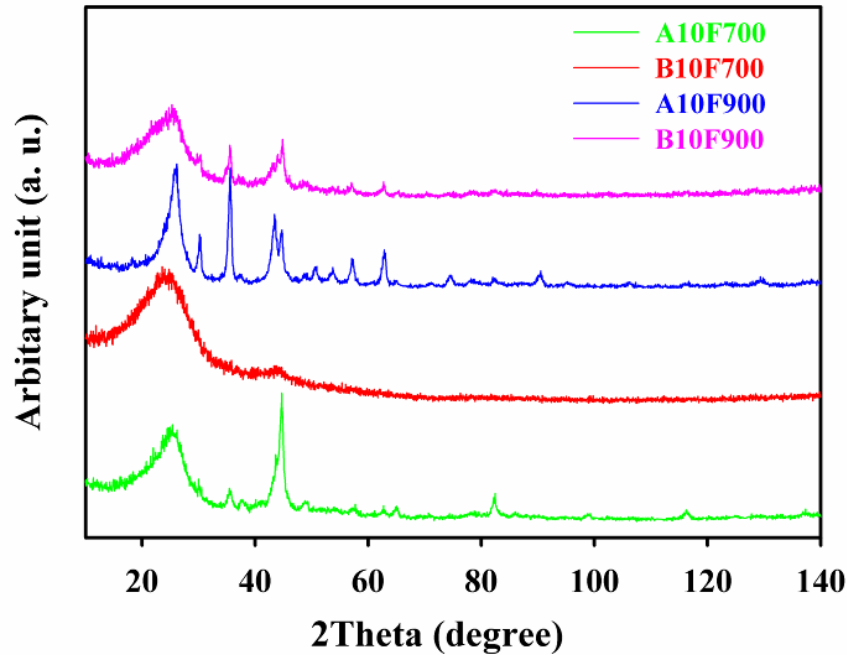


Figure 4-13 XRD patterns of A10F700, B10F700, A10F900 and B10F900 samples.

4.1.4 Raman spectroscopy

One of the most sensitive tools for studying the structural properties and crystalline perfection of carbonaceous materials is Raman spectroscopy. To investigate the graphitic structure of carbon fiber matrix composites, Raman spectroscopy was conducted. The effect of content and size of Fe_3O_4 nanoparticles and also pyrolysis temperature on the graphitization degree of carbon fiber matrix has been studied.

4.1.4.1 GA:20-30nm Fe_3O_4 / carbon nanofiber composites

Figure 4-14(a-d) shows the Raman spectra of pristine carbon nanofiber carbonized at (a) 700°C (APAN700) and (b) 900°C (APAN900) and composite carbon nanofiber containing 5wt.% GA:20-30nm Fe_3O_4 nanoparticles carbonized at (c) 700°C (A5F700) and (d) 900°C (A5F900). Carbon materials display two characteristic peaks correspond to the ordered and

disordered graphitic structure respectively at 1350cm^{-1} and 1600cm^{-1} . The intensity of the disordered graphitic structure (I_D) and ordered graphitic structure (I_G) for carbon fibers corresponds to these characteristic peaks [20]. The Gaussian curve fitting was performed to determine the relative intensities of the D (I_D) and G (I_G) bands from which one can determine $R=I_G/I_D$. The R value is a measure of the degree of graphitization. Accordingly, R ratio was used to investigate the effect of Fe_3O_4 content and pyrolysis temperature on the degree of graphitization. An in-plane size of the graphite crystals (L_a) can also be estimated according to $L_a \approx 4.4(I_G/I_D)$ using the ratio of I_G/I_D [165]. The degree of graphitization represented by the relative intensity of two ordered and disordered graphite peaks defined as $R=I_G/I_D$ and the in-plane size of the graphite crystals (L_a) of pristine carbon nanofiber and GA:20-30nm Fe_3O_4 /carbon nanofiber composites pyrolyzed at both 700°C and 900°C are summarized in Table 4-5. As shown in Figure 4-14(a-d) in comparison with pristine carbon nanofibers, sharper and more intensive graphite peaks are obtained for 5wt.% Fe_3O_4 /carbon nanofiber composite specifically for the sample carbonized at 900°C (A5F900) rather than 700°C (A5F700).

Further evidence on the effect of GA:20-30nm Fe_3O_4 on the degree of graphitization can be found in Table 4-5. It is observed that both R and L_a values increase because of the addition of Fe_3O_4 nanoparticles into the matrix and also higher carbonization temperature. For samples carbonized at 700°C , the R ratio varies slightly from 0.49 ± 0.004 for pristine carbon nanofibers (10PAN700) to 0.48 ± 0.01 for composite containing 3wt.% Fe_3O_4 (A3F700). However, the difference between two is very small and in the error range. By increasing Fe_3O_4 loading from 3wt.% (A3F700) to 5wt.% (A5F700) and 10wt.% (A10F700), the R ratio increases to greater values from 0.48 ± 0.01 to 0.52 ± 0.02 and 0.56 ± 0.01 , respectively. As the temperature increases to 900°C , the R ratio becomes larger than that of samples carbonized at 700°C . As opposed to

700°C, slight increase in Fe₃O₄ content from 0wt.%Fe₃O₄ for pristine carbon nanofiber (10PAN900) to 3wt.%Fe₃O₄(A3F900) causes large enhancement in the R ratio from 0.56±0.02 to 0.61±0.01. By increasing Fe₃O₄ loading from 3 to 5wt.%, the R value continues to grow slightly from 0.61±0.01 to 0.62±0.01. However, further Fe₃O₄ loading to 10wt.% does not consequence in increasing the R level and it slightly decreases to lower number, i.e. 0.61±0.002.

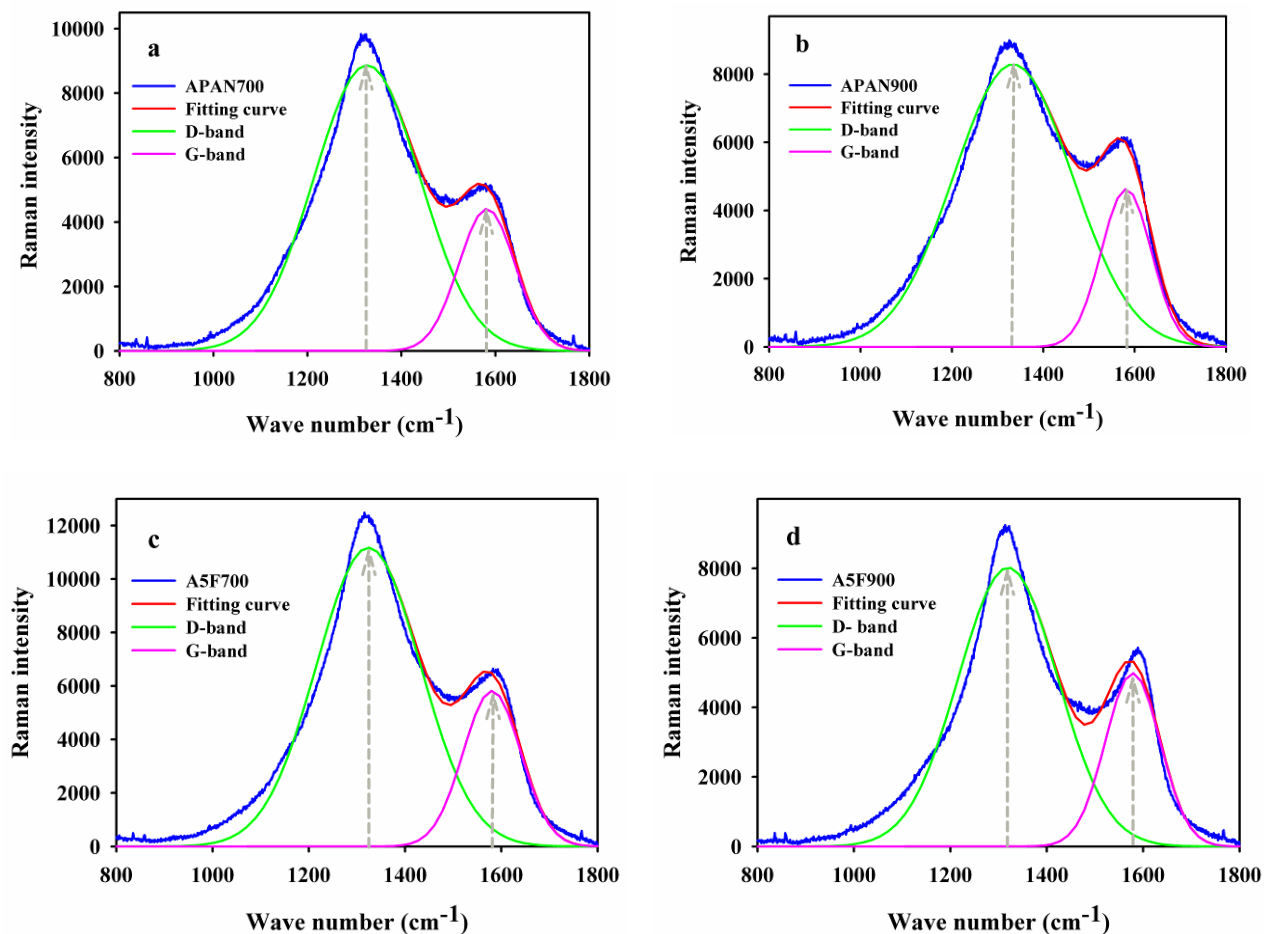


Figure 4-14 Raman spectroscopy of pristine carbon nanofibers carbonized at (a) 700°C and (b) 900°C and composite carbon nanofibers with 5wt.% GA:20-30nm Fe₃O₄ nanoparticles carbonized at (c) 700°C and (d) 900°C.

Therefore, it maybe concluded that probably the graphitization degree can be enhanced with adding Fe₃O₄ nanoparticles in the matrix to a certain level. Further increase in Fe₃O₄

content is not capable of further improvement of the degree of graphitization of carbon matrix and the R value levels off at 5-10wt.%Fe₃O₄ loading range. Since $L_a=4.4(I_G/I_D)$, the L_a follows the same trend as R, as represented in Table 4-5. The in-plane crystallite size (L_a) increases from 2.16nm for 10PAN700 sample to 2.46nm for 10PAN900 sample and becomes larger (2.73nm) with adding Fe₃O₄ to 5wt.% for A5F900 sample.

Table 4-5 Degree of graphitization, $R=I_G/I_D$ and the in-plane sizes of graphite crystals (L_a) of pristine and composite carbon nanofibers containing GA:20-30nm Fe₃O₄

Sample code	R	L_a (nm)	Sample code	R	L_a (nm)
10PAN700	0.49±0.004	2.16	10PAN900	0.56±0.02	2.46
A3F700	0.48±0.01	2.11	A3F900	0.61±0.01	2.64
A5F700	0.52±0.02	2.29	A5F900	0.62±0.01	2.73
A10F700	0.56±0.01	2.46	A10F900	0.61±0.002	2.68

4.1.4.2 GB:10-20nm Fe₃O₄/ carbon nanofiber composites

Raman spectra of pristine carbon nanofibers and composite carbon nanofibers containing 5wt.% GB:10-20nm Fe₃O₄ nanoparticles both carbonized at 700°C and 900°C are shown in Figure 4-15. The R and L_a values of the abovementioned samples are also summarized in Table 4-6. In comparison with the samples containing larger Fe₃O₄ nanoparticles (GA:20-30nm), the R ratio appears to be smaller for those containing smaller Fe₃O₄ nanoparticles (GB:10-20nm). Samples carbonized at 700°C do not exhibit any enhancement in the degree of graphitization by increasing Fe₃O₄ content into the matrix, as the R values for the composite samples (B3F700, B5F700 and B10F700) remain almost the same as that of the pristine carbon nanofiber sample (10PAN700) around 0.49. Increasing the carbonization temperature to 900°C, results in enhancing the degree of graphitization. As shown in Table 4-6, the R ratio varies slightly from 0.56±0.02 to 0.56±0.02, 0.58±0.02 and 0.57±0.008 by adding Fe₃O₄ content from 0wt.%Fe₃O₄

for pristine carbon nanofiber (10PAN900) to 3wt.% Fe_3O_4 (B3F900), 5wt.% Fe_3O_4 (B5F900) and 10wt.% (B10F900). Similarly, in-plane graphite crystallite size (L_a) follows the same trend with Fe_3O_4 loading (wt.%). Besides, the L_a value varies from 2.16nm to 2.46nm by increasing the carbonization temperature from 700°C to 900°C respectively for B3F700 and B3F900 samples. It also slightly varies from 2.46nm for pristine carbon nanofiber (10PAN900) and 3wt.% Fe_3O_4 (B3F900) to 2.55 and 2.50nm as the Fe_3O_4 content increases from 5wt.% Fe_3O_4 (B5F900) to 10wt.% Fe_3O_4 (B10F900), respectively.

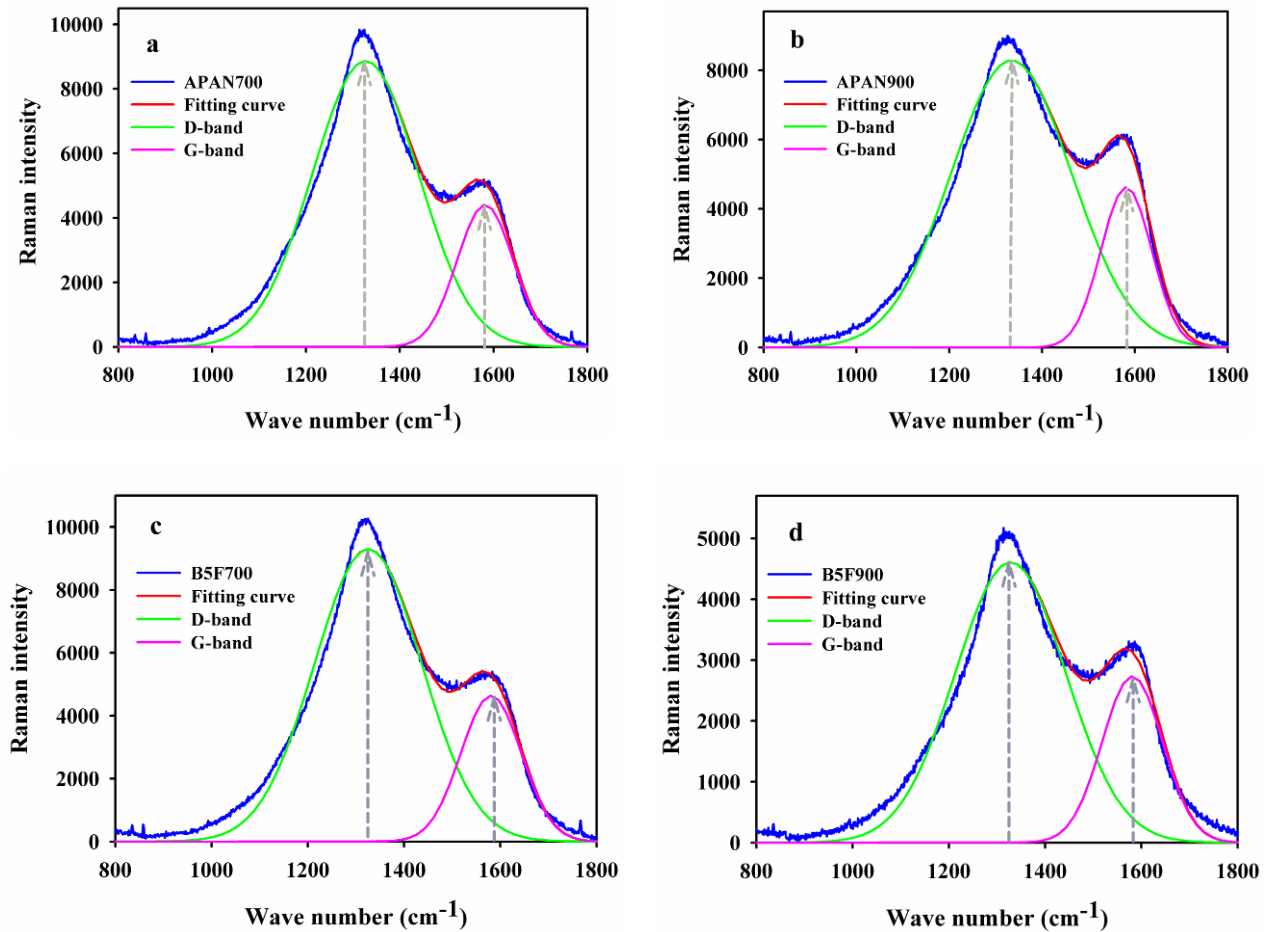


Figure 4-15 Raman spectroscopy of pristine carbon nanofibers carbonized at (a) 700°C and (b) 900°C and composite carbon nanofibers with 5wt.% GB:10-20nm Fe_3O_4 nanoparticles carbonized at (c) 700°C and (d) 900°C.

Table 4-6 Degree of graphitization, $R=I_G/I_D$ and in-plane sizes of graphite crystals (L_a) of pristine and composite carbon nanofibers containing GB:10-20nm Fe_3O_4

Sample code	R	L_a (nm)	Sample code	R	L_a (nm)
10PAN700	0.49±0.004	2.16	10PAN900	0.56±0.02	2.46
B3F700	0.49±0.004	2.16	B3F900	0.56±0.02	2.46
B5F700	0.49±0.01	2.16	B5F900	0.58±0.02	2.55
B10F700	0.49±0.01	2.16	B10F900	0.57±0.01	2.50

4.1.4.3 GA:20-30nm Fe_3O_4 and GB:10-20nm Fe_3O_4 / carbon nanofiber composites

In addition to the effect of Fe_3O_4 content and pyrolysis temperature in the graphitization of carbon fiber matrix, there is evidence that the size of Fe_3O_4 nanoparticles also plays a role in the graphitization of carbon. According to the results shown in Table 4-5 and Table 4-6, composite carbon nanofibers pyrolyzed at 700°C containing smaller GB:10-20nm Fe_3O_4 nanoparticles exhibit constant R value the same as pristine carbon nanofiber, i.e. 0.49. By increasing the temperature to 900°C, the R ratio also increases to the range between 0.56-0.58 for both pristine carbon nanofiber and composite carbon nanofibers (Table 4-6). Therefore, the R value and the corresponding L_a value do not apparently increase with smaller size of Fe_3O_4 nanoparticles (GB:10-20nm). On the other hand, increasing the size of Fe_3O_4 nanoparticles from GB:10-20nm to GA:20-30nm is confirmed to have a slight contributing effect on the degree of graphitization of carbon fiber matrix. The R and L_a values of composites containing larger GA:20-30nm Fe_3O_4 nanoparticles tend to increase in comparison with composites containing smaller GB:10-20nm Fe_3O_4 nanoparticles. The R ratio varies in the range of 0.56-0.58 and 0.56-0.62 for composite carbon nanofiber (carbonized at 900°C) respectively containing GB:10-20nm and GA:20-30nm Fe_3O_4 nanoparticles (Table 4-5 and Table 4-6).

4.2 Physical properties

4.2.1 Electrical conductivity

Electrical conductivity of pristine carbon nanofibers and composite carbon nanofibers containing different sizes (GA:20-30nm and GB:10-20nm) and loadings (0 to 10wt.%) of Fe₃O₄ nanoparticles were measured using a four-point probe.

4.2.1.1 GA:20-30nm Fe₃O₄/carbon nanofiber composites

Figure 4-16 provides a summary of the electrical conductivity of pristine carbon nanofibers and composite carbon nanofibers produced by GA:20-30nm Fe₃O₄ nanoparticles as a function of GA:20-30nm Fe₃O₄ content and pyrolysis temperature.

Results demonstrate that the electrical conductivity increases with Fe₃O₄ content. For samples carbonized at 900°C, electrical conductivity improves significantly by increasing the Fe₃O₄ loading. Figure 4-16 shows that electrical conductivity increases from 2.6±0.9S/cm for pristine carbon nanofiber (10PAN900) to 5.7±0.9S/cm, 7.1±0.7S/cm and 9.2±0.5S/cm respectively for carbonized samples containing 3, 5 and 10wt.% Fe₃O₄ designated as A3F900, A5F900 and A10F900 samples. Similar trend is observed at 700°C.

Furthermore, as illustrated in Figure 4-16, the electrical conductivity is shown to be a strong function of carbonization temperature. The electrical conductivity increases by 40 times from 0.05±0.004S/cm to 2.6±0.9S/cm for pristine carbon nanofiber (10PAN700 and 10PAN900) respectively pyrolyzed at 700°C and 900°C. The same trend was also observed for samples containing 3, 5 and 10wt.% Fe₃O₄ in carbon nanofiber composites with increasing the carbonization temperature as shown in Figure 4-16.

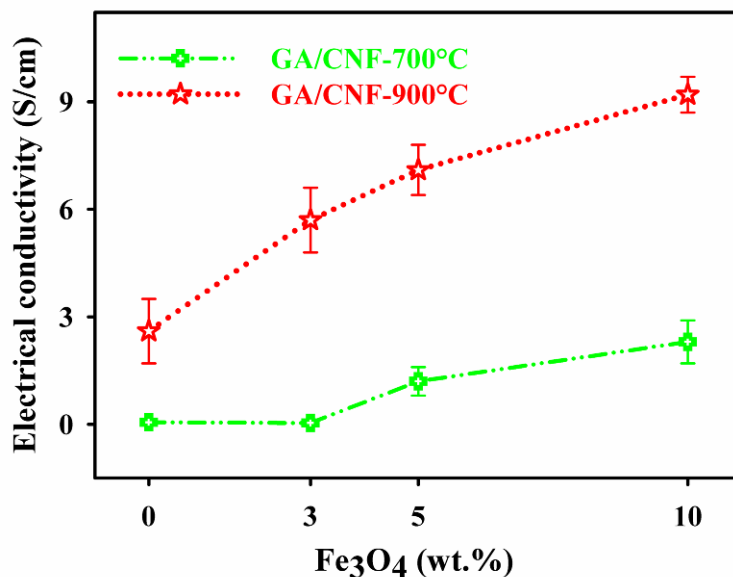


Figure 4-16 Electrical conductivity of pristine carbon nanofiber and composite carbon nanofibers containing GA: 20-30nm Fe₃O₄ nanoparticles as a function of Fe₃O₄ wt.% and carbonization temperature (700°C and 900°C).

4.2.1.2 GB:10-20nm Fe₃O₄/carbon nanofiber composites

Comparison between the electrical conductivity of pristine carbon nanofibers and composite carbon nanofibers containing smaller Fe₃O₄ nanoparticle (GB:10-20nm) is summarized in Figure 4-17. The electrical conductivity of composite carbon nanofibers containing various amounts of GB:10-20nm Fe₃O₄ barely changes in comparison with pristine carbon nanofiber for both carbonization temperatures, i.e. 700°C and 900°C. The electrical conductivity changes slightly from 2.6±0.9S/cm for pristine carbon nanofiber (10PAN900) to 2.89S/cm and 2.92±0.6S/cm respectively for samples containing 3wt.%Fe₃O₄ (B3F900) and 5wt.%Fe₃O₄ (B5F900). The electrical conductivity then decreases to 1.94±0.7S/cm with further Fe₃O₄ loading to 10wt.% for B10F900 sample.

Further, pyrolysis temperature as expected tend to have a contributing effect on the electrical conductivity of carbonized fibers. The electrical conductivity of samples containing 0,

3, 5 and 10wt.% Fe_3O_4 increases from 0.05 S/cm, 0.05 S/cm, 0.05 S/cm and 0.02S/cm for samples carbonized at 700°C respectively to 2.6 S/cm, 2.89 S/cm, 2.92 S/cm and 1.94S/cm for samples carbonized at 900°C.

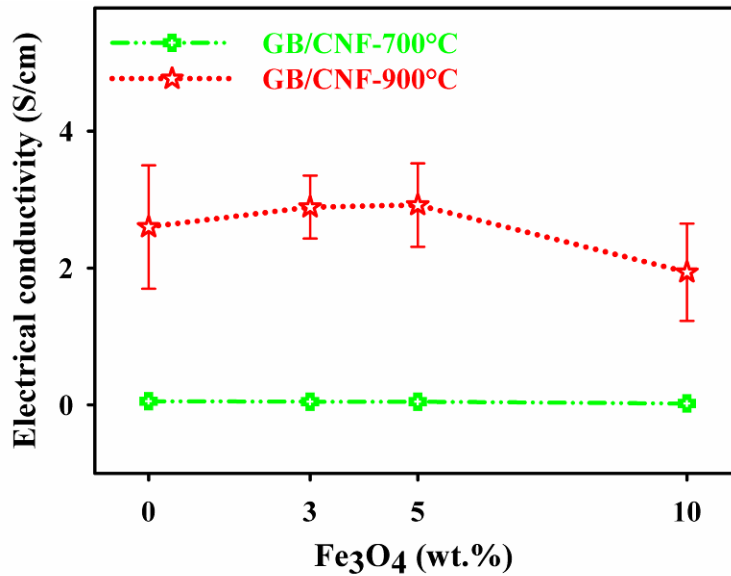


Figure 4-17 Electrical conductivity of pristine carbon nanofiber and composite carbon nanofibers containing GB:10-20nm Fe_3O_4 nanoparticles as a function of Fe_3O_4 wt.% and carbonization temperature (700°C and 900°C).

4.2.1.3 GA:20-30nm Fe_3O_4 and GB:10-20nm Fe_3O_4 /carbon nanofiber composites

As shown in the XRD, Raman spectroscopy and four-point probe measurements, it is of interest to note that electrical conductivity depends on not only the content of nanoparticles and carbonization temperature but also on the size of Fe_3O_4 nanoparticles embedded in the carbon fiber matrix.

Electrical conductivity results demonstrate that the size of Fe_3O_4 nanoparticles also affects the electrical conductivity of composite carbon nanofibers as shown in Figure 4-16 and Figure 4-17. Composites with smaller Fe_3O_4 nanoparticles (GB:10-20nm) show lower electrical conductivity

in comparison with composites containing larger Fe_3O_4 nanoparticles (GA:20-30nm). For example, a fivefold increase in electrical conductivity of composite nanofibers fabricated with 10wt.% Fe_3O_4 nanoparticles carbonized at 900°C is observed with increasing the size from GB:10-20nm to GA:20-30nm. The electrical conductivity increases from $1.94\pm 0.7\text{S/cm}$ to $9.2\pm 0.5\text{S/cm}$ with increasing the size of nanoparticles from GB:10-20nm Fe_3O_4 to GA:20-30nm Fe_3O_4 for both composites with 10wt.% Fe_3O_4 loading.

4.2.2 Magnetic properties

Magnetic properties of Fe_3O_4 nanoparticles, electrospun nanofiber composite and also carbon nanofiber composites were characterized using the SQUID at room temperature (300K). The saturation magnetization (M_s), coercivity (H_c) and remanent magnetization (M_r) values of Fe_3O_4 nanoparticles electrospun composite nanofibers and also composite carbon nanofibers have been summarized in Table 4-7, Table 4-8, Table 4-9, Table 4-10 and Table 4-11. The physical meaning of these parameters is explained in chapter 2.

4.2.2.1 Magnetic properties of Fe_3O_4 nanoparticles

The magnetic moment (M) versus applied magnetic field (H) curves (M-H or hysteresis curves) of GA:20-30nm and GB:10-20nm Fe_3O_4 nanoparticles are exhibited in Figure 4-18. The inset also compares the amount of H_c and M_r for different sizes of nanoparticles. Using M-H curves of nanoparticles shown in Figure 4-18, the M_r , M_s , M_r/M_s and H_c parameters of nanoparticles are summarized in Table 4-7.

The size of Fe_3O_4 nanoparticles is shown to have a significant influence on the magnetic properties as shown in Figure 4-18 and summarized in Table 4-7. Comparing the magnetic properties of two sizes of Fe_3O_4 nanoparticles shows that the M_s decreases from 56.5emu/g to

32emu/g when the size of Fe₃O₄ nanoparticles decreases from GA:20-30nm to GB:10-20nm. The M_s of both GA:20-30nm and GB:10-20nm Fe₃O₄ nanoparticles is also different from bulk magnetite which will be discussed later.

The size of nanoparticle is also found to affect the hysteresis. The H_c decreases from 32Oe for GA:20-30nm representing ferromagnetic behaviour, to 0Oe for GB:10-20nm Fe₃O₄ nanoparticles showing truly superparamagnetic effect. The obtained H_c for both Fe₃O₄ nanoparticles is much smaller than the reported H_c value for bulk Fe₃O₄ (H_c=500-800Oe) [115] (bulk magnetite is the Fe₃O₄ powder with the size around a few micron).

The ferromagnetic nature of nanoparticles is characterized by the squareness ratio (M_r/M_s). The M_r/M_s ratio is calculated from the M-H curves and summarized in Table 4-7. The M_r/M_s ratio is very small for both GA:20-30nm and GB:10-20nm Fe₃O₄ nanoparticles, respectively 0.04 and 0.0007.

Accordingly, the size of magnetic nanoparticles has a profound effect on the magnetic strength and magnetic hysteresis of these particles and hence on the composite nanofibers fabricated with these nanoparticles.

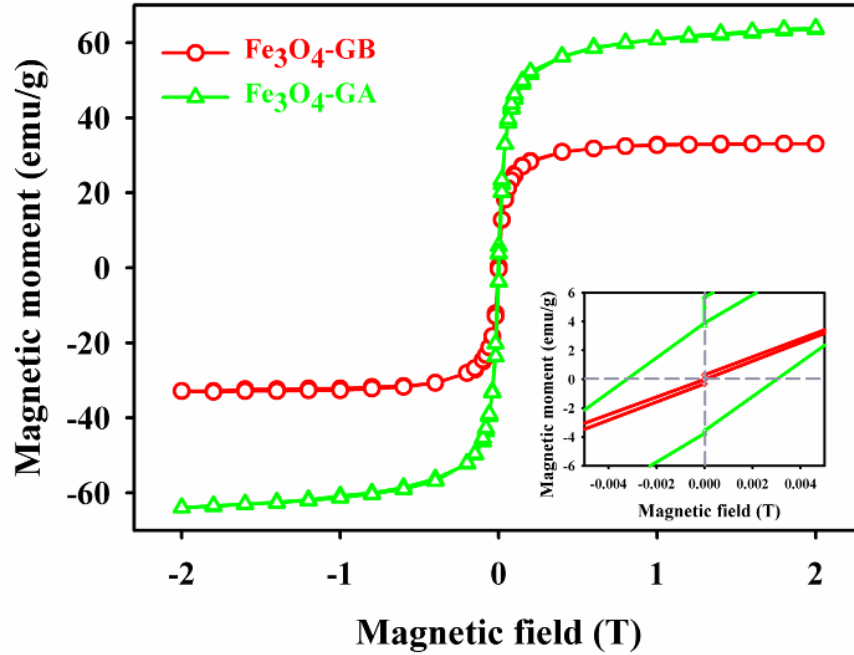


Figure 4-18 M-H curves of GA:20-30nm and GB:10-20nm Fe₃O₄ nanoparticles.

Table 4-7 M_s, M_r and H_c of GA:20-30nm Fe₃O₄ and GB:10-20nm Fe₃O₄ nanoparticles at 300K

Sample code	M _s (emu/g)	M _r (emu/g)	H _c (Oe)	S=M _r /M _s
GA:20-30nm Fe ₃ O ₄ NPs	56.5	3.57	32.5	3.57/56.5=0.063
GB:10-20nm Fe ₃ O ₄ NP	32.00	0.025	0	0.025/32=0.0007

4.2.2.2 Magnetic properties of as-spun nanofibers

The effect of electrospinning on the magnetic properties of electrospun nanofibers containing various sizes and contents of Fe₃O₄ nanoparticles is investigated. Figure 4-19 and Figure 4-20 respectively illustrates the M-H plots of as-spun nanofibers fabricated with 3, 5 and 10wt.% GA:20-30nm (designated respectively as A3F, A5F and A10F) or GB:10-20nm (designated respectively as B3F, B5F and B10F) Fe₃O₄ nanoparticles. The inset in each abovementioned figures compares the hysteresis of as-spun nanofibers with their corresponding Fe₃O₄ nanoparticles. Magnetic properties such as M_s, M_r, H_c and M_r/M_s are summarized in Table 4-8 and Table 4-9.

The M_s value of as-spun nanofibers containing GA:20-30nm Fe_3O_4 nanoparticles are shown to increase from 1.6emu/g to 2.8emu/g and 5.8emu/g with Fe_3O_4 loading from 3wt.% (A3F) to 5wt.% (A5F) and 10wt.% (A10F) (Table 4-8). Similarly, the magnetic moment of as-spun nanofibers made of GB:10-20nm Fe_3O_4 nanoparticles is reinforced with the addition of GB:10-20nm Fe_3O_4 nanoparticles. Fe_3O_4 loading in the fibrous structure results in increase of the M_s value from 0.9emu/g for B3F to 1.5emu/g and 3emu/g respectively for B5F and B10F samples (Table 4-8 and Table 4-9).

Furthermore, the as-spun composite nanofiber samples designated as A3F, A5F and A10F illustrated the same H_c ($\sim 30Oe$) as their corresponding GA:20-30nm Fe_3O_4 nanoparticles ($H_c=32.5Oe$). Similarly, the as-spun composite nanofiber samples designated as B3F, B5F and B10F exhibit no H_c ($\sim 0Oe$) the same as GB:10-20nm Fe_3O_4 nanoparticles ($H_c\sim 0Oe$).

Finally, nanoparticles and as-spun nanofibers show the same $S=M_r/M_s$ ratios as their corresponding nanoparticles. The M_r/M_s ratio of as-spun composite nanofibers of samples A3F, A5F and A10F are equal to 0.06 the same value as GA:20-30nm Fe_3O_4 nanoparticles ($M_r/M_s=0.06$). Similarly, the M_r/M_s ratio is confirmed to be the same for both GB:10-20nm Fe_3O_4 nanoparticles (0.001) and as-spun composite nanofibers containing GB:10-20nm Fe_3O_4 (0.003).

Therefore, it can be concluded that the magnetic properties such as magnetic strength and hysteresis level of Fe_3O_4 nanoparticles have been successfully transferred and scaled up into the higher order structures.

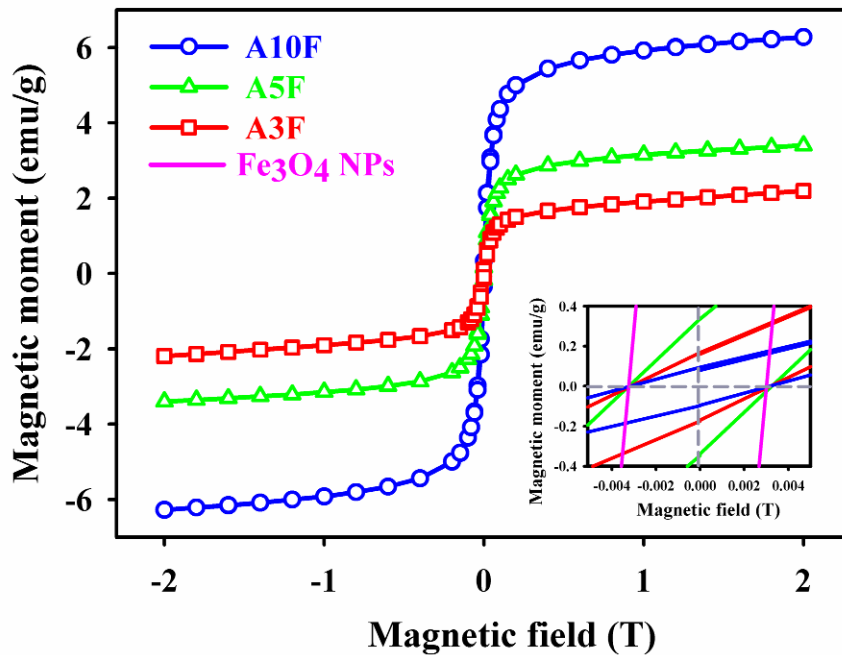


Figure 4-19 M-H curves of as-spun composite nanofibers containing 3, 5 and 10wt.% GA:20-30nm Fe₃O₄ nanoparticles (A3F, A5F and A10F respectively) and GA:20-30nm Fe₃O₄ nanoparticles (added in the inset).

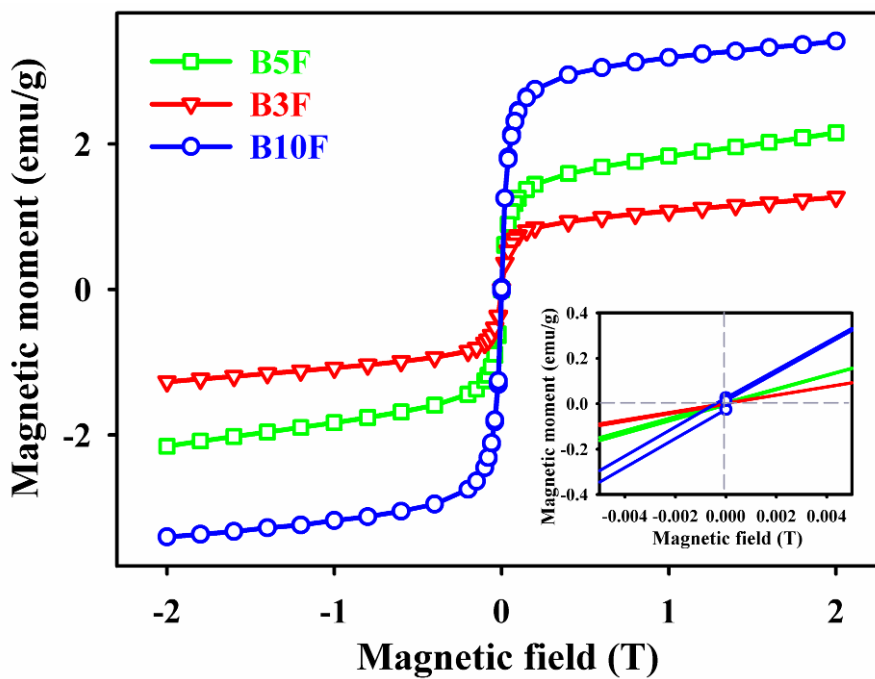


Figure 4-20 M-H curves of as-spun composite nanofibers containing 3, 5 and 10wt.% GB:10-20nm Fe₃O₄ nanoparticles (B3F, B5F and B10F respectively).

Table 4-8 M_s , M_r and H_c of as-spun composite nanofibers containing GA:20-30nm Fe_3O_4 nanoparticles at 300K

Sample code	M_s (emu/g)	M_r (emu/g)	H_c (Oe)	M_r/M_s
A3F	1.6	0.095	30	0.95/1.6=0.06
A5F	2.8	0.17	30	0.17/2.8=0.06
A10F	5.8	0.34	30	0.34/5.8=0.06
GA Fe_3O_4 NPs	56.5	3.57	32	3.57/53=0.06

Table 4-9 M_s , M_r and H_c of as-spun composite nanofibers containing GB:10-20nm Fe_3O_4 nanoparticles at 300K

Sample code	M_s (emu/g)	M_r (emu/g)	H_c (Oe)	M_r/M_s
B3F	0.90	0.0026	0	0.003
B5F	1.50	0.0058	0	0.003
B10F	3.00	0.0133	0	0.003
GB Fe_3O_4 NP	32.00	0.0248	0	0.001

4.2.2.3 Carbonized composite nanofibers

4.2.2.3.1 GA:20-30nm Fe_3O_4 /carbon nanofiber composites

It is of utmost importance to know the effect of carbonization process on the magnetic properties of composite nanofibers. The plots of magnetization (M) versus magnetic field (H) of as-spun and carbonized samples produced by GA:20-30nm Fe_3O_4 nanoparticles are shown in Figure 4-21, Figure 4-22 and Figure 4-23. Table 4-10 also summarizes their magnetic properties as M_s , M_r , H_c and M_r/M_s parameters.

Figure 4-21, Figure 4-22 and Figure 4-23 illustrate the M-H curves of as-spun and carbonized composite nanofibers made of 3, 5 and 10wt.% GA:20-30nm Fe_3O_4 including electrospun nanofibers (A3F, A5F and A10F) and their corresponding carbonized samples at 700°C, (A3F700, A5F700 and A10F700) and 900°C (A3F900, A5F900 and A10F900).

Based on the observations, the magnetic moment is enhanced for the carbonized samples in comparison with as-spun nanofibers. Larger M_s values are acquired for pyrolyzed samples. The M_s value of 5.8emu/g for as-spun A10F sample is proved to increase to 13.4emu/g and 16emu/g respectively after being carbonized at 700°C and 900°C for A10F700 and A10F900 samples.

Accordingly, it increases from 2.8emu/g for A5F sample to 6.85emu/g and 7.5emu/g respectively for A5F700 and A5F900 samples. Unlike the pyrolyzed samples containing 5 and 10wt.% Fe₃O₄, the M_s value of as-spun A3F samples (1.6emu/g) is reduced after carbonization at 700°C (A3F700) to 1.2emu/g and then increased to 4emu/g for sample carbonized at 900°C (A3F900).

Furthermore, it is proved that the hysteresis is enhanced as a result of carbonization of as-spun composite nanofibers. The H_c value increases from 30Oe for as-spun A10F sample to 240Oe and 250Oe respectively for A10F700 and A10F900 samples. Accordingly, the M_r increases from 0.34emu/g for as-spun A10F sample to 3.19emu/g and 5.55emu/g respectively for A10F700 and A10F900 samples. Finally, the M_r/M_s ratio increases from 0.06 to 0.24 and 0.35 respectively for A10F, A10F700 and A10F900 samples (Table 4-10). The inset shown in Figure 4-21 exhibits the larger hysteresis for A10F700 and A10F900 samples compared to that of as-spun A10F sample and GA:20-30nm Fe₃O₄ nanoparticles. Similar trend is observed for composite nanofibers containing 3 and 5wt.% GA:20-30nm Fe₃O₄ (Figure 4-22 and Figure 4-23).

The abovementioned results confirm that both magnetic strength and hysteresis of composite carbon nanofibers increase due to the carbonization process.

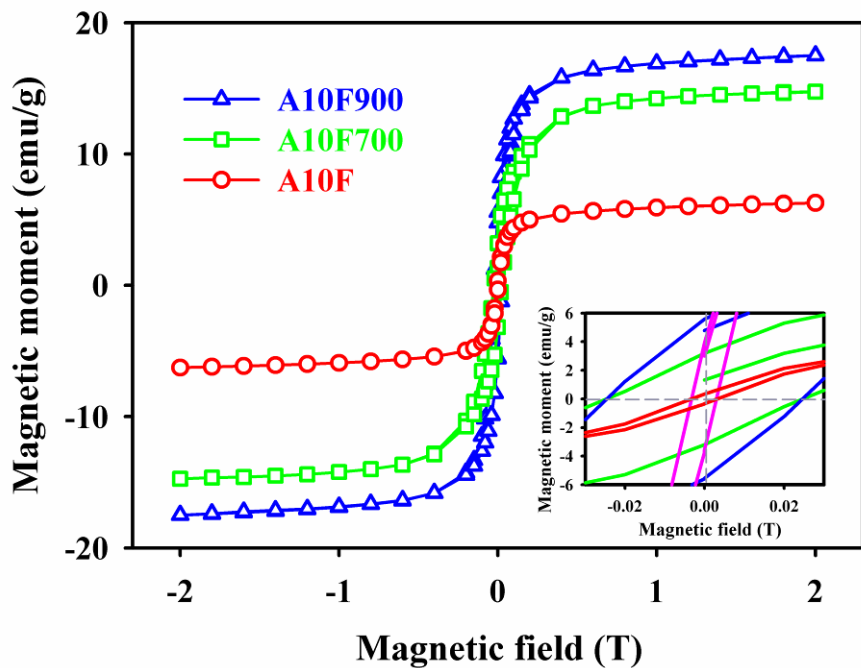


Figure 4-21 M-H curves of as-spun and composite nanofibers containing 10wt.% GA:20-30nm Fe₃O₄ nanoparticles carbonized at 700°C and 900°C, (A10F, A10F700 and A10F900, respectively).

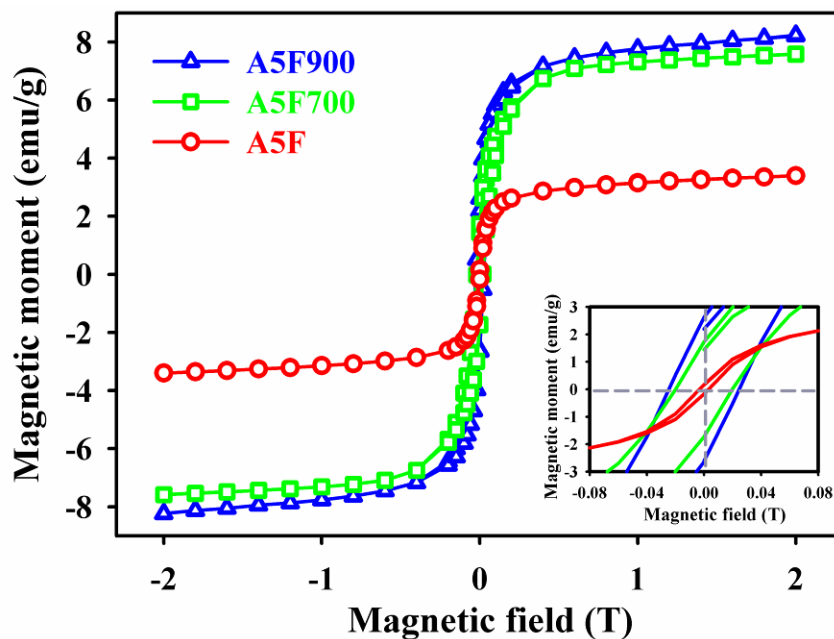


Figure 4-22 M-H curves of as-spun and composite nanofibers containing 5wt.% GA:20-30nm Fe₃O₄ nanoparticles carbonized at 700°C and 900°C, (A5F, A5F700 and A5F900, respectively).

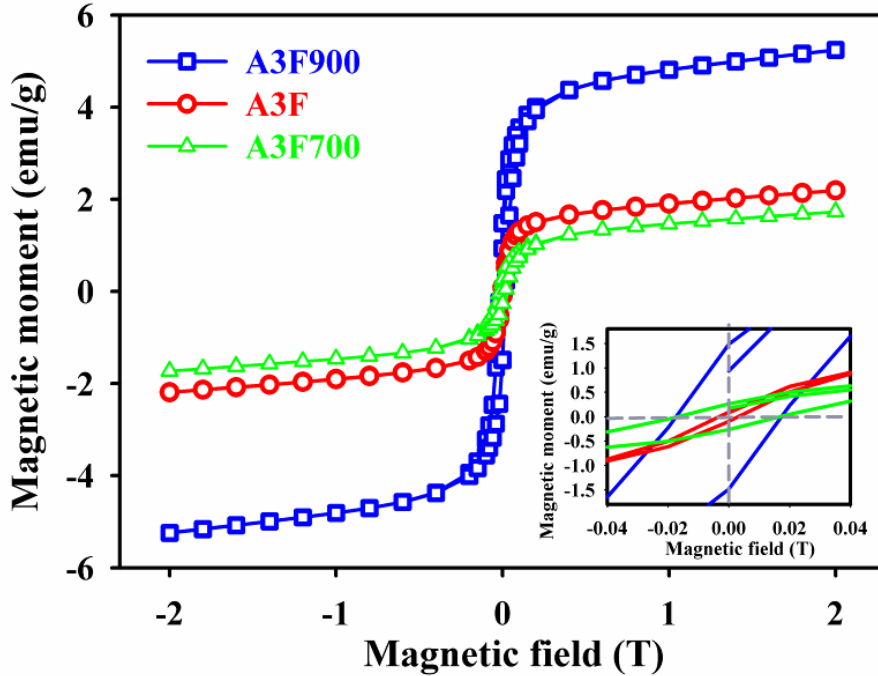


Figure 4-23 M-H curves of as-spun and composite nanofibers containing 3wt.% GA:20-30nm Fe₃O₄ nanoparticles carbonized at 700°C and 900°C, (A3F, A3F700 and A3F900, respectively).

Table 4-10 M_s, M_r and H_c of GA:20-30nm Fe₃O₄/carbon nanofiber composites at 300K

Sample code	M _s (emu/g)	M _r (emu/g)	H _c (Oe)	S=M _r /M _s
A3F	1.60	0.10	30	0.06
A3F700	1.20	0.26	170	0.22
A3F900	4.00	1.49	180	0.37
A5F	2.80	0.17	30	0.06
A5F700	6.85	1.42	220	0.25
A5F900	7.50	2.62	240	0.35
A10F	5.80	0.34	30	0.06
A10F700	13.40	3.19	240	0.24
A10F900	16.00	5.50	250	0.35
Fe ₃ O ₄ NPs	56.50	3.75	32.5	0.06

It is further observed that Fe₃O₄ loading in the nanofibers also affects the magnetic properties of carbonized fibers. A comparison between the M-H curves of samples containing 3, 5 and 10wt.% GA:20-30nm Fe₃O₄ carbonized at 700°C and 900°C are demonstrated respectively in Figure 4-24 and Figure 4-25.

Magnetic strength is shown to be enhanced via increasing Fe₃O₄ loading in the carbon nanofibers at both carbonization temperatures (700°C and 900°C). The M_s increases from 1.2emu/g to 6.85emu/g and 13.4emu/g with increasing Fe₃O₄ content from 3 to 5 and 10wt.% for samples carbonized at 700°C (A3F700, A5F700 and A10F700), respectively. The M_s value also increases from 4emu/g to 7.5emu/g and 16emu/g for composite nanofibers carbonized at 900°C (A3F900, A5F900 and A10F900), respectively.

Meanwhile, it is confirmed that increasing the Fe₃O₄ content in the matrix leads to larger amount of hysteresis. The H_c value is found to become larger with the addition of Fe₃O₄ from 3 to 5 and 10wt.% for samples carbonized at both temperatures. For carbonization at 700°C, H_c increases from 170Oe to 220Oe and 240Oe respectively for A3F700, A5F700 and A10F700 samples. At 900°C, the H_c increases from 180Oe to 240Oe and 250Oe with the addition of Fe₃O₄ wt.% from 3 to 5 and 10wt.%, respectively. This might be attributed to the size effect and interparticle interactions which will be discussed in the next chapter.

At the same time, the M_r value increases from 1.49emu/g for A3F900 sample to 2.62emu/g and 5.55emu/g respectively for A5F900 and A10F900 samples. The same trend is also observed for samples carbonized at 900°C.

The M_r/M_s ratio is also shown to be almost at the same level for all composite nanofibers containing 3, 5 and 10wt.% GA:20-30nm Fe₃O₄ carbonized at 700°C (M_r/M_s=0.22-0.24) and 900°C (M_r/M_s=0.35).

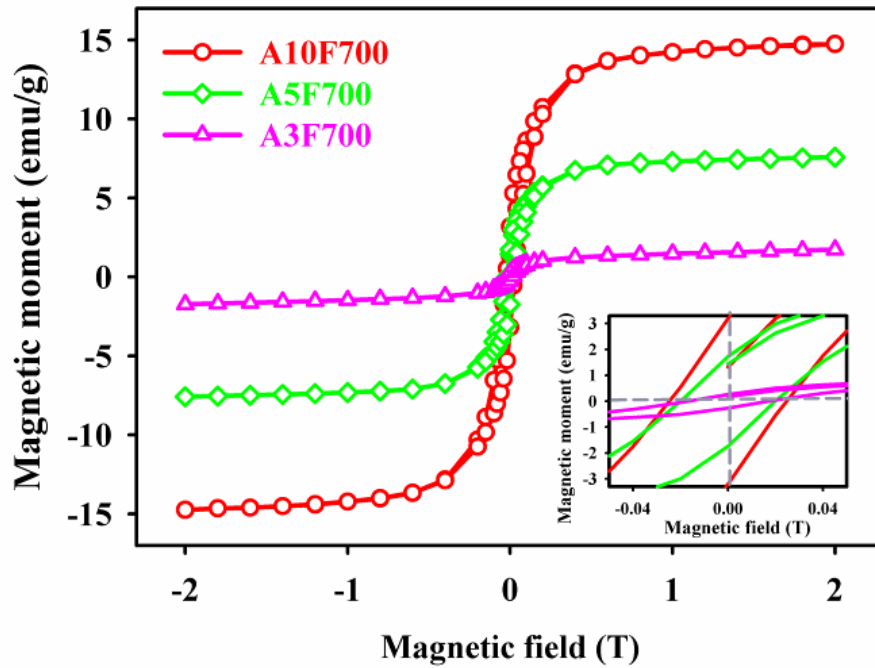


Figure 4-24 M-H curves of composite carbon nanofibers containing GA:20-30nm Fe₃O₄ nanoparticles carbonized at 700°C.

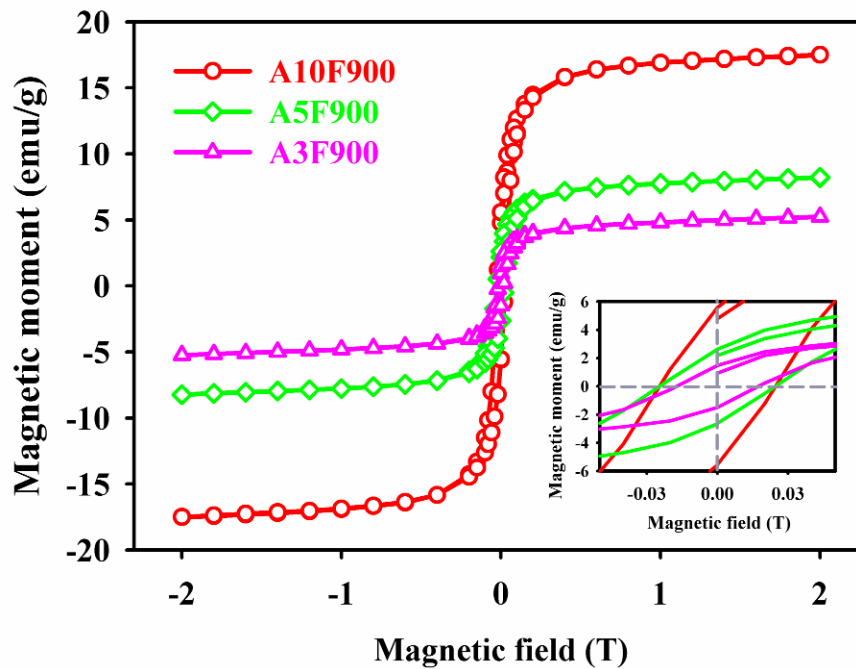


Figure 4-25 M-H curves of composite carbon nanofibers containing GA:20-30nm Fe₃O₄ nanoparticles carbonized at 900°C.

4.2.2.3.2 GB:10-20nm Fe₃O₄/carbon nanofiber composites

The magnetic properties of carbonized samples containing various amounts of GB:10-20nm Fe₃O₄ nanoparticles were also studied using SQUID. The plots of magnetization (M) versus magnetic field (H) of as-spun and carbonized samples containing GB:10-20nm Fe₃O₄ nanoparticles are exhibited in Figure 4-26, Figure 4-27 and Figure 4-28. A summary of the magnetic parameters as M_s, M_r, H_c and M_r/M_s ratio is shown in Table 4-11.

Figure 4-26, Figure 4-27 and Figure 4-28 illustrate the M-H curves of as-spun composite nanofibers and their corresponding carbonized fibers at 900°C respectively with 3, 5 and 10wt.% GB:10-20nm Fe₃O₄ nanoparticles.

The M_s value of as-spun nanofibers containing 3, 5 and 10wt.% Fe₃O₄ (B3F, B5F and B10F) increases from 0.9, 1.5 and 3emu/g to 1.5, 3.8 and 9emu/g respectively for samples carbonized at 900°C (B3F900, B5F900 and B10F900), as summarized in Table 4-11. In addition, it is observed that carbonization induces hysteresis into the carbonized structure. The H_c increases from almost no coercivity for all as-spun nanofibers to 180, 200 and 400Oe respectively for B3900, B5F900 and B10F900 samples (Table 4-11). At the same time, the M_r value increases for carbonized samples from 0.003, 0.006 and 0.013emu/g for as-spun B3F, B5F and B10F samples to larger values of 0.299, 0.857 and 2.44emu/g for B3F900, B5F900 and B10F900 samples (Table 4-11). Finally, the M_r/M_s ratio is much higher for carbonized samples as opposed to as-spun nanofibers. The M_r/M_s ratio increases from 0.003 for as-spun nanofibers (B3F, B5F and B10F) to 0.20, 0.23 and 0.27 values for carbonized samples (B3F900, B5F900 and B10F900) (Table 4-11).

According to the abovementioned results, a superparamagnetic property of electrospun composite nanofibers transfers to ferromagnetic behaviour due to higher H_c and M_r values. Also, results confirm that after carbonization the magnetic strength of all samples enhances.

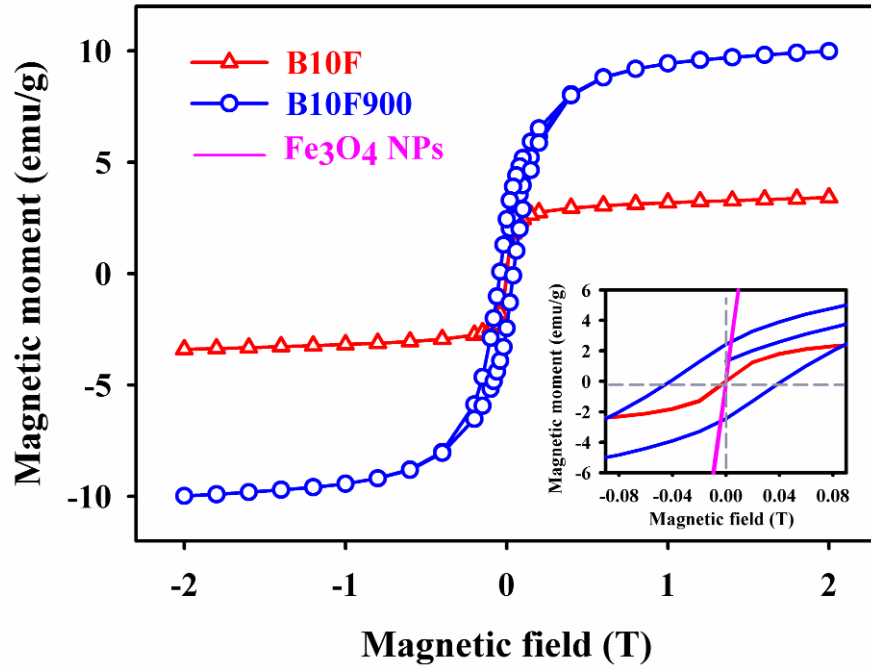


Figure 4-26 M-H curves of as-spun and composite nanofibers containing 10wt.% GB:10-20nm Fe₃O₄ carbonized at 900°C (B10F and B10F900, respectively) and GB:10-20nm Fe₃O₄ nanoparticles in the inset.

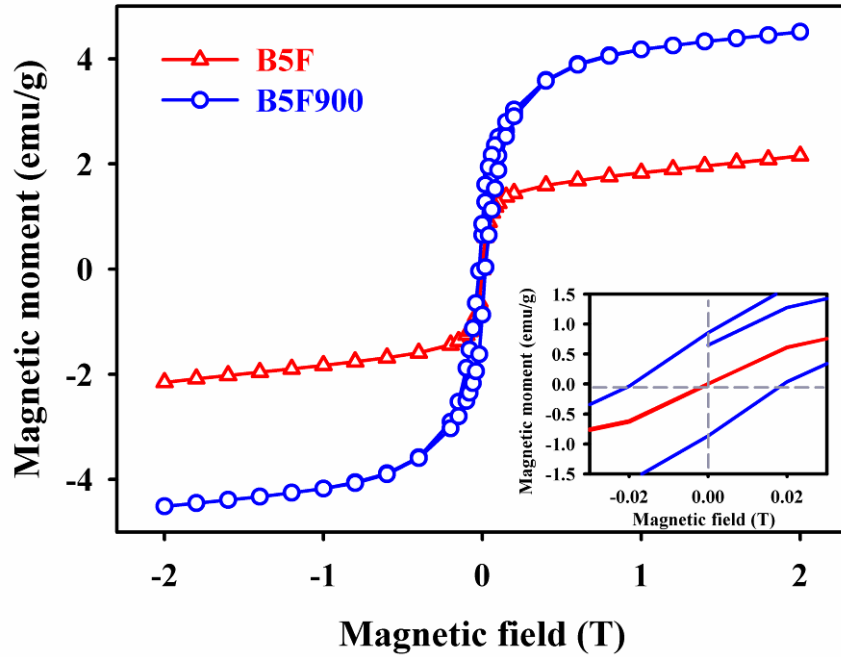


Figure 4-27 M-H curves of as-spun and composite nanofibers containing 5wt.% GB:10-20nm Fe_3O_4 carbonized at 900°C (B5F and B5F900, respectively) and GB:10-20nm Fe_3O_4 nanoparticles in the inset.

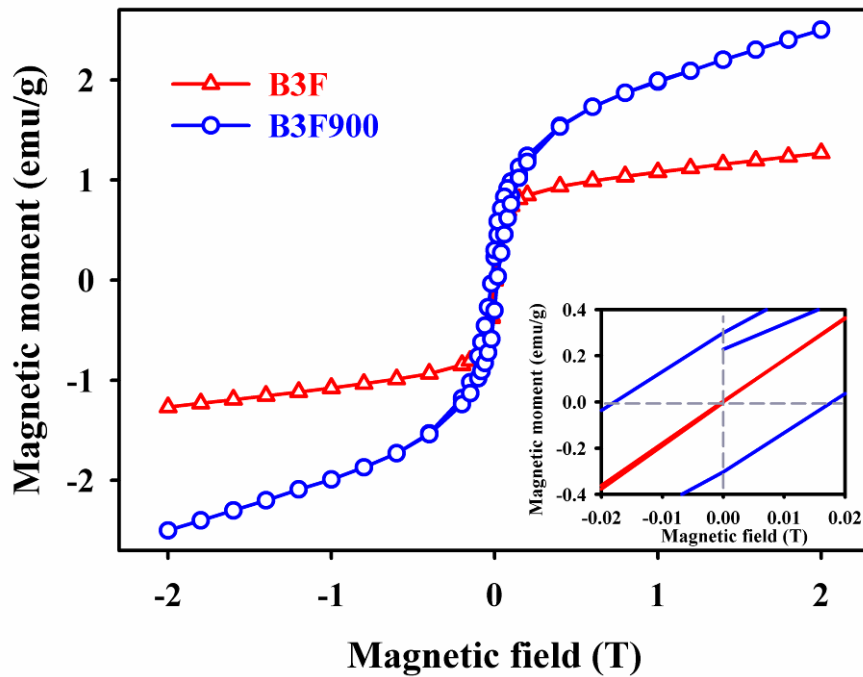
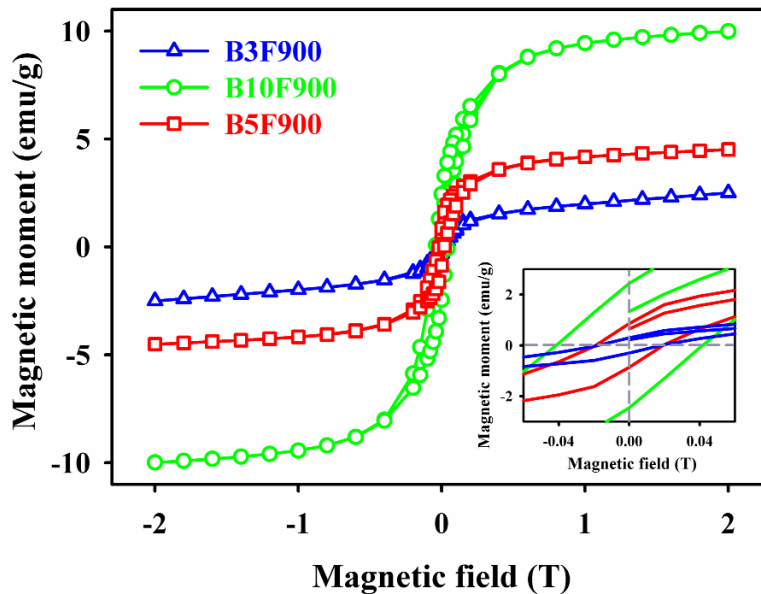


Figure 4-28 M-H curves of as-spun and composite nanofibers containing 3wt.% GB:10-20nm Fe_3O_4 carbonized at 900°C (B3F and B3F900, respectively) and GB:10-20nm Fe_3O_4 nanoparticles in the inset.

Table 4-11 M_s , M_r and H_c of GB:10-20nm Fe_3O_4 /carbon nanofiber composites at 300K

Sample code	M_s (emu/g)	M_r (emu/g)	H_c (Oe)	M_r/M_s
B3F	0.90	0.003	0	0.003
B3F900	1.50	0.299	180	0.200
B5F	1.50	0.006	0	0.004
B5F900	3.80	0.857	200	0.230
B10F	3.00	0.013	0	0.003
B10F900	9.00	2.440	400	0.270
GB Fe_3O_4 NP	32.00	0.025	0	0.0007

A comparison between the magnetic properties of samples carbonized at 900°C is shown in Figure 4-29. It is observed that the M_s increases from 1.5emu/g to 3.8emu/g and 9.0emu/g as Fe_3O_4 wt.% increases from 3 to 5 and 10wt.%. In addition, the H_c and M_r values become larger as the Fe_3O_4 content increases within the carbon matrix. The H_c and M_r values increase from 0.299emu/g and 180Oe for B3F900 sample to 0.857emu/g and 200Oe for B5F900 sample and 2.44emu/g and 400Oe for B10F900 sample. Likely, the M_r/M_s ratio increases with Fe_3O_4 content from 0.2 for B3F900 to 0.23 and 0.27 respectively for B5F900 and B10F900 samples.

**Figure 4-29** M-H curves of composite nanofibers carbonized at 900°C containing 3, 5 and 10wt.%GB:10-20nm Fe_3O_4 nanoparticles respectively designated as B3F900, B5F900 and B10F900.

4.2.2.4 GA:20-30nm and GB:10-20nm Fe₃O₄/carbon nanofiber composites

Comparing the magnetic properties of carbonized samples containing different sizes of Fe₃O₄ nanoparticles reveals that larger M_s values are obtained for samples containing larger Fe₃O₄ nanoparticles (GA:20-30nm). Furthermore, the hysteresis is also confirmed to be dependent on the size of nanoparticles.

4.3 Electromagnetic Interference Shielding Effectiveness

A novel and promising application of electromagnetic carbon nanofibers is the electromagnetic shielding effectiveness. The electromagnetic shielding effectiveness these materials is studied over the X-band (8.2-12.4GHz). The total shielding efficiency (SE_{total}), shielding via reflection (SE_R) and absorption (SE_A) are determined using the scattering parameters obtained from a vector network analyzer. The effect of Fe₃O₄ nanoparticles content and size as well as membrane thickness and pyrolysis temperature are demonstrated in the following section.

4.3.1 Effect of Fe₃O₄ content

The effect of GA:20-30nm Fe₃O₄ nanoparticles content on shielding effectiveness of composite carbon nanofibers is studied. The SE_{total} of as-spun pure PAN nanofiber (10PAN), pristine carbon nanofiber (10PAN900) and composite carbon nanofibers containing 3wt.% GA:20-30nm Fe₃O₄ (A3F900) and 5wt.% GA:20-30nm Fe₃O₄ (A5F900) as a function of working frequency is depicted in Figure 4-30. All the above mentioned samples are carbonized at 900°C with the same thickness of 0.7mm except for as-spun nanofiber which is represented as reference material and is not carbonized. In addition, Figure 4-31 and Figure 4-32 illustrate the SE_R and SE_A efficiencies of the abovementioned samples as a function of working frequency. Table 4-12 reveals the SE_{total}, SE_R and SE_A variations with Fe₃O₄ wt.% at working frequency of 10.4GHz.

The as-spun 10PAN samples does not contribute to the shielding as it shows $SE_{total} \sim 0$. However, SE_{total} is shown to be improved for carbonized samples. Among carbonized samples, overall, SE_{total} increase with the addition of Fe_3O_4 (wt.%) in the carbon nanofiber matrix from 0 (10PAN900) to 3wt.%(A3F900) and 5wt.%(A5F900), as demonstrated in Figure 4-30. The SE_{total} increases from 45dB for pristine carbon nanofiber (10PAN900) to 63dB and 70dB respectively for composite carbon nanofibers containing 3wt.% (A3F900) and 5wt.% Fe_3O_4 (A5F900) (Table 4-12).

The SE_{total} is the sum of SE_R and SE_A (and multiple reflection (SE_M) which is negligible if $SE_A > 15dB$). Neglecting SE_M , the variation of SE_R and SE_A of the above mentioned samples as a function of frequency are demonstrated in Figure 4-31 and Figure 4-32. SE_R slightly increases from 9.88dB for pristine carbon nanofiber (10PAN900) to 11.86dB and 12.38dB respectively for A3F900 and A5F900 samples (Figure 4-31, Figure 4-32 and Table 4-12). The SE_A raises from 34.55dB to 48.97dB and 55.47dB respectively by increasing Fe_3O_4 wt.% from 0 for 10PAN900 to 3 and 5wt.% for A3F900 and A5F900 samples. The SE_R varies in the range between 8-12dB while SE_A is in the range of 30-60dB. Therefore, higher level of SE_A is obtained for pristine and composite carbon nanofibers.

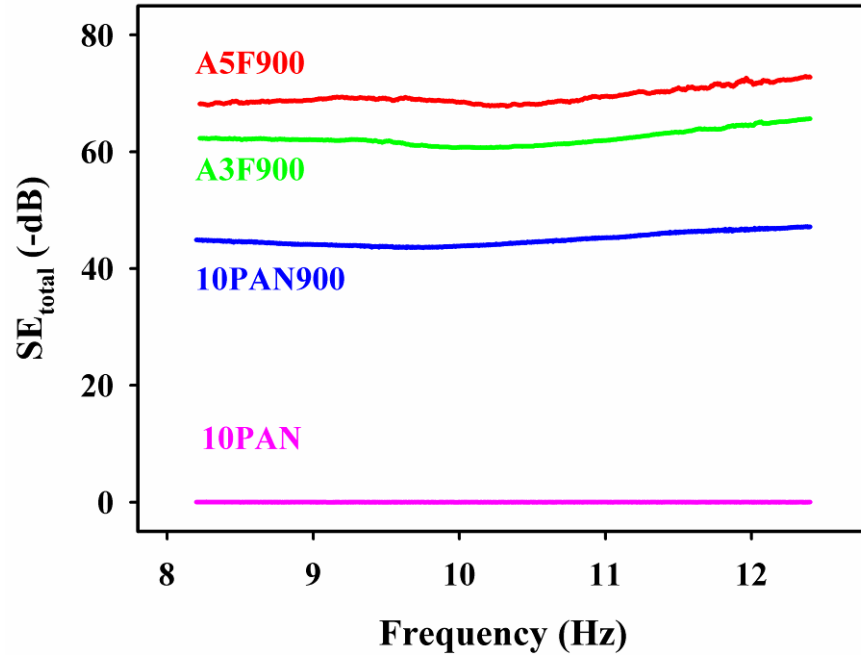


Figure 4-30 The comparison of SE_{total} of 10PAN, 10PAN900, A3F900 and A5F900 samples as a function of frequency (8.2-12.4GHz). (The thickness of all samples is 0.7 mm).

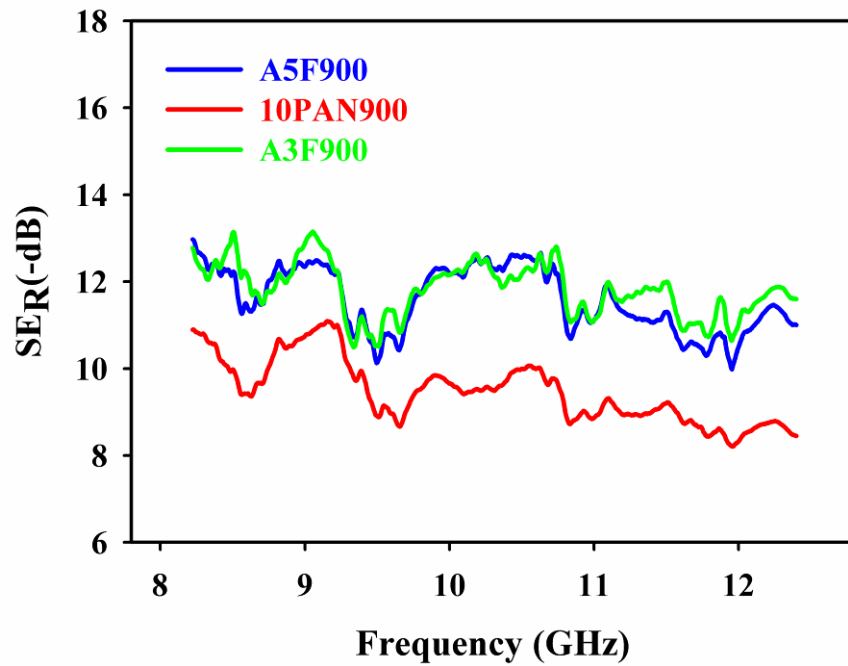


Figure 4-31 SE_R (-dB) of pristine carbon nanofibers, 3wt.% and 5wt.% GA:20-30nm Fe_3O_4 /carbon nanofibers composites all carbonized at 900°C respectively designated as APAN900, A3F900 and A5F900.

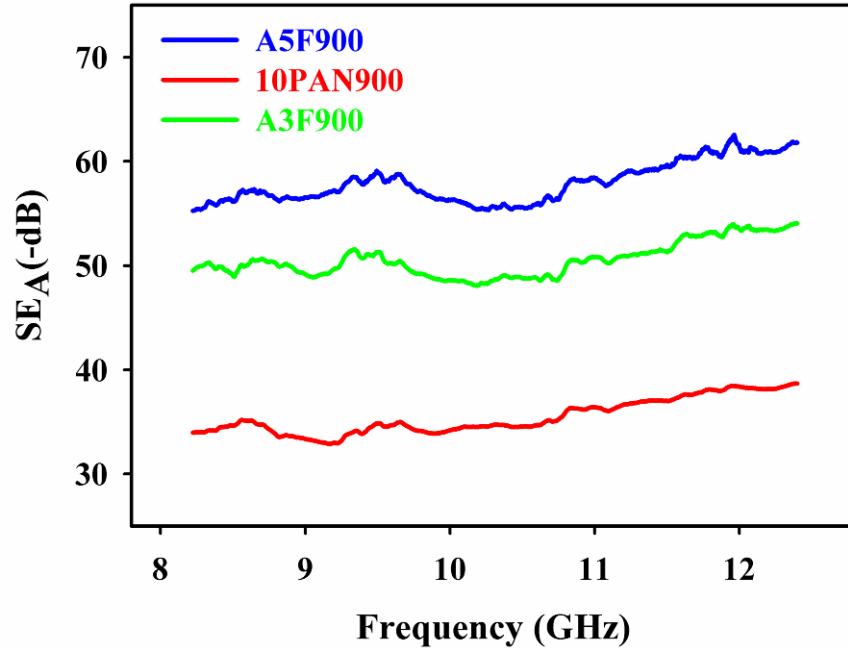


Figure 4-32 SE_A(-dB) of pristine carbon nanofibers, 3wt.% and 5wt.% GA:20-30nm Fe₃O₄/carbon nanofibers composites all carbonized at 900°C respectively designated as 10PAN900, A3F900 and A5F900.

Table 4-12 SE_{total}, SE_R and SE_A as a function of Fe₃O₄ content (wt.%) at f=10.4GHz

Sample	f=10.4GHz		
	SE _{total} (-dB)	SE _R (-dB)	SE _A (-dB)
10PAN900	44.00	9.88	34.55
A3F900	60.00	11.86	48.97
A5F900	67.00	12.38	55.47

4.3.2 Pyrolysis effect

Pyrolysis process is demonstrated to affect on the electrical conductivity of PAN-based composite nanofibers (explained previously). The electrical conductivity is shown to have a contributing effect on the shielding efficiency of a shield. Hence, it is worthwhile to compare the shielding efficiency of non-carbonized and carbonized PAN-based nanofibers.

Figure 4-33 compares the SE_{total} of 10PAN, 10PAN700 and 10PAN900 samples over the X-band frequency range of 8.2-12.4GHz. All samples have the thickness of 0.1mm. The SE_{total} in

average increases from 0.0007dB to 0.2dB and ~15dB respectively for 10PAN, 10PAN700 and 10PAN900 samples. Therefore, it is observed that the shielding performance improves as nanofibers become carbonized more specifically at higher temperature, i.e. 900°C.

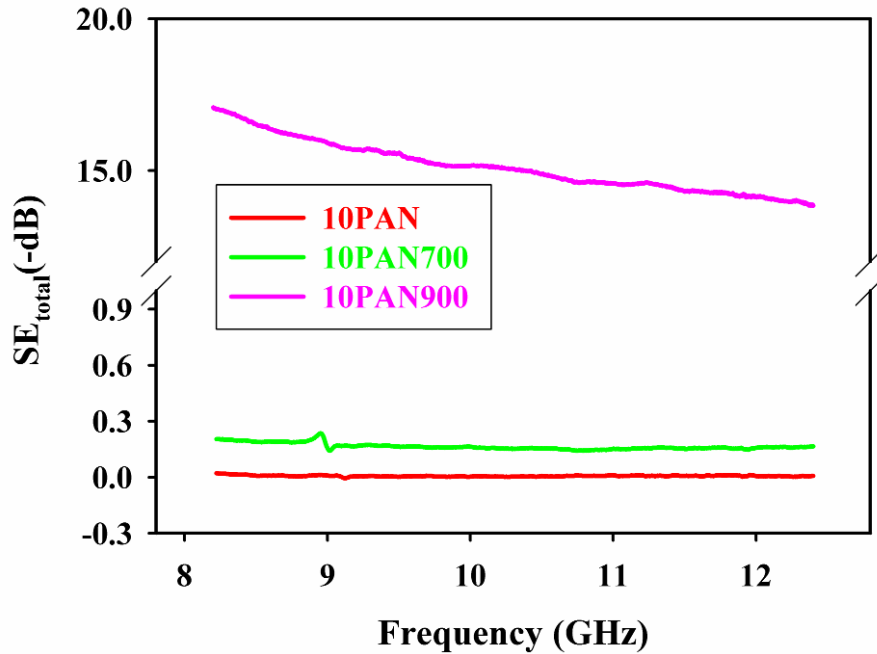


Figure 4-33 Comparison of SE_{total} of 10PAN, 10PAN700 and 10PAN900 samples as a function of frequency. (The thickness of all samples is ~0.1 mm).

4.3.3 Thickness

Figure 4-34 reveals the frequency dependence of the SE_{total} of different A5F900 samples with various thicknesses (0.1mm, 0.25mm, 0.45mm, 0.55mm and 0.7mm) in the X-band frequency range. The SE_{total} , SE_R and SE_A of A5F900 sample with various thicknesses at working frequency of 10.4GHz are also demonstrated in Table 4-13. Results illustrate that the SE_{total} is proportional to the thickness of the membrane and is verified to increase with the thickness as shown in Figure 4-34. SE_{total} increases from 23.6dB to 27.9dB, 45.1dB, 56.3dB and 67.9dB with

increasing the thickness of composite membrane respectively from 0.1mm to 0.25mm, 0.45mm, 0.55mm and 0.7mm as depicted in Table 4-13.

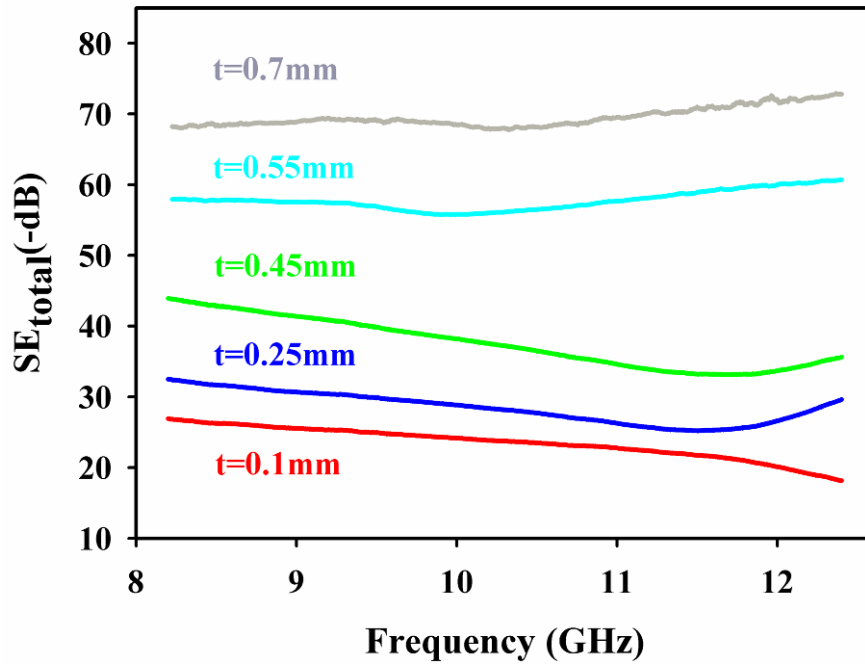


Figure 4-34 SE_{total} as a function of frequency for A5F900 samples with different thicknesses.

Accordingly, comparing the SE_R and SE_A values of A5F900 sample in Table 4-13 illustrates that most of the shielding occurs due to the absorption rather than the reflection mechanism since $SE_A > SE_R$. Average SE_R slightly varies in the range between 9-13dB for samples of different thicknesses (0.1-0.7mm). Whereas SE_A increases monotonically from 13.22dB to 18.82dB, 36.56dB, 43.43 and 55.47dB with raising the thickness respectively from 0.1mm, 25mm to 0.45mm, 0.55mm and 0.7mm (Table 4-13).

Table 4-13 SE_{total} , SE_R and SE_A of 5wt.% GA:20-30nm Fe_3O_4 / carbon nanofiber composite with various thicknesses at working frequency of 10.4GHz

	0.1mm	0.25mm	0.45mm	0.55mm	0.7mm
SE_{total} (dB)	23.62	27.9	45.07	56.3	67.9
SE_R (dB)	10.4	9.11	8.5	12.89	12.39
SE_A (dB)	13.22	18.82	36.56	43.43	55.47

4.3.4 Effect of the size of Fe_3O_4 nanoparticles

The size of Fe_3O_4 nanoparticles embedded in the carbon nanofiber matrix is proved to affect the shielding efficiency of composite nanofibers. The total shielding performance of pristine carbon nanofiber (10PAN900) and composite carbon nanofibers of two different sizes of Fe_3O_4 nanoparticles, i.e. GA:20-30nm and GB:10-20nm Fe_3O_4 nanoparticles (respectively designated as B5F11900 and A5F900) over the working frequency of 8.2-12.4GHz are exhibited in Figure 4-35. The SE_{total} , SE_R and SE_A values of pristine carbon nanofiber (10PAN900) and composite carbon nanofibers made of 5wt.% GA:20-30nm Fe_3O_4 and 5wt.% GB:10-20nm Fe_3O_4 are also summarized in Figure 4-36.

The SE_{total} of composite carbon nanofiber containing larger GA:20-30nm Fe_3O_4 nanoparticles is proved to be higher than the SE_{total} of both pristine carbon nanofiber and composite carbon nanofiber containing 5wt.% GB:10-20nm Fe_3O_4 nanoparticles (Figure 4-35). The SE_{total} increases from 44.4dB for 10PAN900 to 46.6dB and 67.9dB respectively for composite carbon nanofibers of 5wt.% GB:10-20nm Fe_3O_4 nanoparticles (B5F900) and 5wt.% GA:20-30nm Fe_3O_4 nanoparticles (A5F900). Besides, it is observed that shielding by absorption is always higher than shielding by reflection ($SE_A > SE_R$). The SE_R barely changes from 9.88dB to 10.59dB and 12.38dB respectively for 10PAN900, B5F900 and A5F900 samples. On the other hand, the SE_A increases slightly from 34.55dB to 36.03dB for 10PAN900 and B5F900 samples and then to a

fairly larger value, i.e. 55.47dB for A5F900 sample (Figure 4-36). Therefore, composite nanofibers composed of larger nanoparticles show higher shielding efficiency.

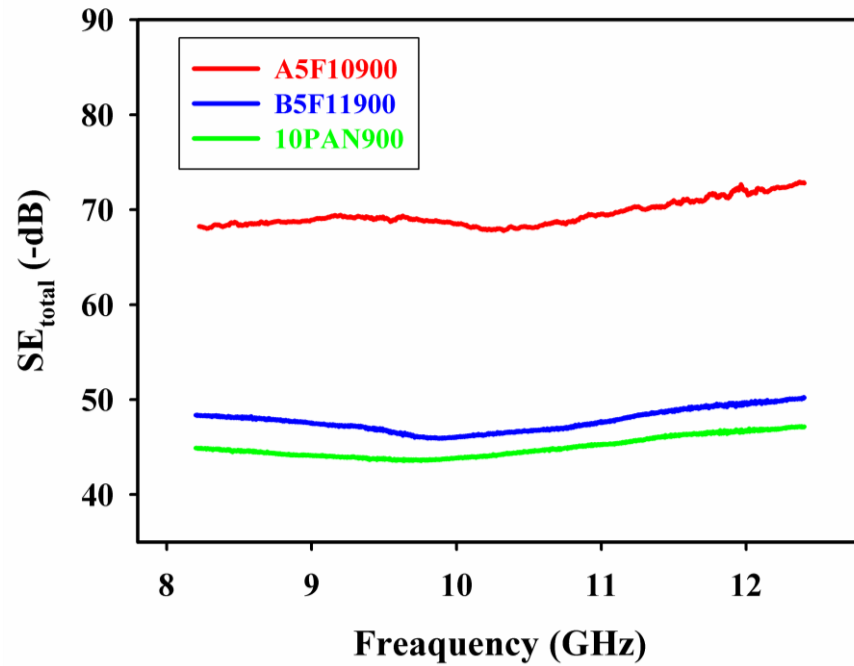


Figure 4-35 SE_{total} as a function of frequency (8.2-12.4GHz) for 10PAN900, A5F900 and B5F900 samples. (The thickness of all samples is ~0.7mm).

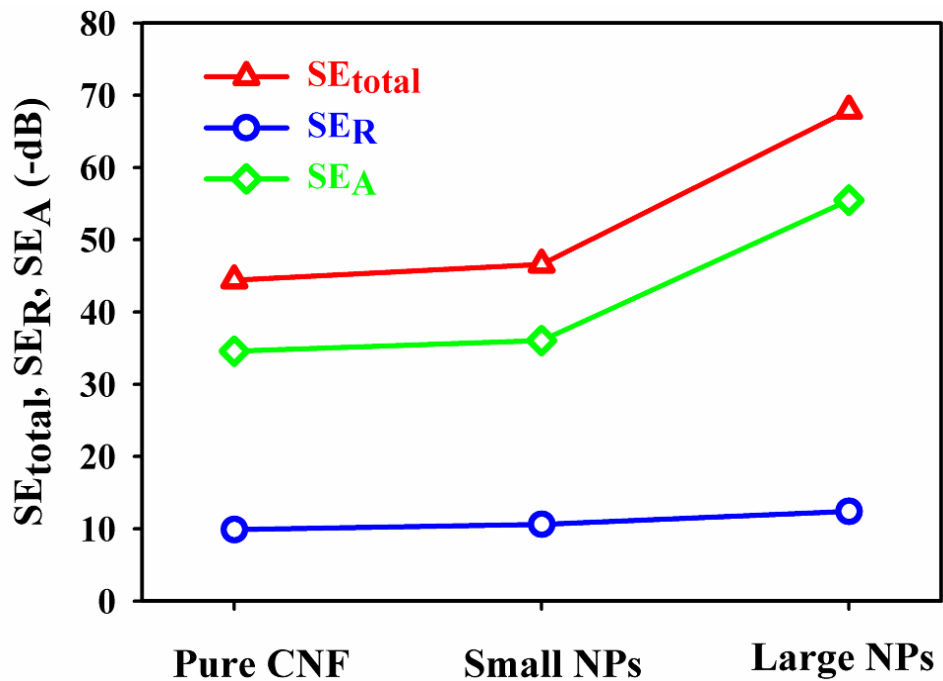


Figure 4-36 SE_{total} , SE_R and SE_A values of pristine carbon nanofiber, 5wt.% GA:20-30nm Fe_3O_4 and 5wt.% GB:10-20nm Fe_3O_4 nanoparticles /carbon nanofiber composites (respectively designated as A5F900 and B5F900) as a function of the size of nanoparticles. Data are reported at working frequency of 10.4GHz.

Chapter 5. Discussion

5.1 Microstructural and compositional characterizations

5.1.1 SEM observations

Uniform nanofibers are obtained by electrospinning of pure 10wt.% PAN/DMF and composite solutions containing different sizes and amounts of Fe_3O_4 in 10wt.%PAN/DMF. According to SEM micrographs shown in Figure 4-1, Figure 4-2 and Figure 4-3 and the results summarized in Table 4-1, the average fiber diameter of all nanofibers decreases after carbonization process. This trend is attributed to the volume shrinkage of PAN because of its weight loss during the pyrolysis process. The decrease in fiber diameter is a result of the evaporation of residual solvent, the removal of unwanted elements and the evolution of various gases such as H_2O , N_2 , HCN from the PAN structure occurred during the carbonization [3, 166]. As mentioned in the SEM results, the fiber diameter increases with the addition of Fe_3O_4 nanoparticles for both groups of composites containing GA:20-30nm and GB:10-20nm Fe_3O_4 nanoparticles, especially for those produced by smaller nanoparticles (GB:10-20nm). This observation is attributed to an increase in the viscosity of the solutions composed of nanoparticles in comparison with pure PAN/DMF solution. Highly viscose solutions are prone to produce uniform nanofibers with larger diameter [31, 36-38]. To confirm this, the viscosity needs to be measured; however, we were unable to measure the viscosity change for the composite solutions.

Further, the presence of ionic salt (NaCl) for GB:10-20nm Fe_3O_4 nanoparticles, as shown in the XRD results in Figure 4-8, increases the fluidity of the solution and the surface charge of the spinning jet. The results in extracting larger amount of fluent spinning jet out of the needle that

eventually increases the fiber diameter. It is found that the dissolution of LiCl and also its spinning process is easier compared to other ionic salts in PAN/DMF solution [44].

5.1.2 TEM observations

As shown in Figure 4-5 and Figure 4-6 the overall dispersion of Fe₃O₄ nanoparticles in nanofibers appears to be relatively uniform. The Triton X-100 is a promising surfactant for relatively uniform dispersion of Fe₃O₄ nanoparticles in PAN-based nanofibers. An important observation from the TEM images of as-spun and carbonized composite nanofibers containing both GA:20-30nm and GB:10-20nm Fe₃O₄ nanoparticles is that the size of nanoparticles become larger due to the carbonization process which is more visible for those samples pyrolyzed at higher temperature, i.e. 900°C. However, larger particles are obtained for those fabricated with bigger particles rather than the smaller ones (Figure 4-6). Also high temperature induces the diffusion of particles and clustering of larger Fe₃O₄. Growth of particles occurs by agglomeration and sintering through the pyrolysis process that is also dependent on the loading of particles. It has been found that higher Fe₃O₄ loading leads to more significant agglomeration and sintering [167, 168] as shown in Figure 4-7.

5.1.3 XRD analysis

5.1.3.1 Nanoparticles

XRD results confirm that both GA:20-30nm and GB:10-20nm Fe₃O₄ nanoparticles are mainly composed of Fe₃O₄ (ref.# 01-071-6337) (Figure 4-8). However, GB:10-20nm Fe₃O₄ nanoparticles contain an impurity which according to MDI Jade software matches with NaCl peaks (ref.: #01-070-2509). NaCl is an ionic salt that has been confirmed to increase the ionic

conductivity of solution dope. It is introduced as an ionic salt which improves the spinnability of polymer solution dope. Its effect on the fiber diameter is discussed in the SEM section.

5.1.3.2 GA:20-30nm Fe₃O₄/carbon nanofiber composites

The two XRD peaks near 2θ angles of 24° and 44° correspond respectively to (002) and (010) layers of graphitic structure. These are the typical graphite peaks [169] and are confirmed to be formed for all carbonized samples (Figure 4-9).

Fe₃O₄ is also detected in the XRD results. The intensity of Fe₃O₄ peaks increases with increasing the Fe₃O₄ content and pyrolysis temperature. Higher Fe₃O₄ loading (wt.%) in the carbon nanofiber matrix results in increasing the intensity of Fe₃O₄ peaks identified in Figure 4-9(a,b). With increasing the carbonization temperature, the Fe₃O₄ diffraction peaks become stronger as shown in Figure 4-9. By considering PAN weight loss during the carbonization process and the possible coarsening of the nanoparticles due to the carbonization process, the formation of larger Fe₃O₄ crystallite phase is further verified. This in turn results in acquiring more intensive Fe₃O₄ peaks. Wang et al. [13] reported that Fe₃O₄ crystal size dispersed in the PAN-based carbon nanofiber becomes larger and forms better Fe₃O₄ crystallites due to the increase in the carbonization temperature from 500°C to 700°C .

The formation of $\alpha\text{-Fe}$ [101, 170] and Fe₃C [20, 101, 170] have been previously reported in electrospun PAN-based carbon nanofibers and electrospun acrylic nanofibers containing Fe₃O₄ precursor as well as aromatic polyimide film containing Fe complex. According to Kaburagi et al. [170], Fe₃C is formed due to the reaction of Fe and C (carbon) during the carbonization process.

The position and the sharpness of the graphite peak at $2\theta=24^\circ$ varies with Fe_3O_4 content in the carbon matrix (Table 4-3 and Figure 4-10). The average interlayer d-spacing of (002) layer ($d_{(002)}$) and the 2θ angles of graphite peak at 24° of pristine and composite carbon nanofibers containing GA:20-30nm Fe_3O_4 nanoparticles are shown in Figure 5-1. The shift of (002) peak towards higher values as well as the decrease in $d_{(002)}$ with increasing Fe_3O_4 loading might be due to the catalytic effect of GA:20-30nm Fe_3O_4 nanoparticles and the enhanced crystallinity of graphitic structure of carbon fiber matrix by Fe_3O_4 . This is in agreement with previous studies as Panel et al. [20] investigated the synthesis and characterization of magnetically active carbon fibers with hierarchical pore structures. They found that the graphite peaks for composite carbon nanofibers with 9wt% and 17wt% iron oxide precursor (iron (III) acetylacetonate: AAI) are much sharper and shift slightly towards higher 2θ angle than pristine carbon nanofiber. The catalytic effect of Fe_3O_4 on the graphitization of carbon has been previously reported [20, 101, 171-173]. The catalytic effect of Fe_3O_4 is confirmed in Raman spectroscopy and electrical conductivity results. The catalytic role that Fe_3O_4 plays in the graphitization of carbon fiber matrix is not clear yet. But it has been explained in terms of reduction of Fe_3O_4 into Fe_3C and Fe reported by Wang et al. [173] in the carbonization process of Fe_2O_3 /pitch mixture. They claimed that Fe_2O_3 is first reduced to Fe_3O_4 through the thermal heat treatment under nitrogen at 350°C . Fe_3O_4 is then reduced to Fe_3C and metallic Fe during the carbonization process at 1000°C . Such a reduction results in the formation of an ordered stacking of carbon layers probably due to deformation and rearrangement of the layers within the carbon grains. Finally, complete decomposition of Fe_3C to metallic Fe occurs at higher temperatures beyond 1000°C contributing to the graphitization of pitch at higher temperatures [173]. The formation of sharp graphite peaks at $2\theta=24^\circ$ is related to the formation of carbon layers around the Fe particles whereas the broad

peaks correspond to the carbon matrix are unaffected by the Fe particles [170]. Kim et al. [174] simply explained the graphitization of carbon matrix by formation of ordered graphite around the Fe_3O_4 particles as represented in Figure 5-2.

The formation of highly ordered graphitic structure is further improved by increasing the carbonization temperature from 700°C to 900°C. Larger 2θ and shorter $d_{(002)}$ for samples carbonized at 900°C (Figure 5-1) provide evidence for contributing effect of carbonization temperature on the graphitization of carbon matrix. The effect of Fe_3O_4 loading and pyrolysis temperature in graphitization of carbon fiber matrix will be further discussed in Raman spectroscopy and electrical conductivity sections.

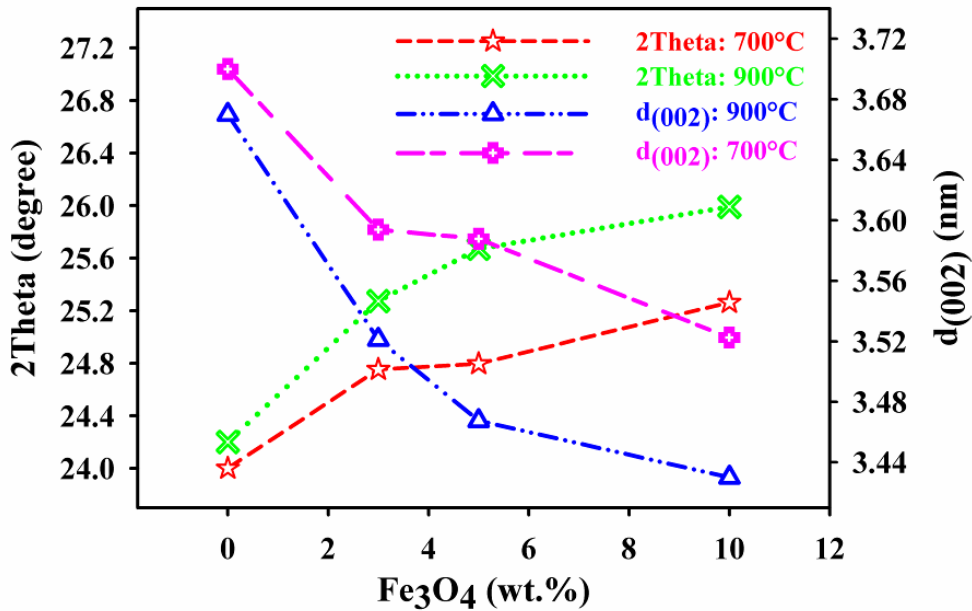


Figure 5-1 2θ and $d_{(002)}$ of pristine and composite carbon nanofibers composed of GA:20-30nm Fe_3O_4 at two carbonization temperatures, 700°C and 900°C.

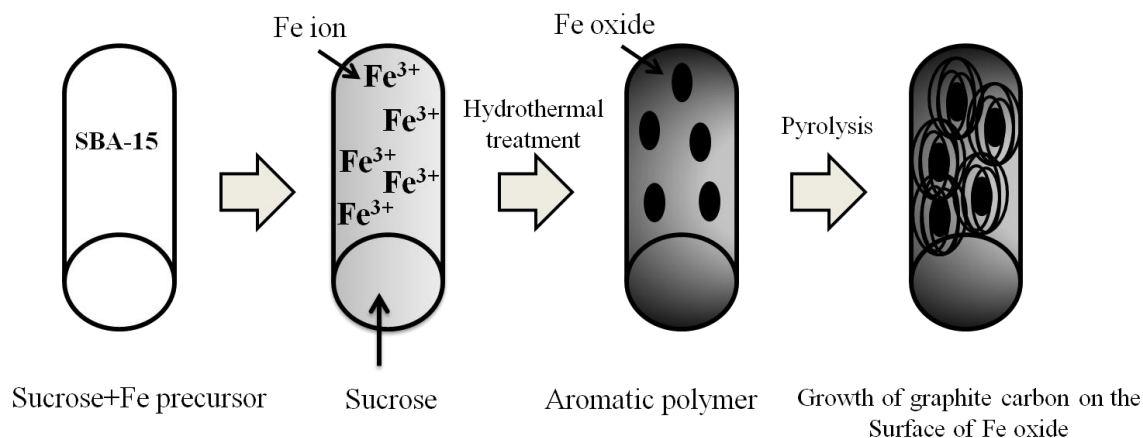


Figure 5-2 Schematic representation for the preparation of G-carbon.

5.1.3.3 GB:10-20nm Fe_3O_4 /carbon nanofiber composites

XRD results show that graphite, Fe_3O_4 and Fe_3C are the available phases after the carbonization at 700°C and 900°C in composites containing smaller (GB:10-20nm) Fe_3O_4 nanoparticles. However, the intensity and sharpness of GB:10-20nm composite carbon nanofibers are smaller than those composed of larger GA:20-30nm Fe_3O_4 nanoparticles.

Fe_3C is only detected for samples containing higher Fe_3O_4 nanoparticles (5wt.% and 10wt.%) carbonized at higher pyrolysis temperature, i.e. 900°C . Also, in comparison with samples containing larger GA:20-30nm Fe_3O_4 nanoparticles, the $\alpha\text{-Fe}$ is not identified as one of the present phases formed after carbonization for these samples as shown in Figure 4-11.

According to Wang et al. [173], less graphitization of carbon matrix is expected for composite carbon fibers containing GB:10-20nm Fe_3O_4 , since no $\alpha\text{-Fe}$ is identified for these samples. This is confirmed by the XRD results for samples containing smaller Fe_3O_4 nanoparticles (GB:10-20nm). Broader (002) carbon peaks (at $2\theta=24^\circ$) is obtained in these

samples. This comparison is demonstrated in Figure 5-3 where all samples are pyrolyzed at 900°C.

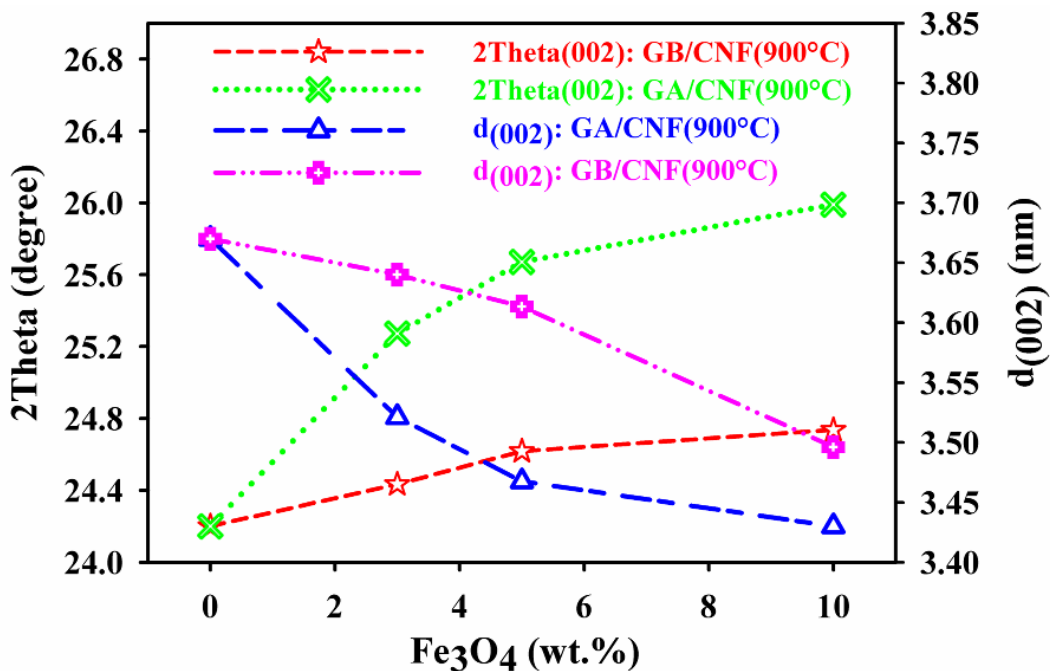


Figure 5-3 $2\theta_{(002)}$ and $d_{(002)}$ of GA:20-30nm Fe₃O₄ and GB: 10-20nm Fe₃O₄-based carbon nanofiber composites obtained at 900°C carbonization temperatures.

5.1.4 Raman spectroscopy

The enhanced graphitic structure due to higher Fe₃O₄ content, larger Fe₃O₄ nanoparticles and higher pyrolysis temperature was further confirmed using Raman spectroscopy.

5.1.4.1 GA:20-30nm Fe₃O₄/carbon nanofiber composites

Degree of graphitization of carbonaceous materials is determined by the relative intensities of the disordered (I_D) and ordered (I_G) bands obtained from Raman spectroscopy and is represented as $R=I_G/I_D$ ratio. The R value is a measure of the degree of graphitization by which

an in-plane size of graphite crystals (L_a) can be estimated using the following relation, $L_a \sim 4.4 \times (I_G/I_D)$ [165]. Raman spectroscopy results of pristine carbon nanofibers and composite carbon nanofibers containing GA:20-30nm Fe_3O_4 nanoparticles reveal that the crystalline structure of carbon matrix is enhanced with Fe_3O_4 loading as sharper and more intensive peaks are obtained for composite samples (shown in Figure 4-14). Figure 5-4 depicts the degree of graphitization in $R=I_G/I_D$ ratio and L_a as a function of Fe_3O_4 content and pyrolysis temperature.

As shown in Figure 5-4, the degree of graphitization (R) and also size of the graphite crystal (L_a) increases with Fe_3O_4 loading. Increasing the R ratio by adding Fe_3O_4 into the carbon matrix proves the catalytic activity of GA:20-30nm Fe_3O_4 nanoparticles in the graphitization of carbon nanofiber matrix. The effective role that Fe_3O_4 plays in enhancing the highly crystalline graphite formation in PAN-based carbon nanofibers is consistent with our XRD observations wherein sharper graphite peaks shifting towards higher $2\theta_{(002)}$ angles with addition of Fe_3O_4 loading (Figure 4-10). Metals and metal oxides have been reported to speed up the graphitization of carbon matrix. Hence they lower down the required carbonization temperature needed to obtain higher ordered graphitic structure [20, 101, 170-172, 174-182]. The catalytic effect of Fe_3O_4 has also been proved to enhance the formation of well-crystalline graphite from Polyvinyl Chloride at lower temperatures like $1000^\circ C$ [172].

Wang et al. [173] reported the catalytic graphitization of pitch containing Fe_2O_3 compound. According to their results Fe_2O_3 leads to the catalytic graphitization of pitch material by first reduction to Fe_3O_4 and then to the mixture of Fe_3C and Fe under the nitrogen atmosphere by calcination at $1000^\circ C$. Finally, the metallic Fe present in the matrix acts as a catalyser and contributes to the crystallinity of the pitch matrix [173]. This is also reported by Dhakate et al.

[171] that iron oxide contributes to the graphitization of pitch by being reduced to iron carbide and then metallic iron.

In addition, results shown in Figure 5-4 proves that R and L_a values increase as the Fe_3O_4 content increases from 0 to 3 and 5wt.% and then levels off by adding Fe_3O_4 from 5 to 10wt.%, for samples carbonized at 900°C respectively designated as A5F900 and A10F900. The R ratios are almost the same for these samples by considering the error bars, i.e. 0.62 and 0.61 (Table 4-5). It can be concluded that Fe_3O_4 contributes to the enhancement of the formation of higher order graphitic structure up to a certain concentration. As reported by Panel et al. [20], Fe_3O_4 enhances the graphitic structure formation for samples containing Fe_3O_4 precursor. However, the (002) graphite peak disappears for sample with larger amount of Fe_3O_4 precursor. This is attributed to the increase in the size of non-conductive Fe_3O_4 crystals. This implies that only certain amount of Fe_3O_4 in the composite matrix is effective in the graphitization of carbon [171].

Further, the carbonization temperature is demonstrated to affect the formation of ordered graphitic structure. The R and L_a values of both pristine carbon nanofibers and composite carbon nanofibers containing GA:20-30nm Fe_3O_4 nanoparticles are shown to increase with increasing the pyrolysis temperature from 700°C to 900°C. Higher pyrolysis temperature results in the transformation of disordered carbon into higher ordered graphitic structure and further growth of graphite crystals. Increasing the pyrolysis temperature results in a reduction of the interlayer spacing of (002) graphite crystals ($d_{(002)}$), a decrease in the void space, growth in the thickness and area of the graphitic crystallites and an increase in the preferred orientation of the microstructure [3]. The effect of carbonization temperature to graphitize the carbon matrix has been also previously reported [103, 166, 183, 184].

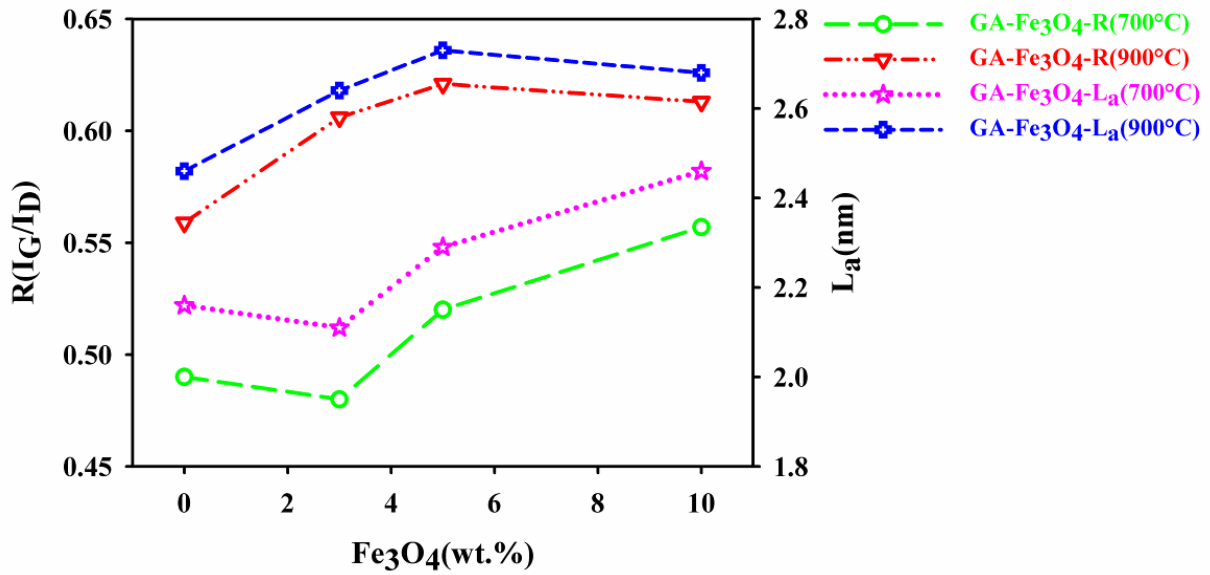


Figure 5-4 R and L_a obtained for pristine carbon nanofiber and GA:20-30nm Fe_3O_4 -based carbon nanofiber composite.

5.1.4.2 GB:10-20nm Fe_3O_4 /carbon nanofiber composites

In comparison with larger GA:20-30nm Fe_3O_4 nanoparticle, results show that smaller GB:10-20nm Fe_3O_4 nanoparticles do not contribute to the graphitization of carbon matrix as shown in Raman spectroscopy results in Table 4-6. This is also confirmed by XRD results (Figure 4-12). Figure 5-5 represents the change in the R values of pristine and composite carbon nanofibers containing two different sizes of nanoparticles (GA:20-30nm and GB:10-20nm). All samples are carbonized at 900°C. As shown in Figure 5-5, almost constant R and L_a values are obtained for composites containing smaller GB:10-20nm Fe_3O_4 nanoparticles. In comparison, larger R and L_a values are obtained for composites containing larger GA:20-30nm Fe_3O_4 nanoparticles. Hence, it can be concluded that the enhancement of graphitization of carbon matrix is due to the larger particles rather than smaller ones. This has also been shown that catalyst size is important in its catalytic activity [185].

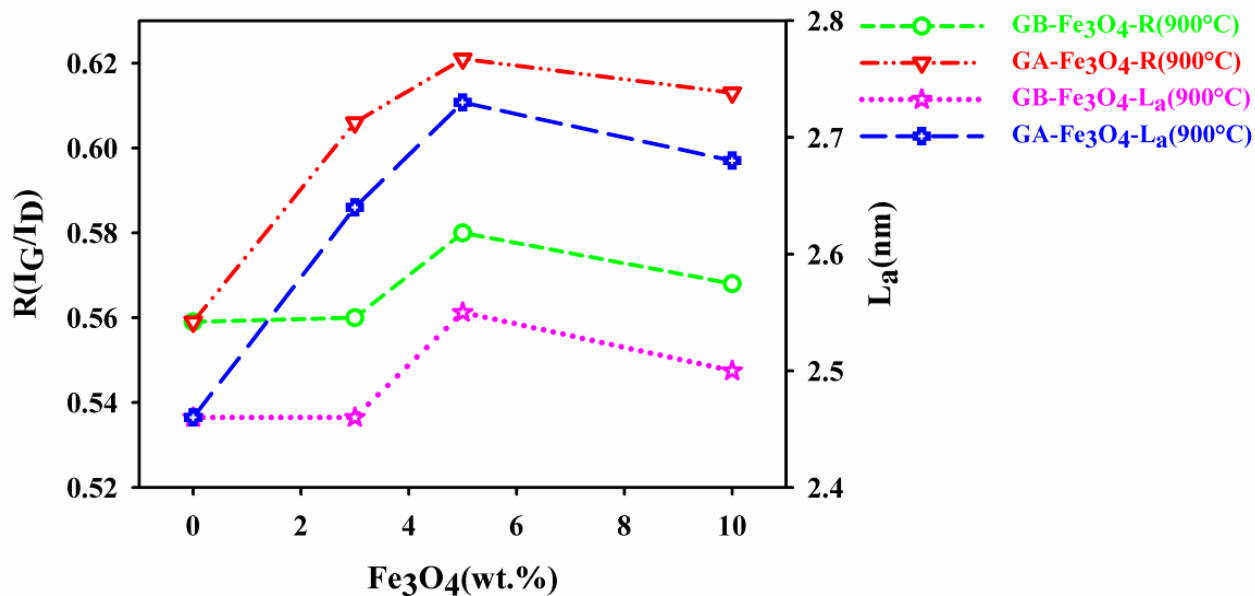


Figure 5-5 Graphitization of carbon nanofiber matrix using different sizes of Fe₃O₄ nanoparticles (GA:20-30nm and GB:10-20nm) carbonized at 900°C.

The abovementioned observations confirm the slight enhancement of the degree of graphitization of carbon matrix (Figure 5-4 and Figure 5-5) by these two variables; size and content of Fe₃O₄ nanoparticles as well as pyrolysis temperature.

5.2 Physical properties

5.2.1 Electrical conductivity

The catalytic role of Fe₃O₄ nanoparticles content and size and contributing effect of pyrolysis temperature on the graphitization of carbon nanofiber matrix was further affirmed by four-point probe measurements.

5.2.1.1 GA:20-30nm Fe₃O₄ /carbon nanofiber composite

Electrical conductivity measurements of pristine carbon nanofiber and composite carbon nanofibers containing GA:20-30nm Fe₃O₄ nanoparticles proves that there is a direct correlation

between the Fe₃O₄ content (wt.%) and increase in the electrical conductivity of composite carbon nanofibers (Figure 4-16). Figure 5-6 demonstrates the effect of Fe₃O₄ content and pyrolysis temperature on the resulting electrical conductivity for samples carbonized at (a) 700°C and (b) 900°C.

The influence of Fe₃O₄ in increasing the electrical conductivity is attributed to its catalytic effect as proved by XRD and Raman spectroscopy results. According to the XRD results, sharper and more intensive (002) graphite peaks are obtained with Fe₃O₄ loading in the carbon matrix. Slight shift of $2\theta_{(002)}$ towards larger angles and shorter $d_{(002)}$ spacing of (002) graphite layers are evident for the formation of ordered graphitic structure (Table 4-3, Figure 4-10). In addition, Raman spectroscopy results showed that the degree of graphitization of carbon matrix increases with Fe₃O₄ content. Consequently, the size of graphite crystals (L_a) grows larger with increasing the Fe₃O₄ concentration (Table 4-5). Hence, Fe₃O₄ loading into the carbon fiber matrix is demonstrated to enhance the graphitization of carbon matrix and increase the structural order of graphite which in turn enhances the electrical conductivity of carbon materials. The catalytic graphitization of carbon matrix by iron oxide has also been reported in other references [170, 176].

A comparison of the R ratios and electrical conductivity of samples with 5wt.% Fe₃O₄ (A5F900) and 10wt.% Fe₃O₄ (A10F900) as shown in Table 4-5 and Figure 5-6 reveals that the R ratio decreases slightly from 0.62 ± 0.010 to 0.61 ± 0.002 . This might show that graphitization of carbon matrix levels off at higher Fe₃O₄ loading. Similar phenomena was reported by panels et al. [20] that electrical conductivity increases first with Fe₃O₄ loading and then decreases as its content increases to larger amount. This might be due to the formation of larger non-conductive Fe₃O₄ crystals which are reported to inhibit the graphitization of carbon matrix [20]. Besides, it

is observed that even though the R ratio of A10F900 sample is slightly lower than that of A5F900 sample, it still shows higher electrical conductivity (9.2S/cm) than A5F900 sample (7.1S/cm). Higher electrical conductivity of A10F900 sample can be probably related to the formation of higher amount of metallic α -Fe phase at higher Fe_3O_4 content (10wt.%). The formation of metallic α -Fe phase is confirmed by XRD results. Reddy et al. [186] and Chen et al. [187] respectively demonstrated that electrical conductivity of CNTs-f-PANI and PPy- Fe_3O_4 increases significantly with the increase of metallic Fe phase.

The contributing effect of pyrolysis temperature on the graphitization of carbon matrix is further confirmed by electrical conductivity results. As shown in Figure 4-16 and demonstrated in Table 5-1, the electrical conductivity increases as a result of the increase in carbonization temperature from 700°C to 900°C. This is due to the increasing degree of graphitization at higher pyrolysis temperature [88, 101-103] which is consistent with Raman spectroscopy analysis. In addition, as reported by Park et al. [101] the intensity and sharpness of metallic α -Fe increases and Fe_3C peaks decreases (until completely decompose and disappear at 1300°C) with increasing the carbonization temperature (Figure 4-9). This observation suggests that the catalytic graphitization of carbon nanofiber is further enhanced by temperature.

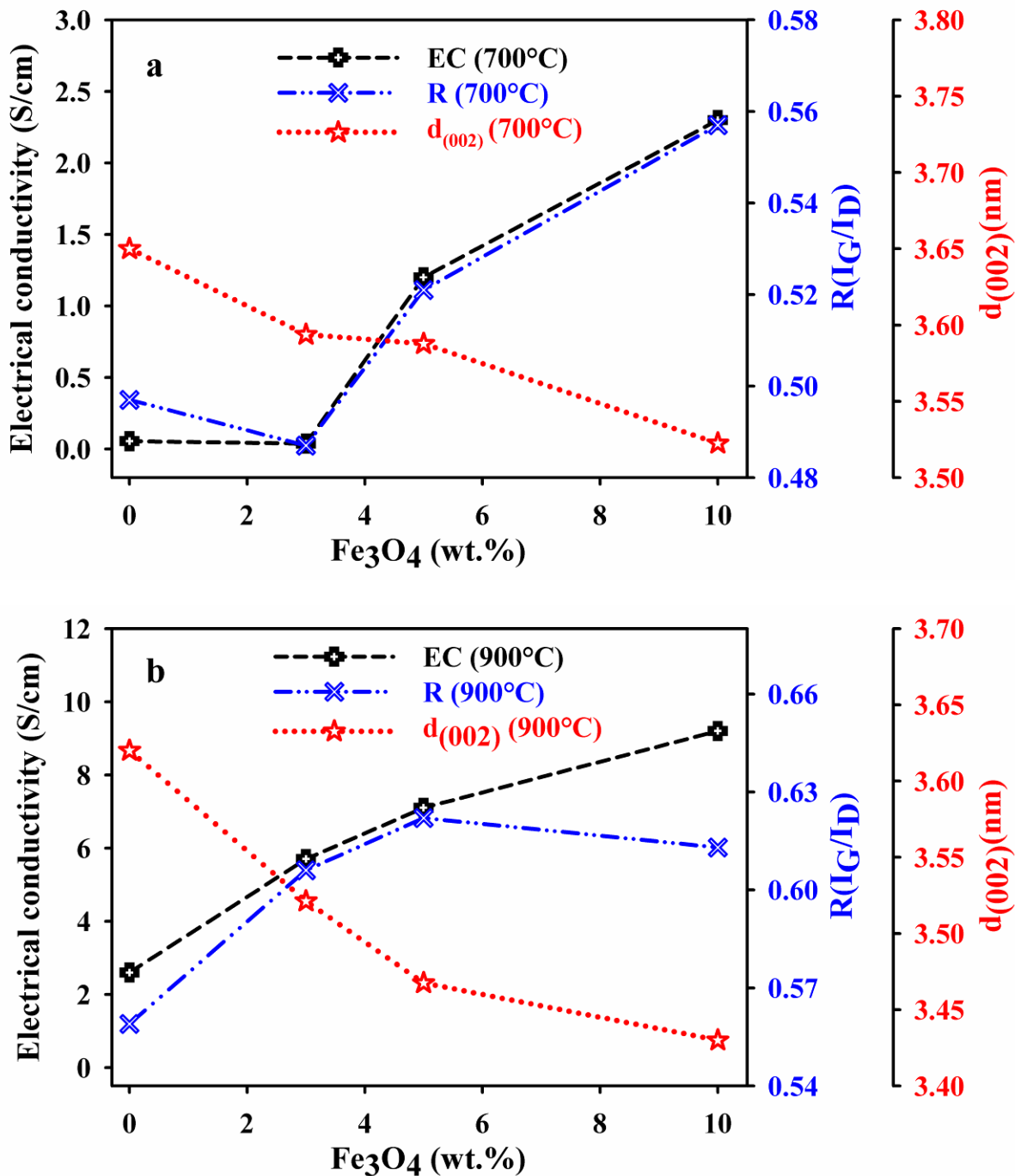


Figure 5-6 The $R=I_G/I_D$ ratio, $d_{(002)}$ and Electrical conductivity of GA:20-30nmFe₃O₄/carbon nanofiber composites carbonized at 700°C and 900°C.

The mechanism for electrical conduction in carbon fiber is related to the movement of π electrons because of the resonance vibration effect of the π bond within the graphite layer [104].

Increasing the electrical conductivity at higher pyrolysis temperature and Fe₃O₄ loading is due to the growth of carbon graphite layers and decrease in the spacing between the graphite layers with carbonization temperature. The growth of carbon graphite layer also occurs with loading of Fe₃O₄ nanoparticles into the carbon matrix as explained previously. As a result, the π electrons become more mobile in the carbon layer resulting in higher electrical conductivity [104, 183]. These observations are in agreement with the Raman spectroscopy results in which increasing carbonization temperature and Fe₃O₄ loading leads to higher R ratios (Table 4-5). This further confirms the formation of higher ordered graphitic structure. Accordingly, both pyrolysis temperature and catalytic action of Fe₃O₄ are essential to obtain highly crystalline graphitic structure as evident in XRD, Raman spectroscopy and electrical conductivity measurements.

Table 5-1 Electrical conductivity (σ) of GA: 20-30nm Fe₃O₄/carbon nanofiber composites

Sample code	σ (S/cm)	Sample code	σ (S/cm)
10PAN700	0.05±0.004	10PAN900	2.60±0.90
A3F700	0.04±0.02	A3F900	5.70±0.90
A5F700	1.20±0.40	A5F900	7.10±0.70
A10F700	2.30±0.60	A10F900	9.20±0.50

5.2.1.2 GB:10-20nm Fe₃O₄/carbon nanofiber composite

As previously explained, the electrical conductivity of composite carbon nanofibers containing GB:10-20nm Fe₃O₄ nanoparticles exhibit very minor change with Fe₃O₄ loading. The dependence of electrical conductivity of these samples to Fe₃O₄ loading and pyrolysis temperature is in good agreement with XRD and Raman spectroscopy results. According to the XRD results demonstrated in Figure 4-12 and Table 4-4, no obvious shift of (002) graphite peaks is observed. In addition, graphitization ratio remains almost constant up to 5wt.%GB:10-20nm Fe₃O₄ and then decreases from 5wt.% to 10wt.%Fe₃O₄ (Table 4-6). The same trend is obtained

from four-point probe measurements that the electrical conductivity increases slightly and then decreases for samples with 10wt.%Fe₃O₄ nanoparticles (B10F700 and B10F900 samples). Table 5-2 illustrate the electrical conductivity of pristine carbon nanofiber and composite carbon nanofibers containing smaller GB:10-20nm Fe₃O₄ nanoparticles as a function of R ratio.

The effect of pyrolysis temperature is also summarized Table 5-2. Electrical conductivity of pristine carbon nanofibers and composite carbon nanofibers increases with carbonization temperature due to the formation of highly crystalline graphitic structure as discussed before.

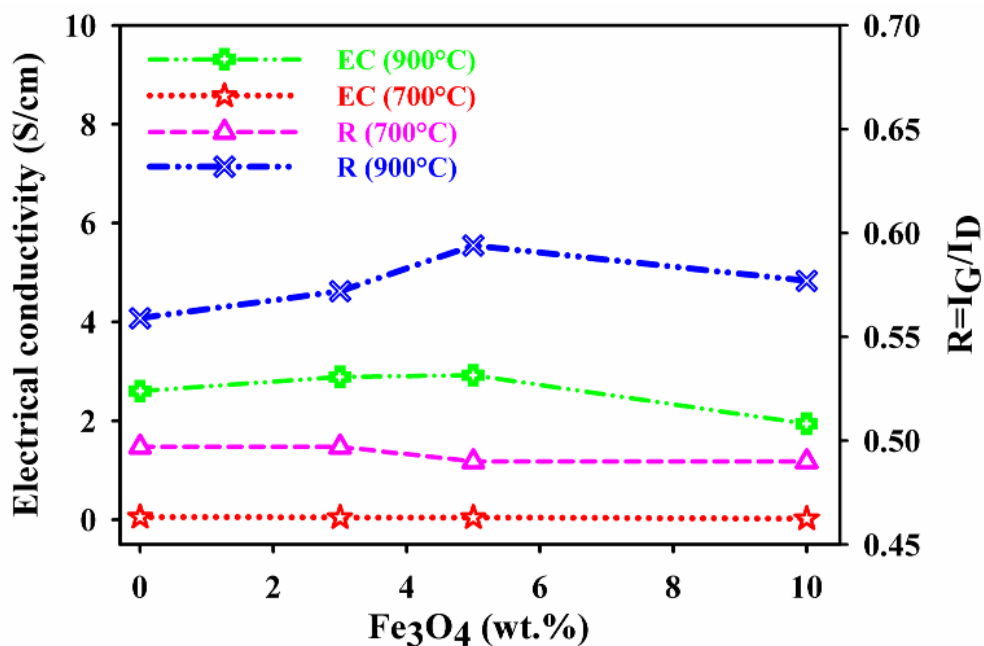


Figure 5-7 $R=I_G/I_D$ ratio, $d_{(002)}$ and electrical conductivity of GA:20-30nmFe₃O₄/carbon nanofiber composites carbonized at 700°C and 900°C.

Table 5-2 Electrical conductivity (σ) of GB:10-20nm Fe₃O₄/carbon nanofiber composites

Sample code	σ (S/cm)	Sample code	σ (S/cm)
10PAN700	0.05±0.004	10PAN900	2.6±0.9
B3F700	0.05±0.02	B3F900	2.89±0.5
B5F700	0.05±0.03	B5F900	2.92±0.6
B10F700	0.02±0.01	B10F900	1.94±0.7

5.2.1.3 GA:20-30nm Fe₃O₄ and GB:10-20nm Fe₃O₄/ carbon nanofiber composites

The use of Fe₃O₄ as catalyst to enhance the graphitization of carbon matrix appears to be size dependent. As revealed previously on XRD and Raman spectroscopy results, the highly crystalline graphitic structure can be produced via using larger GA:20-30nm Fe₃O₄ nanoparticles in matrix rather than smaller GB:10-20nm Fe₃O₄ nanoparticles. Figure 5-8 compares the graphitization (R ratio), interlayer d spacing of (002) graphitic layer (d₍₀₀₂₎) and electrical conductivity of composite carbon nanofibers fabricated with different sizes of Fe₃O₄ nanoparticles for samples carbonized at 900°C.

Larger $2\theta_{(002)}$, larger in-plane graphite crystals as well as shorter d-spacing between graphite (002) layers (d₍₀₀₂₎) and higher degree of graphitization were obtained for composite carbon nanofibers composed of bigger GA:20-30nm Fe₃O₄ nanoparticles. This is also confirmed by electrical conductivity results that composites containing larger nanoparticles acquire highly oriented crystalline graphitic structure and thus higher electrical conductivity.

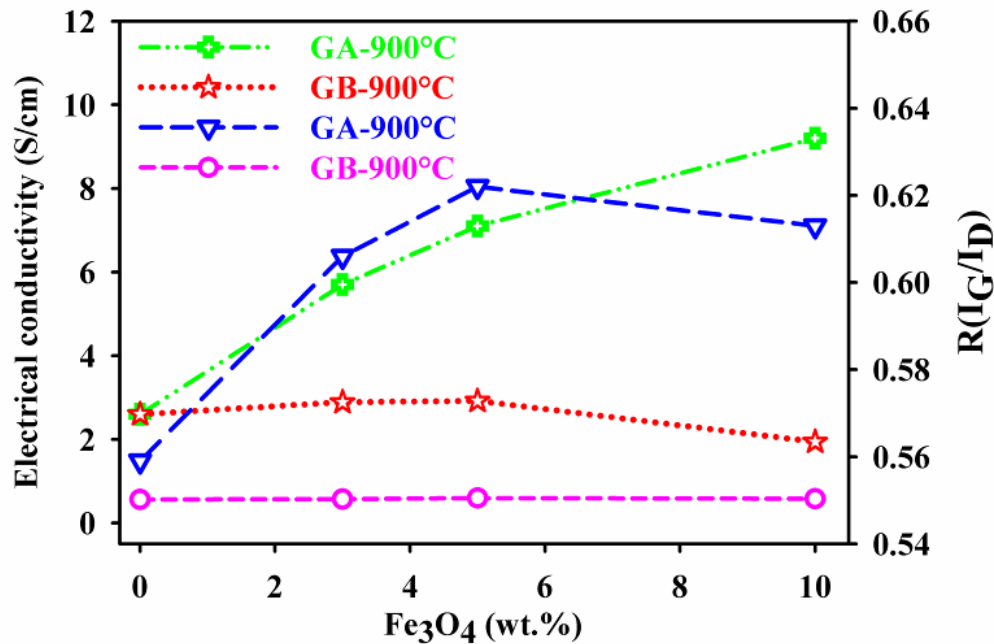


Figure 5-8 Electrical conductivity and $d_{(002)}$ of pure carbon nanofiber and composite carbon nanofibers containing GA: 20-30nm and GB:10-20nm Fe₃O₄ nanoparticles.

5.2.2 Magnetic properties

5.2.2.1 Nanoparticles

Investigating the magnetic behaviour of two different sizes of Fe₃O₄ nanoparticles reveals that magnetic properties of magnetic nanoparticles are different from bulk Fe₃O₄. Figure 5-9 represents the M_r , M_s and H_c values of GA:20-30nm and GB:10-20nm Fe₃O₄ nanoparticles.

It is observed that the M_s value increases from 32emu/g to 53emu/g by increasing the size of nanoparticles from 10-20nm to 20-30nm; however it is still smaller than that of the bulk Fe₃O₄, i.e. 88emu/g [115]. The lower M_s value of Fe₃O₄ nanoparticles in comparison with bulk Fe₃O₄ is attributed to the size effect. Reduction of the size of ferromagnetic particles results in increasing the surface area. The large surface area of nanoparticle leads to the formation of

disordered spin configuration on the surface which in turn lowers the net magnetization level [116, 117].

Similarly, the H_c value of Fe_3O_4 nanoparticles is also demonstrated to be size-dependent. As illustrated in Figure 5-9, the H_c and M_r increases from 0Oe and 0.026emu/g to 32.5Oe and 3.57emu/g respectively for GB:10-20nm and GA:20-30nm Fe_3O_4 nanoparticles. Thus, the GB:10-20nm Fe_3O_4 nanoparticles exhibit superparamagnetic behaviour whereas GA:20-30nm Fe_3O_4 nanoparticles show soft ferromagnetic behaviour. As the size of ferromagnetic particles decreases below certain value that it tends to have little to no H_c and M_r , they are identified as superparamagnetic nanoparticles [109, 113], while magnetic particles with non-zero H_c and M_r are known as ferromagnetic materials [109]. Besides, the hysteresis observed for GA:20-30nm Fe_3O_4 nanoparticles, $H_c=32.5Oe$ is much smaller than the reported H_c value for bulk Fe_3O_4 , $H_c=500-800Oe$ [115, 188] which is due to the size effect.

Ferromagnetic materials depending on their size can be composed of either single domain or multidomain structures. Basically, ferromagnetic particles with the diameter below a critical size known as single domain size (D_{SD}) are composed of single domain particles and above this critical size are composed of multidomain structures. By further decreasing the size of single domain structures to superparamagnetic size (D_{SPM}), ferromagnetic particles exhibit superparamagnetism (no hysteresis). The D_{SD} and D_{SPM} sizes change for different ferromagnetic materials [109, 117]. As explained before, the reported D_{SD} value for Fe_3O_4 nanoparticle is 128nm [109] and the D_{SPM} value is around 25-30nm [113] (these are the values for spherical particles).

The GA:20-30nm and GB:10-20nm Fe_3O_4 nanoparticles used in this study are both made of single domain structures since both are smaller than 128nm. However, GB:10-20nm Fe_3O_4 is

smaller than 25nm exhibiting superparamagnetic behaviour ($D_{GB} < D_{SPM} = 25\text{nm}$) which is also confirmed in our results. The GA:20-30nm Fe_3O_4 nanoparticles are single domain and exhibiting ferromagnetic behaviour since they are somewhat larger than 25nm ($D_{GA} > D_{SPM} = 25\text{nm}$). It is also verified in our results that GA:20-30nm Fe_3O_4 nanoparticles display ferromagnetic behaviour.

The single domain or multidomain structures of ferromagnetic materials can be identified from the M_r/M_s ratio known as the squareness ratio. Values of $M_r/M_s \sim 0.2-0.5$ are characteristics of single domain structures. Thus, it is further confirmed that both nanoparticles are single domain region [189]. The M_r/M_s value for GA:20-30nm Fe_3O_4 nanoparticles was 0.06 and for GB:10-20nm Fe_3O_4 nanoparticles was 0.0007 (Table 4-7).

The abovementioned results are an indication of the fact that the size of ferromagnetic particle affects both magnetic strength and hysteresis.

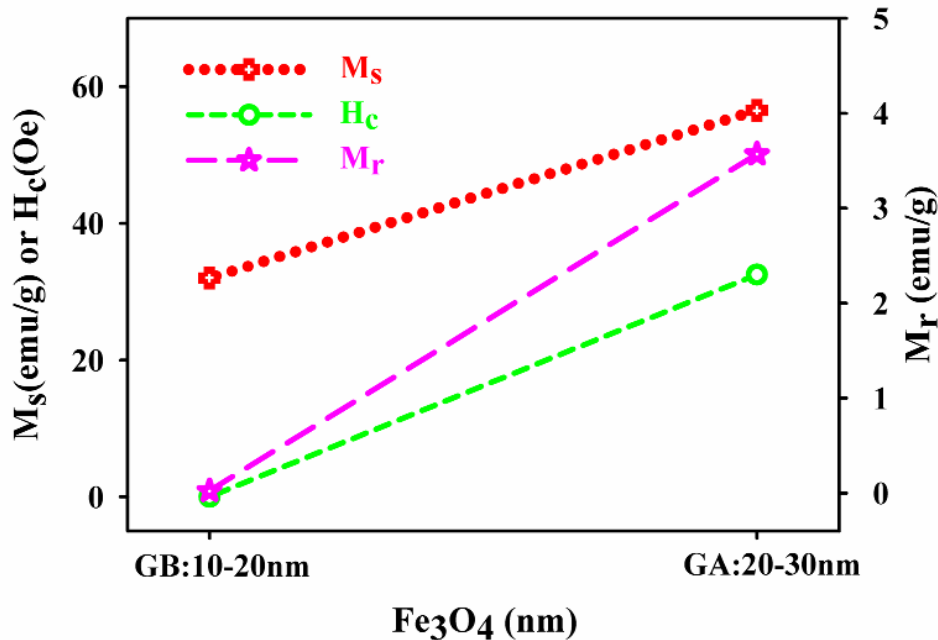


Figure 5-9 Magnetic properties of GA:20-30nm and GB:10-20nm Fe_3O_4 nanoparticles

5.2.2.2 Nanofibers

By embedding magnetic nanoparticles into the polymer matrix (PAN) and converting them into fibers, the structure can be scaled up from nanoscale into a micro- or macro-scale. However, the major challenge of the proposed method of fabricating the one-dimensional composite nanofibers is to demonstrate the capability of preserving magnetic behaviour of Fe₃O₄ nanoparticles and transfer it into the higher order structure. According to our results, it is confirmed that the magnetic properties of Fe₃O₄ nanoparticles are successfully transferred into the electrospun nanofibrous mat for all samples. Figure 5-10 reveals the change of M_s and H_c values of as-spun nanofibers for different amounts of Fe₃O₄ nanoparticles.

The M_s values of all as-spun composite nanofibers (either formed by GB:10-20nm Fe₃O₄ or GA:20-30nm Fe₃O₄ nanoparticles) follows the rule of mixture and is proportional to the amount of Fe₃O₄. This has also been previously reported [170]. The M_s values of 1.6, 2.8 and 5.8emu/g are obtained respectively for A3F, A5F and A10F samples corresponding to 3, 5 and 10% of that of GA:20-30nm Fe₃O₄ nanoparticle, i.e. 56.5emu/g. Similar trend was observed for as-spun nanofibers consisting of GB:10-20nm Fe₃O₄ nanoparticle. The M_s values of B3F, B5F and B10F samples are 0.9emu/g, 1.5emu/g and 3emu/g that are respectively 3%, 5% and 10% of that of GB:10-20nm Fe₃O₄ nanoparticle, i.e. 32emu/g. This means that one can tailor the magnetic properties such as the level of magnetization by adjusting the amount of Fe₃O₄ in the composite fiber.

In addition, the as-spun composite nanofibers have the same H_c as pure Fe₃O₄ nanoparticles (H_c=32.5Oe for those containing GA:20-30nm Fe₃O₄ nanoparticles and zero for those containing GB:10-20nm Fe₃O₄ nanoparticles).

Therefore, ferromagnetic properties of GA:20-30nm Fe_3O_4 nanoparticles and superparamagnetic behaviour of GB:10-20nm Fe_3O_4 nanoparticles are successfully translated from nano to macro scale. Zhang et al. [5] reported the synthesis of one-dimensional magnetic nanocomposites composed of Fe_3O_4 nanoparticles dispersed in a polymer matrix (PAN) in the form of nanofiber. However, the superparamagnetic properties of Fe_3O_4 nanoparticles were not transferred into the fibrous structure as large H_c value of 206.7Oe was obtained for as-electrospun 9wt.% $\text{Fe}_3\text{O}_4/\text{PAN}$ nanofibers. This could be due to the agglomeration of nanoparticles dispersed in the polymer matrix during the sample preparation procedure. It is proved that the sonication with low energy and longer time contributes to the uniform dispersion of nanoparticles in the polymer matrix which is exactly what we did in our experiment.

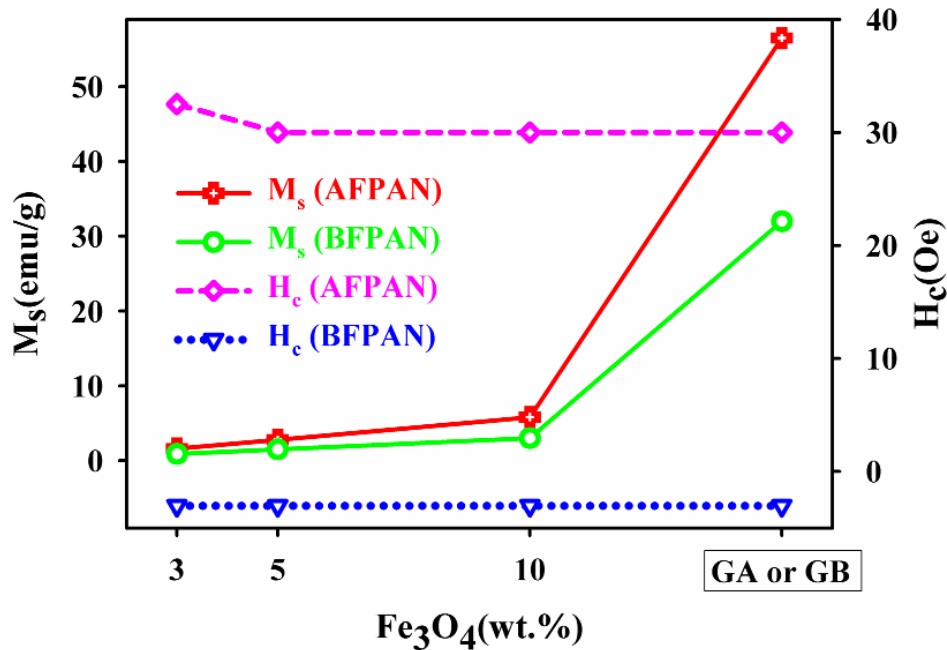


Figure 5-10 Comparison of M_s and H_c of as-spun nanofibers and nanoparticles containing GA:20-30nm and GB:10-20nm Fe_3O_4 nanoparticles. (BFPAN: as-spun nanofibers containing GB nanoparticles, AFPAN: as-spun nanofibers containing GA nanoparticles)

5.2.2.3 Carbonized nanofibers

The magnetic properties of nanoparticles and as-electrospun composite nanofibers were discussed in the previous sections. It is concluded that the properties of Fe₃O₄ nanoparticles are preserved after electrospinning. However, it is of interest to note that different magnetic properties are obtained for carbonized composite nanofibers as compared with their corresponding nanoparticles and as-electrospun composite nanofibers. In the following section, the effect of carbonization on the magnetic strength and hysteresis of composite nanofibers will be discussed.

5.2.2.4 Saturation magnetization (M_s)

The carbonized samples containing GB:10-20nm or GA:20-30nm Fe₃O₄ nanoparticles show larger M_s values as compared with their corresponding electrospun nanofibers. The M_s value is shown to increase with the carbonization temperature from 700°C to 900°C for samples containing GA:20-30nm Fe₃O₄ nanoparticles. Increasing the Fe₃O₄ content in the carbon matrix also confirmed to enhance the magnetic strength level.

Increasing the M_s due to the carbonization process and with carbonization temperature can be described as follow: First of all, the larger M_s of carbonized samples can be partly attributed to the loss of constituents of PAN known as carbon yielding which results in the rise in Fe₃O₄ proportion in the composite. According to our measurements, the PAN weight loss of composite carbon nanofibers is about 48wt.% and 60wt.% for samples carbonized at 700°C and 900°C, respectively. Considering PAN weight loss through the heat treatment process, the increase in total amount of the magnetic phases in the composite is expected. As a result, the larger M_s values are expected to be obtained for carbonized samples in comparison with as-

electrospun nanofibers. Inagaki et al. [180] confirmed that the M_s value is dependent on the amount of magnetic particles inside the composite. Therefore, one can conclude that due to the increasing the total content of magnetic compounds in the carbon nanofiber matrix, the M_s increases to larger values for carbonized samples. The only exception is referred to carbonized sample containing 3wt.% GA:20-30nm Fe_3O_4 nanoparticles (A3F700). The M_s value obtained for this sample, A3F700 (1.2emu/g) is lower than that of its as-spun counterpart, A3F (1.6emu/g).

Another possible explanation for the larger M_s values of carbonized samples is the formation of new magnetic phases during the pyrolysis process. According to the XRD results, the composite carbon nanofibers containing GA:20-30nm Fe_3O_4 nanoparticles contain some new magnetic phases such as Fe_3C and α -Fe (Figure 4-9). The formation of magnetic Fe phase was also reported to increase the M_s in Fe-Cu magnetic alloy [190]. The magnetic Fe nanoparticle was shown to have larger M_s compared to that of Fe_3O_4 nanoparticles [191, 192] and Fe_3C compounds [193]. However, the formation of these magnetic phases did not exist in A3F700 sample which shows the M_s value even lower than its corresponding electrospun nanofiber sample, A3F (Figure 4-9a). And finally, larger M_s values of carbonized samples might be due to the growth and coarsening of the particles after carbonization process (TEM picture shown in Figure 4-6). The average particles' size distributed in the composite for samples A5F700, A5F900, A10F700 and A10F900 are measured and listed in Table 4-2. It is observed that the average size of the particles increases from 20-30nm for starting Fe_3O_4 nanoparticles to 36 ± 13 , 44 ± 17 , 60 ± 22 and 66 ± 30 nm respectively for A5F700, A5F900, A10F700 and A10F900 samples. It is previously reported that M_s value directly correlates with the size of magnetic particles [116, 194]. In comparison, Inagaki et al. [180] reported that the M_s value only depends on the content

of magnetic phase but not the size or the shape of the particles. However, our results demonstrate that the M_s level might also be a function of particles size distributed in the carbon matrix. Similarly, the M_s increases for carbonized samples containing GB:10-20nm Fe_3O_4 nanoparticles after carbonization process. Carbon yielding due to pyrolysis of PAN nanofibers, magnetic phase formation (Fe_3C in this case as shown in Figure 4-11b) and possibly particles' growth due to high temperature (900°C) are the possible reasons for this important observation. Higher Fe_3O_4 loading means higher amount of magnetic phase introduced to the system which was also reported elsewhere [188]. The contributing effect of Fe_3O_4 content in the carbon fiber matrix was also shown in both composites containing various sizes of GA:20-30nm Fe_3O_4 and GB:10-20nm Fe_3O_4 nanoparticles (Figure 5-11).

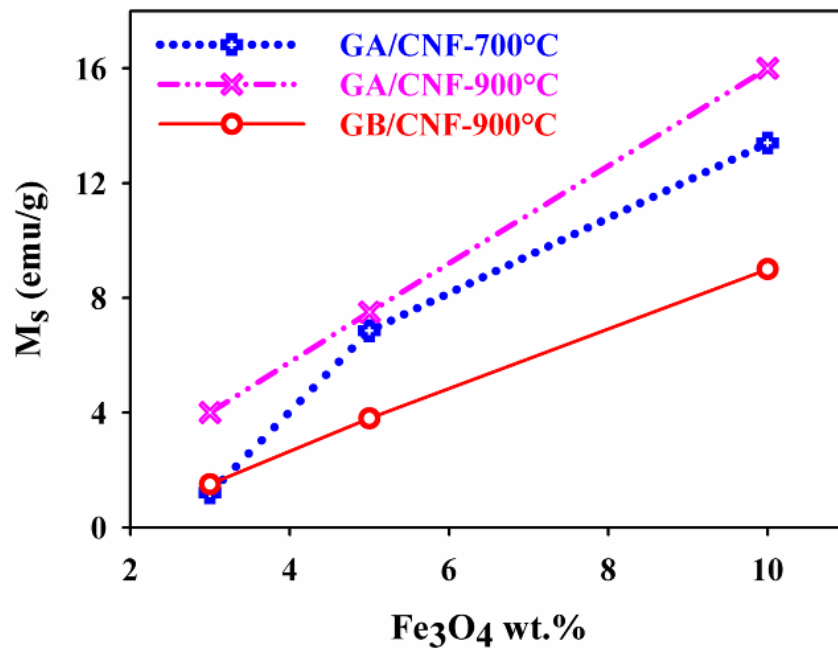


Figure 5-11 M_s as a function of Fe_3O_4 content, size and carbonization temperature. (GA/CNF: carbonized nanofibers containing GA:20-30nm Fe_3O_4 nanoparticles GB/CNF: carbonized nanofibers containing GB:10-20nm Fe_3O_4 nanoparticles).

5.2.2.5 Coercivity (H_c) and remanent magnetization (M_r)

An important observation from the magnetic properties of carbonized samples containing various sizes of Fe_3O_4 nanoparticles is the increase in the hysteresis. It is observed that both H_c and M_r values increase for the carbonized composites implying that hysteresis is enhanced by carbonization. The obtained hysteresis for carbonized samples in comparison with their non-carbonized counterparts might be due to the increase of the particles size [194] and increment of the interparticle interactions [116]. A comparison between the M_r and H_c values of composite carbon nanofibers containing GA:20-30nm and GB:10-20nm Fe_3O_4 nanoparticles is illustrated in Figure 5-12.

As discussed earlier in this section, the starting GA:20-30nm Fe_3O_4 nanoparticles are in single domain size. However, TEM pictures show that after carbonization the particles diffuse together and form larger crystals (see Figure 4-5, Figure 4-6 and Figure 4-7). As summarized in Table 4-2, the nanoparticles grow to larger sizes after carbonization however, they are still within the single domain range since the size does not exceed 128nm (D_{SD} size of Fe_3O_4). According to the Stoner-Wohlfarth theory, the magnetocrystalline anisotropy (E_A) of a single domain particle is defined as: $E_A = KV \sin^2 \theta$ in which K is the magnetocrystalline anisotropy constant, V is the volume of the nanoparticle and θ is the angle between the magnetization direction and the easy axis of magnetization of magnetic nanoparticle (easy axis: the direction that magnetic material can be easily magnetized). This anisotropy serves as energy barrier to prevent the change in the magnetization direction. In the single domain region, the larger the particle size is the higher the magnetocrystalline anisotropy (E_A) is. As the magnetic anisotropy of the nanoparticles increases, the magnetic field required for switching the magnetic moment direction becomes higher. As a result, the H_c increases with increasing the particle size [195] (as shown in Figure 2-14).

Since the particle size does not change for as-spun nanofibers and fairly uniform dispersion of nanoparticles are obtained, the H_c of as-spun composite nanofibers remains similar to that of initial Fe_3O_4 nanoparticles. While after carbonization particles grow to larger than 25-30nm size (D_{SPM} size for Fe_3O_4 nanoparticle). According to Table 4-2, the size of particles enlarges from 22 ± 7 for as-spun A5F sample to 36 ± 13 nm and 66 ± 30 nm respectively for A5F900 and A10F900 samples (in the range between superparamagnetic and single domain region as shown in Figure 2-14). Consequently, the H_c value is enhanced from 30Oe to 220Oe and 250Oe via carbonizing the abovementioned electrospun magnetic nanofibers. Thus, a transition in magnetic properties from very small hysteresis to very large hysteresis can be observed from GA:20-30nm Fe_3O_4 nanoparticles and as-spun nanofiber composites containing GA:20-30nm Fe_3O_4 nanoparticles to carbonized samples, respectively.

Likewise, the carbonized composite nanofibers fabricated with GB:10-20nm Fe_3O_4 also displayed large amount of hysteresis (M_r and H_c) as shown in Figure 5-12. Correspondingly, a transition from superparamagnetism for as-spun nanofibers containing GB:10-20nm Fe_3O_4 nanoparticles to ferromagnetism for their carbonized nanofibers is observed. However, hysteresis (both M_r and H_c) are still below the values obtained for sample containing GA:20-30nm Fe_3O_4 nanoparticles. However, the carbonized sample containing 10wt.% GB:10-20nm Fe_3O_4 nanoparticles (B10F900) shows larger H_c (400Oe) than the one fabricated with GA:20-30nm Fe_3O_4 nanoparticles. The reason can be explained probably as the higher agglomeration and larger particles obtained for B10F900 sample with the largest Fe_3O_4 concentration (10wt.%). In addition, increasing Fe_3O_4 content increases both H_c and M_r values and it is also reported previously by Fang et al. [188] that increasing Fe_3O_4 content in Fe_3O_4 -Polypyrrole (PPy) composite is proved to increase the H_c value. The M_r also follows the same trend as H_c .

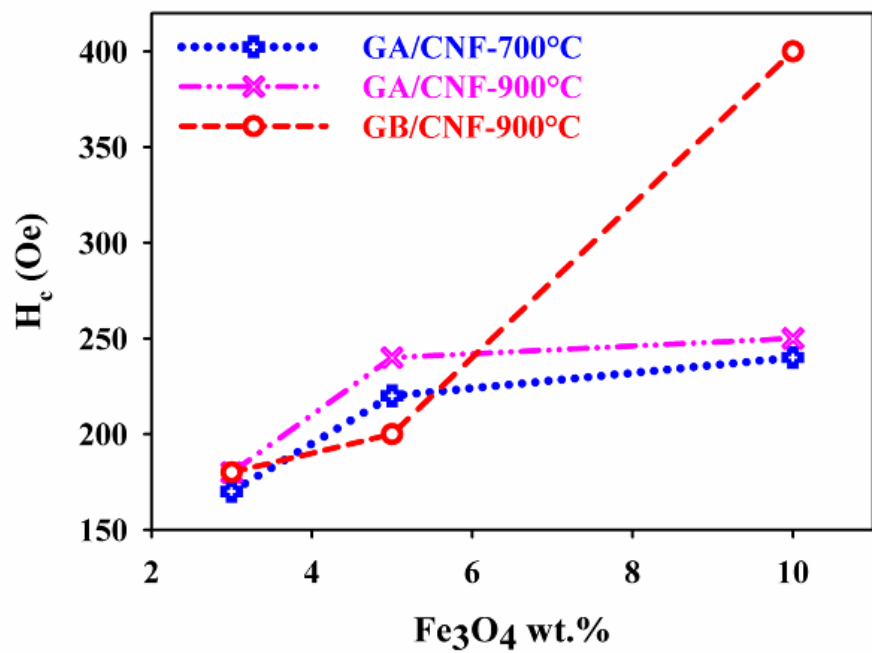
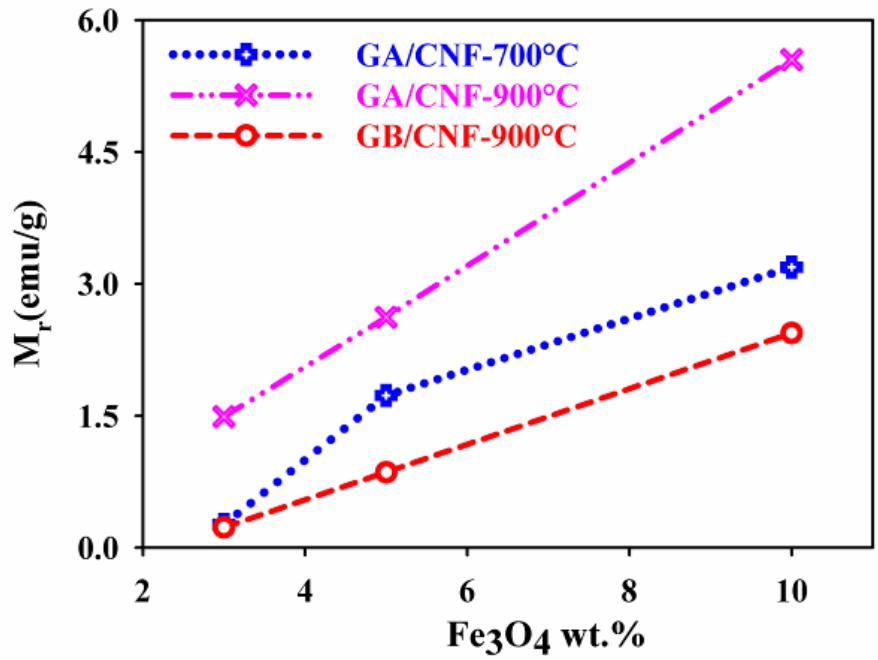


Figure 5-12 M_r and H_c as a function of both carbonization temperature and Fe_3O_4 wt.%. (GA/CNF: carbonized nanofibers containing GA:20-30nm Fe_3O_4 nanoparticles GB/CNF: carbonized nanofibers containing GB:10-20nm Fe_3O_4 nanoparticles)

5.3 Electromagnetic Interference Shielding Effectiveness

The electromagnetic interference shielding performance of electromagnetic Fe₃O₄/carbon nanofiber composite is reported for the first time. In this section, the effect of pyrolysis temperature, Fe₃O₄ content and size and also thickness of the pristine and composite carbon nanofiber mats are discussed. Finally a comparison between the electromagnetic interference shielding performance level of the fabricated electromagnetic Fe₃O₄/carbon nanofiber composite in this work and the results shown in other studies are demonstrated.

Generally, the electromagnetic interference shielding characteristic of any shielding material depends on its dielectric properties (permittivity), magnetic properties (permeability) as a function of frequency, electrical conductivity, thickness, structure and fabrication method and also working frequency [196, 197].

5.3.1 Fe₃O₄ effect on shielding

5.3.1.1 Total shielding effectiveness (SE_{total})

The total shielding efficiency (SE_{total}) of pristine carbon nanofiber and electromagnetic carbon nanofiber composites containing various amounts of GA:20-30nm Fe₃O₄ nanoparticles (3wt.% and 5wt.%) shown in Figure 4-30 reveals that composite carbon nanofibers are better shielding barriers in comparison with pristine carbon nanofiber. The SE_{total}, SE_R and SE_A at working frequency of 10.4GHz are demonstrated in Figure 5-13 as a function of Fe₃O₄ content (wt.%). The SE_{total} remarkably increases with the addition of Fe₃O₄ content (0 to 3wt.% and 5wt.%) in the carbon nanofiber matrix.

The EMI SE represents the reduction of electromagnetic interference in specific frequency range which is defined as the ratio of the incident power (P_i) to the transmitted power (P_t) and is generally expressed in decibel (dB) as equation (1) [161]:

$$SE_{total}(dB) = -10\log(P_t / P_i) \quad (1)$$

Higher SE_{total} value means that higher amounts of the radiation power can be absorbed or reflected rather than transmitted [127].

As-spun pure PAN nanofiber, 10PAN, is used as a reference and does not contribute to the shielding. Contrary to that the carbonized as-spun PAN nanofiber, 10PAN900 sample shows the improved SE_{total} of around 44dB (Figure 4-30 and Figure 5-13). During the pyrolysis process, the pure as-spun PAN nanofibers turns into electrically conductive carbon nanofiber [3]. The SE_{total} increases as DC electrical conductivity (σ_{dc}) of material increases based on the theory of EMI shielding [127, 198]. The EMI SE of carbon nanofiber mat improves with the addition of Fe_3O_4 loading (wt.%) into the carbon nanofiber matrix. According to our results, the SE_{total} increases from 44dB for 10PAN900 with 0wt.% Fe_3O_4 to 60dB and 67dB respectively for A3F900 and A5F900 with 3 and 5wt.% Fe_3O_4 (Figure 5-13) at working frequency of 10.4GHz. As previously explained in the four-point probe method, σ_{dc} increases with Fe_3O_4 loading from $2.6 \pm 0.9S/cm$ to $5.7 \pm 0.9S/cm$ and $7.1 \pm 0.7S/cm$ respectively for 10PAN900, A3F900 and A5F900 samples. Increasing the conductivity minimizes the microwave power transmitted by the shield and hence exhibit high shielding performance [136, 146, 147]. The SE_{total} of the Fe_3O_4 /carbon nanofiber composite is evidently higher than nickel/hexagonal ferrite (Co_2Z)/polymer (PVDF) composite prepared by Li et al. [84] by normalizing the results with thickness of the shield. Fe_3O_4 /carbon nanofiber composite was capable of achieving SE_{total} of

67dB/0.7mm=95.71dB/1mm for A5F900 sample while Li et al. [84] reported the highest SE_{total} of 67dB/2mm=33.5dB/1mm.

The shielding performance of any composite material strongly depends on the intrinsic properties of its fillers [9, 135]. Magnetic nanofillers such as Fe_3O_4 , $\gamma-Fe_2O_3$ [135, 137] and BaF [9, 141] are reported to improve the shielding effectiveness of polymer composites. The contributing effect of various nanofillers is attributed to the enhanced electrical conductivity, magnetic permeability, dielectric permittivity and also nanometer sizes of these fillers.

Ohlan et al. [9] studied the shielding performance of conducting polymer nanocomposites of polyphenyl amine with BaF nanoparticles (50-60nm) over the frequency range of 12-18GHz. They showed that the shielding efficiency improves due to the presence of BaF nanoparticles. Increasing the amount of BaF in the polymer matrix results in increasing both electrical conductivity σ ($\sigma = \omega \epsilon_0 \epsilon''$) and magnetic permeability (μ_r) which lead to the maximum shielding effectiveness of 31dB. The shielding effectiveness of pure PANI and $\gamma-Fe_2O_3-TiO_2$ -PANI polymer composite in the working frequency of 8-12GHz is studied by Singh et al. [135]. The SE_{total} of the $\gamma-Fe_2O_3-TiO_2$ -PANI polymer composite is proved to be larger than that of pure PANI. The presence of magnetic $\gamma-Fe_2O_3$ and TiO_2 nanoparticles are proved to enhance both magnetic permeability and dielectric loss which are previously reported as effective parameters to enhance the microwave absorption characteristics of a shield [196, 197]. In addition to the contributing effect of magnetic nanoparticles on magnetic permeability, single domain magnetic nanoparticles are proved to have large effective anisotropy which causes high hysteresis loss. Hence, it improves the microwave absorption. Furthermore, for the particles in the range of nanometer size, surface area, number of dangling bond atoms and unsaturated coordination on

the surface are all enhanced. These variations lead to the interface polarization and multiple scattering which is useful for the absorption of large number of microwaves [9, 123, 135, 199].

5.3.1.2 Shielding by reflection (SE_R) or absorption (SE_A)

Any shielding material attenuates the electromagnetic radiation via two main mechanisms consisting of reflection (direct reflection R, and multiple reflections B) and absorption (A). SE_M can be neglected if $SE_A > 15dB$ and hence the SE_{total} is represented as follow [133, 146]:

$$SE_{total}(dB) = SE_A + SE_R \quad (3)$$

The SE_A and SE_R are dependent on complex permittivity and permeability according to the equations (10) and (11) [161]:

$$SE_A(dB) = 20d\left(\frac{\mu_r \omega \sigma_{ac}}{2}\right)^{1/2} \text{Log}(e) \quad (10)$$

$$SE_R(dB) = 10\text{Log}\left(\frac{\sigma_{ac}}{16\mu_r \omega \epsilon_0}\right) \quad (11)$$

According to equations (10) and (11), the SE_R is a function of σ_{ac}/μ_r and SE_A varies proportionally with electrical conductivity and magnetic permeability as $\sigma_{ac}\mu_r$. Therefore, microwave absorption properties enhances with both electrical conductivity and magnetic permeability [9, 141, 200]. It is important to determine whether the shielding performance of material is dominated by reflection or absorption mechanism. One of the requirements for radar absorbing materials is efficient shielding via absorption since radar absorbing materials (RAMs) aim at reducing the reflectivity (or detectability) of a target through cancelling the reflections of radar signal incident to their surface [201]. Composites containing conductive fillers such as carbon fibers [156] and carbon nanotubes [152] or pure carbon materials [202] are known to

have major drawback for electromagnetic shielding application purpose. The dominant shielding mechanism reported for these materials is reflection which is attributed to their unbalanced dielectric permittivity and magnetic permeability [142, 144, 145, 200-202]. The lack of magnetic constituent is their key problem which can be achieved via adding magnetic components in order to be capable of enhancing the magnetic permeability [9, 123, 125, 202, 203] to enhance the absorption mechanism.

Overall comparison shows that absorption is the dominant shielding mechanism obtained for pristine and composite Fe₃O₄/carbon nanofibers. The SE_A increases with the addition of Fe₃O₄ loading from ~44.4dB to ~48.97dB and ~55.47dB respectively for 10PAN900, A3F900 and A5F900 samples. Fe₃O₄ is a well-known microwave absorber due to its resonance frequency [204, 205]. Ohlan et al. [141] ascribed the larger SE_A value (22.4dB) of PEDOT-BaF composite to the corresponding SE_A of 8dB of pure PEDOT polymer to the contributing effect of ferrite particles in the enhancement of magnetic losses. The higher SE_A value of MWCNT-poly(methyl methacrylate) composite (PMMA) is also attributed to the increasing magnetic permeability because of magnetic Fe nanoparticle used as a catalyst for MWCNT synthesis [198]. Singh et al. [135] also reported the higher SE_A value of 45dB for γ -Fe₂O₃-TiO₂-PANI nanocomposite for the shield of 2mm (in the P-band: 12.4-18GHz). However, it is still lower than the SE_A level of 45dB for A5F900 sample of 0.7mm thickness in the X-band).

Further, it is observed that even for pristine carbon nanofiber (10PAN900) SE_A is higher than SE_R (even without magnetic filler). Wang et al. [127] related the higher absorption of the ordered mesoporous carbon composites to its unique nanostructure of hexagonally ordered carbon nanowires which results in many times reflection and scattering of the entering radiation between the ordered nanowire arrays inside the shield and finally higher absorption of the

radiation than the reflection. With this, it might be concluded that specific nanofibrous structure of carbon nanofibers with higher aspect ratio and highly porous structure has some contributing effect in acquiring higher SE_A value than SE_R . However, it is still increasing with Fe_3O_4 loading.

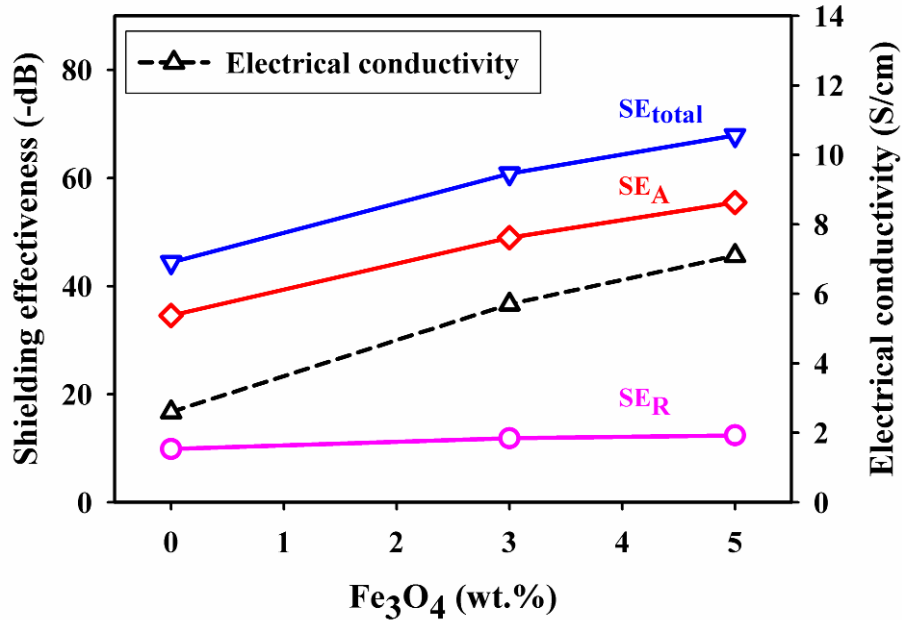


Figure 5-13 Average SE_{total} values of pristine carbon nanofiber (10PAN900) and 3wt.% and 5wt.% GA:20-30nm Fe_3O_4 nanoparticles in carbon nanofiber composites (respectively A3F900 and A5F900) with the thickness of 0.7mm and as a function of electrical conductivity of the composite nanofibers.

5.3.2 Effect of pyrolysis process

Table 5-3 lists the SE_{total} of 10PAN, 10PAN700 and 10PAN900 samples at working frequency of 10.4GHz. As summarized in Table 5-3 and Figure 4-33, the EMI SE enhances remarkably via carbonization at higher temperature, i.e. 900°C. The increment of SE_{total} via carbonization is ascribed to the contributing effect of induced electrical conductivity during the heat treatment. There is also a direct correlation between the electrical conductivity and EMI SE of a shield according to EMI shielding theory [127, 161, 198]. The electrical conductivity increases sharply

from 0.055S/cm to 2.6S/cm as a result of increasing the carbonization temperature from 700°C to 900°C (Table 5-3). This increase can be accredited to the increasing degree of graphitization at higher pyrolysis temperature [88, 101, 103]. Higher electrical conductivity results in better EMI shielding because of the reflection effect in which mobile charge carriers (electrons or holes) are required for interaction with the incident electromagnetic field [200].

Table 5-3 SE_{total} of pristine carbon nanofiber and composite carbon nanofibers at 10.4GHz

	$SE_{total}(-dB)$	$\sigma_{dc}(S/cm)$
10PAN	0.0007dB~0	Non-conductive
10PAN700	0.2dB	0.055S/cm
10PAN900	15dB	2.6S/cm

5.3.3 Effect of thickness on shielding

5.3.3.1 Total shielding effectiveness (SE_{total})

Shielding efficiency is dependent not only on the electrical conductivity and the content of magnetic nanofiller but also on the thickness of a shield. The SE_{total} of composite carbon nanofibers containing 5wt.% GA:20-30nm Fe_3O_4 nanoparticles (A5F900 sample) as a function of thickness of a shield improves the shielding performance (Figure 4-34). Increasing the material thickness from 0.1mm to 0.25mm, 0.45mm, 0.55mm and 0.7mm enhances the SE_{total} respectively from 23.6dB to 27.9dB, 45.07dB, 56.3dB and 67.9dB. The conductive network interacting with electromagnetic radiation increases with increasing the material thickness. Consequently, the electromagnetic shielding improves with material thickness [84, 144, 200]. Park et al. [196] have reported that SE_{total} of MWNT-added glass fabric/epoxy composite improves with increasing the thickness. The SE_{total} of 3%MWCNT/epoxy composite increases from 5dB to 15dB as thickness increases from 2mm to 10mm [196]. The SE_{total} is also reported

to increase monotonically with increasing thickness of carbon nanotube/ethylene vinyl acetate composites as studied by Das et al. [144].

5.3.3.2 Shielding by reflection (SE_R) or absorption (SE_A)

According to equations (10) and (11), the SE_A is a direct function of thickness of a shield [144, 200] while SE_R barely varies with thickness [84, 146, 147]. The SE_{total} , SE_R and SE_A dependence on the thickness of sample A5F900 is represented in Figure 5-14. The SE_A exhibits a sharp increase from 13.22dB to 18.82dB, 36.56dB, 43.43dB and 55.47dB as thickness increases from 0.25mm to 0.45mm, 0.55mm, 0.7mm and 0.8mm (Table 4-13). Li et al. [84] studied the effect of thickness on the electromagnetic shielding performance of Nickel-hexagonal ferrite/PVDF composites. They found that SE_A increased from 21dB to 54dB with increasing the sample thickness from 1.0mm to 2.0mm. On the other hand, the SE_R remains almost unchanged around 11dB. This is also confirmed in our results (Figure 5-14).

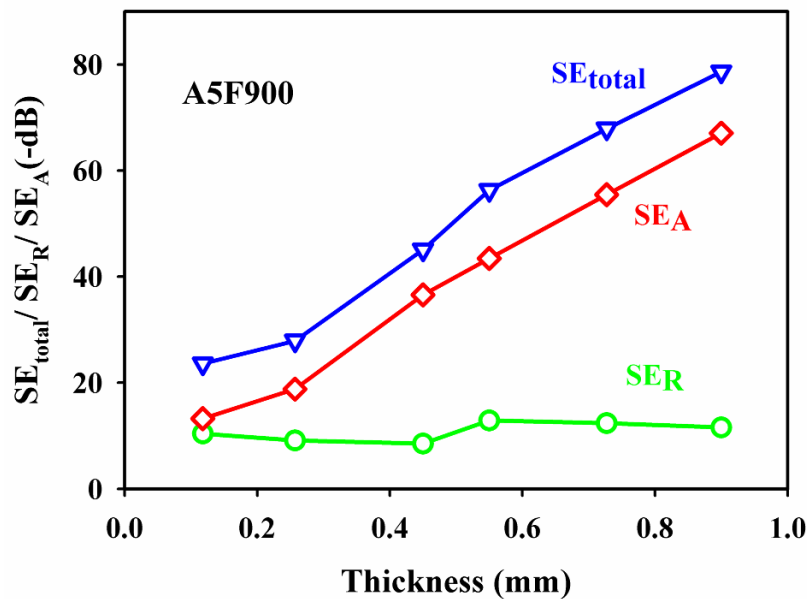


Figure 5-14 SE_{total} , SE_R and SE_A of A5F900 samples with various thicknesses (0.1mm-0.9mm).

5.3.4 The effect of the size of Fe₃O₄ nanoparticles

The size effect of Fe₃O₄ nanoparticles on the SE_{total} of electromagnetic carbon nanofiber composite containing 5wt.% Fe₃O₄ is displayed in Figure 4-35. Overall comparison confirms that carbon nanofiber composites show higher level of SE_{total} in comparison with pristine carbon nanofiber. At the same time, composites containing larger Fe₃O₄ nanoparticles (GA:20-30nm) illustrate higher shielding efficiency than those containing smaller nanoparticles (GB:10-20nm). The SE_{total} slightly increases from 44.40dB to 46.60dB and then increases to a higher value, i.e. 67.90dB. Besides, Table 5-4 compares the SE_{total}, SE_A and SE_R values as well as fiber diameter, sample thickness, saturation magnetization (M_s) and electrical conductivity (σ) of the abovementioned samples at working frequency of 10.4GHz.

Composites fabricated with GB:10-20nm Fe₃O₄ nanoparticles have larger fiber diameter and lower electrical conductivity (597±81nm and 2.92±0.6S/cm) than those containing larger GA:20-30nm Fe₃O₄ nanoparticles (315±37nm and 7.10±0.70S/cm). Therefore, GA:20-30nm Fe₃O₄/carbon nanofiber composites hold larger aspect ratio and higher electrical conductivity which are introduced as contributing factors to achieve high performance shielding effectiveness [146, 147]. Besides, larger M_s value was obtained for samples fabricated with larger nanoparticles (7.5emu/g) than the one made with smaller nanoparticles, i. e. 3.8emu/g. Further, higher SE_A is obtained for samples containing larger GA:20-30nm Fe₃O₄ nanoparticles (A5F900) (SE_A=62.61dB and SE_R=11.99dB) in comparison with the carbon nanofiber composites containing smaller GB:10-20nm Fe₃O₄ nanoparticles (B5F900) (SE_A=43.22dB and SE_R=8.92dB).

Table 5-4 SE_{total} , SE_A and SE_R of composite carbon nanofibers containing various Fe_3O_4 content (wt.%) as a function of fiber diameter, electrical conductivity, particles' size and thickness (at 10.4GHz)

property	10PAN900	B5F900	A5F900
Fiber diameter (nm)	272±33	597±81	315±37
Electrical conductivity (S/cm)	2.60±0.90	2.92±0.60	7.10±0.70
Nanofiller size (nm)	NA	GB:10-20	GA:20-30
Thickness (mm)	~0.70	~0.70	~0.70
M_s (emu/g)	0	~3.80	~7.50
SE_{total} (dB)	44.40	46.60	67.90
SE_A (dB)	34.55	36.03	55.47
SE_R (dB)	9.88	10.59	12.38

5.3.5 EMI SE of PDMS-coated pristine carbon nanofiber

PDMS was used as an elastomeric component to protect the carbon nanofibers and facilitate handling and cutting into various gasket patterns. Therefore, it is worthwhile to observe whether the addition of the PDMS coating would interfere with the shielding performance of the composite nanofiber samples. The EMI SE of pristine carbon nanofiber with and without PDMS coating was studied. Figure 5-15a illustrates the variation of SE_{total} of pristine carbon nanofiber (CNF) and PDMS-coated CNF as a function of frequency (8.2-12.4GHz). Figure 5-15b also demonstrates the high flexibility of PDMS-coated CNF samples. The SE_{total} of pristine carbon nanofiber with and without PDMS coating are virtually the same as shown in Figure 5-15a. We can conclude that the PDMS coating helps toughen the CNF samples without interfering with the shielding performance of the samples.

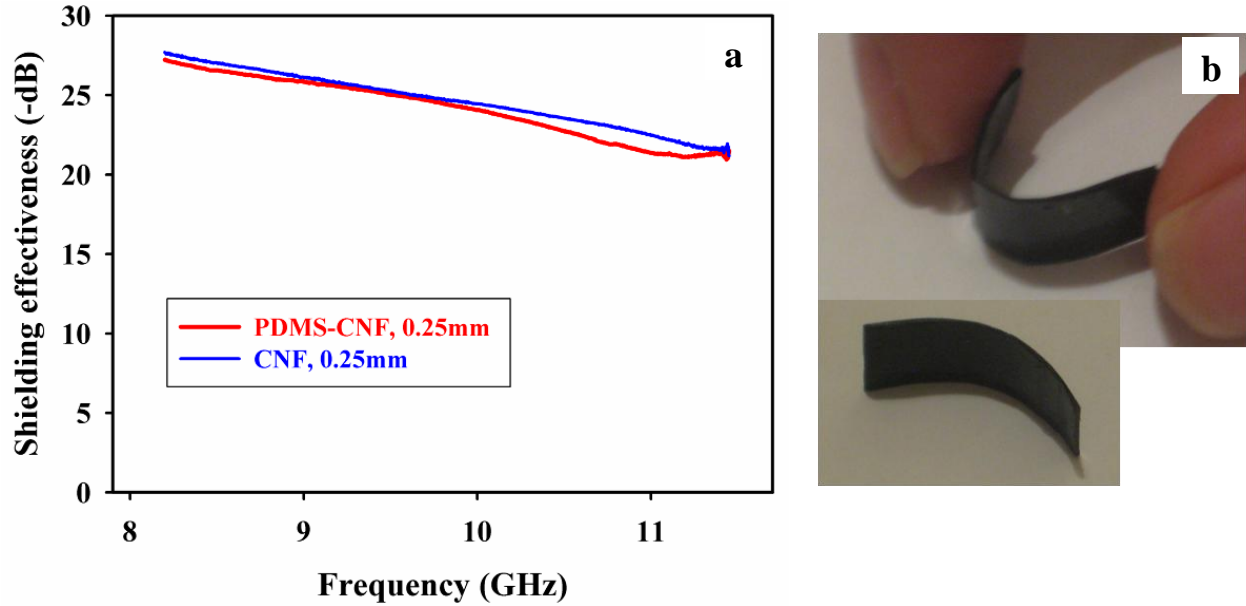


Figure 5-15 (a) SE_{total} as a function of frequency (8.2-11.5GHz) for pristine carbon nanofiber (10PAN900) and PDMS-coated carbon nanofiber (10PAN900), (b) Flexibility of PDMS-coated carbon nanofiber. (The thickness of all samples is ~ 0.25 mm).

5.3.6 Shielding performance at low frequencies

The shielding performance of composite nanofiber containing 3wt.% GA:20-30nm Fe_3O_4 , A3F900 sample, was measured at Laird Technologies Inc in the frequency range of 30kHz to 1GHz as shown in Figure 5-16. The SE_{total} is shown to be almost constant, at 45-46dB from 30kHz to 2MHz. Then, it rises from 60dB to 90dB in the frequency range of 2MHz to 1GHz.

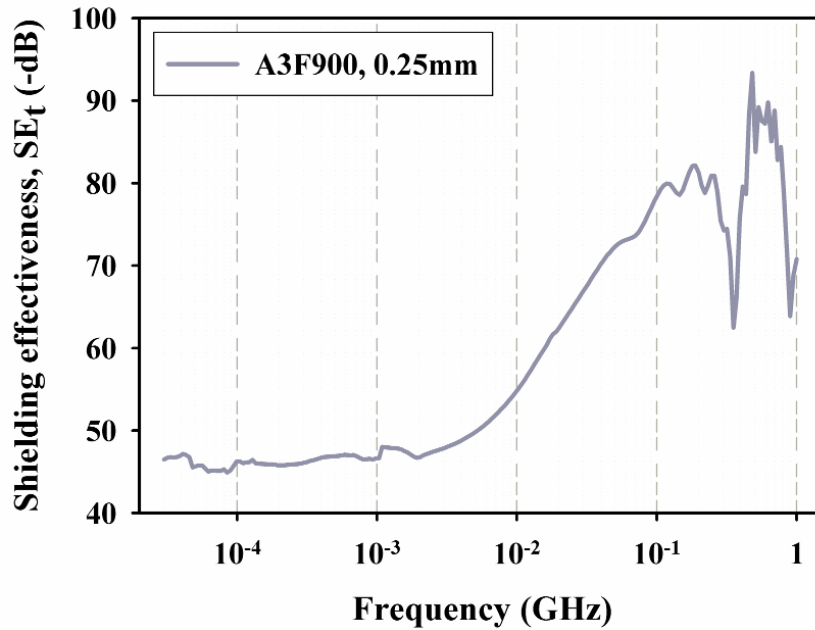


Figure 5-16 SE_{total} of A3F900 sample with the thickness of 0.25mm.

5.3.7 Comparison with published results

Figure 5-17 compares the shielding effectiveness normalized by thickness of 5wt.% GA:20-30nm Fe₃O₄/carbon nanofiber composite carbonized at 900°C with electrically conducting composites such as: SWCNT/epoxy [157]; SWCNT/polyurethane [132] ordered mesoporous carbon/fused silica [127]; electromagnetic composites such as: Ni/Co₂Z/polyvinylidene fluoride [84]; and short CF/polychloroprene containing BaF [146]. These results reveal that higher level of SE_{total}/thickness for electromagnetic composites than for electrically conducting composites. Among electrically conducting composites, the ordered mesoporous carbon/fused silica composites [127] show higher shielding effectiveness. This can be attributed to its unique nanostructure of hexagonally ordered carbon nanowire arrays resulting in many times scattering of electromagnetic radiation thus higher absorption. Among electromagnetic composites, Co₂Z/polyvinylidene fluoride [84] and short CF/polychloroprene

containing BaF [146], higher shielding effectiveness is due to the random alignment of short CFs as well as the increase in complex permeability and permittivity parameters.

In comparison with the results observed in the literature, very encouraging results are obtained for the UBC Fe₃O₄/carbon nanofiber composites. The combination of large available surface area, high magnetic permeability, and moderate electrical conductivity may be the contributing factors to the superior shielding efficiency of Fe₃O₄/carbon nanofiber composite.

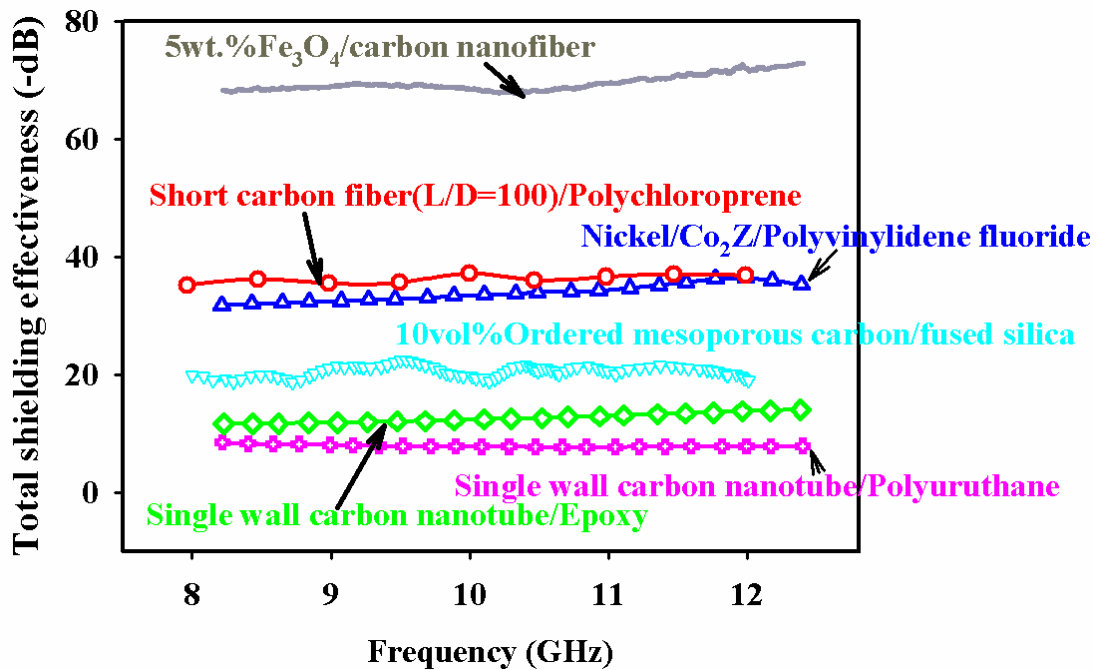


Figure 5-17 A comparison of the EMI SE of 5wt.% GA:20-30nm Fe₃O₄/carbon nanofiber composite with electrically conducting and electromagnetic composites reported in literature.

Chapter 6. Conclusions

PAN based carbon nanofibers containing two different sizes of Fe_3O_4 nanoparticles are developed in this study. The resulted composite structures reveal multifunctional electromagnetic properties. Uniformly distributed nanofibrous mats with even distribution of Fe_3O_4 nanoparticles were obtained using electrospinning process.

Randomly distributed uniform nanofibrous structures were obtained for all pure PAN nanofibers and Fe_3O_4 /PAN samples. The average fiber diameter increases from $390\pm 40\text{nm}$ to $538\pm 60\text{nm}$ for 10PAN and A10F10PAN samples with addition of Fe_3O_4 nanoparticle from 0 to 10wt.%. During the pyrolysis process the average fiber diameter decreases as a result of PAN weight loss from $390\pm 40\text{nm}$ to 290 ± 48 and $272\pm 33\text{nm}$ respectively for 10PAN, 10PAN700 and 10PAN900 samples.

Electrical conductivity is shown to be enhanced with the addition of Fe_3O_4 wt.% in the carbon nanofiber matrix. Electrical conductivity increases from $2.6\pm 0.9\text{S/cm}$ for 10PAN900 to $9.2\pm 0.5\text{S/cm}$ for A10F900 sample with increasing Fe_3O_4 content in the carbon nanofiber matrix respectively from 0 to 10wt.%. The presence of metal oxide (Fe_3O_4 nanoparticles) as well as the formation of Fe_3C and $\alpha\text{-Fe}$ during the pyrolysis process in the carbon matrix enhances the formation of higher order graphitic structure thereby enhancing the mobility of electrons and increasing the electrical conductivity.

Besides, highly ordered graphitic structure (larger graphite crystallites as well as shorter graphite planes) are formed due to the increasing pyrolysis temperature which results in higher electrical conductivity. The electrical conductivity increases from $0.05\pm 0.004\text{S/cm}$ to $2.6\pm 0.9\text{S/cm}$ for pristine carbon nanofibers respectively carbonized at 700°C and 900°C .

The graphitization of carbon fiber composites containing GB:10-20nm Fe₃O₄ nanoparticles was smaller than the ones fabricated with GA:20-30nm Fe₃O₄ nanoparticles. As a result, the electrical conductivity only varies in the range of 1.9-2.9S/cm containing different amounts of Fe₃O₄ wt.%.

GA:20-30nm and GB:10-20nm Fe₃O₄ nanoparticles employed in this work demonstrate ferromagnetic and superparamagnetic properties. The magnetic properties of the particles depend on their size. The larger M_s (56emu/g) as well as H_c (30Oe) are acquired for GA:20-30nm as compared to M_s of 32emu/g and zero H_c for GB:10-20nm Fe₃O₄ particles.

The electrospinning process successfully transferred the magnetic properties of Fe₃O₄ nanoparticles into higher order structures. The feasibility of transferring the magnetic properties of Fe₃O₄ nanoparticle into the higher order fibrous structure is also demonstrated for non-carbonized samples. The M_s values of all non-carbonized as-spun nanofibers containing various contents of Fe₃O₄ nanoparticles are proportional to the content of Fe₃O₄ particles. The same H_c value similar to Fe₃O₄ nanoparticles is obtained for all non-carbonized nanofibers.

However, magnetic hysteresis was observed after heat treatment of as-spun nanofibers due to the particles growth. Larger particles (25nm) were obtained after the heat treatment. The H_c raises from 30Oe for as-spun A10F to 240Oe and 250Oe respectively for A10F700 and A10F900. Furthermore, the level of magnetic strength (M_s) increases from 5.8emu/g for as-spun A10F to 13.40emu/g and 16emu/g respectively for A10F700 and A10F900. The increment of M_s values in carbonized samples was attributed to the formation of larger magnetic particles, PAN weight loss during the carbonization process and the formation of new magnetic phases such as α-Fe and Fe₃C. The magnetic properties of composite fiber assemblies can be tailored by

controlling the size of magnetic particles. This can be achieved through heat treatment of composite nanofibers consisting proper sizes of nanoparticles.

The fragile and brittle Fe₃O₄/carbon nanofiber composites were addressed using PDMS as elastomer coating which makes it as an appropriate flexible composite with similar electromagnetic behaviour. The unique combination of electromagnetic properties of the flexible composite nanofiber assemblies is anticipated to stimulate the development of a new family of electronic devices such as electromagnetic interference shields, sensors and actuators. The Fe₃O₄/carbon nanofiber composite illustrates a promising electromagnetic shielding effectiveness in the X-band frequency region (8.2-12.4GHz). The EMI SE of as high as 70dB was obtained for the A5F900 with 0.7mm thickness.

There are a number of suggestions with regard to the multifunctionality and applications of the prepared composite carbon nanofiber:

1. Fe₃O₄ nanoparticles can be synthesized in-situ in the carbon nanofiber matrix. The in-situ formation of Fe₃O₄ nanoparticles has been studied before. However, more in depth microstructural features, chemical composition, electromagnetic behaviour as well as EMI SE are expected to be investigated.
2. Mechanical properties of pristine and composite carbon nanofibers need to be studied depending on the application. For example, for composite nanofibers used as gasket, more flexible structure with elastomeric behaviour is needed. Therefore, the response of the PDMS-coated samples to the compression loads requires more studies.
3. The addition of functional nanofillers such as carbon nanotube to the Fe₃O₄/carbon nanofiber composites can be considered to enhance the electrical conductivity and possibly the mechanical strength of the carbon nanofibers which are suitable for acquiring better EMI performance.

4. Magnetic nanofibers containing Fe_3O_4 in appropriate matrix can be employed as actuating magnetic membrane. One of the applications of these magnetic membranes is in drug delivery systems that can also be further explored as a future work of this study.

References

1. X.F. Zhang, Q.W. Li, Y. Tu, Y.A. Li, J.Y. Coulter, L.X. Zheng, Y.H. Zhao, Q.X. Jia, D.E. Peterson, and Y.T. Zhu, *Strong carbon-nanotube fibers spun from long carbon-nanotube arrays*. *Small*, 2007. 3(2): p. 244-248.
2. N.A. Frey, S. Peng, K. Cheng, and S.H. Sun, *Magnetic nanoparticles: synthesis, functionalization, and applications in bioimaging and magnetic energy storage*. *Chemical Society Reviews*, 2009. 38(9): p. 2532-2542.
3. K. Lafdi and M.A. Wright, *Handbook of Composites.*, ed. E.b.S.T. Peters. 1998, London Chapman & Hall.
4. D. Li and Y.N. Xia, *Electrospinning of nanofibers: Reinventing the wheel?* *Advanced Materials*, 2004. 16(14): p. 1151-1170.
5. D. Zhang, A.B. Karki, D. Rutman, D.R. Young, A. Wang, D. Cocke, T.H. Ho, and Z.H. Guo, *Electrospun polyacrylonitrile nanocomposite fibers reinforced with Fe_3O_4 nanoparticles: Fabrication and property analysis*. *Polymer*, 2009. 50(17): p. 4189-4198.
6. S. Kedem, J. Schmidt, Y. Paz, and Y. Cohen, *Composite polymer nanofibers with carbon nanotubes and titanium dioxide particles*. *Langmuir*, 2005. 21(12): p. 5600-5604.
7. S.T. Tan, J.H. Wendorff, C. Pietzonka, Z.H. Jia, and G.Q. Wang, *Biocompatible and biodegradable polymer nanofibers displaying superparamagnetic properties*. *Chemphyschem*, 2005. 6(8): p. 1461-1465.
8. S.W. Choi, S.M. Jo, W.S. Lee, and Y.R. Kim, *An electrospun poly(vinylidene fluoride) nanofibrous membrane and its battery applications*. *Advanced Materials*, 2003. 15(23): p. 2027-2032.
9. A. Ohlan, K. Singh, A. Chandra, and S.K. Dhawan, *Microwave absorption properties of conducting polymer composite with barium ferrite nanoparticles in 12.4–18 GHz*. *Applied Physics Letters*, 2008. 93: p. 053114.
10. K. Singh, A. Ohlan, P. Saini, and S.K. Dhawan, *Poly (3,4-ethylenedioxythiophene) γ - Fe_2O_3 polymer composite—super paramagnetic behavior and variable range hopping 1D conduction mechanism—synthesis and characterization*. *Polym. Adv. Technol.* , 2008. 19: p. 229-236.
11. J.L. Wilson, P. Poddar, N.A. Frey, H. Srikanth, K. Mohomed, J.P. Harmon, S. Kotha, and J. Wachsmuth, *Synthesis and magnetic properties of polymer nanocomposites with embedded iron nanoparticles*. *Journal of Applied Physics*, 2004. 95(3): p. 1439-1443.
12. R.A. Silva, M.J.L. Santos, A.W. Rinaldi, A.J.G. Zarbin, M.M. Oliveira, I.A. Santos, L.F. Cotica, A.A. Coellho, A.F. Rubira, and E.M. Giroto, *Low coercive field and conducting nanocomposite formed by Fe_3O_4 and poly(thiophene)*. *Journal of Solid State Chemistry*, 2007. 180(12): p. 3545-3550.
13. L. Wang, Y. Yu, P.C. Chen, D.W. Zhang, and C.H. Chen, *Electrospinning synthesis of C/ Fe_3O_4 composite nanofibers and their application for high performance lithium-ion batteries*. *Journal of Power Sources*, 2008. 183(2): p. 717-723.
14. N.E. Kazantseva, J. VilWakova, V. Kresalek, P. Saha, I. Sapurina, and J. Stejskal, *Magnetic behaviour of composites containing polyaniline-coated manganese–zinc ferrite*. *Journal of Magnetism and Magnetic Materials* 2004. 269: p. 30-37.

15. P. Gomez-Romero, *Hybrid organic-inorganic materials - In search of synergic activity*. *Advanced Materials*, 2001. 13(3): p. 163-174.
16. H. Zheng, Y. Yang, F.S. Wen, H.B. Yi, D. Zhou, and F.S. Li, *Microwave Magnetic Permeability of Fe₃O₄ Nanoparticles*. *Chinese Physics Letters*, 2009. 26(1).
17. A. Petri-Fink, M. Chastellain, L. Juillerat-Jeanneret, A. Ferrari, and H. Hofmann, *Development of functionalized superparamagnetic iron oxide nanoparticles for interaction with human cancer cells*. *Biomaterials*, 2005. 26(15): p. 2685-2694.
18. C.M. Yang, H.Y. Li, D.B. Xiong, and Z.Y. Cao, *Hollow polyaniline/Fe₃O₄ microsphere composites: Preparation, characterization, and applications in microwave absorption*. *Reactive & Functional Polymers*, 2009. 69(2): p. 137-144.
19. H. Zhang, X. Zhong, J.J. Xu, and H.Y. Chen, *Fe₃O₄/Polypyrrole/Au Nanocomposites with Core/Shell/Shell Structure: Synthesis, Characterization, and Their Electrochemical Properties*. *Langmuir*, 2008. 24(23): p. 13748-13752.
20. J.E. Panels, J. Lee, K.Y. Park, S.Y. Kang, M. Marquez, U. Wiesner, and Y.L. Joo, *Synthesis and characterization of magnetically active carbon nanofiber/iron oxide composites with hierarchical pore structures*. *Nanotechnology*, 2008. 19(45).
21. S.K. Nataraj, B.H. Kim, M. dela Cruz, J. Ferraris, T.M. Aminabhavi, and K.S. Yang, *Free standing thin webs of porous carbon nanofibers of polyacrylonitrile containing iron-oxide by electrospinning*. *Materials Letters*, 2009. 63(2): p. 218-220.
22. B. Wang, Y. Sun, and H.P. Wang, *Preparation and Properties of Electrospun PAN/Fe₃O₄ Magnetic Nanofibers*. *Journal of Applied Polymer Science*, 2010. 115(3): p. 1781-1786.
23. <http://www.everythingweather.com/weather-radar/bands.shtml>.
24. Z.M. Huang, Y.Z. Zhang, M. Kotaki, and S. Ramakrishna, *A review on polymer nanofibers by electrospinning and their applications in nanocomposites*. *Composites Science and Technology*, 2003. 63(15): p. 2223-2253.
25. D.H. Reneker, A.L. Yarin, H. Fong, and S. Koombhongse, *Bending instability of electrically charged liquid jets of polymer solutions in electrospinning*. *Journal of Applied Physics*, 2000. 87(9): p. 4531-4547.
26. A. Formhals. 1934: US.
27. A. Formhals. 1939: US
28. A. Formhals. 1940: US
29. A. Formhals. 1943: US.
30. A. Formhals. 1944: US
31. P.K. Baumgart, *Electrostatic spinning of Acrylic Microfibers*. *Journal of Colloid and Interface Science*, 1971. 36(1): p. 71-79.
32. D.H. Reneker and I. Chun, *Nanometre diameter fibres of polymer, produced by electrospinning*. *Nanotechnology*, 1996. 7(3): p. 216-223.
33. Y.M. Shin, M.M. Hohman, M.P. Brenner, and G.C. Rutledge, *Electrospinning: A whipping fluid jet generates submicron polymer fibers* *Applied Physics Letters*, 2001. 78(8).
34. X.H. Zong, K. Kim, D.F. Fang, S.F. Ran, B.S. Hsiao, and B. Chu, *Structure and process relationship of electrospun bioabsorbable nanofiber membranes*. *Polymer*, 2002. 43(16): p. 4403-4412.

35. S. Ramakrishna, K. Fujihara, W.-E. Teo, and Z. Ma, *An Introduction to Electrospinning and Nanofibers*. 2005: World Scientific Publishing Co. Pte. Ltd.
36. S. Koombhongse, W.X. Liu, and D.H. Reneker, *Flat polymer ribbons and other shapes by electrospinning*. *Journal of Polymer Science Part B-Polymer Physics*, 2001. 39(21): p. 2598-2606.
37. J.M. Deitzel, J. Kleinmeyer, D. Harris, and N.C.B. Tan, *The effect of processing variables on the morphology of electrospun nanofibers and textiles*. *Polymer*, 2001. 42(1): p. 261-272.
38. J. Doshi and D.H. Reneker, *Electrospinning Process and Applications of Electrospun Fibers*. *Journal of Electrostatics*, 1995. 35(2-3): p. 151-160.
39. D.S. Gomes, A.N.R. da Silva, N.I. Morimoto, L.T.F. Mendes, R. Furlan, and I. Ramos, *Characterization of an electrospinning process using different PAN/DMF concentrations*. *Polimeros-Ciencia E Tecnologia*, 2007. 17(3): p. 206-211.
40. W.X. Zhang, Y.Z. Wang, and C.F. Sun, *Characterization on oxidative stabilization of polyacrylonitrile nanofibers prepared by electrospinning*. *Journal of Polymer Research*, 2007. 14: p. 467-474.
41. H.Q. Liu and Y.L. Hsieh, *Ultrafine fibrous cellulose membranes from electrospinning of cellulose acetate*. *Journal of Polymer Science Part B-Polymer Physics*, 2002. 40(18): p. 2119-2129.
42. Q.P. Pham, U. Sharma, and A.G. Mikos, *Electrospinning of polymeric nanofibers for tissue engineering applications: A review*. *Tissue Engineering*, 2006. 12(5): p. 1197-1211.
43. Y. Liu, J.H. He, J.Y. Yu, and H.M. Zeng, *Controlling numbers and sizes of beads in electrospun nanofibers*. *Polymer International*, 2008. 57(4): p. 632-636.
44. X.H. Qin, E.L. Yang, N. Li, and S.Y. Wang, *Effect of different salts on electrospinning of polyacrylonitrile (PAN) polymer solution*. *Journal of Applied Polymer Science*, 2007. 103(6): p. 3865-3870.
45. X.H. Qin, Y.Q. Wan, J.H. He, J. Zhang, J.Y. Yu, and S.Y. Wang, *Effect of LiCl on electrospinning of PAN polymer solution: theoretical analysis and experimental verification*. *Polymer*, 2004. 45(18): p. 6409-6413.
46. X.H. Qin, S.Y. Wang, T. Sandra, and D. Lukas, *Effect of LiCl on the stability length of electrospinning jet by PAN polymer solution*. *Materials Letters*, 2005. 59(24-25): p. 3102-3105.
47. L. Wannatong, A. Sirivat, and P. Supaphol, *Effects of solvents on electrospun polymeric fibers: preliminary study on polystyrene*. *Polymer International*, 2004. 53(11): p. 1851-1859.
48. M.M. Demir, I. Yilgor, E. Yilgor, and B. Erman, *Electrospinning of polyurethane fibers*. *Polymer*, 2002. 43(11): p. 3303-3309.
49. E.S. Medeiros, L.H.C. Mattoso, R.D. Offeman, D.F. Wood, and W.J. Orts, *Effect of relative humidity on the morphology of electrospun polymer fibers*. *Canadian Journal of Chemistry-Revue Canadienne De Chimie*, 2008. 86(6): p. 590-599.
50. C.J. Buchko, L.C. Chen, Y. Shen, and D.C. Martin, *Processing and microstructural characterization of porous biocompatible protein polymer thin films*. *Polymer*, 1999. 40(26): p. 7397-7407.

51. C.J. Buchko, K.M. Kozloff, and D.C. Martin, *Surface characterization of porous, biocompatible protein polymer thin films*. *Biomaterials*, 2001. 22(11): p. 1289-1300.
52. A. Greiner and J.H. Wendorff, *Functional Self-Assembled Nanofibers by Electrospinning*. *Self-Assembled Nanomaterials I: Nanofibers*, 2008. 219: p. 107-171.
53. S. Tan, X. Huang, and B. Wu, *Some fascinating phenomena in electrospinning processes and applications of electrospun nanofibers*. *Polymer International*, 2007. 56(11): p. 1330-1339.
54. E.D. Boland, B.D. Coleman, C.P. Barnes, D.G. Simpson, G.E. Wnek, and G.L. Bowlin, *Electrospinning polydioxanone for biomedical applications*. *Acta Biomaterialia*, 2005. 1(1): p. 115-123.
55. D.S. Katti, K.W. Robinson, F.K. Ko, and C.T. Laurencin, *Bioresorbable nanofiber-based systems for wound healing and drug delivery: Optimization of fabrication parameters*. *Journal of Biomedical Materials Research Part B-Applied Biomaterials*, 2004. 70B(2): p. 286-296.
56. P.X. Ma and R.Y. Zhang, *Synthetic nano-scale fibrous extracellular matrix*. *Journal of Biomedical Materials Research*, 1999. 46(1): p. 60-72.
57. W.J. Li, C.T. Laurencin, E.J. Caterson, R.S. Tuan, and F.K. Ko, *Electrospun nanofibrous structure: A novel scaffold for tissue engineering*. *Journal of Biomedical Materials Research*, 2002. 60(4): p. 613-621.
58. S.R. Bhattarai, N. Bhattarai, H.K. Yi, P.H. Hwang, D.I. Cha, and H.Y. Kim, *Novel biodegradable electrospun membrane: scaffold for tissue engineering*. *Biomaterials*, 2004. 25(13): p. 2595-2602.
59. R. Vasita and D.S. Katti, *Nanofibers and their applications in tissue engineering*. *International Journal of Nanomedicine*, 2006. 1(1): p. 15-30.
60. G.L. Bowlin, *Electrospinning Used To Create Small Blood Vessels*. 2003.
61. W.G. Cui, Y. Zhou, and J. Chang, *Electrospun nanofibrous materials for tissue engineering and drug delivery*. *Science and Technology of Advanced Materials*, 2010. 11(1).
62. G. Verreck, I. Chun, J. Rosenblatt, J. Peeters, A. Van Dijck, J. Mensch, M. Noppe, and M.E. Brewster, *Incorporation of drugs in an amorphous state into electrospun nanofibers composed of a water-insoluble, nonbiodegradable polymer*. *Journal of Controlled Release*, 2003. 92(3): p. 349-360.
63. S. Tungrapa, I. Jangchud, and P. Supaphol, *Release characteristics of four model drugs from drug-loaded electrospun cellulose acetate fiber mats*. *Polymer*, 2007. 48: p. 5030-5041.
64. E.R. Kenawy, G.L. Bowlin, K. Mansfield, J. Layman, D.G. Simpson, E.H. Sanders, and G.E. Wnek, *Release of tetracycline hydrochloride from electrospun poly(ethylene-co-vinylacetate), poly(lactic acid), and a blend*. *Journal of Controlled Release*, 2002. 81(1-2): p. 57-64.
65. Z. Jing, X.Y. Xu, X.S. Chen, Q.Z. Liang, X.C. Bian, L.X. Yang, and X.B. Jing, *Biodegradable electrospun fibers for drug delivery*. *Journal of Controlled Release*, 2003. 92(3): p. 227-231.
66. S. Fredenberg, M. Reslow, and A. Axelsson, *Encapsulated zinc salt increases the diffusion of protein through PLG films*. *International Journal of Pharmaceutics*, 2009. 370(1-2): p. 47-53.

67. W.G. Cui, X.H. Li, X.L. Zhu, G. Yu, S.B. Zhou, and J. Weng, *Investigation of drug release and matrix degradation of electrospun poly(DL-lactide) fibers with paracetamol inoculation*. *Biomacromolecules*, 2006. 7(5): p. 1623-1629.
68. Z.C. Sun, E. Zussman, A.L. Yarin, J.H. Wendorff, and A. Greiner, *Compound core-shell polymer nanofibers by co-electrospinning*. *Advanced Materials*, 2003. 15(22): p. 1929-1932.
69. R. Gopal, S. Kaur, Z.W. Ma, C. Chan, S. Ramakrishna, and T. Matsuura, *Electrospun nanofibrous filtration membrane*. *Journal of Membrane Science*, 2006. 281(1-2): p. 581-586.
70. P.P. Tsai, H. Schreuder-Gibson, and P. Gibson, *Different electrostatic methods for making electret filters*. *Journal of Electrostatics*, 2002. 54(3-4): p. 333-341.
71. R. Luoh and H.T. Hahn, *Electrospun nanocomposite fiber mats as gas sensors*. *Composites Science and Technology*, 2006. 66(14): p. 2436-2441.
72. X.Y. Wang, C. Drew, S.H. Lee, K.J. Senecal, J. Kumar, and L.A. Sarnuelson, *Electrospun nanofibrous membranes for highly sensitive optical sensors*. *Nano Letters*, 2002. 2(11): p. 1273-1275.
73. B. Ding, M.R. Wang, J.Y. Yu, and G. Sun, *Gas Sensors Based on Electrospun Nanofibers*. *Sensors*, 2009. 9(3): p. 1609-1624.
74. J.R. Kim, S.W. Choi, S.M. Jo, W.S. Lee, and B.C. Kim, *Electrospun PVDF-based fibrous polymer electrolytes for lithium ion polymer batteries*. *Electrochimica Acta*, 2004. 50: p. 69-75.
75. M.Y. Song, D.K. Kim, K.J. Ihn, S.M. Jo, and D.Y. Kim, *New application of electrospun TiO₂ solid-state dye-sensitized solar electrode to cells*. *Synthetic Metals*, 2005. 153(1-3): p. 77-80.
76. M.Y. Song, Y.R. Ahn, S.M. Jo, D.Y. Kim, and J.P. Ahn, *TiO₂ single-crystalline nanorod electrode for quasi-solid-state dye-sensitized solar cells*. *Applied Physics Letters*, 2005. 87: p. 113113-3.
77. E.J. Ra, K.H. An, K.K. Kim, S.Y. Jeong, and Y.H. Lee, *Anisotropic electrical conductivity of MWCNT/PAN nanofiber paper*. *Chemical Physics Letters*, 2005. 413: p. 188-193.
78. S. Prilutsky, E. Zussman, and Y. Cohen, *The effect of embedded carbon nanotubes on the morphological evolution during the carbonization of poly(acrylonitrile) nanofibers*. *Nanotechnology*, 2008. 19: p. 165603 (9pp).
79. S.J. Park and S.H. Im, *Electrochemical Behaviors of PAN/Ag-based Carbon Nanofibers by Electrospinning*. *Bull. Korean Chem. Soc.*, 2008. 29 (4): p. 777-781.
80. F. Ko, Y. Gogotski, A. Ali, N. Naguib, H. Ye, G. Yang, C. Li, and P. Willis, *Electrospinning continuous carbon nanotube-filled nanofiber yarns* *Adv. Mater.*, 2003. 15(14): p. 1161-1165.
81. Y. Xin, Z.H. Huang, L. Peng, and D.J. Wang, *Photoelectric performance of poly(p-phenylene vinylene)/Fe₃O₄ nanofiber array*. *Journal of Applied Physics*, 2009. 105(8).
82. K.H. Hong, J.L. Park, I.H. Sul, J.H. Youk, and T.J. Kang, *Preparation of Antimicrobial Poly(vinyl alcohol) Nanofibers Containing Silver Nanoparticles*. *Journal of Polymer Science: Part B: Polymer Physics*, 2006. 44: p. 2468-2474.

83. Y.B. Li, G. Chen, Q.H. Li, G.Z. Qiu, and X.H. Liu, *Facile synthesis, magnetic and microwave absorption properties of Fe₃O₄/polypyrrole core/shell nanocomposite*. Journal of Alloys and Compounds, 2011. 509(10): p. 4104-4107.
84. B.W. Li, Y. Shen, Z.X. Yue, and C.W. Nan, *Enhanced microwave absorption in nickel/hexagonal-ferrite/polymer composites*. Applied Physics Letters, 2006. 89(13): p. 132504-3.
85. C. Kim, K.S. Yang, M. Kojima, K. Yoshida, Y.J. Kim, Y.A. Kim, and M. Endo, *Fabrication of electrospinning-derived carbon nanofiber webs for the anode material of lithium-ion secondary batteries*. Advanced Functional Materials, 2006. 16(18): p. 2393-2397.
86. P.G. Bruce, B. Scrosati, and J.M. Tarascon, *Nanomaterials for rechargeable lithium batteries*. Angewandte Chemie-International Edition, 2008. 47(16): p. 2930-2946.
87. W. Watt, *Handbook of Composites*. Kelly, A. Rabotnov, Y. N. ed. Vol. Volume I. 1985: Holland: Elsevier Science Publishers B.V. 327-387.
88. Y. Wang, J.J. Santiago-Aviles, R. Furlan, and I. Ramos, *Pyrolysis temperature and time dependence of electrical conductivity evolution for electrostatically generated carbon nanofibers*. IEEE Transactions on Nanotechnology, 2003. 2(1): p. 39-43.
89. Y. Wang, I. Ramos, R. Furlan, and J.J. Santiago-Aviles, *Electronic transport properties of incipient graphitic domains formation in PAN derived carbon nanofibers*. IEEE Transactions on Nanotechnology, 2004. 3(1): p. 80-85.
90. C. Kim, K.S. Yang, and W.J. Lee, *The use of carbon nanofiber electrodes prepared by electrospinning for electrochemical supercapacitors*. Electrochemical and Solid State Letters, 2004. 7(11): p. A397-A399.
91. C. Kim and K.S. Yang, *Electrochemical properties of carbon nanofiber web as an electrode for supercapacitor prepared by electrospinning*. Applied Physics Letters, 2003. 83(6): p. 1216-1218.
92. J.K. Lee, K.W. An, J.B. Ju, B.W. Cho, W.I. Cho, D. Park, and K.S. Yun, *Electrochemical properties of PAN-based carbon fibers as anodes for rechargeable lithium ion batteries*. Carbon 2001. 39 p. 1299-1305.
93. J.H. He, Y.Q. Wan, and J.Y. Yu, *Effect of concentration on electrospun polyacrylonitrile (PAN) nanofibers*. Fibers and Polymers, 2008. 9(2): p. 140-142.
94. T. Wang and S. Kumar, *Electrospinning of polyacrylonitrile nanofibers*. Journal of Applied Polymer Science, 2006. 102(2): p. 1023-1029.
95. S.Y. Gu, J. Ren, and G.J. Vancso, *Process optimization and empirical modeling for electrospun polyacrylonitrile (PAN) nanofiber precursor of carbon nanofibers*. European Polymer Journal, 2005. 41(11): p. 2559-2568.
96. H.T. Niu, J. Zhang, Z.L. Xie, X.G. Wang, and T. Lin, *Preparation, structure and supercapacitance of bonded carbon nanofiber electrode materials*. Carbon. 49(7): p. 2380-2388.
97. F. Agend, N. Naderi, and R. Fareghi-Alamdari, *Fabrication and electrical characterization of electrospun polyacrylonitrile-derived carbon nanofibers*. Journal of Applied Polymer Science, 2007. 106(1): p. 255-259.
98. S. Dalton, F. Heatley, and P.M. Budd, *Thermal stabilization of polyacrylonitrile fibres*. Polymer, 1999. 40(20): p. 5531-5543.

99. D. Zhu, A. Koganemaru, C.Y. Xu, Q.D. Shen, S.L. Li, and M. Matsuo, *Oxidative stabilization of PAN/VGCF composite*. Journal of Applied Polymer Science, 2003. 87(13): p. 2063-2073.
100. Y. Wang, S. Serrano, and J.J. Santiago-Aviles, *Conductivity measurement of electrospun PAN-based carbon nanofiber*. Journal of Materials Science Letters, 2002. 21(13): p. 1055-1057.
101. S.H. Park, S.M. Jo, D.Y. Kim, W.S. Lee, and B.C. Kim, *Effects of iron catalyst on the formation of crystalline domain during carbonization of electrospun acrylic nanofiber*. Synthetic Metals 2005. 150 p. 265-270.
102. V.S. Babu and M.S. Seehra, *Modeling of Disorder and X-Ray Diffraction in Coal-based Graphitic Carbon*. Carbon 1996. 34: p. 1259-1265.
103. C. Kim, S.H. Park, J.K. Cho, D.Y. Lee, T.J. Park, W.J. Lee, and K.S. Yang, *Raman spectroscopic evaluation of polyacrylonitrile-based carbon nanofibers prepared by electrospinning*. Journal of Raman Spectroscopy, 2004. 35(11): p. 928-933.
104. T.-H. Ko, *The influence of pyrolysis on physical properties and microstructure of modified PAN fibers during carbonization*. Journal of Applied Polymer Science, 1991. Volume 43(Issue 3): p. pages 589-600.
105. http://www.irm.umn.edu/hg2m/hg2m_index.html.
106. J. Smit and H.P.J. Wijn, *Ferrites*. 1959: Eindhoven: John Wiley and Sons.
107. Z. Szotek, W.M. Temmerman, A. Svane, L. Petit, G.M. Stocks, and H. Winter, *Ab initio study of charge order in Fe₃O₄*. Physical Review B, 2003. 68(5).
108. B.D. Cullity, *Introduction to Magnetic Materials*. 1972: Reading: Addison-Wesley.
109. A.L. Lu, E.L. Salabas, and F. Schüth, *Magnetic NPs: synthesis, protection, functionalization, and application*. Angew. Chem. Int. Ed. , 2007. 46: p. 1222-1244.
110. D.J. Dunlop, *Phys. Earth Planet. Inter.* 1981. 26: p. 1-26.
111. <http://info.ee.surrey.ac.uk/Workshop/advice/coils/mu/#itns>.
112. Q.A. Pankhurst, J. Connolly, S.K. Jones, and J. Dobson, *Applications of magnetic nanoparticles in biomedicine*. Journal of Physics D-Applied Physics, 2003. 36(13): p. R167-R181.
113. D.J. Dunlop, *Phys. Earth Planet. Inter.* 1981. 26: p. 1-26.
114. D. Thapa, V.R. Palkar, M.B. Kurup, and S.K. Malik, *Properties of magnetite nanoparticles synthesized through a novel chemical route*. Materials Letters, 2004. 58(21): p. 2692-2694
115. D.J. Craik, *Magnetic oxides*. Vol. part 2. 1981, New York: Wiley. 703.
116. P. Poddar, J.L. Wilson, H. Srikanth, B.G. Ravi, J. Wachsmuth, and T.S. Sudarshan, *Grain size influence on soft ferromagnetic properties in Fe-Co nanoparticles*. Materials Science and Engineering B-Solid State Materials for Advanced Technology, 2004. 106(1): p. 95-100.
117. R.D. Sanchez, J. Rivas, P. Vaqueiro, M.A. Lopez-Quintela, and D. Caeiro, *Particle size effects on magnetic garnets prepared by a properties of yttrium iron sol-gel method*. Journal of Magnetism and Magnetic Materials, 2002. 247(1): p. 92-98.
118. D.L. Huber, *Synthesis, properties, and applications of iron nanoparticles*. Small, 2005. 1(5): p. 482-501.
119. C.C. Mi, J.P. Zhang, H.Y. Gao, X.L. Wu, M. Wang, Y.F. Wu, Y.Q. Di, Z.R. Xu, C.B. Mao, and S.K. Xu, *Multifunctional nanocomposites of superparamagnetic (Fe₃O₄) and*

- NIR-responsive rare earth-doped up-conversion fluorescent (NaYF₄:Yb, Er) nanoparticles and their applications in biolabeling and fluorescent imaging of cancer cells.* *Nanoscale*, 2010. 2(7): p. 1141-1148.
120. N. Arsalani, H. Fattahi, and M. Nazarpour, *Synthesis and characterization of PVP-functionalized superparamagnetic Fe₃O₄ nanoparticles as an MRI contrast agent.* *Express Polymer Letters*, 2010. 4(6): p. 329-338.
 121. D.L. Zhao, P. Teng, Y. Xu, Q.S. Xia, and J.T. Tang, *Magnetic and inductive heating properties of Fe₃O₄/polyethylene glycol composite nanoparticles with core-shell structure.* *Journal of Alloys and Compounds*, 2010. 502(2): p. 392-395.
 122. H. Zheng, Y. Yang, M. Zhou, and F. Li, *Microwave absorption and Mössbauer studies of Fe₃O₄ nanoparticles.* *Hyperfine Interact*, 2009. 189: p. 131-136.
 123. S.K. Dhawan, K. Singh, A.K. Bakhshi, and A. Ohlan, *Conducting polymer embedded with nanoferrite and titanium dioxide nanoparticles for microwave absorption.* *Synthetic Metals*, 2009. 159(21-22): p. 2259-2262.
 124. N. Hatoum. *Electromagnetic interferences (EMI) and their effect on the nervous system.* 2007.
 125. J.H. Wu and D.D.L. Chung, *Combined use of magnetic and electrically conductive fillers in a polymer matrix for electromagnetic interference shielding.* *Journal of Electronic Materials*, 2008. 37(8): p. 1088-1094.
 126. D.D.L. Chung, *Materials for electromagnetic interference shielding.* *Journal of Materials Engineering and Performance*, 2000. 9(3): p. 350-354.
 127. J.C. Wang, C.S. Xiang, Q. Liu, Y.B. Pan, and J.K. Guo, *Ordered Mesoporous Carbon/Fused Silica Composites.* *Advanced Functional Materials*, 2008. 18(19): p. 2995-3002.
 128. J. Rodriguez, *FATIGUE EVALUATION OF NANOCOMPOSITES AS LIGHTWEIGHT ELECTRONIC ENCLOSURES FOR SATELLITES' APPLICATIONS* in *Department of Aeronautics and Astronautics 2009*, Air Force Institute of Technology, Air University p. 104.
 129. <http://www.intlmag.org/phys23.html>.
 130. W. Mingzhong, Y.D. Zhang, S. Hui, T.D. Xiao, S. Ge, W.A. Hines, J.I. Budnick, and G.W. Taylor, *Microwave magnetic properties of Co₅₀/(SiO₂)₅₀ nanoparticles.* *Applied Physics Letters*, 2002. 80(23): p. 4404-4406.
 131. J.L. Violette, D.R. White, and M.F. Violette, *Electromagnetic Compatibility Handbook.* 1987, New York: Van Nostrand Reinhold Company.
 132. Z.F. Liu, G. Bai, Y. Huang, Y.F. Ma, F. Du, F.F. Li, T.Y. Guo, and Y.S. Chen, *Reflection and absorption contributions to the electromagnetic interference shielding of single-walled carbon nanotube/polyurethane composites.* *Carbon*, 2007. 45(4): p. 821-827.
 133. Y.K. Hong, C.Y. Lee, C.K. Jeong, D.E. Lee, K. Kim, and J. Joo, *Method and apparatus to measure electromagnetic interference shielding efficiency and its shielding characteristics in broadband frequency ranges.* *Review of Scientific Instruments*, 2003. 74(2): p. 1098-1102.
 134. D.D.L. Chung, *Electromagnetic interference shielding effectiveness of carbon materials.* *Carbon*, 2001. 39(2): p. 279-285.

135. K. Singh, A. Ohlan, A.K. Bakhshi, and S.K. Dhawan, *Synthesis of conducting ferromagnetic nanocomposite with improved microwave absorption properties*. *Materials Chemistry and Physics*, 2010. 119(1-2): p. 201-207.
136. S.W. Phang, T. Hino, M.H. Abdullah, and N. Kuramoto, *Applications of polyaniline doubly doped with p-toluene sulphonic acid and dichloroacetic acid as microwave absorbing and shielding materials*. *Materials Chemistry and Physics*, 2007. 104(2-3): p. 327-335.
137. K. Singh, A. Ohlan, R.K. Kotnala, A.K. Bakhshi, and S.K. Dhawan, *Dielectric and magnetic properties of conducting ferromagnetic composite of polyaniline with γ -Fe₂O₃ nanoparticles*. *Materials Chemistry and Physics* 2008. 112 p. 651-658.
138. K.Y. Park, J.H. Han, S.B. Lee, J.B. Kim, J.W. Yi, and S.K. Lee, *Fabrication and electromagnetic characteristics of microwave absorbers containing carbon nanofibers and magnetic metals*. *Behavior and Mechanics of Multifunctional and Composite Materials* 2008, 2008. 6929: p. G9292-G9292.
139. Z. Zou, A.G. Xuan, Z.G. Yan, Y.X. Wu, and N. Li, *Preparation of Fe₃O₄ particles from copper/iron ore cinder and their microwave absorption properties*. *Chemical Engineering Science*, 2010. 65(1): p. 160-164.
140. J.H. Zhou, J.P. He, G.X. Li, T. Wang, D. Sun, X.C. Ding, J.Q. Zhao, and S.C. Wu, *Direct Incorporation of Magnetic Constituents within Ordered Mesoporous Carbon-Silica Nanocomposites for Highly Efficient Electromagnetic Wave Absorbers*. *Journal of Physical Chemistry C*, 2010. 114(17): p. 7611-7617.
141. A. Ohlan, K. Singh, A. Chandra, and S.K. Dhawan, *Microwave Absorption Behavior of Core-Shell Structured Poly (3,4-Ethylenedioxy Thiophene)-Barium Ferrite Nanocomposites*. *Acs Applied Materials & Interfaces*, 2010. 2(3): p. 927-933.
142. S.L. Shi and J. Liang, *The effect of multi-wall carbon nanotubes on electromagnetic interference shielding of ceramic composites*. *Nanotechnology*, 2008. 19(25).
143. S.L. Shi, L.Z. Zhang, and J.S. Li, *Complex permittivity and electromagnetic interference shielding properties of Ti₃SiC₂/polyaniline composites*. *Journal of Materials Science*, 2009. 44(4): p. 945-948.
144. N.C. Das and S. Maiti, *Electromagnetic interference shielding of carbon nanotube/ethylene vinyl acetate composites*. *Journal of Materials Science*, 2008. 43(6): p. 1920-1925.
145. N. Li, Y. Huang, F. Du, X.B. He, X. Lin, H.J. Gao, Y.F. Ma, F.F. Li, Y.S. Chen, and P.C. Eklund, *Electromagnetic interference (EMI) shielding of single-walled carbon nanotube epoxy composites*. *Nano Letters*, 2006. 6(6): p. 1141-1145.
146. P.B. Jana, A.K. Mallick, and S.K. De, *Effects of Sample Thickness and Fiber Aspect Ratio on EMI Shielding Effectiveness of Carbon-Fiber Field Polychloroprene Composites in the X-band Frequency-Range*. *IEEE Transactions on Electromagnetic Compatibility*, 1992. 34(4): p. 478-481.
147. P.B. Jana, A.K. Mallick, and S.K. De, *Electromagnetic interference shielding effectiveness of short carbon fibre-filled polychloroprene vulcanized by barium ferrite*. *Journal of Materials Science*, 1993. 28: p. 2097-210.
148. F. Nanni, P. Travaglia, and M. Valentini, *Effect of carbon nanofibres dispersion on the microwave absorbing properties of CNF/epoxy composites*. *Composites Science and Technology*, 2009. 69(3-4): p. 485-490.

149. Y. Yang, M.C. Gupta, and K.L. Dudley, *Studies on electromagnetic interference shielding characteristics of metal nanoparticle- and carbon nanostructure-filled polymer composites in the Ku-band frequency*. *Micro & Nano Letters*, 2007. 2(4): p. 85-89.
150. S.Y. Yang, K. Lozano, A. Lomeli, H.D. Foltz, and R. Jones, *Electromagnetic interference shielding effectiveness of carbon nanofiber/LCP composites*. *Composites Part a-Applied Science and Manufacturing*, 2005. 36(5): p. 691-697.
151. J.G. Park, J. Louis, Q. Cheng, J. Bao, J. Smithyman, R. Liang, B. Wang, C. Zhang, J.S. Brooks, L. Kramer, P. Fanchasis, and D. Dorough, *Electromagnetic interference shielding properties of carbon nanotube buckypaper composites*. *Nanotechnology*, 2009. 20(41): p. 415702-9.
152. Y.L. Yang and M.C. Gupta, *Novel carbon nanotube-polystyrene foam composites for electromagnetic interference shielding*. *Nano Letters*, 2005. 5(11): p. 2131-2134.
153. D.A. Dimitrov and G.M. Wysin, *Magnetic Properties of Spherical Fcc Clusters with Radial Surface Anisotropy*. *Physical Review B*, 1995. 51(17): p. 11947-11950.
154. Y.Y. Wang and X.L. Jing, *Intrinsically conducting polymers for electromagnetic interference shielding*. *Polymers for Advanced Technologies*, 2005. 16(4): p. 344-351.
155. X.L. Jing, Y.Y. Wang, and B.Y. Zhang, *Electrical conductivity and electromagnetic interference shielding of polyaniline/polyacrylate composite coatings*. *Journal of Applied Polymer Science*, 2005. 98(5): p. 2149-2156.
156. Y. Yang, C.M. Gupta, K.L. Dudley, and R.W. Lawrence, *Conductive Carbon Nanofiber-Polymer Foam structure*. *Adv. Mater.*, 2005. 17: p. 1999-2003
157. Y. Huang, N. Li, Y.F. Ma, D. Feng, F.F. Li, X.B. He, X. Lin, H.J. Gao, and Y.S. Chen, *The influence of single-walled carbon nanotube structure on the electromagnetic interference shielding efficiency of its epoxy composites*. *Carbon*, 2007. 45(8): p. 1614-1621.
158. R.C. Che, L.M. Peng, X.F. Duan, Q. Chen, and X.L. Liang, *Microwave absorption enhancement and complex permittivity and permeability of Fe encapsulated within CNTs*. *Adv. Mater.*, 2004. 16: p. 401-405.
159. B.O. Lee, W.J. Woo, and M.S. Kim, *EMI shielding effectiveness of carbon nanofiber filled poly(vinyl alcohol) coating materials*. *Macromolecular Materials and Engineering*, 2001. 286(2): p. 114-118.
160. S.W. Phang, M. Tadokoro, J. Watanabe, and N. Kuramoto, *Effect of Fe₃O₄ and TiO₂ addition on the microwave absorption property of polyaniline micro/nanocomposites*. *Polymers for Advanced Technologies*, 2009. 20(6): p. 550-557.
161. N.F. Colaneri and L.W. Shacklette, *EMI shielding measurements of conductive polymer blends*. *IEEE Transactions on Instrumentation and Measurement*, 1992. Vol. 41.
162. S. Ramo, J.R. Whinnery, and T.V. Duzer, *Fields and Waves in Communication Electronics*. 1984 Wiley, New York.
163. X.F. Zhang, X.L. Dong, H. Huang, Y.Y. Liu, W.N. Wang, X.G. Zhu, B. Lv, J.P. Lei, and C.G. Lee, *Microwave absorption properties of the carbon-coated nickel nanocapsules*. *Applied Physics Letters*, 2006. 89(5).
164. S.L. Liu, L. Zhang, J.P. Zhou, and R.X. Wu, *Structure and properties of cellulose/Fe₂O₃ nanocomposite fibers spun via an effective pathway*. *Journal of Physical Chemistry C*, 2008. 112(12): p. 4538-4544.

165. D.S. Knight and W.B. White, *CHARACTERIZATION OF DIAMOND FILMS BY RAMAN-SPECTROSCOPY*. Journal of Materials Research, 1989. 4(2): p. 385-393.
166. Z.P. Zhou, C.L. Lai, L.F. Zhang, Y. Qian, H.Q. Hou, D.H. Reneker, and H. Fong, *Development of carbon nanofibers from aligned electrospun polyacrylonitrile nanofiber bundles and characterization of their microstructural, electrical, and mechanical properties*. Polymer, 2009. 50(13): p. 2999-3006.
167. K. Matsutani, K. Hayakawa, and T. Tada, *Effect of Particle Size of Platinum and Platinum-Cobalt Catalysts on Stability Against Load Cycling*. Platinum Metals Review. 54(4): p. 223-232.
168. K.S. Han, Y.S. Moon, O.H. Han, K.J. Hwang, I. Kim, and H. Kim, *Heat treatment and potential cycling effects on surface morphology, particle size, and catalytic activity of Pt/C catalysts studied by C-13 NMR, TEM, XRD and CV*. Electrochemistry Communications, 2007. 9(2): p. 317-324.
169. V. Suresh Babu and M.S. Seehra, *Modeling of Disorder and X-Ray Diffraction in Coal-based Graphitic Carbon*. Carbon 1996. Vol. 34(No. 10): p. 1259-1265.
170. Y. Kaburagi, Y. Hishiyama, H. Oka, and M. Inagaki, *Growth of iron clusters and change of magnetic property with carbonization of aromatic polyimide film containing iron complex*. Carbon, 2001. 39(4): p. 593-603.
171. S.R. Dhakate, R.B. Mathur, and O.P. Bahl, *Catalytic effect of iron oxide on carbon/carbon composites during graphitization*. Carbon, 1997. 35(12): p. 1753-1756.
172. M. Inagaki., Y. Okada, V. Nignal, H. Konno, and K. Oshida, *Graphite formation from a mixture of Fe₃O₄ and polyvinylchloride at 1000°C*. Carbon, 1998. 36(11): p. 1706-1708.
173. Y.G. Wang, Y. Korai, I. Mochida, K. Nagayama, H. Hatano, and N. Fukuda, *Modification of synthetic mesophase pitch with iron oxide, Fe₂O₃*. Carbon, 2001. 39(11): p. 1627-1634.
174. P. Kim, J.B. Joo, J. Kim, W. Kim, I.K. Song, and J. Yi, *Sucrose-derived graphitic porous carbon replicated by mesoporous silica*. Korean Journal of Chemical Engineering, 2006. 23(6): p. 1063-1066.
175. X.L. Dong, Z.D. Zhang, Q.F. Xiao, X.G. Zhao, Y.C. Chuang, S.R. Jin, W.M. Sun, Z.J. Li, Z.X. Zheng, and H. Yang, *Characterization of ultrafine c-Fe(C), a-Fe(C) and Fe₃C particles synthesized by arc-discharge in methane*. Journal of Materials Science, 1998. 33 p. 1915-1919.
176. J. Xu, H. Yang, W. Fu, Y. Sui, H. Zhu, M. Li, and G. Zou, *Preparation and characterization of carbon fibers coated by Fe₃O₄ nanoparticles*. Materials Science and Engineering B, 2006. 132: p. 307-310.
177. I. Mochida, S.H. Yoon, and W.M. Qiao, *Catalysts in syntheses of carbon and carbon precursors*. Journal of the Brazilian Chemical Society, 2006. 17(6): p. 1059-1073.
178. F.J. Maldonado-Hodar, C. Moreno-Castilla, J. Rivera-Utrilla, Y. Hanzawa, and Y. Yamada, *Catalytic graphitization of carbon aerogels by transition metals*. Langmuir, 2000. 16(9): p. 4367-4373.
179. J.M. Skowronski and K. Knofczynski, *Catalytically graphitized glass-like carbon examined as anode for lithium-ion cell performing at high charge/discharge rates*. Journal of Power Sources, 2009. 194(1): p. 81-87.

180. M. Inagaki, K. Fujita, Y. Takeuchi, K. Oshida, H. Iwata, and H. Konno, *Formation of graphite crystals at 1000–1200°C from mixtures of vinyl polymers with metal oxides*. Carbon, 2001. 39 p. 921-929.
181. J. Huo, H. Song, X. Chen, S. Zhao, and C. Xu, *Structural transformation of carbon-encapsulated iron nanoparticles during heat treatment at 1000 °C*. Materials Chemistry and Physics 2007. 101: p. 221-227.
182. W. Qian, J.F. Chen, L.S. Wu, F.Y. Cao, and Q.W. Chen, *Synthesis of polygonized carbon nanotubes utilizing inhomogeneous catalyst activity of nonspherical Fe₃O₄ nanoparticles*. Journal of Physical Chemistry B, 2006. 110(33): p. 16404-16407.
183. M. Panapoy, A. Dankeaw, and B. Ksapabutr, *Electrical Conductivity of PAN-based Carbon Nanofibers Prepared by Electrospinning Method*. Thammasat Int. J. Sc. Tech., 2008. 13: p. 11-17.
184. Z. Zhu, Z. Liu, and Y. Gu, *Formation of N₂ during carbonization of polyacrylonitrile using iron catalyst*. Fuel 1997. 76(2).
185. A. Oya and H. Marsh, *Review Phenomena of catalytic graphitization*. Journal of Materials Science 1982. 17: p. 309--322.
186. K.R. Reddy, B.C. Sin, K.S. Ryu, J.C. Kim, H. Chung, and Y. Lee, *Conducting polymer functionalized multi-walled carbon nanotubes with noble metal nanoparticles: Synthesis, morphological characteristics and electrical properties*. Synthetic Metals, 2009. 159(7-8): p. 595-603.
187. A.H. Chen, H.Q. Wang, and X.Y. Li, *Influence of concentration of FeCl₃ solution on properties of polypyrrole-Fe₃O₄ composites prepared by common ion absorption effect*. Synthetic Metals, 2004. 145(2-3): p. 153-157.
188. L. Fang, T. Dai, and Y. Lu, *Electromagnetic composite films based on polypyrrole hydro-sponge and Fe₃O₄ ferrofluid*. Synthetic Metals 2009. 159: p. 2101-2107.
189. Richard J. Harrison, Rafal E. Dunin-Borkowski, and A. Putnis, *Direct imaging of nanoscale magnetic interactions in minerals*. PNAS, 2002. 99(26): p. 16556–16561.
190. Y. Watanabe, J. Murakami, and H. Miura, *Effect of annealing on saturation magnetization in deformed Cu-Fe alloys with transformed Fe particles*. Materials Science and Engineering a-Structural Materials Properties Microstructure and Processing, 2002. 338(1-2): p. 299-304.
191. O. Schneeweiss, R. Zboril, N. Pizurova, M. Mashlan, E. Petrovsky, and J. Tucek, *Novel solid-state synthesis of alpha-Fe and Fe₃O₄ nanoparticles embedded in a MgO matrix*. Nanotechnology, 2006. 17(2): p. 607-616.
192. H.T. Yang, T. Ogawa, D. Hasegawa, and M. Takahashi, *Shape-controlled synthesis of Fe nanoparticles with high-Ms via modest-temperature reduction method*. phys. stat. sol. (a) 2007. 204(No. 12): p. 4013-4016
193. E.P. Sajitha, V. Prasad, S.V. Subramanyam, S. Eto, K. Takai, and T. Enoki, *Synthesis and characteristics of iron nanoparticles in a carbon matrix along with the catalytic graphitization of amorphous carbon*. Carbon, 2004. 42(14): p. 2815-2820.
194. C.-R. Lin, Chu, Yuan-Ming, Wang, Sheng-Chang *Magnetic properties of magnetite nanoparticles prepared by mechanochemical reaction*. Materials Letters, 2006. 60: p. 447-450.

195. C. Liu, Zhang, Z. John, *Size-Dependent Superparamagnetic Properties of Mn Spinel Ferrite Nanoparticles Synthesized from Reverse Micelles*. Chem. Mater. , 2001. 13: p. 2092-2096.
196. K.Y. Park, S.E. Lee, C.G. Kim, and J.H. Han, *Application of MWNT-added glass fabric/epoxy composites to electromagnetic wave shielding enclosures*. Composite Structures, 2007. 81(3): p. 401-406.
197. K.Y. Park, S.E. Lee, C.G. Kim, and J.H. Han, *Fabrication and electromagnetic characteristics of electromagnetic wave absorbing sandwich structures*. Composites Science and Technology, 2006. 66(3-4): p. 576-584.
198. H.M. Kim, K. Kim, C.Y. Lee, J. Joo, S.J. Cho, H.S. Yoon, D.A. Pejakovic, J.W. Yoo, and A.J. Epstein, *Electrical conductivity and electromagnetic interference shielding of multiwalled carbon nanotube composites containing Fe catalyst*. Applied Physics Letters, 2004. 84(4): p. 589-591.
199. J.X. Qiu, H.G. Shen, and M.Y. Gu, *Microwave absorption of nanosized barium ferrite particles prepared using high-energy ball milling*. Powder Technology, 2005. 154(2-3): p. 116-119.
200. N.C. Das, Y.Y. Liu, K.K. Yang, W.Q. Peng, S. Maiti, and H. Wang, *Single-Walled Carbon Nanotube/Poly(methyl methacrylate) Composites for Electromagnetic Interference Shielding*. Polymer Engineering and Science, 2009. 49(8): p. 1627-1634.
201. I. Huynen, L. Bednarz, J.M. Thomassin, C. Pagnouille, R. Jerome, and C. Detrembleur, *Microwave absorbers based on foamed nanocomposites with graded concentration of carbon nanotubes*. 2008 European Microwave Conference, Vols 1-3, 2008: p. 1514-1517.
202. X.G. Zhang, Y. Liu, and J.G. Qin, *The dielectric properties of (N-doped carbon)- and carbon-coated iron nanocrystals in the X band*. Carbon, 2004. 42(4): p. 888-890.
203. J.R. Liu, M. Itoh, T. Horikawa, K. Machida, S. Sugimoto, and T. Maeda, *Gigahertz range electromagnetic wave absorbers made of amorphous-carbon-based magnetic nanocomposites*. Journal of Applied Physics, 2005. 98(5).
204. B.K. Kuanr, V. Veerakumar, K. Lingam, S.R. Mishra, A.V. Kuanr, R.E. Camley, and Z. Celinski, *Size dependent microwave properties of ferrite nanoparticles: Application to microwave devices*. Journal of Applied Physics, 2009. 105(7).
205. J.L. Kirschvink, *Microwave absorption by magnetite: A possible mechanism for coupling nonthermal levels of radiation to biological systems*. Bioelectromagnetics, 1996. 17(3): p. 187-194.